

Freie Universität  Berlin

Optimal control of ladle stirring

Dissertation

zur Erlangung des Grades eines
Doktors der Naturwissenschaften (Dr. rer. nat.)
am Fachbereich Mathematik und Informatik
der Freien Universität Berlin

vorgelegt von

Najib Alia

Berlin, Juli 2019

- 1. Gutachter:** Prof. Dr. Volker John (Betreuer)
Freie Universität Berlin und
Weierstraß-Institut für Angewandte Analysis und Stochastik, Berlin
- 2. Gutachter:** Prof. Dr. Timo Fabritius
University of Oulu, Oulu

Tag der Disputation: 30 Oktober 2019

Abstract

This thesis studies the mathematical modeling, simulation, and optimization of an industrial process called steel ladle stirring. In this process, gas is injected continuously from the bottom of the bath and rises by buoyancy through the liquid steel, thereby causing a turbulent stirring, i.e., a mixing of the bath. The process has been extensively studied in the literature both experimentally and numerically in order to understand the influence of control parameters on the stirring and to improve the mixing conditions in the industrial practice. Nevertheless, optimal control problems in mathematical sense have still to be explored in this area. The main contributions of this thesis can be divided into three parts.

First, multiphase modeling of ladle stirring can become computationally expensive, especially when used within optimal flow control problems. This is why this thesis focuses on simplified models based on the single-phase incompressible Navier–Stokes equations. Three variants are formulated: a 2d Cartesian model, where the effect of the gas is modeled as a vertical boundary velocity, a 2d axial-symmetrical one with a central nozzle where it is modeled as a buoyancy force, and a 3d model of a laboratory-scale real ladle with two excentric nozzles, where the gas also appears as a volume force. The main differences with existing models from the literature are highlighted, and numerical simulations are compared with experimental measurements.

Second, optimal control problems are investigated. The main difficulties come, on the one hand, from the formulation of the actual industrial problem, and, on the other hand, on the mathematical formulation of the control and cost functionals. In practice, the main control parameter is the volumetric flow rate of the injected gas. In addition, process constraints have to be taken into account. Due to the complexity of the industrial problem, several overlapping objectives are involved, such as maximize homogenization, minimize treatment time, minimize concentrations of inclusions, etc. A mathematical translation of the practical control and constraints is given, leading to so-called box constraints, and several cost functionals are proposed to describe the stirring efficiency. Numerical simulations are performed and conclusions are drawn for the industrial practice.

Finally, as part of the cooperation project with the industrial partner, the main technological solutions for ladle stirring control are reviewed, leading to the choice of vibrations sensors. Thus, an experimental investigation of the vibrations of ladle stirring is conducted. This allows to formulate some practical recommendations for the industrial practice and improves our understanding of vibration phenomena for future modeling work.

Acknowledgments

I am sincerely grateful to my advisor Prof. Dr. Volker John who gave me the opportunity to join his group in the Weierstrass Institute and to work on this project. His constant availability, his valuable feedbacks, and his investment were of decisive help during my thesis. I thank him for his strong support, his patience, and also the weekly discussions we had when I was in Finland, at distance from WIAS. I could not have imagined a better advisor for my thesis.

I am also thankful to my industrial advisor Seppo Ollila. His warm welcome in SSAB contrasted with the cold Finnish weather and made my stay in Finland a nice experience. Not to mention the enriching discussions we had about the industrial practice and his readiness to provide information and help.

I would like to thank Prof. Timo Fabritius, Head of the Process Metallurgy Research Unit in the University of Oulu, for having accepted being a reviewer of my thesis.

To the organizers of the project MIMESIS, Prof. Dietmar Hömberg and Dr. Thomas Petzold, who offered to my doctoral fellows and myself the ideal conditions to fulfill our PhDs, as well as important ideas to progress in our work. Thank you for accompanying us all along these years. I would like to acknowledge Dr. Ville-Valtteri Visuri, with whom I had regular and fruitful discussions during my stay in Finland, Mika Pylvänäinen, Eshwar Ramasetti for their special support, and all the people from the University of Oulu, from SSAB, and from Outokumpu, who helped in the organization of my secondments in the Northern regions of Finland. I also would like to say thank you to all my MIMESIS fellows, especially Manuel, for the nice time we shared during the project.

Coming back to Germany, I am very grateful to my colleagues from WIAS. Thank you to Dr. Alfonso Caiazzo and Dr. Alexander Linke for their support. I wish to express in particular my deepest appreciation to Clemens and Ulrich for their help. It was a great chance to work with them. To everyone who shared an interesting idea, a wise advice, or a nice word, thank you.

Finally, I would like to tell my gratitude and love to all my friends and my family. To my beloved brother and sister, thank you for your presence. And to my mother and my father. The best way to express my gratitude towards you is to say “My Lord, have mercy upon them as they brought me up when I was small”.

رَبِّ اَرْحَمَهُمَا كَمَا رَبَّيْتَانِي صَغِيرًا،

وَالْحَمْدُ لِلّٰهِ رَبِّ الْعَالَمِينَ.

À mes parents.

Contents

1	Introduction	5
1.1	Industrial context	5
1.1.1	Advanced high-strength steels	5
1.1.2	Ladle stirring	7
1.1.3	Process control in the industrial practice	9
1.2	Experimental ladles and numerical modeling	10
1.2.1	Laboratory-scale ladle stirring	10
1.2.2	Numerical ladle stirring	12
1.3	Objective	13
1.4	Main contributions	14
1.5	Outline	14
2	The time-dependent incompressible Navier–Stokes equations	17
2.1	Introduction	18
2.1.1	Partial Differential Equations	18
2.1.2	Boundary and initial conditions	23
2.1.3	Summary	26
2.2	Theoretical background	27
2.2.1	Weak formulation	27
2.2.2	A few words about existence and uniqueness	28
2.3	Numerical methods	29
2.3.1	Time discretization and linearization	30
2.3.2	Space discretization and the Galerkin Finite Element Method	32
2.3.3	Axisymmetric formulation	38
2.4	Linear solvers	39
2.4.1	Introduction	39
2.4.2	FGMRES with LSC preconditioner	40
2.5	Turbulence	41
2.5.1	Physical and mathematical background	42
2.5.2	Large Eddy Simulation (LES) Smagorinsky turbulence model	43
2.5.3	Other turbulence models	46
3	Single-phase models for ladle stirring	47
3.1	Literature review	48
3.1.1	Definitions of the gas phase fraction α	48
3.1.2	Boundary conditions	52

3.1.3	Reynolds number in ladle stirring	53
3.2	Description of the models	54
3.2.1	The 2d boundary-driven ladle model	55
3.2.2	The 2d axisymmetric ladle model	57
3.2.3	The 3d ladle model	59
3.3	Numerical results in 2d	61
3.3.1	Implementation	63
3.3.2	Numerical solution	65
3.3.3	Comparison with experimental measurements	70
3.3.4	Comparison with the commercial software COMSOL	73
3.3.5	Summary and outlook to 3d	73
3.4	Numerical results in 3d	75
3.4.1	Implementation	75
3.4.2	Preliminary study with $Re = 1$	76
3.4.3	Numerical results	77
3.5	Conclusion	81
4	Optimal flow control in the ladle	85
4.1	Industrial problem	86
4.1.1	Physical control and constraints	87
4.1.2	Physical objectives	92
4.2	Mathematical modeling of the control and objective functionals	94
4.2.1	Control variables	94
4.2.2	Objective functionals: review and discussion	96
4.2.3	First objective: Maximization of vorticity	97
4.2.4	Second objective: Regulation of vorticity	98
4.2.5	Control cost	99
4.3	Optimal flow control problem	100
4.3.1	Definition of the optimal control problem	101
4.3.2	Formal derivation of the optimality system	102
4.3.3	Adjoint equations and optimality conditions	107
4.3.4	Numerical aspects: gradient-based vs. gradient-free solvers	112
4.4	Numerical results for the 2d boundary-driven ladle	113
4.4.1	Description of the numerical studies	113
4.4.2	Results with constant control	115
4.4.3	Results with time-dependent control	117
4.4.4	Summary and outlook to 3d	120
4.5	Numerical results for the 3d ladle	121
4.5.1	Description of the numerical studies	121
4.5.2	Results with constant control	123
4.5.3	Results with time-dependent control	126
4.5.4	Optimization of the nozzles' positions	130
4.5.5	Summary	134
4.6	Conclusion	135
4.6.1	Limits and outlook	135
4.6.2	Towards new approaches for the optimal stirring control	137

5	Ladle vibrations induced by gas stirring: a first step towards an operational stirring control	139
5.1	Literature review of stirring control techniques	140
5.2	Description of the industrial process	142
5.2.1	Vacuum tank degasser (VTD)	142
5.2.2	Vibrations of the VTD	143
5.2.3	From industrial to laboratory measurements	143
5.3	Laboratory-scale ladle experiment with multiple sensors	145
5.3.1	Experimental set-up	145
5.3.2	Experimental results	146
5.4	Conclusion	148
6	Conclusion	151
	Appendix A Detailed form of the Navier–Stokes equations	153
A.1	In Cartesian coordinates (x, y, z)	153
A.2	In cylindrical coordinates (r, θ, z)	154
	Appendix B Unit convention for gas flow rates	157
	List of notations	159
	List of abbreviations	165
	List of units	167
	Bibliography	169

1. Introduction

1.1 Industrial context

1.1.1 Advanced high-strength steels

Steel is one of the most used and versatile materials in the world. The alloying of iron with a small percentage of carbon and other elements can lead to very different material properties and can be thus adapted to different application sectors: buildings, bridges, cars, machines, home equipment, etc. One small but important family of steels is known as advanced high-strength steels (AHSS). They fulfill, more specifically, the needs of the mining, building, and automotive markets.

Applications and material properties. For example, companies from the mining sector can use high performance steels instead of standard ones in order to increase the lifetime of their hoppers, containers, and excavation equipment (Figure 1.1), and achieve more cost-efficient operations. Indeed, such steels have a composition which yields higher strength, hardness, and resistance to surface damage like abrasion or erosion (also called wear resistance) than standard steels. Cranes in the building industry are another examples of steel-based products which need to be as strength and as light as possible to increase their payload. The vehicle frames in the car industry also illustrate the need for steel-based products to be crash resistant for the safety of its passengers and to be light to reduce energy consumption and CO₂ emissions. Furthermore, the automotive market increasingly needed ductile and strong steels as the car producers intensively used deep drawing to produce more complex and esthetic body panels.



Figure 1.1: Applications of advanced high-strength steels for the mining and automotive sectors. Left: wear-resistant hoppers. Right: deep drawn car inner door.

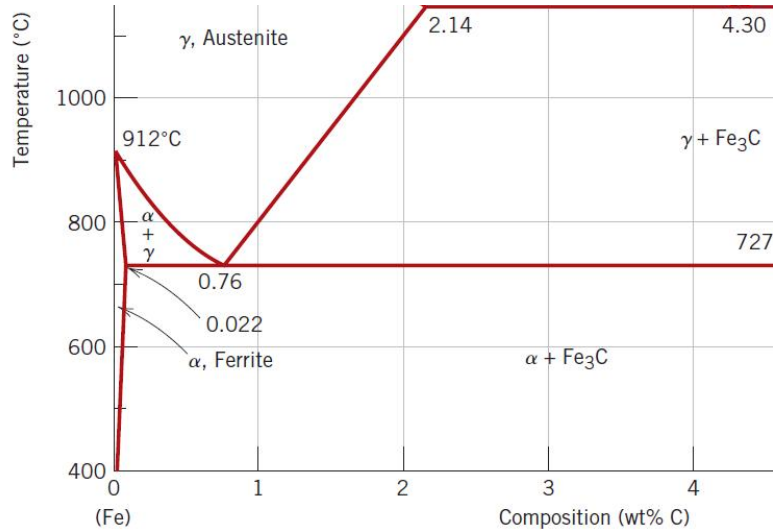


Figure 1.2: Zoom in the iron-iron carbide phase diagram (Callister, 2007). With a carbon content lower than 0.022 wt% (or 220 ppm), ULC and IF steels are on the left side of the diagram. They are mainly composed of α -ferrite, like pure iron.

This process is possible only if the metal sheets are highly ductile and do not crack during the drawing. The ultra-low carbon (ULC) steels and interstitial-free (IF) steels, which have a carbon content between 60 and 200 ppm, and inferior to 30 ppm, respectively (Takechi, 1994, Hoile, 2000), match these requirements. They are used, for instance, for front and rear inner doors (Figure 1.1) or spare wheel wells.

Microstructure of ULC and IF steels. At such a low level of carbon, the steel is composed mainly of one phase at room temperature: the α -ferrite phase, as illustrated in the equilibrium phase diagram of iron-iron carbide system (Figure 1.2). The α -ferrite is an iron-carbon solid solution and has a Body-Centered Cubic (BCC) crystal structure in which carbon is an interstitial impurity (Figure 1.3). In the BCC α -ferrite, only small concentrations of carbon are soluble; the maximum solubility is 0.022 wt% at 727 °C. This limit is explained by the shape and size of the BCC interstitial positions, which make it difficult to accommodate the carbon atoms (Callister, 2007). This crystal structure and the low level of carbon play an important role in the mechanical performance of the steel.

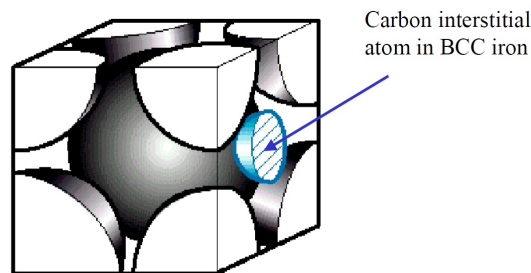


Figure 1.3: Interstitial impurity in a ferrite BCC unit cell (Callister, 2007).

A low level of C and N in the interstices of the steel is more beneficial for high formability. If these particles remain in the liquid steel, they will be imprisoned during solidification, resulting in a weak point in the steel where cracks are more likely to appear, provoking early brittle fracture.

1.1.2 Ladle stirring

In order to manage the manufacturing of such high performance steels, the steel-making companies refine the liquid steel in a process called refinement metallurgy. The ladle stirring is a central part of this process.

Place of ladle stirring in the steelmaking process. The steelmaking process is composed of two main steps: the primary metallurgy and the secondary metallurgy (Figure 1.4). In the primary metallurgy, the solid material (iron ore or scrap) is transformed into liquid iron, which is then converted to liquid steel. The first transformation takes place in Blast Furnaces (BFs), while the second transformation is done in converters, for example in Basic Oxygen Furnaces (BOFs) or Electric Arc Furnaces (EAFs). The liquid steel obtained in the converter needs to be refined to reach the quality required by the client in terms of steel grade. This refinement is done during the secondary metallurgy process in tanks called *ladles* (Figure 1.5, left). The secondary metallurgy is thus also called refinement metallurgy or *ladle metallurgy*.

Description of the process. The refinement process starts when the liquid steel obtained in the converter is transferred into the ladle. The bath is stirred by injecting a gas from the bottom of the ladle through one or several gas nozzles (Figure 1.5, right). Usually, the gas used for stirring is argon, as it does not react chemically with the liquid steel. Induction stirring is also used in some cases. The stirring enhances the composition and temperature homogenization, as well as chemical reactions and removal of impurities. During ladle stirring, a slag phase floats on the top of the steel. It is a viscous liquid phase which is formed from added materials and from reaction products during treatments. The slag is necessary for the chemical reactions and it also acts as a thermal insulation layer. The refractory bricks cover the inner ladle wall and are resistant to high temperatures and chemical wear. They form the *refractory lining*. The main objective of ladle stirring is to obtain the final steel grade required by the customer.

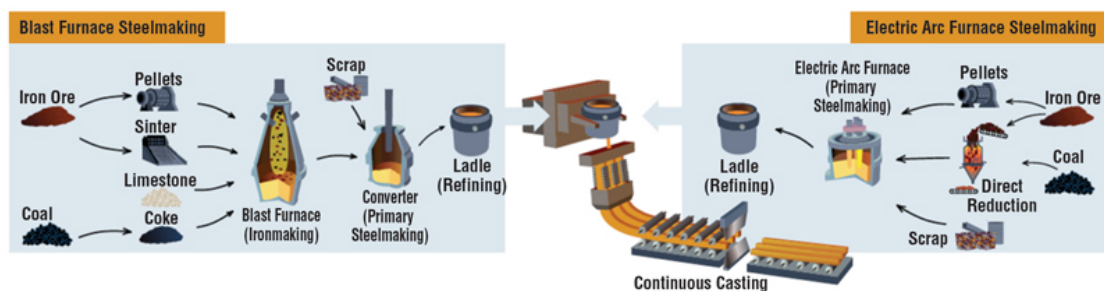


Figure 1.4: Overview of the steelmaking process (World Steel Association).

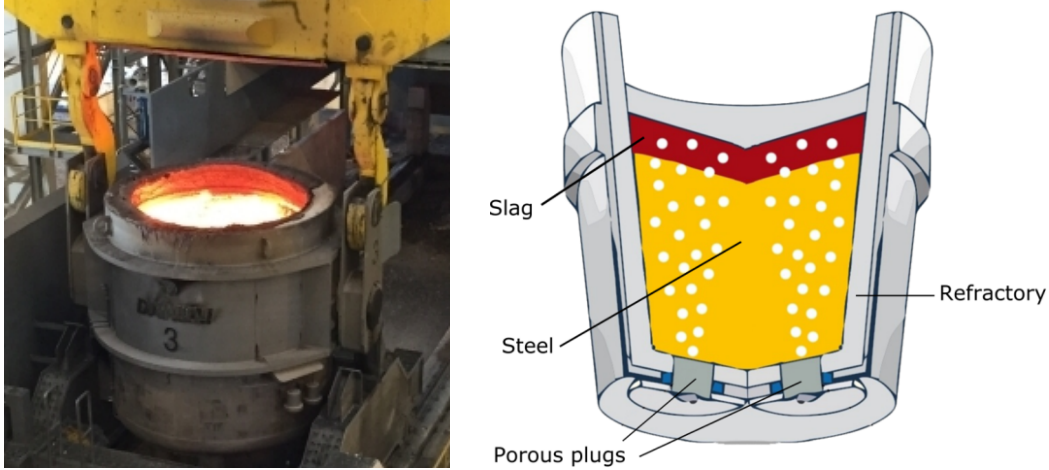


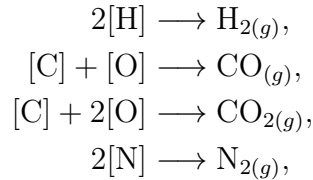
Figure 1.5: Photograph of a real ladle and scheme of ladle stirring.

Several operations take place during ladle stirring to reach this objective (Kor and Glaws, 1998):

- addition of alloying elements to reach the right composition,
- temperature adjustment before casting, if needed,
- composition and temperature homogenization of the liquid steel bath, and
- removal of unwanted inclusions such as oxides, sulfurs, and gas elements (O, H, C, N). These last reactions are equivalently referred to as *deoxidation*, *dehydrogenation*, *decarburization*, and *denitrogenation*.

Different types of treatments exist depending on the steel grade required. For example, in order to obtain ULC and IF steels, it is necessary to reduce significantly the carbon and nitrogen solutes from the ferrite matrix. An effective suppression of these elements can be achieved with vacuum degassing.

Vacuum degassing and reduction of interstitial impurities. Vacuum degassing consists of making ladle stirring in vacuum conditions. It allows to reach a higher purity in the steel. Indeed, the vacuum created in the ladle induces a lower pressure of gases such as H_2 , CO , CO_2 , and N_2 , which induces an increased activity of the following degassing reactions (Kor and Glaws, 1998):



where the index (g) stands for gas and the left-hand sides of the reactions describe species dissolved in the liquid steel. This process can achieve very low carbon and nitrogen contents. Typically, the standard Vacuum Tank Degassers (VTD) can reduce C and N below 30 ppm, while the RH degassing technology can reduce C to as far as 10 ppm (Kor and Glaws, 1998).

To give an idea of the production rate of high performance steels with VTDs, we cite the example of the Swedish company SSAB and its plant in Raahé, Finland. From the 2.5 Mt/year of steel produced, 20% go through the VTD of the plant.

For information, the VTD has a capacity of 105 tons, i.e., each *heat* being processed weighs 105 tons. The typical duration of vacuum processing is 40 to 50 minutes and the operation is performed around 15 times each day. Since this work is a joint cooperation with SSAB and may have a potential application on its VTD, we will discuss the vacuum case at several sections of the thesis.

Subsequent production steps. It should be kept in mind that ladle stirring is only one small part of the complex steel production process. The microstructure and properties of the final product depend strongly on various process parameters acting in the following steps, e.g., hot rolling, coiling, cold reduction, and annealing processes, each of which plays a role on the formation of the precipitates, on the grain size and on the recrystallization texture. Careful controls of all process steps are necessary to achieve required AHSS. In the case of deep drawing steels for example, the hot rolling process should reduce the grain size as much as possible, while cold rolling and annealing should optimize the grains for formability. Details on the process parameters can be found in (Hoile, 2000).

1.1.3 Process control in the industrial practice

In practice, the main parameters influencing the refinement process are:

- the flow rate of the stirring gas injected: the higher the flow rate, the more intense the stirring, and
- the duration of the process: the longer the process, the higher the removal of impurities.

Other parameters also play a role on the stirring, for instance, the position of the gas injection nozzles or the vacuum pressure in the case of a VTD. However, in the industrial practice, they are usually fixed.

Issues in practice. The values of each parameter are determined by a balance between quality requirements and operational costs. For example, one could operate with the maximum gas flow rate to enhance the removal of impurities, but this has several drawbacks, e.g.:

- increased consumption of gas,
- splashes of steel on top of the slag, causing material loss, or outside the ladle, causing safety concerns,
- increased damaging of the refractory lining on the ladle walls (and, consequently, maintenance costs).

On the other hand, operating a too low flow rate could be not enough to obtain the required purity. Moreover, several known problems make it difficult to manage the stirring operation properly:

- gas leakage or failure in the gas injection system,
- clogging of a gas injection nozzle, due to solidified steel located on the nozzle or a too low gas pressure,
- gas flowing preferentially in the porous refractory bricks surrounding the nozzle: this phenomena is also called gas channeling.

These failures have often several, technical and process-related, causes and are generally difficult to tackle.

Process optimization. An a posteriori quality control based on metal samples checks if the steel grade is correct. If it is not the case, the whole heat which was treated in the VTD has to be downgraded. It is thus necessary to find the right parameters to reduce costs (gas consumption, process duration, maintenance costs) while achieving a given level of steel quality. One way to optimize the stirring control is to use numerical modeling.

1.2 Experimental ladles and numerical modeling

A relevant numerical modeling of ladle stirring requires to understand the complex mixing happening inside the ladle and to have precise measurements of physical quantities in order to validate the computed results. However, in-situ observation of the stirring is almost unfeasible in the industrial practice due to the extreme conditions inside ladles. For this reason, laboratory experiments have been developed since the middle of the XXth century. Thanks to geometrical and physical similarities, ladle stirring in experimental set-ups can approximately reproduce real industrial stirring and can be used for the validation of numerical models. Among other things, numerical modeling allows to:

- compute stirring in industrial conditions,
- better understand the coupling between physical and chemical phenomena (e. g., melting of alloying elements or removal of inclusions),
- study the impact of different process parameters on stirring performance, and
- investigate alternative configurations (e. g., new position of gas injection nozzle, or new shape of ladle) without having to invest in expensive test campaigns.

1.2.1 Laboratory-scale ladle stirring

Most of the ladles in the laboratories use water instead of steel, and air instead of argon or nitrogen. In the literature, they are sometimes called *water models* or *physical models* (in opposition to numerical models).

Scaling of the ladle and similarity criteria. In order to ensure that the flow is similar to real-scale steel ladles, the water models are designed and scaled using a similarity criterion based on the Froude number (Castillejos and Brimacombe, 1989, Sheng and Irons, 1993, Krishnapisharody and Irons, 2015, Haiyan et al., 2016, Yu et al., 2017). The Froude number is a dimensionless quantity describing the flow inertia over gravity,

$$\text{Fr} = \frac{U}{\sqrt{gL}},$$

where U is some fluid characteristic velocity, g the gravity, and L the characteristic length. It is often used in vessel and tank dynamics to describe the wake of a submerged body or the free surface waves.

Table 1.1: Examples for the bath height H and radius R (Castillejos and Brimacombe, 1989, Mazumdar and Guthrie, 1995a, Yu, 2014).

	Laboratory ladles					Industrial ladles		
	Water		Mercury			Steel		
Height H (m)	1	1	0.67	0.465	0.4	0.21	2.5	2.3
Radius R (m)	0.5	0.315	0.33	0.21	0.1	0.1	1.3	1.5
Ratio H/R	2	3.2	2	2.2	4	2.1	1.9	1.5

Ladle geometry and gas plume. The geometry of a laboratory ladle is often assimilated to a cylinder, although real ladles are rather slightly inclined truncated cones. To give an idea of the ladle shapes, some values of the bath height H and the ladle radius R are given in Table 1.1. Usually, the ratio H/R is around 2 in most industrial and laboratory ladles. The gas nozzles are generally positioned away from the ladle center in order to avoid so-called *dead zones* at the periphery of the bottom diameter, i. e., areas with a low fluid circulation. Figure 1.6 shows two types of ladles modeled as cylinders in laboratories and numerical simulations.

During stirring, a *gas plume* forms. It can be divided into three parts (Mazumdar and Guthrie, 1995b). In the bottom, the gas injected has a high velocity. In the bath height, the gas plume has a smaller, nearly constant, velocity of the order 1 m s^{-1} (Mazumdar and Guthrie, 1995b, Sheng and Irons, 1993); and on the top, the gas exits to the atmosphere through the slag and induces a locally complex flow involving steel, slag, and gas. In vacuum, the same pattern is observed, but with a bigger bubble size and velocity, as well as an exponentially increasing size near the free surface, (Wichterle, 2010). The local flows at the bottom and the top of the bath play a negligible role on the global flow pattern, which is mainly induced by the central part of the rising gas. In fact, the bulk liquid velocity near the gas plume has the same order of magnitude as the gas velocity (often less than 1 m s^{-1} , because of a possible slip at the interface between gas bubbles and liquid), and decreases towards the ladle wall (Mazumdar and Guthrie, 1995b).

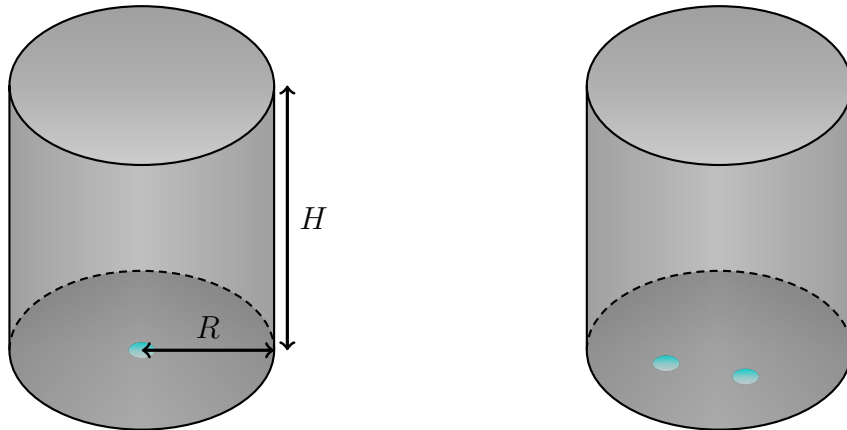


Figure 1.6: Cylindrical modeling of industrial or laboratory ladles. Left: with one centered gas nozzle (blue area). Right: with two gas nozzles.

1.2.2 Numerical ladle stirring

The equations which describe ladle stirring are based on multiphase flow models because several phases intervene in the process: one gas phase and two viscous liquid phases, i.e., the steel and the slag. As described in (Andrianov, 2003, Table 1.1), multiphase flows can be classified according to two main criteria:

- the physical state of their components (gas, liquid, and solid), and
- the interface between them:
 - a separated interface, where the phases are separated by a unique and clearly defined interface,
 - a dispersed interface, where one phase is distributed in another phase, and
 - a transitional interface, which is between the two previous types.

More than the number and type of phases, it is mainly the complexity of their interfaces that has led to several classes of mathematical and numerical models for multiphase flows. In the case of ladle stirring, the interface between the gas and steel phases evolves with the gas flow rate, from a dispersed to a nearly separated interface. For this reason, a wide range of models can be used, e.g., Euler–Euler, Euler–Lagrange, or mixture models.

Euler–Euler and Euler–Lagrange models. In two-phase flows of immiscible fluids, two sets of incompressible Navier–Stokes equations intervene. The phases are treated as a so-called Euler–Euler model, referring to the Eulerian frame used for both phases. In the case of a dispersed phase with a low phase fraction, it can be computationally more advantageous and physically more relevant to solve one ordinary differential equation (ODE) for each individual particle, than considering it as a continuous phase. This approach is called Euler–Lagrange, referring to the Lagrangian frame for the dispersed bubbles.

Mixture models. Often, the detailed knowledge of the interface position is not necessary. This is typically the case with transitional interfaces. Then, the so-called homogenized or averaged mixture models are a good alternative to the Euler–Euler and Euler–Lagrange methods. In this approach, introduced in (Ishii, 1975, Ishii and Hibiki, 2010), the equations of the phases are averaged in volume and in time, such that they are condensed to the equations of the fluids’ mixture. The averaging process results in additional terms, which describe the interaction between phases, e.g., drag and lift. Empirical formulas or simplifying assumptions are often needed to determine these terms and close the system. The material properties (density, viscosity) and physical variables (velocity, pressure) are shared, i.e., averaged, among the phases via phase functions. Bubbly flows, which are typical of gas-stirred processes in steelmaking, are often modeled with the mixture model. The review (Tryggvason et al., 2006) focuses on bubbly flow models using the Volume Of Fluid (VOF) or Level-Set (LS) techniques to capture the interface.

Single-phase models. In the above multiphase models, the phase function is an unknown variable which is solved by a separate equation. However, it is also possible to use an empirical formula for the phase fraction, as the ones derived in

the literature from experimental measurements. In other words, the interface is known *a priori*, and the mixture model is simplified by suppressing one equation. This approach, which was the first one used for ladle stirring, is also called “quasi-single” phase, or, equivalently, single-phase model. Its simplicity and relative cheap cost make it suitable for low computational resources, as it was the case at the time of their use, or for repeated computations, as in parametric or optimization studies. The main single-phase models are reviewed in (Alia et al., 2019a).

1.3 Objective

The main motivation of the thesis is to use mathematical modeling and numerical simulations to optimize the ladle stirring process control, in terms of cost-effectiveness (reduction of gas consumption, shorter treatment) and steel quality.

Challenges. As described earlier, several physical and chemical phenomena intervene in the stirring process, e. g., fluid dynamics, temperature homogenization, or degassing reactions. Furthermore, the literature about numerical modeling is very rich, as seen in Section 1.2.2. It is thus important to limit the scope of the work by defining the assumptions clearly. This helps to formulate a suitable model for the optimal control problem.

If optimization of the stirring is the main topic, one other important obstacle is the process control *in practice*. So far, the operations are performed manually. The main information available for the operators is the camera on top of the ladle. One can monitor the intensity of stirring at the liquid surface. In addition, a gas flow meter measures the injected gas flow rate but lacks sometimes of reliability, e. g., when a gas nozzle is clogged or when a gas leakage occurs. The observation of the ladle surface, the flow meter, and the operators’ own experience are qualitative and subjective estimations of the real mixing. A stirring considered as good for one heat or one operator can turn out to be insufficient for another heat or another operator, and vice-versa. Consequently, one needs to find an objective, quantitative, and reliable measurement of stirring to make the optimal control successful.

Assumptions. This dissertation focuses on the *fluid dynamics* of ladle stirring. Aspects such as temperature homogenization or mass transfer are not considered. Since they are implicitly influenced by the flow pattern, this restriction seems to be acceptable. It will introduce major simplifications in the definition of the stirring and optimization models. Furthermore, only laboratory water ladles are modeled because they provide real velocity measurements which are important to validate the numerical results. As explained in Section 1.2.1, they are designed to describe satisfyingly the stirring in real steel ladles. We further assume that two-phase flow models are not suitable for optimal control problems because of their high computational cost. This seems to be a reasonable assumption, given the fact that they are described by a larger number of equations. This, in turn, requires more resources in terms of computational time and memory, which are of critical importance for solving optimal control problems. Thus, we employ the simplified single-phase models.

1.4 Main contributions

Three main topics are addressed in the thesis:

1. model the ladle stirring with a simple single-phase approach,
2. formulate and solve an optimal control problem for the stirring, and
3. study the usage of accelerometers on the ladle wall to measure stirring intensity.

These three parts constitute the main contributions of the dissertation. Although the single-phase model for ladle stirring has been already defined in the 1980s, it was studied in this dissertation for mainly three reasons: propose a proper definition of the model to clear some unclarity found in the literature, review the main models to choose the best variant among all the research papers, and apply this approach in the optimal control problem. As mentioned earlier, a “cheap” forward model is more advantageous in optimal control problems, rather than more expensive approaches, like multiphase models. Furthermore, the optimization work focuses on the hydrodynamics of stirring. These are sufficiently well-described with single-phase models. The main results of this first part are summarized in (Alia et al., 2019a). Second, the results of the optimal control problem is the main interest for the industry. However, due to the simplified approaches used in the dissertation, the second part should be rather considered as a *proof-of-concept*, i.e., an exploratory study to verify if optimal controls obtained numerically can improve the industrial practice. Finally, a separate experimental campaign has been performed concerning the measurement of stirring efficiency using vibrations sensors. Its results are available in (Alia et al., 2019b).

1.5 Outline

The thesis is organized in :

- one chapter about the equations studied in this work, i.e., the Navier–Stokes equations (NSE),
- two chapters related to the ladle stirring, and
- one independent chapter on the vibration.

The structure and the main dependencies between the sections are illustrated in Figure 1.7. In Chapter 2, the main partial differential equations (PDEs) of the thesis are presented: the time-dependent incompressible NSE (Section 2.1). The weak formulation (2.2), the numerical methods (2.3), e.g., the time and space discretizations, and some solvers (2.4) are then described. Turbulence modeling to resolve high Reynolds number flows is also discussed (2.5).

The single-phase model for ladle stirring is studied in Chapter 3. First, the literature and the main formulas for the gas fraction are briefly reviewed (Section 3.1). Three variants of the models are presented: a 2d boundary-driven, an axisymmetrical, and a 3d ladle stirring model (3.2). The numerical results are discussed in 2d and 3d successively (3.3 and 3.4). They are validated with experimental measurements from the literature. Some comparison between the in-house code PARMOON and the commercial software COMSOL is done with the 3d model to study the effect of two different turbulent models. In the conclusion (3.5), a two-phase flow approach is briefly presented as an outlook.

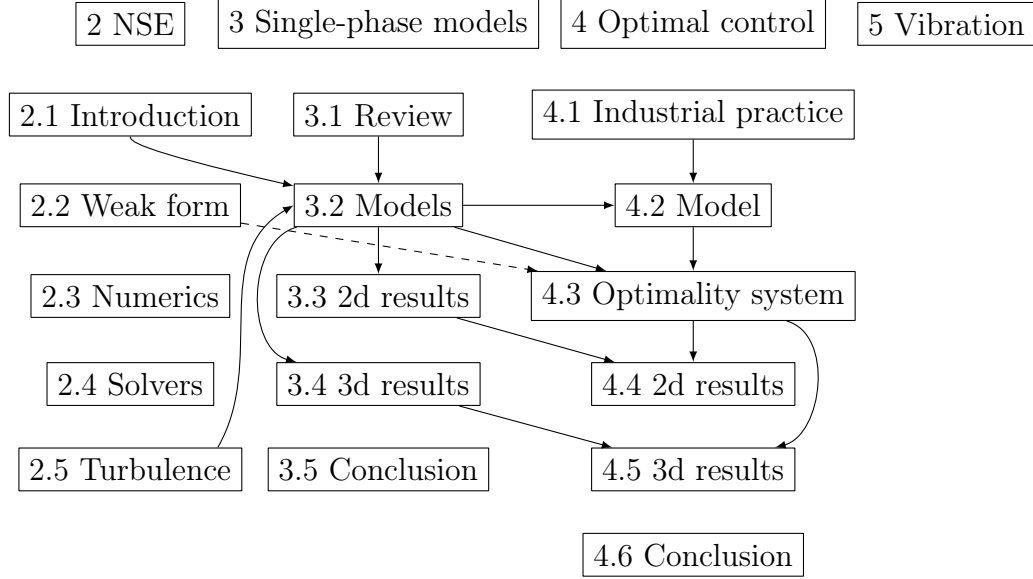


Figure 1.7: A graph showing the structure of the thesis and the main dependencies between its sections.

The results obtained in Chapter 3 help to choose the appropriate ladle stirring model for the optimal control problem (Chapter 4), namely, the 2d boundary-driven and the 3d models. The axisymmetrical ladle will not be considered for optimization. In order to formulate the optimization model, the process objectives, control parameter, and constraints from the industrial point of view are discussed (4.1). They are then formulated mathematically (4.2). Section 4.3 summarizes the optimal control problem and presents the formal derivation of the optimality system, i.e., the adjoint equations and the optimality conditions. Sections 4.3.2 and 4.3.3 are mathematically quite technical and may be skipped by readers who are not familiar with the theory of optimal control of PDEs. They can continue from Section 4.3.4. Numerical results in 2d and 3d are then presented (4.4 and 4.5). In particular, two cases are studied in both models: one with constant-in-time control variables and one with time-dependent variables. In addition, the optimization of the positions of the two nozzles is investigated in the 3d model. Finally, some limits of the modeling approach are discussed leading to an alternative and novel optimization problem (4.6).

Chapter 5 can be read independently from the others because it treats another work direction of the thesis: the vibration of the ladle wall induced by stirring. After a brief review (Section 5.1), the context of ladle vibration in the real industrial case is described (5.2). The results of an experimental campaign on a laboratory physical model are presented (5.3). Similarly to the two previous chapters, an outlook is discussed in the conclusion (5.4). It concerns the use of fluid-structure interaction models for ladle vibration.

Finally, the conclusion 6 summarizes the main achievements of the dissertation and provides some perspectives about potential extensions of this work and novel ways to overcome its limits.

2. The time-dependent incompressible Navier–Stokes equations

Motivation. The modeling of ladle stirring can be divided into two distinct aspects: the physics of fluid flow, which are essentially based on the instationary (i. e., time-dependent) incompressible Navier–Stokes equations (NSE), and the modeling of gas-stirring. It is well-known that the NSE are, for several reasons, numerically difficult to solve and require special care with respect to discretization and solver (Ferziger and Peric, 2002, John, 2016). These subjects have been largely investigated in the literature of applied mathematics and computational science, leading to important results which should be taken into consideration in the numerical simulations. On the contrary, gas-stirring covers questions which are not directly related to the theory of the NSE. For these reasons, these two subjects are split into two different chapters. This chapter intends to introduce the main results needed in this work concerning the NSE. It describes the difficulties emerging with these equations and how to deal with them numerically. Furthermore, we try to keep in mind the practical problem (ladle stirring) all along the chapter, and discuss the necessary modeling assumptions and tools according to our needs. Correspondingly, the suitable boundary conditions, e. g., free slip condition, and the modeling of turbulence are discussed. The part concerning gas-stirring is presented in Chapter 3.

Outline. First, the NSE and appropriate boundary conditions are introduced and discussed from a physical background. Moving step by step to numerical aspects, more mathematical background and results are given, e. g., weak formulation, existence and uniqueness of its solution. General time discretization schemes are briefly presented before focusing on the main scheme used in this work: the Crank–Nicolson scheme. Similarly, general concepts of space discretization are described (Galerkin finite element method), before introducing inf-sup stability and deriving the discrete equations solved in this work. A short introduction to linear solvers is then given, before moving to sophisticated solvers specific to the NSE. Finally, a whole section concerns the modeling of turbulence using similar lines of development: physical background, mathematical background (weak formulation, existence, uniqueness), discretization, and numerical aspects.

2.1 Introduction

Whether being water flows, or liquid steel in ladles, the physics of fluid movements are governed by the so-called Navier–Stokes equations. In a lot of applications, the fluid is incompressible, leading to the class of incompressible flows. For the sake of clarity, the equations are presented from the more general to the more specific case, by detailing the assumptions between each cases.

2.1.1 Partial Differential Equations

Notations. In the rest of this dissertation, $d \in \{2, 3\}$ is the dimension of the problem, and bold symbols denote vector-valued quantities of dimension d .

Let $\Omega \subset \mathbb{R}^d$ designate an open, bounded Lipschitz domain corresponding to a fixed volume occupied by the fluid, with the boundary $\partial\Omega$. The length of the time interval is given by $T \in \mathbb{R}^+$. Let us define the (*unknown*) velocity vector field $\mathbf{u} : [0, T] \times \Omega \mapsto \mathbb{R}^d$ and the (*unknown*) pressure scalar field $p : [0, T] \times \Omega \mapsto \mathbb{R}$ of the fluid. Let $\mathbf{f} : [0, T] \times \Omega \mapsto \mathbb{R}^d$ be a *given* volume (or body) force. Typically, it represents the gravitational force, but can also be some other source term causing the fluid to move (for example, electro-magnetic force in magnetohydrodynamics). Partial derivatives are denoted by a subscript. In particular, \mathbf{u}_t designates the time derivative of \mathbf{u} .

The physical units of the three previous fields are, respectively: m s^{-1} , Pa (Pascal), and $\text{N m}^{-3} = \text{kg m}^{-2} \text{s}^{-2}$. The fluid properties of interest are:

- its density ρ (in kg m^{-3}),
- its dynamic viscosity μ (in $\text{kg m}^{-1} \text{s}^{-1}$), and
- its kinematic viscosity $\nu = \mu/\rho$ (in $\text{m}^2 \text{s}^{-1}$).

We also introduce the stress and velocity deformation tensors

$$\mathbb{S} = 2\mu\mathbb{D}(\mathbf{u}) + pI, \quad (2.1)$$

where I is the identity matrix, and

$$\mathbb{D}(\mathbf{u}) = \frac{\nabla \mathbf{u} + (\nabla \mathbf{u})^\top}{2}, \quad (2.2)$$

respectively.

Navier–Stokes equations in dimensional form. The general form of the NSE read

$$\rho(\mathbf{u}_t + (\mathbf{u} \cdot \nabla)\mathbf{u}) - 2\mu\nabla \cdot \mathbb{D}(\mathbf{u}) + \nabla p = \mathbf{f} \quad \text{in } (0, T] \times \Omega, \quad (2.3)$$

$$\rho_t + \nabla \cdot (\rho \mathbf{u}) = 0 \quad \text{in } (0, T] \times \Omega. \quad (2.4)$$

The vectorial equation (2.3), which is composed of d scalar equations, corresponds to the *momentum equation*, and is derived from the principle of conservation of linear momentum (Newton’s second law of motion applied to a fluid particle). The second equation derives from the conservation of mass. It is also called the *continuity equation*. For a detailed derivation of these equations from the principles

of continuum mechanics, the reader is referred to (Ferziger and Peric, 2002, John, 2016). Note that, if the volume force represents the gravitational force, it would be equal to $\rho \mathbf{g}$, where the constant gravity vector \mathbf{g} is defined as $(0, -g)^\top$ in 2d, and $(0, 0, -g)^\top$ in 3d.

Incompressible Navier–Stokes equations in dimensional form. If the fluid is incompressible and homogeneous, its density ρ is constant in time and space. This simplifies the second equation to¹ $\nabla \cdot \mathbf{u} = 0$. The incompressible NSE thus read

$$\begin{aligned} \rho(\mathbf{u}_t + (\mathbf{u} \cdot \nabla)\mathbf{u}) - 2\mu \nabla \cdot \mathbb{D}(\mathbf{u}) + \nabla p &= \mathbf{f} & \text{in } (0, T] \times \Omega, \\ \nabla \cdot \mathbf{u} &= 0 & \text{in } (0, T] \times \Omega. \end{aligned}$$

The second equation can be interpreted as an incompressibility (or divergence-free) constraint for the velocity \mathbf{u} . This term is often linked with the pressure term, in the sense that the pressure acts as a Lagrangian multiplier of the continuity equation, see for example (John, 2016).

In most applications of incompressible fluids, not only ρ , but also μ is constant. One can therefore reduce the fluid properties to the kinematic viscosity ν , and write the previous equations, still in dimensional form, as

$$\mathbf{u}_t + (\mathbf{u} \cdot \nabla)\mathbf{u} - 2\nu \nabla \cdot \mathbb{D}(\mathbf{u}) + \nabla p = \mathbf{f} \quad \text{in } (0, T] \times \Omega, \quad (2.5)$$

$$\nabla \cdot \mathbf{u} = 0 \quad \text{in } (0, T] \times \Omega. \quad (2.6)$$

For the sake of brevity, the same notation for p and \mathbf{f} has been used, although they have been both divided by the constant ρ . Their units are now expressed as $\text{Pa}(\text{kg m}^{-3})^{-1} = \text{m}^2 \text{s}^{-2}$ and N kg^{-1} (body force per unit mass), respectively. In case of inhomogeneous fluids (in time and/or in space), the simplifications introduced here do not hold: one has to consider the more general NSE (2.3) and (2.4).

Incompressible Navier–Stokes equations in dimensionless form. The concept of dimensionless equations has physical, mathematical, and numerical foundations, but the experimental, or phenomenological, background is maybe the most convenient to explain its importance. The development of fluid dynamics is closely related to that of the experimental settings, especially wind tunnels, which were exploited to understand the behavior of a car on the road, or the aerodynamics of a wing. One key question is the scaling of the experiment: how to reproduce on a small scale the same flow structures as on real large-scale problems? Thanks to the works of (Reynolds, 1895), flow structures can be classified according to one quantity: the *Reynolds number* Re , which depends on a characteristic velocity U and length L of the flow, and on the *physical* kinematic viscosity of the fluid ν . It is defined as

$$\text{Re} := \frac{LU}{\nu},$$

¹An equivalent definition of incompressible fluids, is that the material derivative of the density should be 0: $\frac{D\rho}{Dt} = \rho_t + (\mathbf{u} \cdot \nabla)\rho = 0$. Using this property and the identity $\nabla \cdot (\rho \mathbf{u}) = \rho(\nabla \cdot \mathbf{u}) + (\mathbf{u} \cdot \nabla)\rho$, it remains from the continuity equation that $\nabla \cdot \mathbf{u} = 0$.

and is the most important (and simple) criterion to answer the previous question. For example, in order to reproduce the aerodynamics of a one-meter high object moving at 800 km h^{-1} in air, one can choose L , U , and ν in such a way that the Reynolds number is kept constant, i.e., the flow structures are preserved. Note that it has no dimensions, since the units of L and U cancel out with the one of ν .

Coming to the physical meaning of Re , one can re-write the convection and viscous terms with respect to the characteristic quantities

$$(\mathbf{u} \cdot \nabla) \mathbf{u} \sim \frac{U^2}{L}, \quad \nu \nabla \cdot \mathbb{D}(\mathbf{u}) \sim \frac{\nu U}{L^2},$$

and observe that the Reynolds number consists of the *ratio of the convection and viscous terms*

$$Re \sim \frac{(\mathbf{u} \cdot \nabla) \mathbf{u}}{\nu \nabla \cdot \mathbb{D}(\mathbf{u})} \sim \frac{U^2/L}{\nu U/L^2} = \frac{UL}{\nu}.$$

One retrieves the classification of the flows. A low Reynolds number, e.g., $Re \ll 1$, indicates a slow flow dominated by viscous forces, while a large Re is a sign of convection-dominated flows, or, for very high Re , turbulent flows. Mathematically, the dimensionless form allows the analysis and error estimations based on only one constant coefficient. From a computational point of view, dimensionless equations can be advantageously used as a scaling in the order of 1 of numerical solutions. This avoids rounding precision issues on floating point numbers.

One question remains: how to choose the characteristic length L and velocity U ? In practice, it is usual to compare one's application with well-understood, widely spread benchmark problems, e.g., flow around cylinders or channel flows. For more specific problems, one should consider the order of magnitude of the domain, or the size of an obstacle, depending on the flow structure of interest. For example, in ladle stirring, if one is interested in the flow in the immediate vicinity of the nozzle, one could use its diameter for L and the inlet gas velocity for U . Alternatively, one could use the ladle height for the bulk flow. Sometimes, the choice of the one or the other quantity does not change Re considerably, for instance the ladle radius or its height for L . They differ by a factor of around 2, which is quite negligible in the scale of the Reynolds number.

The detailed derivation of the dimensionless form of the NSE can be found in (John, 2016). For completeness, a short version is given here. It consists of re-writing the equations (2.5) and (2.6) in terms of the dimensionless and characteristic quantities (designated with the asterisk)

$$\mathbf{u}^*(t^*, \mathbf{x}^*) = \frac{\mathbf{u}(t, \mathbf{x})}{U}, \quad \mathbf{x}^* = \frac{\mathbf{x}}{L}, \quad t^* = \frac{t}{T^*}, \quad T^* = \frac{L}{U}.$$

Additional factors L and T^* appear from the time and space derivatives. Multiplying the momentum equation by L/U^2 , one obtains

$$\begin{aligned} \mathbf{u}_{t^*}^* + (\mathbf{u}^* \cdot \nabla_{\mathbf{x}^*}) \mathbf{u}^* - 2 \frac{\nu}{LU} \nabla_{\mathbf{x}^*} \cdot \mathbb{D}(\mathbf{u}^*) + \nabla_{\mathbf{x}^*} \frac{p}{U^2} &= \frac{L}{U^2} \mathbf{f} & \text{in } (0, T] \times \Omega, \\ \nabla_{\mathbf{x}^*} \cdot \mathbf{u}^* &= 0 & \text{in } (0, T] \times \Omega. \end{aligned}$$

All the terms in these equations are now dimensionless (unit 1). For more clarity, we drop the asterisks, and re-define the pressure and the volume force, as the dimensionless pressure and volume force, respectively, keeping the same notation. One can verify the consistency of the units: in the previous paragraph, the pressure unit was $\text{m}^2 \text{s}^{-2}$, now, it is divided by U^2 , leading to the dimensionless pressure. Furthermore, we now define the *dimensionless (kinematic) viscosity* as

$$\nu := \frac{1}{Re}.$$

All in all, the incompressible Navier–Stokes equations *in dimensionless form* can be written similarly to (2.5) and (2.6)

$$\mathbf{u}_t + (\mathbf{u} \cdot \nabla) \mathbf{u} - 2\nu \nabla \cdot \mathbb{D}(\mathbf{u}) + \nabla p = \mathbf{f} \quad \text{in } (0, T] \times \Omega, \quad (2.7)$$

$$\nabla \cdot \mathbf{u} = 0 \quad \text{in } (0, T] \times \Omega. \quad (2.8)$$

Completed with appropriate boundary and initial conditions (discussed in the next section), these equations are the main partial differential equations (PDEs) studied mathematically and numerically for the simulations of fluid flows.

Main difficulties arising with the NSE. Besides of being vectorial equations, the NSE are well-known for their theoretical and numerical difficulties (John, 2016, p. 23):

1. The special coupling of velocity and pressure. Indeed, the pressure does not appear explicitly in the continuity equation. As described earlier, the pressure field can be considered as a Lagrangian multiplier to enforce the incompressibility condition for the velocity (i. e., the continuity equation). This type of coupling is characteristic of so-called *saddle-point problems*.
2. The nonlinearity introduced in the convective term.
3. The convection-domination, or turbulence, features which occurs when ν is small (high Re). This situation concerns numerical schemes and analysis.
4. The three-dimensional case, which is an additional source of difficulties, in theoretical aspects (see Section 2.2.2), and numerical aspects (3d simulations are much more challenging computationally than 2d ones). These reasons often favor 2d computations, although real flows are usually three-dimensional. In some cases, 2d simulations are also grounded physically, e. g., when the flow is (virtually) independent of one direction. An intermediate case, which is also very practical, is described by *axisymmetrical flows*, sometimes called *2.5d flows*. The different behaviors between 2d, 2.5d, and 3d flows, will be discussed in Chapter 3.

Simplified cases of the incompressible NSE. As pointed out by (Bartsch, 2018), Equations (2.7) and (2.8) are called the *full NSE* for two reasons. First, they offer a full description of the flow structures, such that details up to the micro-scale can be resolved with them. Second, they contain all the needed terms, in opposition to simplified cases where some terms are neglected or modified. The main purpose of such cases is to reduce the complexity of the NSE and offer, nevertheless, interesting results for some real-life applications:

1. If the problem is independent of time (velocity, pressure, volume force, boundary conditions), the time term \mathbf{u}_t can be dropped, leading to *the stationary NSE*:

$$\begin{aligned} (\mathbf{u} \cdot \nabla) \mathbf{u} - 2\nu \nabla \cdot \mathbb{D}(\mathbf{u}) + \nabla p &= \mathbf{f} & \text{in } (0, T] \times \Omega, \\ \nabla \cdot \mathbf{u} &= 0 & \text{in } (0, T] \times \Omega. \end{aligned}$$

Physically, this assumption can be consistent in case of a (very) slow flow, which can occur obviously only with (very) low Re.

2. Assuming further that the flow is very viscous, the viscous term becomes dominant, and one can neglect the convection term, ending up with the *(linear) Stokes flow*:

$$\begin{aligned} -2\nu \nabla \cdot \mathbb{D}(\mathbf{u}) + \nabla p &= \mathbf{f} & \text{in } (0, T] \times \Omega, \\ \nabla \cdot \mathbf{u} &= 0 & \text{in } (0, T] \times \Omega. \end{aligned}$$

This problem is generally well-understood, and describes the so-called *creeping flows*, which are driven by viscous forces mainly.

3. Replacing, in the stationary NSE, the nonlinear convection term by a linearized version $(\mathbf{w} \cdot \nabla) \mathbf{u}$ with a known wind \mathbf{w} , one defines so-called *Oseen equations*:

$$\begin{aligned} (\mathbf{w} \cdot \nabla) \mathbf{u} - 2\nu \nabla \cdot \mathbb{D}(\mathbf{u}) + \nabla p &= \mathbf{f} & \text{in } (0, T] \times \Omega, \\ \nabla \cdot \mathbf{u} &= 0 & \text{in } (0, T] \times \Omega. \end{aligned}$$

They have the advantage of being linear, but have no physical meaning. They are rather auxiliary problems appearing in the numerical methods for solving the full NSE.

Finally, high Reynolds number flows can be tackled using turbulence models, such as Large Eddy Simulations (LES) or the $k - \epsilon$ model. These approaches can also be considered as tools to reduce the complexity of the full NSE. Turbulence modeling is discussed more in detail in Section 2.5.

Different formulations of the viscous term. The convection and the diffusion² terms can have several equivalent expressions. This is possible thanks to the divergence-free constraint (2.8), and equalities based on vector calculus. In this work, we always consider the convective form for the convection term $(\mathbf{u} \cdot \nabla) \mathbf{u}$, but we alternate between two forms of the viscous term $-2\nu \nabla \cdot \mathbb{D}(\mathbf{u})$. Using

$$\nabla \cdot (\nabla \mathbf{u}) = \Delta \mathbf{u} \quad \text{and} \quad \nabla \cdot (\nabla \mathbf{u}^\top) = \begin{pmatrix} (\nabla \cdot \mathbf{u})_x \\ (\nabla \cdot \mathbf{u})_y \\ (\nabla \cdot \mathbf{u})_z \end{pmatrix} = 0,$$

the last equality coming from the divergence constraint, the viscous term is equivalent to

$$-2\nu \nabla \cdot \mathbb{D}(\mathbf{u}) = -2\nu \nabla \cdot \left(\frac{\nabla \mathbf{u} + \nabla \mathbf{u}^\top}{2} \right) = -\nu \Delta \mathbf{u}.$$

²The viscous term in the NSE can equivalently be called the diffusion term.

These expressions are always equivalent in the continuous setting, but this does not necessarily hold in the discrete setting. In fact, the discrete velocity is generally not exactly divergence-free, so that the simplifications are not possible anymore, or they introduce an additional error, see (Hannasch and Neda, 2012) for a comparison. If the discrete velocity is exactly divergence-free, then one can use these forms equivalently. The following form of the NSE, based on the last expression of the viscous term, is the most popular one in the literature:

$$\mathbf{u}_t + (\mathbf{u} \cdot \nabla) \mathbf{u} - \nu \Delta \mathbf{u} + \nabla p = \mathbf{f} \quad \text{in } (0, T] \times \Omega, \quad (2.9)$$

$$\nabla \cdot \mathbf{u} = 0 \quad \text{in } (0, T] \times \Omega. \quad (2.10)$$

In the rest of the thesis, the choice of the viscous term will be written explicitly.

2.1.2 Boundary and initial conditions

The Navier–Stokes equations are first-order-in-time and second-order-in-space partial differential equations. They have to be equipped with conditions on the “space and time boundaries”, i. e., boundary conditions on $\partial\Omega$, and initial condition at $t = 0$. In this dissertation, we are concerned only with *enclosed flows*, i. e., there are no in- and outflows³. We will therefore focus only on two types of boundary conditions of interest: Dirichlet and free slip with no penetration. For more clarity, we consider a general case where:

- the domain boundary can be separated in three parts: $\partial\Omega = \Gamma_D \cup \Gamma_0 \cup \Gamma_{\text{slip}}$,
- the boundaries are pairwise disjoint: $\Gamma_D \cap \Gamma_0 = \emptyset$, $\Gamma_D \cap \Gamma_{\text{slip}} = \emptyset$, and $\Gamma_{\text{slip}} \cap \Gamma_0 = \emptyset$,
- only Γ_D can be presumably empty, while the others are not: $\Gamma_0 \neq \emptyset, \Gamma_{\text{slip}} \neq \emptyset$.

Dirichlet boundary conditions. One of the most classical boundary condition consists in imposing the velocity field on the boundary,

$$\mathbf{u}(t, \mathbf{x}) = \mathbf{b}(t, \mathbf{x}) \text{ in } (0, T] \times \Gamma_D. \quad (2.11)$$

They are called *Dirichlet boundary conditions*. Sometimes, they can be referred to as *essential boundary conditions* for a reason related to the weak formulation, see Section 2.2.1. It is most often used to describe inflows into or outflows out from Ω . In Eq. (2.11), \mathbf{b} can be nonzero, or zero in part of, or on all, the boundary Γ_D . In the case where $\mathbf{b} = \mathbf{0}$, the boundary condition specifies that the velocity is zero, and can neither penetrate the wall (zero normal component, no inflow and outflow), neither slip along it (zero tangential component). Indeed, one can write

$$\mathbf{u} = \mathbf{0} \iff \mathbf{u} \cdot \mathbf{n} = 0, \quad \mathbf{u} \cdot \mathbf{t}_i = 0, \quad 1 \leq i \leq d-1,$$

where \mathbf{n} and \mathbf{t}_i are the unit normal and tangential vectors on Γ_D , such that $\{\mathbf{n}, \mathbf{t}_1, \mathbf{t}_2\}$ build a local orthonormal system of vectors. This situation is referred to as *homogeneous Dirichlet* boundary condition, or *no-slip condition*.

³This assumption is due to the simplified approach used for ladle stirring, see Chapter 3. If two-phase flows are considered, the use of inlet and outlet conditions for the gas phase are necessary. More details on the outlet boundary condition and the two-phase model are given in the paragraph **Three remarks** and in Section 3.5, respectively.

In this work, we choose to distinguish explicitly areas with homogeneous and non-homogeneous boundary conditions:

$$\mathbf{u} = \mathbf{0} \quad \text{in } (0, T] \times \Gamma_0, \quad (2.12)$$

$$\mathbf{u} = \mathbf{b} \quad \text{in } (0, T] \times \Gamma_D, \quad (2.13)$$

$$\mathbf{b} \neq \mathbf{0}.$$

This distinction should improve clarity of the models introduced in Chapter 3, since they have different types of boundary conditions depending on the dimension d of the problem (2d, axisymmetric, or 3d). In 2d, $\Gamma_D \neq \emptyset$ and \mathbf{b} will always refer to a nonzero boundary velocity. In axisymmetric and 3d cases, we will have $\Gamma_D = \emptyset$, i.e., the Dirichlet conditions are homogeneous. Similarly, in Chapter 4, \mathbf{b} will play the role of the control variable in the 2d optimal control model. Therefore, it will be more convenient that \mathbf{b} designates a nonzero velocity, and is independent of the non-controlled boundaries Γ_0 with homogeneous Dirichlet.

When Dirichlet conditions are prescribed on the whole boundary ($\Gamma_D = \partial\Omega$), one has to take into account two additional constraints. First, the pressure can only be determined up to one additive constant, since only its gradient appears in the whole system of equations. The typical constraint to fix it reads

$$\int_{\Omega} p(t, \mathbf{x}) \, d\mathbf{x} = 0 \quad \forall t, \quad (2.14)$$

i.e., the integral mean value of the pressure should vanish. A more physical constraint, often used in commercial softwares, consists of fixing the pressure value at one point of the domain. Typically, the pressure at the free surface is equal to the atmospheric pressure ($\sim 10^5$ Pa). Second, the prescribed velocity \mathbf{b} should be compatible with the divergence-free condition. Indeed, using the divergence theorem (Gauss or Ostrogradsky theorem),

$$\int_{\Omega} \nabla \cdot \mathbf{u} \, d\mathbf{x} = \int_{\Gamma_D} \mathbf{u} \cdot \mathbf{n} \, d\mathbf{s},$$

and applying the incompressibility condition (2.10) with (2.11), yield the condition

$$\int_{\Gamma_D} \mathbf{b} \cdot \mathbf{n} \, d\mathbf{s} = 0. \quad (2.15)$$

Free slip with no penetration boundary conditions. We start from the general *slip with friction and penetration with resistance condition* (John, 2002):

$$\mathbf{u} \cdot \mathbf{n} + \gamma_1 \mathbf{n}^T \mathbb{S} \mathbf{n} = 0 \quad \text{in } (0, T] \times \Gamma_{\text{slip}}, \quad (2.16)$$

$$\mathbf{u} \cdot \mathbf{t}_i + \gamma_2^{-1} \mathbf{n}^T \mathbb{S} \mathbf{t}_i = 0 \quad \text{in } (0, T] \times \Gamma_{\text{slip}}, \quad 1 \leq i \leq d-1, \quad (2.17)$$

where γ_1 and γ_2 are the resistance and the friction coefficients, respectively, and \mathbb{S} is the stress tensor (2.1). In a more explicit form, they read

$$\begin{aligned} \mathbf{u} \cdot \mathbf{n} + \gamma_1 \mathbf{n}^T (2\nu \mathbb{D}(\mathbf{u}) - pI) \mathbf{n} &= 0 & \text{in } (0, T] \times \Gamma_{\text{slip}}, \\ \gamma_2 \mathbf{u} \cdot \mathbf{t}_i + \mathbf{n}^T (2\nu \mathbb{D}(\mathbf{u}) - pI) \mathbf{t}_i &= 0 & \text{in } (0, T] \times \Gamma_{\text{slip}}, \quad 1 \leq i \leq d-1. \end{aligned}$$

These conditions state that there can be some penetration (inflow or outflow) and tangential friction at the boundary Γ_{slip} . If $\gamma_1 \rightarrow \infty$ ($\gamma_1^{-1} = 0$), one obtains a free penetration condition. If $\gamma_1 = 0$, slip with no penetration is modeled. If, furthermore, $\gamma_2 = 0$ ($\gamma_2^{-1} \rightarrow \infty$), one gets the *free slip with no penetration condition*, which will be used very often in this work:

$$\mathbf{u} \cdot \mathbf{n} = 0 \quad \text{in } (0, T] \times \Gamma_{\text{slip}}, \quad (2.18)$$

$$\mathbf{n}^\top \mathbb{S} \mathbf{t}_i = \mathbf{n}^\top (2\nu \mathbb{D}(\mathbf{u}) - pI) \mathbf{t}_i = 0 \quad \text{in } (0, T] \times \Gamma_{\text{slip}}, \quad 1 \leq i \leq d-1. \quad (2.19)$$

Free slip allows a non-zero tangential velocity at the boundaries. Physically, this might be relevant on interfaces between fluids, although some friction is normally always present. In the models of this dissertation, this condition has to be understood as a simple model of the velocity at the free surface of the liquid: there is no inflow or outflow, and, at the same time, the velocity is not zero as on the walls (where no-slip conditions apply). Note also that, when $\gamma_2 \rightarrow \infty$ ($\gamma_2^{-1} = 0$), the no-slip or homogeneous Dirichlet condition is recovered.

Altogether, Equations (2.16) and (2.17) are quite practical, because they can be used as a general condition, where classical boundary conditions can be retrieved (in a weak sense) by choosing, for example, arbitrarily high coefficients γ_1 and γ_2 . This can be convenient from the implementation point of view. On the other hand, imposing no-slip, no-friction, or no-penetration conditions in a weak sense can be numerically less stable than strongly imposed conditions, i. e., ones where the values of the velocity components are exactly prescribed. For example, they can cause convergence difficulties for linear solvers (John, 2002). One further difficulty associated with the general conditions (2.16) and (2.17) is how to find physically-relevant values for γ_1 and γ_2 . These coefficients depend on the material at the boundary, its geometry, its rugosity, etc. Since we apply the free slip with no penetration condition (2.18) and (2.19), this will not be a problem in the present work.

Three remarks. The models used in this dissertation have some specific features regarding boundary conditions. First, they are *enclosed flows*, i. e., there are neither inflows nor outflows. As described previously, an additional constraint on the pressure, e. g., Eq. (2.14), should hold. One could notice, at first glance, that the presence of the pressure in the free slip condition (2.19) could fix naturally the additional constant, solving the problem of the non-uniqueness of pressure. However, since \mathbf{n} and \mathbf{t}_i are orthogonal, the pressure does not play any role in (2.19):

$$\mathbf{n}^\top \mathbb{S} \mathbf{t}_i = \mathbf{n}^\top (2\nu \mathbb{D}(\mathbf{u}) - pI) \mathbf{t}_i = \mathbf{n}^\top (2\nu \mathbb{D}(\mathbf{u})) \mathbf{t}_i - p \mathbf{n}^\top \mathbf{t}_i = \mathbf{n}^\top (2\nu \mathbb{D}(\mathbf{u})) \mathbf{t}_i. \quad (2.20)$$

Hence, the additional constraint on the pressure is still needed. Second, the compatibility condition (2.15) holds naturally in this work, because the imposed boundary velocity \mathbf{b} (in 2d and in the optimal control applications) will always be tangent to the boundary: $\mathbf{b} \cdot \mathbf{n} = 0$. Finally, for completeness, we should mention a few words concerning the *Neumann, or natural, boundary condition*, which plays a role as central as the Dirichlet condition in the NSE. It reads

$$\mathbb{S} \cdot \mathbf{n} = \mathbf{0} \iff (2\nu \mathbb{D}(\mathbf{u}) - pI) \cdot \mathbf{n} = \mathbf{0}, \quad (2.21)$$

and usually model the *outflow* from Ω . The term natural has a double meaning. It can refer to the fact that the Neumann condition, as a balance between physical quantities, is a better description of natural phenomena, than the Dirichlet condition, where the imposed velocity is rather artificial than physical. Indeed, fixing a velocity on the boundary is often the sign of a “human-driven” or a “data-driven” flow. Artificial has to be understood in this sense. In a more mathematical sense, the left-hand side of Equation (2.21) appears (and vanishes) naturally in the weak formulation of the Navier–Stokes equations. The Neumann condition is also known as *do-nothing* condition, since the velocity or the pressure are not forced to prescribed values. If Eq. (2.21) is not to be used in the models employed later, it is of major importance in two-phase models for ladle stirring. It is indeed used as an outlet condition for the gas phase. This is briefly discussed in Section 3.5.

Initial conditions. At $t = 0$, the fluid can be at rest: $\mathbf{u}(0, \mathbf{x}) = \mathbf{0}$ in Ω , or can be already developed. We will consider the general initial condition $\mathbf{u}(0, \mathbf{x}) = \mathbf{u}^0(\mathbf{x})$. It has to be compatible with the divergence constraint and the boundary conditions. Namely, \mathbf{u}_0 must be divergence-free in some sense: $\nabla \cdot \mathbf{u}^0 = 0$ (see (John, 2016, p. 334, Definition 7.6) for more details). Its boundary condition should be compatible with the limit (for $t \mapsto 0, t > 0$) of the prescribed boundary conditions, i. e., $\mathbf{u}|_{\partial\Omega} \mapsto \mathbf{u}^0|_{\partial\Omega}$. For completeness, we also introduce an initial pressure such that: $p(0, \mathbf{x}) = p^0(\mathbf{x})$ in Ω . The role of the initial pressure in the numerical method will be described later on. In some cases, the presence of a nonzero p^0 can help solvers to converge. It is for example recommended in commercial softwares. A popular and physically consistent initial condition is given by the *hydrostatic*⁴ pressure:

$$p^0(x, y, z) = \rho(z - H)\mathbf{g} \cdot \mathbf{e}_z,$$

where H is the liquid height.

2.1.3 Summary

Let us gather all the pieces and restate the whole problem which will be used all along the thesis:

Problem 2.1 (Strong form of the Navier–Stokes equations):

$$\mathbf{u}_t + (\mathbf{u} \cdot \nabla)\mathbf{u} - 2\nu\nabla \cdot \mathbb{D}(\mathbf{u}) + \nabla p = \mathbf{f} \quad \text{in } (0, T] \times \Omega, \quad (2.22)$$

$$\nabla \cdot \mathbf{u} = 0 \quad \text{in } (0, T] \times \Omega, \quad (2.23)$$

$$\mathbf{u} = \mathbf{b} \quad \text{in } (0, T] \times \Gamma_D, \quad (2.24)$$

$$\mathbf{u} = \mathbf{0} \quad \text{in } (0, T] \times \Gamma_0, \quad (2.25)$$

$$\mathbf{u} \cdot \mathbf{n} = 0 \quad \text{in } (0, T] \times \Gamma_{\text{slip}}, \quad (2.26)$$

$$\mathbf{n}^\top \mathbf{S} \mathbf{t}_i = 0, \quad 1 \leq i \leq d-1, \quad \text{in } (0, T] \times \Gamma_{\text{slip}}, \quad (2.27)$$

$$\int_{\Omega} p \, d\mathbf{x} = 0 \quad \text{in } [0, T], \quad (2.28)$$

$$\mathbf{u}(0, \cdot) = \mathbf{u}^0 \quad \text{in } \Omega, \quad (2.29)$$

where the boundaries Γ_D , Γ_0 , and Γ_{slip} are mutually disjoint.

⁴The term hydrostatic refers to water. For liquid steel, one uses the term *ferrostatic pressure*.

2.2 Theoretical background

The main purpose of this section is to introduce the *weak or variational formulation* of the Navier–Stokes equations. In fact, they play a central role in theoretical results concerning the existence and uniqueness of a solution, as well as in numerical methods. Space discretizations following the Galerkin Finite Element Method are based on the weak formulation of the Navier–Stokes equations.

2.2.1 Weak formulation

Let \mathbf{V} and \mathcal{Q} be some function spaces, which will be specified later. A weak formulation consists in multiplying the momentum equation with an arbitrary test function $\mathbf{v} \in \mathbf{V}$ and the continuity equation with an arbitrary test function $q \in \mathcal{Q}$, and then integrate over Ω . Finally, integration by parts is applied to reduce the derivative order of some terms. The variational form of the continuity equation reads directly

$$-\int_{\Omega} (\nabla \cdot \mathbf{u}) q \, d\mathbf{x} = -(\nabla \cdot \mathbf{u}, q) = 0,$$

where the notation (\cdot, \cdot) indicates the L_2 -inner product. Note that a minus sign has been added, allowing to have the symmetry of two blocks in the final problem (Section 2.3.2). The time derivative, right-hand side and convective terms are also straightforward:

$$\int_{\Omega} \mathbf{u}_t \cdot \mathbf{v} \, d\mathbf{x} = (\mathbf{u}_t, \mathbf{v}), \quad \int_{\Omega} \mathbf{f} \cdot \mathbf{v} \, d\mathbf{x} = (\mathbf{f}, \mathbf{v}), \quad \int_{\Omega} (\mathbf{u} \cdot \nabla) \mathbf{u} \cdot \mathbf{v} \, d\mathbf{x} = ((\mathbf{u} \cdot \nabla) \mathbf{u}, \mathbf{v}),$$

respectively. Applying integration by parts (theorem of Gauss), the weak form of the pressure term is given by

$$\begin{aligned} \int_{\Omega} \nabla p \cdot \mathbf{v} \, d\mathbf{x} &= \int_{\partial\Omega} p \mathbf{v} \cdot \mathbf{n} \, d\mathbf{s} - \int_{\Omega} p \nabla \cdot \mathbf{v} \, d\mathbf{x} \\ &= \int_{\Gamma_D \cup \Gamma_0 \cup \Gamma_{\text{slip}}} p \mathbf{v} \cdot \mathbf{n} \, d\mathbf{s} - (p, \nabla \cdot \mathbf{v}). \end{aligned} \quad (2.30)$$

Using the similar procedure on the viscous term yields

$$\begin{aligned} -2\nu \int_{\Omega} (\nabla \cdot \mathbb{D}(\mathbf{u})) \cdot \mathbf{v} \, d\mathbf{x} &= -2\nu \left(\int_{\partial\Omega} \mathbb{D}(\mathbf{u}) \mathbf{n} \cdot \mathbf{v} \, d\mathbf{s} - \int_{\Omega} \mathbb{D}(\mathbf{u}) \cdot \nabla \mathbf{v} \, d\mathbf{x} \right) \\ &= -2\nu \left(\int_{\Gamma_D \cup \Gamma_0} \mathbb{D}(\mathbf{u}) \mathbf{n} \cdot \mathbf{v} \, d\mathbf{s} + \int_{\Gamma_{\text{slip}}} \mathbb{D}(\mathbf{u}) \mathbf{n} \cdot \mathbf{v} \, d\mathbf{s} - (\mathbb{D}(\mathbf{u}), \nabla \mathbf{v}) \right). \end{aligned} \quad (2.31)$$

The last term can be reformulated using the symmetry of $\mathbb{D}(\mathbf{u})$:

$$\begin{aligned} (\mathbb{D}(\mathbf{u}), \nabla \mathbf{v}) &= \left(\mathbb{D}(\mathbf{u}), \frac{\nabla \mathbf{v}}{2} \right) + \left(\mathbb{D}(\mathbf{u})^T, \frac{\nabla \mathbf{v}^T}{2} \right) \\ &= \left(\mathbb{D}(\mathbf{u}), \frac{\nabla \mathbf{v}}{2} \right) + \left(\mathbb{D}(\mathbf{u}), \frac{\nabla \mathbf{v}^T}{2} \right) = (\mathbb{D}(\mathbf{u}), \mathbb{D}(\mathbf{v})). \end{aligned}$$

By decomposing the test function into normal and tangential components $\mathbf{v} = (\mathbf{v} \cdot \mathbf{n})\mathbf{n} + \sum_i (\mathbf{v} \cdot \mathbf{t}_i)\mathbf{t}_i$, the boundary term on Γ_{slip} in (2.31) can be written as

$$\int_{\Gamma_{\text{slip}}} \mathbb{D}(\mathbf{u})\mathbf{n} \cdot \mathbf{v} \, ds = \int_{\Gamma_{\text{slip}}} \mathbf{n}^\top \mathbb{D}(\mathbf{u})\mathbf{n}(\mathbf{v} \cdot \mathbf{n}) \, ds + \int_{\Gamma_{\text{slip}}} \sum_i \mathbf{n}^\top \mathbb{D}(\mathbf{u})\mathbf{t}_i(\mathbf{v} \cdot \mathbf{t}_i) \, ds, \quad (2.32)$$

where the last term vanishes because of the free slip condition (2.19) and (2.20).

Let us now specify the spaces \mathbf{V} and \mathcal{Q} to take into account the remaining boundary conditions and constraints:

$$\begin{aligned} \mathbf{V} &= \{\mathbf{v} \in (H^1(\Omega))^d, \mathbf{v} = \mathbf{0} \text{ on } \Gamma_D \cup \Gamma_0, \mathbf{v} \cdot \mathbf{n} = 0 \text{ on } \Gamma_{\text{slip}}\}, \\ \mathcal{Q} &= L_0^2(\Omega) = \{q \in L^2(\Omega), \int_{\Omega} q \, d\mathbf{x} = 0\}. \end{aligned}$$

The homogeneous boundary conditions (2.25) have to be incorporated into the velocity space in order to be used in the weak formulation. This is why they are also called *essential boundary conditions*. Note also that the constraint (2.28) for the additive constant of the pressure is included in the pressure space \mathcal{Q} . Using now $\mathbf{v} = \mathbf{0}$ on $\Gamma_D \cup \Gamma_0$ and $\mathbf{v} \cdot \mathbf{n} = 0$ on Γ_{slip} , three boundary terms vanish from the weak formulation, namely, the first terms in (2.30), (2.31), and (2.32),

$$\int_{\Gamma_D \cup \Gamma_0 \cup \Gamma_{\text{slip}}} p\mathbf{v} \cdot \mathbf{n} \, ds, \quad 2\nu \int_{\Gamma_{\text{slip}}} \mathbf{n}^\top \mathbb{D}(\mathbf{u})\mathbf{n}(\mathbf{v} \cdot \mathbf{n}) \, ds, \quad -2\nu \int_{\Gamma_D \cup \Gamma_0} \mathbb{D}(\mathbf{u})\mathbf{n} \cdot \mathbf{v} \, ds.$$

Before putting all the pieces together, there remains the initial condition and the Dirichlet condition on Γ_D . The first one can be either kept in the strong form (2.29) or added in the momentum equation by noticing that

$$\int_{\Omega} (\mathbf{u}(0) - \mathbf{u}^0) \cdot \mathbf{v} \, d\mathbf{x} = (\mathbf{u}(0) - \mathbf{u}^0, \mathbf{v}) = 0.$$

Let us define $\mathbf{u}_b \in H^1(\Omega)$ as an extension of \mathbf{b} into Ω for all t in $[0, T]$. It is used to construct the solution with the correct prescribed boundary velocity on Γ_D .

Altogether, the weak formulation of equations (2.22) to (2.29) reads:

Problem 2.2 (Weak formulation of the continuous Navier–Stokes equations): *Find $(\mathbf{u}, p) \in H^1(\Omega) \times \mathcal{Q}$, with $\mathbf{u} - \mathbf{u}_b \in V$ and $\mathbf{u}(0, \cdot) - \mathbf{u}_b(0, \cdot) = \mathbf{u}^0$, such that*

$$(\mathbf{u}_t, \mathbf{v}) + (2\nu \mathbb{D}(\mathbf{u}), \mathbb{D}(\mathbf{v})) + ((\mathbf{u} \cdot \nabla)\mathbf{u}, \mathbf{v}) - (\nabla \cdot \mathbf{v}, p) = (\mathbf{f}, \mathbf{v}), \quad (2.33)$$

$$-(\nabla \cdot \mathbf{u}, q) = 0, \quad (2.34)$$

for all $(\mathbf{v}, q) \in \mathbf{V} \times \mathcal{Q}$ and for all $t \in (0, T]$.

2.2.2 A few words about existence and uniqueness

Before going into the numerical methods to solve Problem 2.2, it should be noted that the well-posedness of the NSE is a difficult problem. The existence and uniqueness of its solution have been proved in the 2d case, but not in 3d.

The questions of the existence of a strong solution in 3d, for a so-called *classical problem* with C^∞ functions \mathbf{u} and p , and the uniqueness of the weak solution in 3d, are both major mathematical challenges of this century (Fefferman, 2006). These questions should be kept in mind in the context of optimal control problems (Chapter 4). There, a solution operator S of the NSE, defined as

$$S(\mathbf{f}, \mathbf{b}) = (\mathbf{u}, p),$$

intervenes in the derivation of the optimality system. We will have to assume that it is well defined, such that (\mathbf{u}, p) exists and is unique.

In the rest of this thesis, we shall rather focus on the solvability of the discrete equations. In this regard, one important tool is the *discrete inf-sup stability* (Section 2.3.2). It guarantees that the discrete velocity and pressure spaces are chosen in such a way that the problem is well-posed, ensuring in particular the uniqueness of the pressure. Thanks to the inf-sup condition, linear saddle point problems, such as the ones obtained after linearizing and fully discretizing the Navier–Stokes equations, can be solved correctly.

2.3 Numerical methods

The process leading from the continuous form of the NSE (2.22) to (2.29) to a numerically computable solution is composed of several steps, the main ones being: discretization with respect to the time and space variables, and the linearization of the nonlinear convective term. Furthermore, pressure and velocity can be treated either in a coupled way, or split into decoupled equations. All these aspects have led to a large number of numerical techniques to solve the NSE. In (John, 2016), the reader can find an overview of these different approaches. To give a short illustration, let us consider the discretization part. One can discretize time and space separately: for example, first in time and then in space (*horizontal method of lines*), or first in space and then in time (*vertical method of lines*). The equations obtained half way of these processes are called *semi-discretized* equations (in time or space), and, at the end, the *fully discretized* equations. A more sophisticated approach consists in discretizing simultaneously in space and time to get directly a full discretization, e.g., the space-time discontinuous Galerkin Finite Element Method (Van der Vegt and Van der Ven, 2002). Concerning space discretizations, one usually distinguishes between the Finite Element Method (FEM), the Finite Volume Method (FVM), and the Finite Difference Method (FDM). Real-life applications of incompressible flows are often solved using FVM. Indeed, two popular softwares for Computational Fluid Dynamics (CFD) are based on this method: the commercial software FLUENT and the open-source software OPENFOAM. This method conserves fluxes in each cell (volume) of the mesh, (Ferziger and Peric, 2002). Applied on structured meshes, it offers a comparably easy discretization with good conservation properties and matrix structures, making it suitable for engineering applications. On the other hand, FEMs can be more easily applied on complicated geometries and unstructured meshes, and dispose of an important background in numerical analysis.

In this dissertation, we apply a widely used numerical approach for the Navier–Stokes equations, (John, 2016). It consists first in the time discretization, then in the linearization of the convective term, and finally, in the space discretization with the Galerkin Finite Element Method. The pressure and velocity will always be treated in a coupled way.

2.3.1 Time discretization and linearization

Time discretization. Discretizing in time a first-order-in-time PDE as Equation (2.22) consists of balancing the time derivative term with an average of the remaining terms between two time steps. Let $k \in \mathbb{N}$, $\Delta t \in \mathbb{R}^+$ be the length of the time step ($\Delta t = t^k - t^{k-1}$), $\theta \in [0, 1]$, and \mathbf{u}^{k-1} , p^{k-1} , and \mathbf{f}^{k-1} be known evaluations of the functions at time step t^{k-1} . We also assume that the initial condition \mathbf{u}^0 is known. Then, using forward difference for the time term, the unknown quantities \mathbf{u}^k and p^k at the current time step t^k solve the equations

$$\begin{aligned} \frac{\mathbf{u}^k - \mathbf{u}^{k-1}}{\Delta t} &= (1 - \theta)(\nu \Delta \mathbf{u}^{k-1} - (\mathbf{u}^{k-1} \cdot \nabla) \mathbf{u}^{k-1} + \mathbf{f}^{k-1} - \nabla p^{k-1}) \\ &\quad + \theta(\nu \Delta \mathbf{u}^k - (\mathbf{u}^k \cdot \nabla) \mathbf{u}^k + \mathbf{f}^k - \nabla p^k), \\ \nabla \cdot \mathbf{u}^k &= 0. \end{aligned} \quad (2.35)$$

Here, it is important to note that the pressure terms $-(1 - \theta)\nabla p^{k-1}$ and $-\theta\nabla p^k$ do not usually appear as such in the literature. Instead, only one term appears, namely $-\nabla p^k$ (without the coefficient θ), leading to the more standard formulation

$$\begin{aligned} \frac{\mathbf{u}^k - \mathbf{u}^{k-1}}{\Delta t} &= (1 - \theta)(\nu \Delta \mathbf{u}^{k-1} - (\mathbf{u}^{k-1} \cdot \nabla) \mathbf{u}^{k-1} + \mathbf{f}^{k-1}) - \nabla p^k \\ &\quad + \theta(\nu \Delta \mathbf{u}^k - (\mathbf{u}^k \cdot \nabla) \mathbf{u}^k + \mathbf{f}^k), \\ \nabla \cdot \mathbf{u}^k &= 0. \end{aligned} \quad (2.36)$$

This formulation, which has the advantage of not requiring the initial pressure p^0 , is derived as follows⁵: one writes the time discretization of Equations (2.9) and (2.10) with respect to \mathbf{u} only, and adds the pressure term ∇p^k as the Lagrange multiplier enforcing the incompressibility condition at time t^k : $\nabla \cdot \mathbf{u}^k = 0$. To the best of the author's knowledge, only a few papers investigate formulations similar to (2.35) which use p^0 , e. g., (Rang, 2008). Their superiority over the more standard formulation could not be demonstrated. Therefore, we employ the standard form of semi-discretization (2.36).

By multiplying by Δt and re-ordering the terms, they can be re-written as

$$\begin{aligned} \mathbf{u}^k + \theta \Delta t (-\nu \Delta \mathbf{u}^k + (\mathbf{u}^k \cdot \nabla) \mathbf{u}^k) + \Delta t \nabla p^k \\ = \mathbf{u}^{k-1} + (1 - \theta) \Delta t (\nu \Delta \mathbf{u}^{k-1} - (\mathbf{u}^{k-1} \cdot \nabla) \mathbf{u}^{k-1}) \\ + (1 - \theta) \Delta t \mathbf{f}^k + \theta \Delta t \mathbf{f}^k, \\ \Delta t \nabla \cdot \mathbf{u}^k = 0. \end{aligned}$$

⁵However, the lack of the term in p^{k-1} in the Crank–Nicolson method leads to an approximation of p at an intermediate time, namely: $t^{k-1} + \frac{\Delta t}{2}$, (Bartsch, 2018, p. 20).

Note that the continuity equation has been scaled with the time step Δt . From numerical experience, this scaling makes the computations more efficient, (John, 2016, Remark 7.47).

Many time-stepping schemes belong to the family of *one-step θ -schemes*, which is itself a subclass of the more general *fractional-step θ -schemes*, (John, 2016, Chapter 7). The choices $\theta = 0$ and $\theta = 1$ lead to the first-order *forward* and *backward Euler methods*, respectively. The first type is an explicit method and requires a Courant–Friedrichs–Lewy (CFL) condition to be fulfilled to ensure stability, (Courant et al., 1928). This often leads to very small time steps and, therefore, very high computational time. The backward Euler is implicit: it has no restriction on the time step but is often too dissipative and therefore inaccurate. Using $\theta = \frac{1}{2}$, one obtains the popular *Crank–Nicolson* method, which is second-order and A-stable. Although it can suffer from instabilities in certain cases, it will be the time-stepping scheme of choice in the simulations of the next chapters.

Linearization. The basic idea to numerically solve a nonlinear equation is to solve linear approximations of the problem iteratively, until one converges to the actual solution. In the case of the semi-discretized NSE, two common types of methods (or iterations) are used to linearize the nonlinear part of the equations, i. e., the convective term $(\mathbf{u}^k \cdot \nabla)\mathbf{u}^k$: the *fixed-point or Picard iteration*, and the *Newton iteration*. The Picard iteration approximates the convective term at time t^k using a previously computed velocity \mathbf{u}^k as a “wind”:

$$(\mathbf{u}^k \cdot \nabla)\mathbf{u}^k \approx (\mathbf{u}^{k-1} \cdot \nabla)\mathbf{u}^k,$$

while the Newton method uses the following linearization (based on the gradient of the convective term):

$$(\mathbf{u}^k \cdot \nabla)\mathbf{u}^k \approx (\mathbf{u}^{k-1} \cdot \nabla)\mathbf{u}^k + (\mathbf{u}^k \cdot \nabla)\mathbf{u}^{k-1} - (\mathbf{u}^{k-1} \cdot \nabla)\mathbf{u}^{k-1}.$$

In these equations, one has to iterate and replace, in each iteration, \mathbf{u}^{k-1} by the newly computed solution, until convergence is reached.

Let n be the index of the nonlinear iterations, \mathbf{u}_n^k the velocity at the n -th iteration at time step k . At the first iteration, the initial “guess” \mathbf{u}_0^k is taken as the solution of the previous time step: $\mathbf{u}_0^k = \mathbf{u}^{k-1}$. Then, assuming that \mathbf{u}_{n-1}^k is known, the nonlinear term in the n -th Picard iteration can be written as

$$(\mathbf{u}_n^k \cdot \nabla)\mathbf{u}_n^k \approx (\mathbf{u}_{n-1}^k \cdot \nabla)\mathbf{u}_n^k,$$

and the Newton iteration as

$$(\mathbf{u}_n^k \cdot \nabla)\mathbf{u}_n^k \approx (\mathbf{u}_{n-1}^k \cdot \nabla)\mathbf{u}_n^k + (\mathbf{u}_n^k \cdot \nabla)\mathbf{u}_{n-1}^k - (\mathbf{u}_{n-1}^k \cdot \nabla)\mathbf{u}_{n-1}^k.$$

In each nonlinear iteration, the whole problem (2.9) and (2.10) has to be solved, replacing the convection term by one of these two approximations.

For more clarity, let us re-write Equations (2.9) and (2.10) with the Picard iteration (and the Crank–Nicolson scheme: $\theta = 1/2$):

$$\begin{aligned} \mathbf{u}_n^k + \frac{\Delta t}{2}(-\nu \Delta \mathbf{u}_n^k + (\mathbf{u}_{n-1}^k \cdot \nabla) \mathbf{u}_n^k) + \Delta t \nabla p^k \\ = \mathbf{u}^{k-1} + \frac{\Delta t}{2}(\nu \Delta \mathbf{u}^{k-1} - (\mathbf{u}^{k-1} \cdot \nabla) \mathbf{u}^{k-1}) + \frac{\Delta t}{2}(\mathbf{f}^{k-1} + \mathbf{f}^k), \end{aligned} \quad (2.37)$$

$$\Delta t \nabla \cdot \mathbf{u}_n^k = 0. \quad (2.38)$$

The iterations are said to have converged when the Euclidean norm of the residual vector of the equations is small enough, i. e., smaller than a fixed tolerance value. If this value is very small, e. g., 10^{-10} , the solution may be very accurate, but the number of iterations may be too high for a reasonable computational time. On the other hand, a coarser tolerance threshold may need a few number of iterations and be faster to compute, but may lead to poor results. Altogether, the choice of this tolerance value has to balance accuracy and computational cost, and depends on the application. Regarding the comparison between the Picard and Newton iterations for the steady-state NSE, the reader can find more details in (John, 2016, Chapter 6). In some cases, the Newton method converges faster (e. g., in the time-dependent case given in (John, 2016, Example 7.57)), but the Picard iteration is generally less dependent on the choice of the initial guess \mathbf{u}_0^k , and is quite efficient in terms of computational time and memory usage. Furthermore, it is well adapted for high Re. For example, in Ahmed et al. (2018), the authors have a positive experience of the Picard iterations. In the rest of this work, we will only consider the equations linearized with the Picard method, i. e., (2.37) and (2.38).

2.3.2 Space discretization and the Galerkin Finite Element Method

The space discretization we use is the *Galerkin Finite Element Method (FEM)*. The main idea of the FEM is to approximate the infinite-dimensional function spaces \mathbf{V} and \mathcal{Q} by discrete (i. e., finite-dimensional) spaces \mathbf{V}_h and \mathcal{Q}_h , and compute the discrete approximation (\mathbf{u}_h, p_h) of (\mathbf{u}, p) .

As explained earlier, the starting point of this method is the weak formulation (Problem 2.2). The procedures and the results are similar to the ones presented in Section 2.2.1, except that we now consider the semi-discrete in time and linearized equations (2.37) and (2.38). Basically, one has to replace \mathbf{u} in the weak form (2.33) and (2.34) by \mathbf{u}_n^k and adjust the terms according to the manipulations performed in the previous section. Let us recall the spaces of interest, knowing that the (\mathbf{u}_n^k, p^k) are now functions of the space variables only:

$$\mathbf{V} = \{\mathbf{v} \in (H^1(\Omega))^d, \mathbf{v} = \mathbf{0} \text{ on } \Gamma_D \cup \Gamma_0, \mathbf{v} \cdot \mathbf{n} = 0 \text{ on } \Gamma_{\text{slip}}\}, \quad (2.39)$$

$$\mathcal{Q} = L_0^2(\Omega) = \{q \in L^2(\Omega), \int_{\Omega} q \, d\mathbf{x} = 0\}. \quad (2.40)$$

The variational form of the time-discretized and linearized NSE is given in Problem 2.3.

Problem 2.3 (Weak formulation of the semi-discrete in time, linearized Navier–Stokes equations): *Given the nonlinear iteration $n \in \mathbb{N}$, the time step $k \in \mathbb{N}$, and given $\mathbf{u}_{n-1}^k \in H^1(\Omega)$ (with $\mathbf{u}_{n-1}^k - \mathbf{u}_b \in \mathbf{V}$), find $(\mathbf{u}_n^k, p^k) \in H^1(\Omega) \times \mathcal{Q}$, such that $\mathbf{u}_n^k - \mathbf{u}_b \in \mathbf{V}$ and*

$$\begin{aligned} & (\mathbf{u}_n^k, \mathbf{v}) + \frac{\Delta t}{2} [(2\nu \mathbb{D}(\mathbf{u}_n^k), \mathbb{D}(\mathbf{v})) + ((\mathbf{u}_{n-1}^k \cdot \nabla) \mathbf{u}_n^k, \mathbf{v})] - \Delta t (\nabla \cdot \mathbf{v}, p^k) \\ &= (\mathbf{u}^{k-1}, \mathbf{v}) - \frac{\Delta t}{2} [(2\nu \mathbb{D}(\mathbf{u}^{k-1}), \mathbb{D}(\mathbf{v})) + ((\mathbf{u}^{k-1} \cdot \nabla) \mathbf{u}^{k-1}, \mathbf{v})] \\ &+ \frac{\Delta t}{2} ((\mathbf{f}^{k-1}, \mathbf{v}) + (\mathbf{f}^k, \mathbf{v})), \end{aligned}$$

$$-\Delta t (\nabla \cdot \mathbf{u}_n^k, q) = 0,$$

for all $(\mathbf{v}, q) \in \mathbf{V} \times \mathcal{Q}$.

Note that the initial term \mathbf{u}^0 is implicitly included in the time discretization. One can now write the space discretization. Let us assume $d = 3$; the two-dimensional case is obtained similarly. Let \mathbf{V}_h and \mathcal{Q}_h be finite-dimensional spaces. We consider only *conforming finite element spaces*, i. e., \mathbf{V}_h and \mathcal{Q}_h are subspaces of the infinite spaces \mathbf{V} and \mathcal{Q} used in the weak formulation. They are equipped with the basis

$$\begin{aligned} \mathbf{V}_h &= \text{span}\{\phi_{h,i}\}_{i=1}^{3N_v} \\ &= \text{span} \left\{ \begin{Bmatrix} \phi_{h,i} \\ 0 \\ 0 \end{Bmatrix}_{i=1}^{N_v}, \begin{Bmatrix} 0 \\ \phi_{h,i} \\ 0 \end{Bmatrix}_{i=1}^{N_v}, \begin{Bmatrix} 0 \\ 0 \\ \phi_{h,i} \end{Bmatrix}_{i=1}^{N_v} \right\}, \\ \mathcal{Q}_h &= \text{span}\{\psi_{h,i}\}_{i=1}^{N_p}, \end{aligned}$$

where dN_v and N_p are the dimensions of the vector-valued function spaces \mathbf{V}_h and the scalar-valued space \mathcal{Q}_h , respectively. They are also called the *number of degrees of freedom*. We can now define the discrete velocity and pressure $(\mathbf{u}_h, p_h) \in \mathbf{V}_h \times \mathcal{Q}_h$, having the unique representation

$$\mathbf{u}_h = \left(\sum_{i=1}^{N_v} u_i^1 \phi_{h,i}, \sum_{i=1}^{N_v} u_i^2 \phi_{h,i}, \sum_{i=1}^{N_v} u_i^3 \phi_{h,i} \right)^T, \quad (2.41)$$

$$p_h = \sum_{i=1}^{N_p} p_i \psi_{h,i}, \quad (2.42)$$

and introduce the vectors which collect the unknown coefficients:

$$\underline{\mathbf{u}}_h = \begin{pmatrix} (u_i^1)_{i=1}^{N_v} \\ (u_i^2)_{i=1}^{N_v} \\ (u_i^3)_{i=1}^{N_v} \end{pmatrix} \in \mathbb{R}^{3N_v}, \quad \underline{p}_h = (p_i)_{i=1}^{N_p}.$$

In total, there are $3N_v + N_p$ unknowns. The same number of equations is provided by choosing, in the weak formulation, test functions equal to each of the basis function $(\phi_{h,i})_{i=1}^{3N_v}$ and $(\psi_{h,i})_{i=1}^{N_p}$. First, let us replace the infinite-dimensional spaces in Problem 2.3 by the finite-dimensional ones, in order to get the *fully discretized, in time and space, and linearized Navier–Stokes equations*.

Problem 2.4 (Fully discretized and linearized NSE, with Crank-Nicolson time discretization, Galerkin Finite Element Method, and Picard iteration): *Let \mathbf{V}_h be a finite-dimensional subspace of $H^1(\Omega)$. Given the nonlinear iteration $n \in \mathbb{N}$, the time step $k \in \mathbb{N}$, and given $\mathbf{u}_{h,n-1}^k \in \mathbf{V}_h$ (with $\mathbf{u}_{h,n-1}^k - \mathbf{u}_{g,h} \in \mathbf{V}_h$), find $(\mathbf{u}_{h,n}^k, p_h^k) \in \mathbf{V}_h \times \mathcal{Q}_h$, such that $\mathbf{u}_{h,n}^k - \mathbf{u}_{g,h} \in \mathbf{V}_h$ and*

$$\begin{aligned} & (\mathbf{u}_{h,n}^k, \mathbf{v}_h) + \frac{\Delta t}{2} [(2\nu \mathbb{D}(\mathbf{u}_{h,n}^k), \mathbb{D}(\mathbf{v}_h)) + ((\mathbf{u}_{h,n-1}^k \cdot \nabla) \mathbf{u}_{h,n}^k, \mathbf{v}_h)] - \Delta t (\nabla \cdot \mathbf{v}_h, p_h^k) \\ &= (\mathbf{u}_{h,n-1}^k, \mathbf{v}_h) - \frac{\Delta t}{2} [(2\nu \mathbb{D}(\mathbf{u}_{h,n-1}^k), \mathbb{D}(\mathbf{v}_h)) + ((\mathbf{u}_{h,n-1}^{k-1} \cdot \nabla) \mathbf{u}_{h,n-1}^{k-1}, \mathbf{v}_h)] \\ &+ \frac{\Delta t}{2} ((\mathbf{f}^{k-1}, \mathbf{v}_h) + (\mathbf{f}^k, \mathbf{v}_h)), \end{aligned}$$

$$-\Delta t (\nabla \cdot \mathbf{u}_{h,n}^k, q_h) = 0,$$

for all $(\mathbf{v}_h, q_h) \in \mathbf{V}_h \times \mathcal{Q}_h$.

Note the index h for the test functions \mathbf{v}_h and q_h : they belong also to the discrete spaces. Inserting the representations (2.41) and (2.42) into Problem 2.4, one

can test the momentum equation by the test functions $\mathbf{v}_h = \begin{Bmatrix} \phi_{h,j} \\ 0 \\ 0 \end{Bmatrix}$, $\mathbf{v}_h = \begin{Bmatrix} 0 \\ \phi_{h,j} \\ 0 \end{Bmatrix}$,

$\mathbf{v}_h = \begin{Bmatrix} 0 \\ 0 \\ \phi_{h,j} \end{Bmatrix}$, for $j = 1 \dots N_v$, and the continuity equation with $q_h = \psi_{h,j}$, for $j = 1 \dots N_p$ to obtain the desired $3N_v + N_p$ independent linear equations. We explicitly write the expressions and matrix form term by term (without the coefficients Δt and ν) before gathering everything:

$$(\mathbf{u}_{h,n}^k, \phi_{h,j}) = \left(\sum_{i=1}^{3N_v} u_i \phi_{h,i}, \phi_{h,j} \right) = \sum_{i=1}^{3N_v} u_i (\phi_{h,i}, \phi_{h,j}), \quad (2.43)$$

$$(\mathbb{D}(\mathbf{u}_{h,n}^k), \mathbb{D}(\phi_{h,j})) = \left(\mathbb{D} \left(\sum_{i=1}^{3N_v} u_i \phi_{h,i} \right), \mathbb{D}(\phi_{h,j}) \right) = \sum_{i=1}^{3N_v} u_i (\mathbb{D}(\phi_{h,i}), \mathbb{D}(\phi_{h,j})), \quad (2.44)$$

$$((\mathbf{u}_{h,n-1}^k \cdot \nabla) \mathbf{u}_{h,n}^k, \phi_{h,j}) = \sum_{i=1}^{3N_v} u_i ((\mathbf{u}_{h,n-1}^k \cdot \nabla) \phi_{h,i}, \phi_{h,j}), \quad (2.45)$$

$$(p_h^k, \nabla \cdot \phi_{h,j}) = \sum_{i=1}^{N_p} p_i (\psi_{h,i}, \nabla \cdot \phi_{h,j}), \quad (2.46)$$

$$(\nabla \cdot \mathbf{u}_{h,n}^k, \psi_{h,j}) = \sum_{i=1}^{3N_v} u_i (\nabla \cdot \phi_{h,i}, \psi_{h,j}). \quad (2.47)$$

The first term (2.43) is nonzero only when $j = i$, which gives a mass matrix with the following block structure:

$$M = \begin{pmatrix} M_{11} & 0 & 0 \\ 0 & M_{11} & 0 \\ 0 & 0 & M_{11} \end{pmatrix} \in \mathbb{R}^{3N_v \times 3N_v}. \quad (2.48)$$

By developing the tensor \mathbb{D} , the viscous term (2.44) can be written explicitly:

$$\begin{aligned}
(\mathbb{D}(\phi_{h,i}), \mathbb{D}(\phi_{h,j})) &= \int_{\Omega} \mathbb{D}(\phi_{h,i}) : \mathbb{D}(\phi_{h,j}) \, d\mathbf{x} \\
&= \int_{\Omega} \sum_{k,l=1}^3 \frac{1}{2} \left(\frac{\partial(\phi_{h,i})^k}{\partial x_l} + \frac{\partial(\phi_{h,i})^l}{\partial x_k} \right) \frac{1}{2} \left(\frac{\partial(\phi_{h,j})^k}{\partial x_l} + \frac{\partial(\phi_{h,j})^l}{\partial x_k} \right) d\mathbf{x} \\
&= \frac{1}{4} \int_{\Omega} \sum_{k,l=1}^3 \left(\frac{\partial(\phi_{h,i})^k}{\partial x_l} \frac{\partial(\phi_{h,j})^k}{\partial x_l} + \frac{\partial(\phi_{h,i})^k}{\partial x_l} \frac{\partial(\phi_{h,j})^l}{\partial x_k} \right. \\
&\quad \left. + \frac{\partial(\phi_{h,i})^l}{\partial x_k} \frac{\partial(\phi_{h,j})^k}{\partial x_l} + \frac{\partial(\phi_{h,i})^l}{\partial x_k} \frac{\partial(\phi_{h,j})^l}{\partial x_k} \right) d\mathbf{x},
\end{aligned}$$

which has to be multiplied by 2ν . Thus, the corresponding matrix has the following matrix structure:

$$A = \begin{pmatrix} A_{11} & A_{12} & A_{13} \\ A_{12}^T & A_{22} & A_{23} \\ A_{13}^T & A_{23}^T & A_{33} \end{pmatrix} \in \mathbb{R}^{3N_v \times 3N_v}. \quad (2.49)$$

The convective term (2.45) reads

$$((\mathbf{u}_{h,n-1}^k \cdot \nabla) \phi_{h,i}, \phi_{h,j}) = \int_{\Omega} \sum_{l=1}^3 (\mathbf{u}_{h,n-1}^k)^l \left(\frac{\partial}{\partial x_l} \phi_{h,i} \right) \phi_{h,j} \, d\mathbf{x},$$

which is zero whenever $\phi_{h,i}$ and $\phi_{h,j}$ do not represent the same component. If they have the same non-vanishing components, the contribution is the same for any of $l = 1 \dots 3$. Thus, the matrix structure of the convective term is

$$C(\mathbf{u}_{h,n-1}^k) = \begin{pmatrix} C_{11} & 0 & 0 \\ 0 & C_{11} & 0 \\ 0 & 0 & C_{11} \end{pmatrix} \in \mathbb{R}^{3N_v \times 3N_v}. \quad (2.50)$$

Note also that these contributions are nonsymmetric, and deteriorates thereby the “quality” of the matrix, in terms of convergence of iterative solvers. Similarly, the velocity-pressure terms (2.46) and (2.47) are given by

$$(\psi_{h,i}, \nabla \cdot \phi_{h,j}) = \int_{\Omega} \sum_{l=1}^3 \psi_{h,i} \frac{\partial \phi_{h,j}}{\partial x_l} \, d\mathbf{x}, \quad B^T = \begin{pmatrix} B_1^T \\ B_2^T \\ B_3^T \end{pmatrix} \in \mathbb{R}^{3N_v \times N_p} \quad (2.51)$$

$$(\nabla \cdot \phi_{h,i}, \psi_{h,j}) = \int_{\Omega} \sum_{l=1}^3 \psi_{h,j} \frac{\partial \phi_{h,i}}{\partial x_l} \, d\mathbf{x}, \quad B = (B_1 \ B_2 \ B_3) \in \mathbb{R}^{N_p \times 3N_v}. \quad (2.52)$$

The right-hand side can be written in vector form using the matrices introduced above:

$$\mathbf{r}_u = M \underline{\mathbf{u}}_h^{k-1} - \frac{\Delta t}{2} (A + C(\underline{\mathbf{u}}_h^{k-1})) \underline{\mathbf{u}}_h^{k-1} + \frac{\Delta t}{2} ((\mathbf{f}^k, \phi_{h,i}) + (\mathbf{f}^{k-1}, \phi_{h,i})).$$

Altogether, the linear system of equations can be written in a compact matrix form, by adding all the terms (2.48), (2.49), (2.50), (2.51), and (2.52):

$$\begin{pmatrix} M + \frac{\Delta t}{2}(A + C(\mathbf{u}_{h,n-1}^k)) & -\Delta t B^\top \\ -\Delta t B & 0 \end{pmatrix} \begin{pmatrix} \mathbf{u}_h \\ p_h \end{pmatrix} = \begin{pmatrix} \mathbf{r}_u \\ 0 \end{pmatrix}. \quad (2.53)$$

This form of linear system is called a *saddle point problem*. The computation of the matrix entries follows a standard procedure in the FEM. Basis functions are generally chosen to have non-zero values only locally and such that the integral expressions can be computed efficiently. Typically, they consist of *elementwise polynomials*, i.e., with small support (only a few neighboring mesh cells). The small support of the basis functions allows the system matrix to be *sparse* and the fact that they are polynomials allows the application of *quadrature formulas* to evaluate the integrals, up to the machine precision. In the next paragraph, we focus on the specific finite element spaces used to solve the fully discretized NSE.

Choice of the finite element spaces – The discrete inf-sup condition.

As mentioned earlier, the spaces \mathbf{V}_h and \mathcal{Q}_h have to fulfill the discrete inf-sup condition to ensure that the discrete Problem 2.4 is well-posed, i.e., it has a unique solution, (John, 2016, p.55):

Definition 2.5 (The discrete inf-sup condition for conforming FE spaces): *The pair of conforming finite element spaces \mathbf{V}_h and \mathcal{Q}_h is said to fulfill the discrete inf-sup condition if there exists $\gamma > 0$ such that*

$$\inf_{q_h \in \mathcal{Q}_h, q_h \neq 0} \sup_{\mathbf{v}_h \in \mathbf{V}_h, \mathbf{v}_h \neq 0} \frac{-(q_h, \nabla \cdot \mathbf{v}_h)}{\|\mathbf{v}_h\|_{\mathbf{V}_h} \|q_h\|_{\mathcal{Q}_h}} > \gamma.$$

Since polynomial (Taylor-Lagrange) basis functions are the most popular in the FEM literature, a lot of studies investigated the inf-sup stability of spaces spanned by such polynomials. It turns out that the Taylor–Hood finite element spaces, given by $P_k/P_{k-1}, k \geq 2$ (on triangular and tetrahedral grids), and $Q_k/Q_{k-1}, k \geq 2$ (on quadrilateral and hexahedral meshes) are inf-sup stable. In particular, the popular low order finite elements P_2/P_1 and Q_2/Q_1 (piecewise quadratic for the velocity and piecewise linear for the pressure) are inf-sup stable. As it can be seen in different comparison studies (Ahmed et al., 2018, John, 2016, John and Matthies, 2001), the performance of the finite elements, in terms of accuracy and computational time, depends on the mesh and the type of solver and/or preconditioner. In general, the FE P_2/P_1 and Q_2/Q_1 perform quite satisfactorily. Hence, they will be used in the applications of this thesis. Using lower order (such as P_1/P_0) or same order (e.g., P_1/P_1) elements leads to instabilities in the pressure. It is possible to use stabilization methods (John et al., 2019), but this would introduce multiple other difficulties, such as the dependency on further stabilization parameters (John, 2016, Chapter 3). This highlights the importance of inf-sup stable elements in saddle-point problems. Other classical FE used in the NSE can be found in (John, 2016, Chapter 3), for example: P_1^{nc}/P_0 (non-conforming linear or Crouzeix-Raviart elements), P_1^{bubble}/P_0 (MINI elements), Q_1^{rot}/P_0 , Q_2/P_1^{disc} , and $P_2^{\text{bubble}}/P_1^{\text{disc}}$.

Treatment of the boundary conditions. In Problem 2.4, three types of boundary conditions are prescribed “strongly”, i.e., they appear in the definition of the velocity space \mathbf{V} (2.39) and not in the terms of the variational formulation: the homogeneous and non-homogeneous Dirichlet on Γ_0 and Γ_D , respectively, and the no-penetration condition on Γ_{slip} . They have to be taken into account in the matrix system (2.53). The typical way of proceeding in the FEM consists of “manually” modifying the equations concerned by a degree of freedom at the domain boundary, such that the velocity is equal to the prescribed value at that degree of freedom. To illustrate this, consider a degree of freedom i_D on a Dirichlet boundary, where the velocity is \mathbf{b} ($= \mathbf{0}$ or $\neq \mathbf{0}$). Then, the three rows (i.e., the three equations) of the system matrix at $(i_D, i_D^2 = i_D + N_v, i_D^3 = i_D + 2N_v)$ are replaced by three lines filled with 0 except on the one (diagonal) entry corresponding to $u_{i_D}^1, u_{i_D}^2, u_{i_D}^3$, where it has the value 1:

$$\begin{array}{lcl} i_D & \longrightarrow & \begin{pmatrix} \vdots & \vdots & \vdots \\ 0 \dots 0 & 1 & 0 \dots \dots \dots 0 \\ \vdots & \vdots & \vdots \\ 0 \dots \dots \dots 0 & 1 & 0 \dots \dots \dots 0 \\ \vdots & \vdots & \vdots \\ 0 \dots \dots \dots \dots \dots 0 & 1 & 0 \dots 0 \\ \vdots & \vdots & \vdots \end{pmatrix} \begin{pmatrix} \vdots \\ u_{i_D}^1 \\ \vdots \\ u_{i_D}^2 \\ \vdots \\ u_{i_D}^3 \\ \vdots \end{pmatrix} = \begin{pmatrix} \vdots \\ b_{i_D}^1 \\ \vdots \\ b_{i_D}^2 \\ \vdots \\ b_{i_D}^3 \\ \vdots \end{pmatrix}. \end{array} \quad (2.54)$$

These modified equations directly yield

$$u_{i_D}^1 = b_{i_D}^1, \quad u_{i_D}^2 = b_{i_D}^2, \quad u_{i_D}^3 = b_{i_D}^3,$$

where $b_{i_D}^j, j = 1 \dots 3$, is set to 0 (homogeneous Dirichlet) or to a nonzero prescribed value if a non-homogeneous condition applies.

The no-penetration condition follows a similar treatment. For simplicity, assume that Γ_{slip} is a plane (or a line in 2d) orthogonal to the vertical direction. This will be the case in the applications of this thesis. Then, the no-penetration condition reads $\mathbf{u} \cdot \mathbf{e}_z = 0$, such that only the third component of \mathbf{u} should be forced to 0. The implementation is then simply

$$i_D + 2N_v \longrightarrow \begin{pmatrix} \vdots & \vdots & \vdots \\ \dots & \ddots & \dots \dots \dots \dots \dots \\ \vdots & \vdots & \vdots \\ \dots & \dots & \dots \ddots & \dots \dots \dots \\ \vdots & \vdots & \vdots \\ 0 \dots \dots \dots \dots \dots 0 & 1 & 0 \dots 0 \\ \vdots & \vdots & \vdots \end{pmatrix} \begin{pmatrix} \vdots \\ \vdots \\ \vdots \\ \vdots \\ u_{i_D}^3 \\ \vdots \end{pmatrix} = \begin{pmatrix} \vdots \\ \vdots \\ \vdots \\ \vdots \\ 0 \\ \vdots \end{pmatrix}. \quad (2.55)$$

Note that a weak implementation of the free slip with no-penetration condition (2.17) and (2.16) would have led to additional entries in the matrix, see (John, 2002), replacing the manipulation (2.55). In this case, the penetration coefficient is chosen arbitrarily high, e. g., 10^{12} , such that the no-penetration condition reads

$$10^{12}u_{i_D}^3 = b_{i_D}^3,$$

resulting in a vanishing velocity component. However, as experienced in (John, 2002, Remark 4.2), the weak imposition of no-penetration condition deteriorates significantly the performance of iterative solvers. On the contrary, applying the modifications (2.54) and (2.55) improve the convergence of iterative solvers and delivers the exact value at the boundary.

A final word about the implementation of strong conditions: the pressure field also needs to be corrected according to the definition of the pressure space \mathcal{Q} in (2.40). Indeed, the constraint on the zero integral mean value does not appear in the variational formulation. This is done by subtracting the mean value of the computed p from all $p_{h,i}$, $i = 1 \dots N_p$.

2.3.3 Axisymmetric formulation

In some applications, as in ladle stirring, flows are assumed to have an axial symmetry. They are called *axisymmetrical flows*, or *2.5d flows*, because their behavior in terms of physical realism is somehow between two- and three-dimensional. The axisymmetrical equations are best formulated in a cylindrical space frame (r, θ, z) . They are based on two main assumptions: the velocity and pressure are independent of the angular coordinate θ :

$$\frac{\partial u_r}{\partial \theta} = 0, \quad \frac{\partial u_\theta}{\partial \theta} = 0, \quad \frac{\partial u_z}{\partial \theta} = 0, \quad \frac{\partial p}{\partial \theta} = 0,$$

and there is no angular velocity:

$$u_\theta = 0.$$

The derivation of the strong form of the axisymmetrical NSE can be found in Annex A. Equation (A.4) can be multiplied by the factor r or r^2 for a better numerical behavior. The case $r = 0$ is given by a naturally imposed symmetry condition on the symmetry axis Γ_{axis} (Ganesan and Tobiska, 2008, p.125):

$$u_r = 0, \quad \frac{\partial u_z}{\partial r} = 0 \quad \text{on } \Gamma_{\text{axis}}. \quad (2.56)$$

For more details on the axisymmetric NSE, the reader is referred to (Bartsch, 2018, p.122-130). Here, we restrict ourselves to the impact of the axisymmetrical formulation on numerical implementation. The weak formulation of the equations is given by (Bartsch, 2018, p.128-129):

Problem 2.6 (Weak form of the time-discretized nonlinear axisymmetrical Navier–Stokes equations): *Given the r -weighted space $L^2(\Omega, r)$, the r -weighted*

Sobolev spaces $H^1(\Omega, r) = W^{1,2}(\Omega, r)$ and $V^1(\Omega, r) = H^1(\Omega, r) \cap L^2(\Omega, r^{-1})$, find $\mathbf{u} = (u_r, u_z) \in H^1(\Omega, r) \times V^1(\Omega, r)$ and $p \in L^2(\Omega, r)$ such that

$$\begin{aligned} \int_{\Omega} \left[\mathbf{u} \cdot \mathbf{v} - \frac{\Delta t}{2} \nu \left(\nabla_{r,z} \mathbf{u} : \nabla_{r,z} \mathbf{v} + \frac{u_r v_r}{r^2} \right) + \frac{\Delta t}{2} ((\mathbf{u} \cdot \nabla_{r,z}) \mathbf{u}) \cdot \mathbf{v} \right. \\ \left. + \Delta t (\nabla_{r,z} p) \cdot \mathbf{v} \right] r \, dr \, dz - \int_{\Omega} (\mathbf{f} \cdot \mathbf{v}) r \, dr \, dz = 0, \\ \Delta t \int_{\Omega} \left(\nabla_{r,z} \mathbf{u} + \frac{u_r}{r} \right) q r \, dr \, dz = 0, \end{aligned}$$

for all $\mathbf{v} = (v_r, v_z) \in H^1(\Omega, r) \times V^1(\Omega, r)$ and $q \in L^2(\Omega, r)$.

Comparing this axisymmetric problem with the Cartesian problem 2.3, one observes one extra-term in each of the momentum and continuity equations ($\frac{u_r v_r}{r^2}$ and $\frac{u_r}{r}$, respectively), and the factor r in all the integrals. Thus, as pointed by (Bartsch, 2018, p.128), a standard 2d flow solver in Cartesian frame can easily be adapted to the axisymmetrical case: one only needs to add these two terms and multiply the integrands by the coordinate r . This is the implementation used for the corresponding simulations in Chapter 3.

2.4 Linear solvers

2.4.1 Introduction

As described earlier, numerical methods for PDEs leads to linear systems of equations of the form

$$\mathcal{A} \mathbf{x} = \mathbf{r}. \quad (2.57)$$

Depending on the properties of \mathcal{A} (symmetry, definiteness, block structure, sparsity, size...), one can use different tools from linear algebra to solve the system efficiently, e. g., direct solvers, iterative solvers, and preconditioners. For a detailed introduction to linear solvers, the reader is referred to (Saad, 2003). In this section, we briefly describe the specificities of the linear system obtained from the discretization of the NSE and present the main techniques used in the numerical simulations of this dissertation.

Saddle point problems. The system (2.53) is a so-called *saddle point problem*

$$\begin{pmatrix} A & B^T \\ B & 0 \end{pmatrix} \begin{pmatrix} \mathbf{u}_h \\ \underline{p}_h \end{pmatrix} = \begin{pmatrix} \mathbf{r}_u \\ 0 \end{pmatrix}, \quad (2.58)$$

characterized by the lower right 0-block. It comes from the usage of inf-sup stable spaces: in this case, there is no stabilizing pressure-pressure coupling term. The difficulties associated with such systems are its indefiniteness, the non-symmetry of the A -block due to the convection term, and the zero diagonal in the lower right block, (Bartsch, 2018, Ahmed et al., 2018).

The solvers for linear systems of equations can be classified in *direct and iterative solvers*. Direct solvers perform an LU factorization of \mathcal{A} , leading to a triangular matrix which can be solved easily and exactly (i.e., up to the machine precision). Furthermore when the system of equations is fixed, the LU decomposition does not change, and can be re-used with different right-hand sides, saving computational time. However, the computation of the LU factorization itself can be prohibitively expensive for large matrices with “bad” properties, as in the Navier–Stokes equations, especially in 3d. Therefore, in this work, direct solvers are mainly used for small to medium 2d problems. The well-known packages UMFPACK for sequential programming, (Davis, 2004), and MUMPS for parallel programming, (Amestoy et al., 2001), are used. Contrary to direct solvers, iterative solvers do not try to solve (2.57) exactly, but compute successive approximations of its solution. One of the most popular iterative methods is FGMRES (Flexible Generalized Minimal RESidual), which belongs to the class of Krylov subspace methods, (Saad, 2003), and which can be used for non-symmetric matrices. This is the main iterative method used in this work. In order to perform the best, iterative solvers need to be used together with *preconditioners*. Roughly speaking, a preconditioner \mathcal{P} is an appropriately chosen matrix such that the system

$$\begin{aligned}\mathcal{A}\mathcal{P}^{-1}\mathbf{y} &= \mathbf{r}, \\ \mathcal{P}\mathbf{x} &= \mathbf{y},\end{aligned}$$

which has the same solution as (2.57), is easier to solve (faster convergence). Note that there are also left-preconditioners, but, since we are interested here on the LSC method, we consider only right preconditioners.

In other words, a successful preconditioning modifies \mathcal{A} , in such a way that $\mathcal{A}\mathcal{P}^{-1}$ has a smaller condition number than \mathcal{A} , becoming easier to solve for iterative solvers. Often, preconditioners are tailored specifically for different applications to exploit the system properties and block structures. For saddle point problems coming from the Navier–Stokes equations, examples of well-known preconditioners are the Geometric Multigrid Method and the Least Squares Commutator (LSC). The latter is often used in this work and will be shortly detailed in the next section. Combinations of iterative solvers with preconditioners, e.g., FGMRES with LSC preconditioner, become computationally more efficient for large 2d, or medium to large 3d problems, than other types of solvers.

2.4.2 FGMRES with LSC preconditioner

This section is based on the work from (Ahmed et al., 2018) and (Bartsch, 2018). Further details on the LSC preconditioner can also be found in (Elman, 2005). A good starting point to derive a preconditioner is to write the blockwise LU decomposition of the system matrix (2.58):

$$\mathcal{A} = \begin{pmatrix} I & 0 \\ BA^{-1} & I \end{pmatrix} \begin{pmatrix} A & B^\top \\ 0 & S_C \end{pmatrix} = LU,$$

where we have introduced the *Schur complement*:

$$S_C = -BA^{-1}B^\top.$$

The matrix $\mathcal{A}U^{-1} = L$ having perfectly clustered eigenvalues (triangular matrix with ones on the diagonal), the matrix U can be considered as a good preconditioner. However, the Schur complement S_C is quite difficult to compute: one has to invert A , and A^{-1} is not sparse in general. Constructing an approximation of S_C which is easier to compute, is the main purpose of the LSC preconditioner.

Denoting by D the diagonal of the velocity mass matrix, the LSC preconditioner uses the following approximation of the Schur complement (Bartsch, 2018),

$$S_{C,\text{LSC}} = -(BD^{-1}B^\top)(BD^{-1}AD^{-1}B^\top)^{-1}(BD^{-1}B^\top).$$

Now, one preconditioning step consists in solving

$$\begin{pmatrix} A & B^\top \\ 0 & S_{C,\text{LSC}} \end{pmatrix} \begin{pmatrix} \underline{\mathbf{u}}_h \\ \underline{p}_h \end{pmatrix} = \begin{pmatrix} \mathbf{r}_u \\ \mathbf{r}_p \end{pmatrix}.$$

Two subproblems are computed in a decoupled way: first, the pressure subproblem, corresponding to the lower part (Schur complement part),

$$S_{C,\text{LSC}} \underline{p}_h = \mathbf{r}_p.$$

This subproblem can be efficiently solved with direct solvers. Indeed, first, it is generally small because of the relatively small size of the pressure space. Furthermore, it is independent of time, such that its inverse needs to be computed only once and can be re-used at all time steps and all nonlinear steps. Thus, direct solvers for this subproblem are a good choice. Then, the velocity subproblem

$$A\underline{\mathbf{u}}_h = \mathbf{r}_u - B^\top \underline{p}_h. \quad (2.59)$$

can be computed either with direct or iterative solvers: Since this problem is quite big (almost as big as the whole system) and includes the matrix A , which changes at every nonlinear step, direct solvers are not efficient here. Iterative solvers are preferred for this subproblem. (Ahmed et al., 2018) recommend using BiCGStab with SSOR preconditioner for (2.59). Once the solution $(\underline{\mathbf{u}}_h, \underline{p}_h)$ of (2.58) is found, we can step to the next FGMRES iteration.

In terms of computational performance, (Ahmed et al., 2018) concluded that, in the time-dependent case, FGMRES+LSC combined with small time steps was the fastest solver tested, for most of the finite element pairs employed. Using Taylor-Hood Q_2/Q_1 elements, the time advantage was the most remarkable. This is attributed to the better properties of the A -block, which is more influenced by the mass matrix when the time step Δt is small. Based on these findings, the solver FGMRES+LSC will be the solver of choice for the large 3d models studied in this dissertation.

2.5 Turbulence

In Section 2.1.1, the inherent difficulties of the full NSE were mentioned. One of them concerns the possible domination of the convective term, occurring at high Reynolds numbers. In fact, most real-life applications of incompressible flows have

a high Reynolds number. Given the density and viscosity of, for example, water (or liquid steel which is physically very similar), the ratio ρ/μ has an order of magnitude of already 10^6 . One needs therefore very low characteristic velocity U and length L to keep Re reasonably small, in order to stay in the *regime of laminar flows*. Otherwise, one has to consider *high Reynolds number and turbulent flows*. This is the case in this dissertation (see Chapter 3).

The numerical simulation of such flows has been largely investigated in the literature. In this section, we introduce basic notions to understand how to compute numerical solutions of the turbulent flows encountered later on. In particular, some physical and mathematical background about the theory of turbulent incompressible flows is given, and numerical aspects are presented. Large parts of this section are based on (John, 2016, Chapter 8).

2.5.1 Physical and mathematical background

As mentioned above, turbulent flows occur at high Reynolds numbers. However, this is more an observation from the mathematical point of view rather than a definition of turbulence. In fact, it is difficult to define turbulence. Instead, one recognizes it thanks to physical characteristics. Typically, turbulent flows possess flow structures, e. g., eddies, of very different scales: from large structures to very small eddies up to the microscale, (John, 2016, Chapter 8). They are multiscale flows, where the smallest eddies play a major role and cannot be simply neglected. Indeed, they are part of the *energy cascade* described in (Richardson, 1922). It states that the largest eddies, being unstable, break up into smaller ones and transfer kinetic energy, in the mean, to eddies of smaller scale. This process takes place at all scales δ , such that the local Reynolds number decreases from scale to scale because of its dependency on δ : $Re(\delta) := U_\delta \delta / \nu$. Consequently, the energy cascade continues until $Re(\delta)$ is sufficiently small (e. g., laminar flow, $Re = 1$), which happens at sufficiently small eddies of size δ_K . At this scale, the molecular viscosity becomes effective, balances or dissipates the kinetic energy, and keeps the eddy stable. The size of the smallest eddy δ_K is also called the *Kolmogorov length, or dissipative scale*. Based on physical considerations, it can be estimated as

$$\delta_K = \mathcal{O}\left(Re^{-3/4}\right),$$

see (John, 2016, Remarks 8.7-8.10) for a derivation of this result.

This quantity is of particular interest for numerical applications, because one can estimate up to which scale the flow can be resolved for a given Re , or, the other way round, up to which Re the NSE can be solved on a given mesh. For example, for Reynolds number of the order 10^5 as in ladle stirring applications (see Section 3.1.3), the Kolmogorov scale is in the order of $\delta_K = 10^{-3.75}$. To resolve these scales on a unit cubic domain $\Omega = (0, L)^3$, with $L = 1$, one needs a cell size inferior to δ_K in each direction, leading to a total number of $\mathcal{O}\left(\left(\frac{L}{\delta_K}\right)^3\right) = \mathcal{O}\left(Re^{-9/4}\right) \approx 10^{11}$. Numerical simulations on such meshes cannot be afforded today or in the near future, even on supercomputers. Reciprocally, with more

feasible (but still very fine) meshes, e.g., 10^8 cells ($\sim 464^3$), scales up to $\delta_K = \frac{1}{464} \approx 0.0021$ unit can be resolved, corresponding to a Reynolds number of $\delta_K^{-4/3} = 464^{4/3} \approx 3590$. This is much lower than in common industrial applications.

In theory, the application of the full NSE without any simplifying assumptions is capable of resolving the different scales of all flow structures and eddies. This approach is also called *Direct Numerical Simulation (DNS)* in the context of turbulent flows. In numerical practice, if the mesh is not fine enough to capture δ_K , the Direct Numerical Simulation typically blows up. This is why alternatives to DNS have to be used for turbulent flows. The basic idea of alternative approaches consists to model the small, unresolved, eddies, or model their influence on the coarser, resolved, scales. This defines what a turbulence model is. In this sense, it can be considered as a simplification of the full NSE. The reduction of complexity becomes obvious in theoretical results: existence, uniqueness, and improved error estimates can be proven in some turbulent models, see (John, 2016, Remark 8.22).

Before presenting the Large Eddy Simulation Smagorinsky turbulence model, it is important to mention the fundamental differences between 2d and 3d flows with respect to turbulence, (John, 2016, Remark 8.14). First, the smallest dissipative length δ_K is bigger in 2d than in 3d:

$$\delta_{K,2d} = \mathcal{O}\left(\text{Re}^{-1/2}\right).$$

Consequently, a mesh size which is too big to resolve the flow in 3d may be small enough to resolve it in 2d. As a corollary, a flow which is turbulent in 3d is not necessarily turbulent in 2d. Numerically, it can thus happen that, if a 3d application requires a turbulence model, the two-dimensional case with the same Reynolds number may be solved without a turbulence model, i.e., with a Direct Numerical Simulation. It turns out that ladle stirring simulations are a good example of this fundamental difference (Chapter 3). The flow is also qualitatively different in 2d and 3d: vortex stretching is absent from 2d cases, see (John, 2016, Remark 8.14). Furthermore, in 2d, the small eddies tend to merge into larger more stable eddies, which is the opposite effect of turbulence observed in 3d, where large eddies break up to smaller structures, (Schroeder et al., 2019). These aspects will be illustrated and discussed in Chapter 3.

2.5.2 Large Eddy Simulation (LES) Smagorinsky turbulence model

Short derivation. The basic idea of Large Eddy Simulations (LES) consists to resolve numerically the large scales (large eddies) and model the effect of the small dissipative scales. This can be done by decomposing the velocity and pressure fields (\mathbf{u}, p) into average fields $(\bar{\mathbf{u}}, \bar{p})$ and fluctuations (\mathbf{u}', p') :

$$\mathbf{u} = \bar{\mathbf{u}} + \mathbf{u}', \quad p = \bar{p} + p'.$$

This decomposition, which is used in a process called *space averaging*, distinguishes the *large eddies* where $(\bar{\mathbf{u}}, \bar{p})$ live, from small unresolved scales where the fluctuations (\mathbf{u}', p') live. The latter are also known as the *subgrid scales* because they

represent flow structures which are smaller than the grid and which are not captured by the space discretization. The *space-averaged Navier–Stokes equations* (or *Reynolds equations*) can now be written as, (John, 2016, Eq. 8.28),

$$\begin{aligned}\bar{\mathbf{u}}_t - 2\nu\nabla \cdot \mathbb{D}(\bar{\mathbf{u}}) + \nabla \cdot (\overline{\mathbf{u}\mathbf{u}^\top}) + \nabla \bar{p} &= \bar{\mathbf{f}}, \\ \nabla \cdot \bar{\mathbf{u}} &= 0,\end{aligned}$$

where the nonlinear term has still to be expressed in terms of the unknown variables $(\bar{\mathbf{u}}, \bar{p})$, instead of $\overline{\mathbf{u}\mathbf{u}^\top}$. For example,

$$\nabla \cdot (\overline{\mathbf{u}\mathbf{u}^\top}) = \nabla \cdot (\bar{\mathbf{u}}\bar{\mathbf{u}}^\top) + \nabla \cdot (\overline{\mathbf{u}\mathbf{u}^\top} - \bar{\mathbf{u}}\bar{\mathbf{u}}^\top) = \nabla \cdot (\bar{\mathbf{u}}\bar{\mathbf{u}}^\top) + \nabla \cdot \mathbb{T}.$$

Thus, the space averaging process introduces an additional tensor \mathbb{T} in the NSE:

$$\mathbb{T} = \overline{\mathbf{u}\mathbf{u}^\top} - \bar{\mathbf{u}}\bar{\mathbf{u}}^\top,$$

called *subgrid-scale (sgs) stress tensor*, or *Reynolds stress tensor*. The first term of \mathbb{T} contains new unknown quantities that require new equations and assumptions in order to be solved. Thus, a *closure problem* arises. It is the role of LES turbulence models to model the subgrid scale tensor \mathbb{T} and close the system.

We give here a brief derivation of the Smagorinsky model. More details can be found in (John, 2016, Section 8.3). Like the stress tensor \mathbb{S} , \mathbb{T} can be decomposed into a deviatoric (trace-free) part and a “pressure part”. The pressure part can be absorbed by the average pressure term \bar{p} , such that only the deviatoric component has to be determined. For simplicity, we refer to it with the same notation \mathbb{T} . The main idea is to apply the *Boussinesq hypothesis*, stating that “turbulent fluctuations are dissipative in the mean”. Expressing it in terms of \mathbb{T} yields

$$\mathbb{T} = -\nu_T \mathbb{D}(\bar{\mathbf{u}}),$$

where $\nu_T \geq 0$ is the *turbulent, or eddy, viscosity*. It can be estimated using the Reynolds number. At small scales δ , Re should be one:

$$\text{Re}(\delta) = \frac{U_\delta \delta}{\nu_T} = 1. \quad (2.60)$$

The velocity at these scales is given by assuming that the dissipation of turbulent energy ϵ verifies $\epsilon \sim \frac{U^3}{L}$, at small and bigger (resolved) scales L , such that

$$U_\delta \sim U \left(\frac{\delta}{L} \right)^{1/3}.$$

It is then inserted in (2.60) to give: $\nu_T \sim UL^{-1/3}\delta^{4/3}$. By further assuming that $U \sim L\|\mathbb{D}(\bar{\mathbf{u}})\|_F$, where $\|\mathbb{D}(\cdot)\|_F$ is the Frobenius norm of the tensor, that $L \sim \delta$, and by introducing a constant to account for all the approximations, one obtains

$$\nu_T = C_S \delta^2 \|\mathbb{D}(\bar{\mathbf{u}})\|_F, \quad (2.61)$$

where $C_S \geq 0$ is the *dimensionless Smagorinsky constant*. In numerical practice, δ is related to the local mesh size. Altogether, the Smagorinsky model introduces the following extra viscous term in the NSE:

$$\nabla \cdot (C_S \delta^2 \|\mathbb{D}(\bar{\mathbf{u}})\|_F \mathbb{D}(\bar{\mathbf{u}})).$$

In practice, $\bar{\mathbf{u}}$ is approximated by the computed velocity field \mathbf{u} . For clarity, we re-write the equations by dropping the bars over the space-averaged fields:

$$\mathbf{u}_t + (\mathbf{u} \cdot \nabla) \mathbf{u} - 2\nabla \cdot ((\nu + C_S \delta^2 \|\mathbb{D}(\mathbf{u})\|_F) \mathbb{D}(\mathbf{u})) + \nabla p = \mathbf{f}, \quad (2.62)$$

$$\nabla \cdot \mathbf{u} = 0. \quad (2.63)$$

Since the turbulent viscosity ν_T depends on \mathbf{u} , the new term is nonlinear. Note that the following equality holds for the Froebenius norm

$$\|\mathbb{D}(\mathbf{u})\|_F = (\mathbb{D}(\mathbf{u}) : \mathbb{D}(\mathbf{u}))^{1/2}, \quad (2.64)$$

such that the turbulent viscosity can be expressed more explicitly as

$$\nu_T = C_S \delta^2 (\mathbb{D}(\mathbf{u}) : \mathbb{D}(\mathbf{u}))^{1/2}. \quad (2.65)$$

One can also find the following notation, often used in engineering literature: $\nu_T = 2(C_S \delta)^2 (2\mathbb{D}(\mathbf{u}) : \mathbb{D}(\mathbf{u}))^{1/2}$.

Numerical aspects. As pointed out in (John, 2016, Remark 8.70), the Smagorinsky model is somewhat less complex than the NSE, despite the additional nonlinear term. Indeed, existence and uniqueness of the weak solution have been proved in (Ladyzhenskaya, 1967). The weak formulation is similar to the one from the NSE, but with the new eddy viscosity term. Furthermore, the velocity space in the Smagorinsky model has a higher regularity than in the NSE, in order to ensure that the new term is also well-defined:

$$\mathbf{W}_0^{1,3}(\Omega) = \{\mathbf{v} \in (W^{1,3}(\Omega))^d, \mathbf{v} = \mathbf{0} \text{ on } \partial\Omega\},$$

For the sake of simplicity, we consider only homogeneous Dirichlet conditions and omit other types of boundary conditions, as well as initial conditions. Then, the variational form reads:

Problem 2.7 (Weak formulation of the Smagorinsky model): *Find $(\mathbf{u}, p) \in \mathbf{W}_0^{1,3}(\Omega) \times \mathcal{Q}$, such that*

$$\begin{aligned} (\mathbf{u}_t, \mathbf{v}) + (2(\nu + C_S \delta^2 \|\mathbb{D}(\mathbf{u})\|_F) \mathbb{D}(\mathbf{u}), \mathbb{D}(\mathbf{v})) + ((\mathbf{u} \cdot \nabla) \mathbf{u}, \mathbf{v}) - (\nabla \cdot \mathbf{v}, p) &= (\mathbf{f}, \mathbf{v}) \\ -(\nabla \cdot \mathbf{u}, q) &= 0, \end{aligned}$$

for all $(\mathbf{v}, q) \in \mathbf{W}_0^{1,3}(\Omega) \times \mathcal{Q}$, and for all $t \in [0, T]$.

From the computational point of view, the Smagorinsky model is relatively easy to implement. One basically has to add the contribution of the turbulent viscosity ν_T to the viscous term. This is one of its main advantages. Furthermore, no further unknowns are introduced, and it has proved robustness, i. e., simulations

do generally not blow up. On the other hand, its results depend on the coefficient C_S . If values between 0.01 and 0.1 are sometimes recommended, there is no general rule to choose C_S appropriately. Often, it has to be chosen on a trial-and-error basis, depending on the application, mesh size, etc. Eventually, several values of the Smagorinsky constant with different meshes have to be tested and the best way to determine the correct value is to compare the computed results with real measurements. Besides the problem of choosing C_S , it is also well-known that the Smagorinsky model introduces too much viscosity, even in low Reynolds number regimes (laminar flows). This “overdiffusion” is nothing else but artificial viscosity: it does not correspond to reality and can lead to bad results. Several improvements of the Smagorinsky model have been developed to overcome its weaknesses, e. g., space-dependent (dynamic) C_S , and van Driest damping, (John, 2016, Section 8.3). In this dissertation, the basic model (2.62) and (2.63) has given satisfactory results, such that it was not necessary to employ more advanced approaches.

2.5.3 Other turbulence models

The previous developments have evidenced a simple interpretation of how turbulence models work: roughly speaking, it consists of adding artificial viscosity to counterbalance the high convection term. Introducing a too large amount of viscosity tends to “laminarize” the flow, thus losing its turbulent features. If it is too small, the flow would not be enough stabilized, leading to simulations’ blow-up. In other words, turbulence models can be understood as *stabilization methods for convection-dominated flows*. Reciprocally, standard stabilization methods, e. g., SUPG, (Ahmed and Rubino, 2019), might work as well for high Reynolds number flows, at least in the more simple two-dimensional case.

There are other classes of turbulence models used in engineering applications and softwares. One of the most popular is the $k - \epsilon$ turbulence model. Here, the additional turbulent viscosity ν_T depends on the kinetic turbulent energy k and the rate of dissipation of turbulent energy ϵ , such that these three quantities solve the system of equations:

$$\nu_T = C_\nu \frac{k^2}{\epsilon}, \quad (2.66)$$

$$\frac{\partial k}{\partial t} + (\mathbf{u} \cdot \nabla)k = \nabla \cdot \left(\left(\nu + \frac{\nu_T}{\sigma_k} \right) \nabla k \right) + G - \epsilon, \quad (2.67)$$

$$\frac{\partial \epsilon}{\partial t} + (\mathbf{u} \cdot \nabla)\epsilon = \nabla \cdot \left(\left(\nu + \frac{\nu_T}{\sigma_\epsilon} \right) \nabla \epsilon \right) + C_1 \frac{\epsilon}{k} G - C_2 \frac{\epsilon^2}{k}, \quad (2.68)$$

$$G = \nu_T (\nabla \mathbf{u} : (\nabla \mathbf{u} + (\nabla \mathbf{u})^\top)), \quad (2.69)$$

where G is the turbulent kinetic energy production rate, and C_ν , σ_k , σ_ϵ , C_1 , and C_2 are some model constants. The derivation of this model is based on physical rather than mathematical arguments. Experimental benchmarks allow to fix default values for the constants. The turbulent viscosity ν_T is then added to ν in the viscous term of the NSE. In this thesis, this model has been applied in a commercial software for some of the simulations, with the only purpose of comparing it with the Smagorinsky model. Thus, it is not presented in detail here. The reader is referred to (Chacón Rebollo and Lewandowski, 2014, Chapter 4) for a more thorough introduction to the $k - \epsilon$ model.

3. Single-phase models for ladle stirring

Motivation. As introduced in Section 1.2.2, two-phase bubbly flows can be approximated in a single-phase model, where the gas fraction is known. It is given by empirical formulas, instead of being considered as an unknown and solved by an additional equation. They are also known as *quasi-single phase* models in the literature and are among the first models used for ladle stirring. After the beginning of the 2000s, multiphase approaches took over the quasi-single phase approach. As pointed out in (Mazumdar and Guthrie, 1995a, Alia et al., 2019a), single-phase models have some well-known limits. For example, they are restricted to rough estimations of the bulk liquid flow. They also result in large discrepancies with experimentally measured turbulent kinetic energy, and cannot model properly the wandering effect of the bubbles, the influence of slag on the bulk liquid, the slag “eye” area, or the emulsification of slag in the steel. Moreover, they have been validated mainly for cylindrical laboratory ladles with a central nozzle. Only one paper (Goldschmit and Owen, 2001) applied it for real 3d ladles with two nozzles.

However, they are rather simple and computationally cheaper than two- or three-phase models. This feature is of importance when dealing with optimal control problems, since the optimization algorithm requires the repeated simulations of the forward flow problem. According to the literature, they can also describe the bulk liquid flow quite satisfactorily. Since the objective functional will focus on the hydrodynamics of stirring, it is sufficient to have a model which describes the liquid flow correctly. For these reasons, this work focuses on the single-phase approach for ladle stirring. The main objectives of this chapter are to compare the main models and show that they are suitable to describe the flow pattern.

Outline. First, a review of the models is given in Section 3.1. This review reveals that there are actually two approaches to imitate the effect of the rising gas: a 2d model with a non-homogeneous boundary velocity, similar to the lid-driven benchmark problem, and an axisymmetric (“2.5d”) configuration. In Section 3.2, those two configurations, as well as a realistic 3d ladle model, are presented. The results of the numerical simulations are discussed in Section 3.3. For the numerical application, the geometry and parameters’ values are taken from the literature, and the computed results are compared with the corresponding experimental measurements. In Section 3.4, the 3d application on the water ladle of the Process Metallurgy Research Unit of the University of Oulu is performed.

Different aspects are taken into account in these simulations:

- influence of the mesh size,
- influence of the turbulent viscosity constant (in axisymmetrical and 3d cases),
- long-term behavior of the flow (“nearly-periodic” regime),
- comparison with experimental measurements for validation, and
- comparison between the Smagorinsky model (in an in-house code) and the $k - \epsilon$ model (in a commercial software).

The numerical results presented in this chapter help to better understand the single-phase approach for ladle stirring and to find an appropriate forward model for the optimal control problem (which will be treated in Chapter 4), along with relevant parameters’ values and initial conditions. This will be summarized in Section 3.5.

3.1 Literature review

In the literature, quasi-single phase models reduce to the incompressible Navier–Stokes equations with inhomogeneous, sometimes called reduced, density. The dynamic viscosity is constant, equal to the one of the liquid. The gas fraction and the density are independent of time. The numerous variants of the gas fraction found in the literature lead to different single-phase models. However, the papers do not differ only from the gas fraction, but also on slightly different formulations of the original models, and on different modeling assumptions regarding the density, the way it is incorporated in the equations, and the geometry. The main common features of quasi-single phase models are the followings:

- the geometry is a 2d axisymmetric ladle with one central nozzle, except in (Zhu et al., 1996) and (Goldschmit and Owen, 2001) where a 3d ladle is considered, with one excentric and two nozzles, respectively,
- the boundary conditions are all the same, except in (Grevet et al., 1982) and (Sahai and Guthrie, 1982b), which are based on non-homogeneous boundary conditions at the nozzle and at the central axis, respectively,
- all models use the $k - \epsilon$ turbulence model.

Before detailing the quasi-single phase models, the next section reviews the existing formulas for the gas fraction.

3.1.1 Definitions of the gas phase fraction α

(Mazumdar and Guthrie, 1995b) published a survey on ladle stirring, where the quasi-single phase models are briefly reviewed. Because of the variants introduced to the models in the different applications, we propose a more comprehensive review. From the literature, it is possible to distinguish three types of empirical formulas for the gas fraction α (Table 3.1):

- formulas based on an empirical plume velocity: Eqs. (3.1) to (3.5),
- power law determined by experimental measurements: Eqs. (3.6) and (3.7), and
- laws determined by other experimental results, e. g., (Irons et al., 2015).

Only three papers applied the formulas from (Castillejos and Brimacombe, 1987, 1989), while the others used one of the first five gas fractions written in Table 3.1.

Table 3.1: Review of the main gas phase fraction α from literature (only those used in the quasi-single phase numerical models).

α	Original ref.
$\alpha = \frac{Q}{2\pi \int_0^{r_c} u_z r dz} \quad (3.1)$	(Debroy et al., 1978)
$\alpha = \frac{Q - \pi r_c^2 \alpha (1 - \alpha) U_S}{2\pi \int_0^r u_z r dz}, \quad u_z \text{ solved by ODE} \quad (3.2)$	(Grevet et al., 1982)
$\alpha = \frac{Q}{\pi r_{av}^2 U_P}, \quad U_P = 4.4 \frac{Q^{1/3} H^{1/4}}{R^{1/3}} \quad (3.3)$	(Sahai and Guthrie, 1982a,b)
$\alpha = \frac{Q - \pi r_c^2 \alpha (1 - \alpha) U_S}{2\pi \int_0^{r_c} U_P r dr}, \quad U_P = 4.5 \frac{Q^{1/3} H^{1/4}}{R^{1/4}} \quad (3.4)$	(Balaji and Mazumdar, 1991)
$\alpha = \begin{cases} \frac{1}{2} \left(\frac{U_P}{U_S} + 1 \right) & \text{if } z \leq z_C, \\ \frac{1}{2} \left(\left(\frac{U_P}{U_S} + 1 \right) - \sqrt{\left(\frac{U_P}{U_S} + 1 \right)^2 - \frac{4Q}{\pi r_c^2(z) U_S}} \right) & \text{if } z \geq z_C. \end{cases} \quad (3.5)$	(Alia et al., 2019a)
$\alpha = \alpha_{\max} \exp \left[-0.7 \left(\frac{r}{r_{\max/2}} \right)^{2.4} \right] \quad (3.6)$	
$\begin{aligned} \alpha_{\max} &= 100 N^{-0.22} \text{ if } N < 4, \\ &= 293.77 N^{-1} \text{ if } N \geq 4, \\ N &= F_r^{-0.269} \left(\frac{\rho_l - \rho_g}{\rho_g} \right)^{0.269} \left(\frac{z}{d_{\text{nozzle}}} \right)^{0.993} \\ r_{\max/2} &= 0.243 \left[F_r^{-0.184} \left(\frac{\rho_l - \rho_g}{\rho_g} \right)^{0.184} \left(\frac{z}{d_{\text{nozzle}}} \right)^{0.48} \right] \left(\frac{Q^2}{g} \right)^{1/5} \\ \text{Fr} &= \frac{Q^2}{g d_{\text{nozzle}}^5} \end{aligned}$	(Castillejos and Brimacombe, 1987)
$\alpha = \alpha_{\max} \exp \left[-0.7 \left(\frac{r}{r_{\max/2}} \right)^{2.4} \right] \quad (3.7)$	
$\begin{aligned} \alpha_{\max} &= 81.5 N^{-0.10} \text{ if } N < 1.35, \\ &= 106.9 N^{-1} \text{ if } N \geq 1.35, \\ N &= F_r^{-0.26} \left(\frac{\rho_l}{\rho_g} \right)^{0.13} \left(\frac{z}{d_{\text{nozzle}}} \right)^{0.94} \\ r_{\max/2} &= 0.275 \left[F_r^{-0.155} \left(\frac{\rho_l}{\rho_g} \right)^{0.11} \left(\frac{z}{d_{\text{nozzle}}} \right)^{0.51} \right] \left(\frac{Q^2}{g} \right)^{1/5} \\ \text{Fr} &= \frac{Q^2}{g d_{\text{nozzle}}^5} \end{aligned}$	(Castillejos and Brimacombe, 1989)

Table 3.2: Review of the references which use the gas fraction α and its variants.

α	Original ref.	Applied/mentioned in	Changes vs original
$\alpha = \frac{Q}{2\pi \int_0^{r_c} u_z r dz}$	(Debrov et al., 1978)	(Woo et al., 1990) (Mazumdar and Guthrie, 1995b)	- $\int_0^{r_c} (u + U_S) r dr$
$\alpha = \frac{Q - \pi r_c^2 \alpha (1 - \alpha) U_S}{2\pi \int_0^{r_c} u_z r dz}$, u_z solved by ODE	(Grevet et al., 1982)	(Woo et al., 1990) (Balaji and Mazumdar, 1991) (Mazumdar et al., 1993) (Mazumdar and Guthrie, 1995b)	$U_S = 0.4$ - - -
$\alpha = \frac{Q}{\pi r_{av}^2 U_P}$, $U_P = 4.4 \frac{Q^{1/3} H^{1/4}}{R^{1/3}}$	(Sahai and Guthrie, 1982a,b)	(Mazumdar and Guthrie, 1985) (Balaji and Mazumdar, 1991) (Mazumdar et al., 1993) (Mazumdar and Guthrie, 1995b) (Ganguly and Chakraborty, 2004)	$U_P = k \beta^{1/3} \frac{Q^{1/3} H^{1/4}}{R^{1/3}}$ - $U_P = 4.5 \frac{Q^{1/3} H^{1/4}}{R^{1/4}}$ - 4.17 instead of 4.4
$\alpha = \frac{Q - \pi r_c^2 \alpha (1 - \alpha) U_S}{2\pi \int_0^{r_c} U_P r dr}$, $U_P = 4.5 \frac{Q^{1/3} H^{1/4}}{R^{1/4}}$	(Balaji and Mazumdar, 1991)	(Mazumdar et al., 1992) (Mazumdar et al., 1993) (Mazumdar and Guthrie, 1994) (Mazumdar and Guthrie, 1995a) (Mazumdar and Guthrie, 1995b) (Goldschmit and Owen, 2001)	$U_S = 0.6$ - 4.4 instead of 4.5 4.4 and $\int_z \int_r$ instead of $\int_0^{r_c}$ $R^{-1/3}$ instead of $R^{-1/4}$ -
1st formula (water)	(Castillejos and Brimacombe, 1987)	(Woo et al., 1990) (Zhu et al., 1996)	- -
2nd formula (water+mercury)	(Castillejos and Brimacombe, 1989)	(Mazumdar and Guthrie, 1995b) (Mukhopadhyay et al., 2001)	- -

Gas phase fractions based on the plume velocity U_P . Using the following expression for the gas flow rate,

volumetric gas flow rate = gas flow cross-sectional \times gas plume velocity,

and assuming that the gas flow cross-sectional is a fraction of the plume cross-sectional,

gas flow cross-sectional = gas fraction \times plume cross-sectional,

it is possible to express the gas fraction α as

$$\text{gas fraction} = \frac{\text{volumetric gas flow rate}}{\text{plume cross-sectional} \times \text{gas plume velocity}}.$$

This approach has been used in the first approximations of the gas phase fractions, see formulas (3.1) to (3.4) in Table 3.1.

The differences between the formulas appear in:

- the plume velocity U_P (for example, solved by an additional ODE (3.2) or obtained by empirical measurements (3.3)),
- the cross-sectional (for example, constant if a cylindrical plume is assumed (3.3), or dependent on z if it is conical), and
- the presence of an additional term which includes the slip velocity U_S between gas and liquid (referred to as “drift-flux models”).

In all cases, α depends on z only, except in (3.3) where it is constant. More details on the drift-flux model are given in (Mazumdar and Evans, 2009). Note that several papers have introduced variants of these formulas in their applications (Table 3.2).

Two remarks regarding the formulas (3.1) to (3.4). The formulas given in Table 3.1 are reproduced as in the original references. It is unclear what is meant by the integrals in the bottom part of the fractions. Assuming they should describe the cross-sectional of the plume, they should be written as

$$\pi r_c^2(z) U_P(z).$$

If $r_c(z)$ is a constant, say r_{av} (meaning that the plume is cylindrical), and if its velocity U_P is independent of z , one ends up with (3.3). If it is conical, $r_c(z)$ depends linearly on z , and the proposed formula should then describe the same as (3.4) if U_P is a constant, or (3.1) and (3.2) if U_P depends on z .

Another remark regards the drift-flux model applied in (3.2) and (3.4). Although the gas fraction can be solved numerically, it is possible, for more clarity, to derive a closed formula for α by solving a simple second-order polynomial, see (Alia et al., 2019a). The new explicit and exact formula (3.5) also gives a correct definition for low heights, i.e., close to the nozzle.

Gas phase fractions based on a power law. Instead of expressing α in terms of the plume velocity, it is possible to correlate a power-law directly to measurements of gas fraction. This approach has been applied in (Castillejos and Brimacombe, 1987) with water and air, and again in (Castillejos and Brimacombe, 1989) with mercury and nitrogen. In the latter, the formulas obtained include the data from the first experiment and become slightly different, so that the power-law takes into account several types of fluids. They also included the effect of different nozzle diameters d_{nozzle} . Their formulas are based on the assumption that the gas phase fraction follows a Gaussian distribution, see Eqs. (3.6) and (3.7) in Table 3.1. Again, they have been applied in several numerical models (Table 3.2). In these models, α depends on both r and z , and is discontinuous in z .

Other formulas. For completeness, let us mention that there are actually other empirical formulas for α . For example, (Irons et al., 2015) propose a gas fraction averaged over the plume cross-section: $\bar{\alpha} = 1.13(Q^*)^{0.63}(z^*)^{-1.57}$, where $Q^* = \frac{Q}{\sqrt{gH^5}}$ and $z^* = \frac{z}{H}$ are the dimensionless flow rate and height, respectively. However, the “quasi-single phase” models make use only of the first two types of formulas, which were the only ones available at their time.

Finally, let us mention that quasi-single phase models were also used in processes other than metallurgy, where bubble columns intervene. This is the case, for example, in (Bernard et al., 2000), where the plume is assumed to be cylindrical instead of conical. The gas fraction applied is similar to (Sahai and Guthrie, 1982b), except that it includes a height correction factor to take into account the volumetric expansion of the rising gas bubbles.

3.1.2 Boundary conditions

In the beginning of Section 3.1, the difference between some papers regarding the boundary conditions in single-phase models was mentioned. In particular, the condition on the central (symmetry) axis Γ_{axis} showed some discrepancy.

In axisymmetrical flows, a free slip condition on the central axis is naturally imposed by the axial symmetry, as described in Section 2.3.3 (Eq. (2.56)). This is the case in most of the quasi-single phase models. However, in (Sahai and Guthrie, 1982b), a vertical velocity, equal to the plume velocity U_P , is imposed on the axis to simulate the upward movement of the gas plume. Non-homogeneous Dirichlet boundary conditions are used in this case (Eq. (2.13) with $\Gamma_D = \Gamma_{\text{axis}}$):

$$\mathbf{u} = \mathbf{b} = (0, U_P)^\top \quad \text{in } (0, T] \times \Gamma_{\text{axis}}. \quad (3.8)$$

Such a tangent boundary velocity is usual in Cartesian coordinates, e.g., the lid-driven cavity benchmark problem (Bruneau and Saad, 2006). However, it is quite unusual to apply it on the symmetry axis in cylindrical frame, as in (Sahai and Guthrie, 1982b). In addition to this boundary velocity, they apply a volume force based on the gas fraction α , as in standard single-phase models. In other words, they apply two mechanisms simultaneously to induce the stirring flow. However, since their gas fraction α is constant (Eq. (3.3)), the mixture density and the volume force they apply are also constant. Consequently, these parameters would only reduce the density of the liquid in the right-hand side of the Navier–Stokes equations, and, thereby, reduced the pressure gradient without impacting the velocity. In other words, they would not have induced the liquid to flow. This might explain why the authors have chosen to impose a non-zero boundary velocity, where it should have normally been a symmetry boundary condition. Only in later publications, the inhomogeneous density and space-dependent α appeared, making the boundary velocity assumption (3.8) not necessary anymore to induce a movement of the fluid.

An alternative modeling possibility consists in imposing a vertical velocity only at the origin of the domain, i.e., at the gas injection nozzle. This is the approach used in (Grevet et al., 1982). However, a discontinuity with the rest of the boundary appears because of the homogeneous Dirichlet conditions on the bottom boundary. To avoid this discontinuity, one can use some regularization in the numerical implementation, e.g., the inflow should take place on a small length of the bottom boundary, and not only at the origin. Still, this might lead to numerical instability, since a normal inflow at the bottom boundary without outflow boundaries violates the divergence-free condition. A more proper way to use this approach would have been to apply a two-phase flow model. Then, inflow

and outflow conditions can be prescribed for the gas, rather than on the liquid. These remarks have not been addressed in (Grevet et al., 1982).

To summarize the above discussion, the literature review reveals two types of models in 2d:

- the standard axisymmetric one (“2.5d”) using different gas fractions α , and
- the one using a boundary velocity to simulate the effect of the rising gas, as in (Sahai and Guthrie, 1982b).

In 3d, a boundary-driven mechanism would impose a boundary velocity on the exterior wall of the ladle and cannot realistically model the gas stirring, as in 2d. Therefore, the 3d ladle stirring is always based on the gas fraction α applied in a buoyancy force, such as in (Zhu et al., 1996, Goldschmit and Owen, 2001).

The remaining conditions on the top surface of the bath Γ_{top} , on the side walls, and on the ladle bottom follow standard assumptions in single-phase models. In industry and laboratories, the liquid bath surface is a free surface covered by a slag layer, and subject to an unsteady movement, which intensity depends on the gas flow rate. Although, for small gas flow rates, the slag does not open and the free surface is relatively flat, this is not true anymore for flow rates of interest, which are usually high enough to form an open eye in the slag. The single-phase model being a simplified approach, in comparison to multiphase or free surface models, the slag is not modeled explicitly. Instead, one has to apply a boundary condition on the top surface Γ_{top} , e. g., homogeneous Dirichlet or free slip conditions. Usually, it is a free slip with no penetration (Equations (2.18) and (2.19) with $\Gamma_{\text{slip}} = \Gamma_{\text{top}}$),

$$\begin{aligned} \mathbf{u} \cdot \mathbf{n} &= 0 && \text{in } (0, T] \times \Gamma_{\text{top}}, \\ \mathbf{n}^\top \mathbb{S} \mathbf{t}_i &= \mathbf{n}^\top (2\nu \mathbb{D}(\mathbf{u}) - pI) \mathbf{t}_i = 0 && \text{in } (0, T] \times \Gamma_{\text{top}}, \quad 1 \leq i \leq d-1. \end{aligned}$$

This reduces unphysical flow braking close to the top surface, which would have been otherwise induced by homogeneous Dirichlet conditions. Moreover, it is expected to deliver a bulk flow closer to the one with a real free surface.

On the walls and the bottom part of the ladle, the fluid velocity is assumed to be zero. In terms of boundary conditions, homogeneous Dirichlet conditions (Eq. (2.12)) are applied, with different Γ_0 in 2d and 3d,

$$\begin{aligned} \mathbf{u} &= \mathbf{0} && \text{in } (0, T] \times \Gamma_0, \\ \text{in 2d: } \Gamma_0 &= \partial\Omega \setminus \{\Gamma_{\text{axis}} \cup \Gamma_{\text{top}}\}, \\ \text{in 3d: } \Gamma_0 &= \partial\Omega \setminus \Gamma_{\text{top}}. \end{aligned}$$

3.1.3 Reynolds number in ladle stirring

The main non-dimensional numbers used in the metallurgy literature to characterize the flow is the Froude number, which can be found with different definitions. However, it is not enough for describing the flow. The Reynolds number is needed in order to characterize properly the liquid flow (laminar, turbulent) and to choose suitable numerical methods.

The characteristic velocity and length can be chosen by analogy to a benchmark flow problem. As mentioned in the previous section, the liquid flow is similar to the lid-driven cavity benchmark problem (Bruneau and Saad, 2006), in the sense

Table 3.3: Reynolds number for different characteristic lengths L and velocities U .

	Laboratory ladles						Industrial ladles			
	Water			Mercury			Steel			
Density ρ (kg m ⁻³)	10 ³			1.3 .10 ⁴			7 .10 ³			
Viscosity μ (Pa s)	10 ⁻³			1.5 .10 ⁻³			5 .10 ⁻³			
L (m)	0.1 0.5 1			0.5 1 1			1.3 2.5			
U (m s ⁻¹)	0.1 0.5 1			0.5 1 1			0.1 1		0.1 1	
$Re = \frac{\rho UL}{\mu}$ (10 ⁴)	1	5	10	25	50	100	217	18	180	35 350

that it is induced by an imposed parallel velocity at one side. In this benchmark problem, the characteristic velocity U and length L correspond to the imposed constant velocity 1 m s⁻¹ on the boundary and to the unit square domain size 1 m, respectively. By analogy, the characteristic velocity and length of ladle flows are the gas plume U_P or bulk liquid velocity (same order of magnitude) and the height H or radius R of the ladle (same order of magnitude), respectively. The bulk liquid velocity depends on the gas flow rate, but its order of magnitude remains less than 1 m s⁻¹, see (Mazumdar and Guthrie, 1995b).

Possible Reynolds numbers for ladle stirring are listed in Table 3.3, corresponding to different ladle configurations and characteristic values. The smallest Reynolds number can be reached in small laboratory models with a low gas flow rate, whereas industrial ladles in operating conditions have a Reynolds number which can be more than ten times higher. In all cases, the order of magnitude of Re exceeds 10⁴ for laboratory ladles and 10⁵ for industrial ladles. These high Reynolds numbers are characteristic of convection-dominated and turbulent flows. As it will be seen later, a DNS approach with a mesh fine enough is sufficient in 2d, while axisymmetric and 3d flows require a turbulence model.

3.2 Description of the models

Based on the previous review, we study three models in this dissertation. The first one is a 2d model with a boundary velocity, similarly to the problem of the lid-driven cavity (Bruneau and Saad, 2006). It is designated as the *2d boundary-driven ladle*. Contrary to (Sahai and Guthrie, 1982b), we do not assume the axial symmetry, in order to avoid the confusion on the boundary Γ_{axis} , and do not apply the gas fraction in a buoyancy force to generate the stirring. Thus, we employ a 2d Cartesian frame and a boundary-driven stirring only. The second model is a 2d axisymmetrical ladle with a buoyancy-driven stirring, i. e., the flow is generated by the gas fraction α in the volume force. This is the classical model found in the literature. Finally, a more realistic 3d ladle model is studied, also with a buoyancy force based on α .

Table 3.4: Parameters of the 2d and 3d ladle stirring models.

2d ladle	Parameters specific to...		3d ladle
	...boundary-driven	...axisymmetric	
$H = 0.6$ m	$z_0 = 0.001$ m	$\chi = 10^\circ$	$H = 0.65$ m
$R = 0.3$ m	$t_0 = 0.1$ s	$a = 0.08$ m	$R_{\text{top}} = 0.29$ m
$Q = 13$ l min ⁻¹ ($2.2 \cdot 10^{-4}$ m ³ s ⁻¹)		$U_S = 0.4$ m/s	$Q = 17$ l min ⁻¹ ($2.83 \cdot 10^{-4}$ m ³ s ⁻¹)
$Re = 96000$		$\rho_l = 1000$ kg m ⁻³	$Re = 96000$
$T = 600$ s		$\rho_g = 1$ kg m ⁻³	$T = 200$ s
$U_P = 0.32$ m s ⁻¹		$d_{\text{nozzle}} = 12.7$ mm	$U_P = 0.36$ m s ⁻¹
			$R_{\text{bot}} = 0.27$ m
			$x_{n1} = -0.105$
			$y_{n1} = -0.105$
			$x_{n2} = -0.105$
			$y_{n2} = 0.105$

The geometry corresponds to a laboratory-scale physical model of the steel-making ladle, which uses water instead of steel. Argon is described using air, but this information is not used in the models, except in a particular formula of α where ρ_g intervenes. The common notations to all models are: the height H and the radius R of the experimental ladle, the top boundary Γ_{top} , corresponding to the free surface of the fluid, and, in 2d, the vertical (symmetry) wall Γ_{axis} . Table 3.4 summarizes the geometrical and physical parameters of the models, which are detailed in the next sections.

3.2.1 The 2d boundary-driven ladle model

As mentioned in the outline of this chapter, the numerical study is performed on an existing laboratory ladle, whose parameters and experimental results are available in literature. A review of the different experiments and simulations given in Table 3.2 has led to the choice of the ladle from (Woo et al., 1990), because the experimental set-up and measurements, as well as the numerical results of three models are described in detail. Another reason is that the geometry of the ladle and the range of the gas flow rate studied in this experiment are close to the ones of the water ladle of the Process Metallurgy Research Unit of the University of Oulu, which will be the focus of the 3d model (Section 3.2.3).

Modeling assumptions. The geometry of the 2d boundary-driven ladle, defined in a Cartesian frame (x, z) , is given in Figure 3.1 (middle scheme). This model uses the non-homogeneous boundary condition (3.8). The plume velocity from (Balaji and Mazumdar, 1991) is applied,

$$U_P = 4.5 \frac{Q^{1/3} H^{1/4}}{R^{1/4}}, \quad (3.9)$$

instead of the original one (3.3), because it has proved to yield more accurate velocities (Mazumdar et al., 1993). A well-known issue of the lid-driven cavity

problem concerns the irregularity of the boundary conditions due to the jump of the velocity at the left corners (De Frutos et al., 2016). In order to avoid this irregularity, the boundary velocity can be regularized by being multiplied by, for example, the following function, (John, 2016),

$$\text{reg}(z) = \begin{cases} 1 - \frac{1}{4} \left(1 - \cos \left(\frac{z_0 - z}{z_0} \pi \right) \right)^2 & \text{for } z \in [0, z_0], \\ 1 & \text{for } z \in [z_0, H - z_0], \\ 1 - \frac{1}{4} \left(1 - \cos \left(\frac{z - (H - z_0)}{z_0} \pi \right) \right)^2 & \text{for } z \in [H - z_0, H], \end{cases} \quad (3.10)$$

where $z_0 = \frac{H}{60}$. Furthermore, it is also smoothed in time, using a “ramp-like” function to facilitate numerical convergence in the first iterations, e. g.,

$$\ell(t) = \begin{cases} t/t_0 & \text{for } 0 \leq t \leq t_0, \\ 1 & \text{for } t \geq t_0, \end{cases} \quad (3.11)$$

where $t_0 = 0.1$ s. Since we are interested in the long-term behavior of the flow, the initial transition between 0 and t_0 , i. e., from a fluid at rest to a fully developed boundary velocity U_P , does not need to match precisely the physical reality. The Reynolds number is computed as $\text{Re} = \frac{\rho U_P R}{\mu}$, where $\rho = 1000$ and $\mu = 0.001$ are the fluid density and viscosity, respectively. The values of the parameters which are specific to the boundary-driven ladle are given in Table 3.4. Finally, contrary to (Sahai and Guthrie, 1982a), the density in the whole domain is that of the liquid (water). The only volume force is the gravity, and the gas fraction α is not considered, as mentioned earlier.

The 2d boundary-driven ladle model can now be formulated, based on Problem 2.1 and on the assumptions of the current application:

Problem 3.1 (Strong form of the NSE for the 2d boundary-driven ladle stirring):

$$\begin{aligned} \mathbf{u}_t + (\mathbf{u} \cdot \nabla) \mathbf{u} - 2\nu \nabla \cdot (\mathbb{D}(\mathbf{u})) + \nabla p &= \mathbf{g} && \text{in } (0, T] \times \Omega \\ \nabla \cdot \mathbf{u} &= 0 && \text{in } (0, T] \times \Omega \\ \mathbf{u} &= (0, U_P \text{reg}(z) \ell(t))^T && \text{in } (0, T] \times \Gamma_{\text{axis}} \\ \mathbf{u} &= \mathbf{0} && \text{in } (0, T] \times \partial\Omega \setminus \{\Gamma_{\text{axis}} \cup \Gamma_{\text{top}}\} \\ \mathbf{u} \cdot \mathbf{n} &= 0 && \text{in } (0, T] \times \Gamma_{\text{top}} \\ \mathbf{n}^T \mathbb{S} \mathbf{t}_i &= 0, \quad 1 \leq i \leq d-1 && \text{in } (0, T] \times \Gamma_{\text{top}} \\ \mathbf{u}(0, \mathbf{x}) &= \mathbf{0} && \text{in } \Omega \\ \int_{\Omega} p \, d\mathbf{x} &= 0 && \text{in } (0, T] \\ U_P &= 4.5 \frac{Q^{1/3} H^{1/4}}{R^{1/4}} \\ \text{reg}(z) &\text{ defined as (3.10),} \\ \ell(t) &\text{ defined as (3.11).} \end{aligned}$$

In Cartesian frame, the Navier–Stokes equations can be written as shown in Appendix A (Eqs. (A.2)).

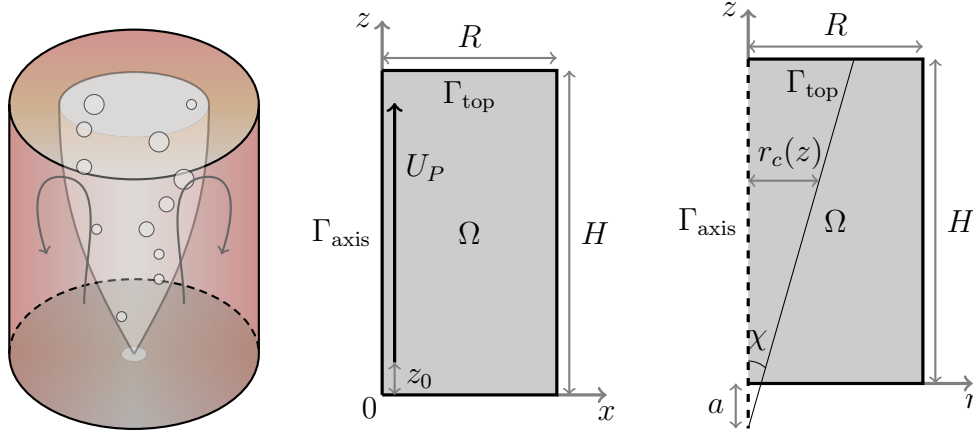


Figure 3.1: Ladle stirring with a centered nozzle. Left: Schematic illustration. Center: 2d boundary-driven ladle geometry in Cartesian frame (x, z) . Right: 2d axisymmetric fluid domain in cylindrical frame (r, z) .

3.2.2 The 2d axisymmetric ladle model

In addition to the discussion in Section 3.1, (Alia et al., 2019a) also attempted to unify the mathematical formulation of quasi-single phase models. Some modeling work and results presented in the following sections are based on the paper. The geometry of the 2d axisymmetric ladle, defined in cylindrical coordinates (r, z) , is illustrated in Figure 3.1 (right picture).

Modeling assumptions. In this model, the effect of stirring is simulated with a volume force dependent on space through the gas fraction $\alpha(r, z)$. The upwards boundary velocity on the axis is replaced by a free slip condition with no penetration, similarly to the top boundary. Although it is, again, a variant of the quasi-single phase models of the literature, its modeling assumptions simplify somewhat the mathematical formulation and numerical implementation.

Indeed, in the models used in the literature, not only the volume force depends on space, but also the liquid density ρ is inhomogeneous, i. e., space-dependent. It is equal to the gas-liquid mixture density inside the gas plume, and to the liquid density outside the plume: $\rho = \rho_g \alpha + \rho_l (1 - \alpha)$ if $r \leq r_c(z)$, and $\rho = \rho_l$ if $r \geq r_c(z)$, where $r_c(z) = \tan(\chi) (z + a)$ is the radius of the plume at height z , χ and a being the apex and origin of the conical plume, respectively (Figure 3.1). In these models, α is either constant or z -dependent. The simplifications introduced in (Alia et al., 2019a) are the following:

- the density is constant equal to the one of the liquid $\rho = \rho_l$,
- the distinction between the gas-liquid mixture and the liquid is moved from the definition of ρ to α , so that $\alpha = \alpha(r, z)$,
- the volume force is $\mathbf{g}(1 - \alpha(r, z))$.

They enable a clearer physical interpretation of the model, since the flow is induced exclusively by the space-dependent volume force (acting as a buoyancy), and the possibility to use standard methods and solvers for the incompressible Navier–Stokes equations rather than treating numerically the variable density.

Concerning the gas fraction α , the same formulas as in (Alia et al., 2019a) are studied, namely,

$$\alpha_1(r, z) = \begin{cases} \frac{Q}{\pi r_{av}^2 U_P} & \text{if } r \leq r_c(z), \\ 0 & \text{if } r > r_c(z), \end{cases} \quad (3.12)$$

where $r_{av} = \frac{1}{2} \tan(\chi)(2a + H)$,

$$\alpha_2(r, z) = \begin{cases} \frac{1}{2} \left(\frac{U_P}{U_S} + 1 \right) & \text{if } z \leq z_C \text{ and } r \leq r_c(z), \\ \frac{1}{2} \left(\left(\frac{U_P}{U_S} + 1 \right) - \sqrt{\left(\frac{U_P}{U_S} + 1 \right)^2 - \frac{4Q}{\pi r_c^2(z) U_S}} \right) & \text{if } z \geq z_C \text{ and } r \leq r_c(z), \\ 0 & \text{if } r > r_c(z), \end{cases} \quad (3.13)$$

where $z_C = \frac{1}{\tan(\chi)} \left(\sqrt{\frac{4Q}{\pi U_S \left(\frac{U_P}{U_S} + 1 \right)^2}} \right) - a$, and the two variants (3.6) and (3.7) rewritten in a more compact way:

$$\alpha_i(r, z) = \begin{cases} 0.01 \ c_0 z^{c_3} \exp \left[-0.7 \left(\frac{r}{c_1 z^{c_5}} \right)^{2.4} \right] & \text{if } z < z_C, \\ 0.01 \ c_2 z^{c_4} \exp \left[-0.7 \left(\frac{r}{c_1 z^{c_5}} \right)^{2.4} \right] & \text{if } z \geq z_C, \end{cases} \quad (3.14)$$

where $i = 3, 4$, and the constants c_0, c_1, c_2, c_3, c_4 , and c_5 depend on geometrical and physical parameters, such as the gas flow rate Q , the nozzle diameter d_{nozzle} , and the densities of gas and liquid ρ_g and ρ_l (Castillejos and Brimacombe, 1987, 1989). Since the original formulas express the gas fraction in percentage, a factor 0.01 is needed for units consistency. Note that the critical height z_C is not the same for α_2, α_3 , and α_4 . We omit the formulas for α_3 and α_4 since they will not be used in the rest of the work. The parameters for the numerical application are listed in Table 3.4 and the corresponding values for the constants of α_3 and α_4 are given in Table 3.5. It is already possible to gain some insight on the difference between the four formulas by comparing their isolines directly, without requiring numerical simulations. This comparison can be found in (Alia et al., 2019a) and is illustrated in Figure 3.2. It is shown that the order of magnitude and the shape of the different gas fraction fields are not fundamentally different and that both formulas (Castillejos and Brimacombe, 1987, 1989) are very similar. For this reason, one of these two formulas can be ignored in the study, for example α_4 .

Table 3.5: Constants of Eq. (3.14) (Castillejos and Brimacombe, 1987, 1989).

	c_0	c_1	c_2	c_3	c_4	c_5	z_C
α_3	29.8785	0.0934	1.2114	-0.218	-0.993	0.48	0.016
α_4	52.9798	0.0781	1.4405	-0.094	-0.94	0.51	0.0141

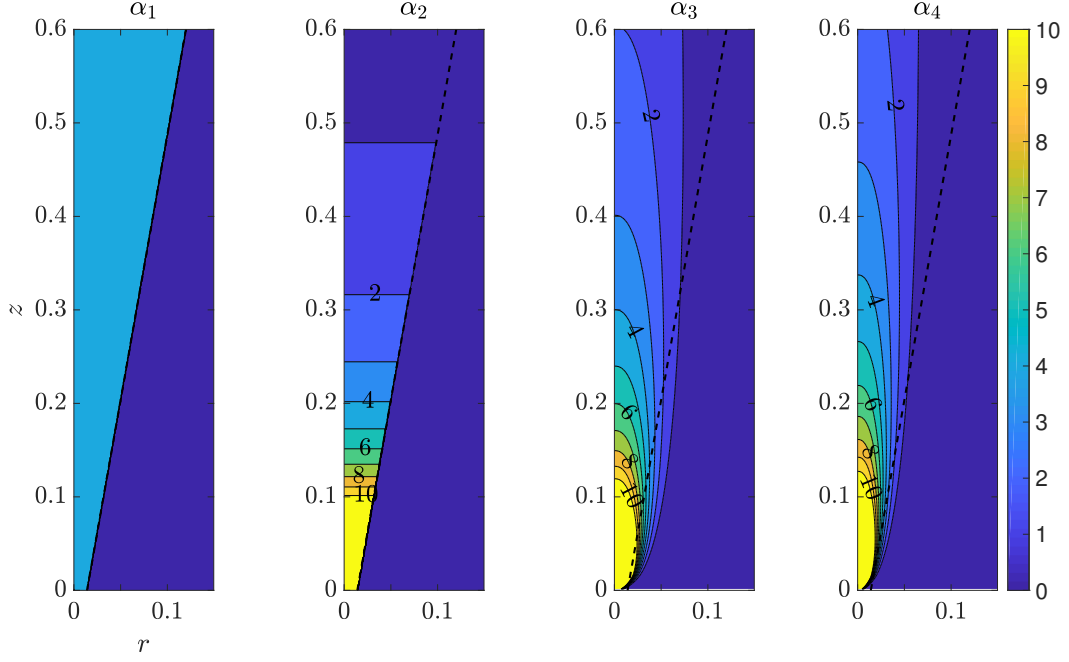


Figure 3.2: Isolines of the four different formulas for α (from (Alia et al., 2019a)). The colors indicate the gas volume fraction in percentage.

Altogether, the 2d axisymmetric problem reads:

Problem 3.2 (NSE for the 2d axisymmetric (“2.5d”) ladle stirring):

$$\begin{aligned}
 \mathbf{u}_t + (\mathbf{u} \cdot \nabla) \mathbf{u} - 2\nu \nabla \cdot (\mathbb{D}(\mathbf{u})) + \nabla p &= (1 - \alpha(r, z)) \mathbf{g} && \text{in } (0, T] \times \Omega \\
 \nabla \cdot \mathbf{u} &= 0 && \text{in } (0, T] \times \Omega \\
 \mathbf{u} &= \mathbf{0} && \text{in } (0, T] \times \partial\Omega \setminus \{\Gamma_{\text{axis}} \cup \Gamma_{\text{top}}\} \\
 \mathbf{u} \cdot \mathbf{n} &= 0 && \text{in } (0, T] \times \{\Gamma_{\text{axis}} \cup \Gamma_{\text{top}}\} \\
 \mathbf{n}^\top \mathbb{S} \mathbf{t}_i &= 0, \quad 1 \leq i \leq d-1 && \text{in } (0, T] \times \{\Gamma_{\text{axis}} \cup \Gamma_{\text{top}}\} \\
 \mathbf{u}(0, \mathbf{x}) &= \mathbf{0} && \text{in } \Omega \\
 \int_{\Omega} p \, d\mathbf{x} &= 0 && \text{in } (0, T].
 \end{aligned}$$

In cylindrical frame, the Navier–Stokes equations can be written as shown in Appendix A (Eqs. (A.4)).

3.2.3 The 3d ladle model

In this application, the geometry corresponds to the water ladle of the Process Metallurgy Research Unit of the University of Oulu. It is a laboratory-scale of the steel ladles from Outokumpu’s plant in Tornio, Finland, and has two excentric nozzles (Figure 3.3). The experimental ladle was designed by (Palovaara et al., 2018), using physical and geometrical similarity criteria. Although, the main purpose of the experiment was to measure the mixing time, the authors also measured the average velocity at the vertical line in the middle of one of the gas plume. These measurements will serve in this work to check the results of the numerical model. It is assumed that the measured velocities are the same in both gas plumes.

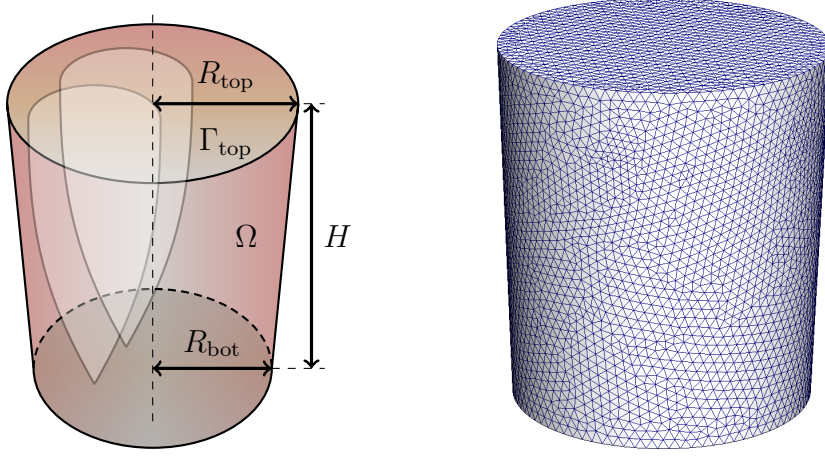


Figure 3.3: Sketch of the 3d laboratory-scale water ladle with two excentric nozzles and a coarse tetrahedral mesh obtained with GMSH (~ 71000 cells).

Geometry. The geometrical parameters for this application are listed in Table 3.4. The ladle is quite similar to the one of the 2d applications: the ratio H/R is ~ 2.32 , to compare with 2 in 2d. One important difference is the gas flow rate. Here, we have $Q = 17 \text{ l min}^{-1}$ since the measurements in (Palovaara et al., 2018) were done under this flow rate, whereas in 2d, the flow rate is similar to (Woo et al., 1990): $Q = 13 \text{ l min}^{-1}$. Note that the values have to be converted to $\text{m}^3 \text{ s}^{-1}$ for the units to be consistent in the numerical applications. Concerning the parameters needed for the gas fraction, such as χ , a , or U_S , they are the same as in the 2d axisymmetrical case, see Table 3.4. The Reynolds number can be computed as $\text{Re} = \frac{\rho U_P R}{\mu}$. Depending on the value of R (top, bottom, or average radius), the Reynolds number is in the range $[97000, 103000]$. This range is not far from the value applied in the 2d applications. Thus, for more convenience, the same Re has been employed (96000). As described in Section 3.1.2, the boundary conditions are similar to the 2d models, except that there is no axis boundary ($\Gamma_{\text{axis}} = \emptyset$).

Modeling of the two gas plumes. The single-phase model applied here is similar to the axisymmetric model and is detailed in (Alia et al., 2019a). The main novelty concerns the volume force: because of the two nozzles, it is defined as the sum of the buoyancy of both gas plumes, i.e., $(-\rho g + (\alpha_{n1} + \alpha_{n2})\rho g) \mathbf{e}_z$. The gas fractions α_1 , α_2 or α_3 are all suitable. However, preliminary tests have shown some convergence difficulty in 3d. They are due, on the one hand, to the discontinuous plume shape in Eq. (3.12) and (3.13), and, on the other hand, to the blow-up of Eq. (3.14) at the origin. We therefore define a smoother version of α_2 for 3d applications, which is also more realistic from the physical point of view:

$$\alpha_{ni}(x, y, z) = \begin{cases} \frac{1}{2} \left(\frac{U_P}{U_S} + 1 \right) \exp \left(-2 \left(\frac{(x-x_{ni})^2 + (y-y_{ni})^2}{r_c(z)^2} \right)^2 \right), & \text{if } z \leq z_C, \\ \frac{1}{2} \left(\left(\frac{U_P}{U_S} + 1 \right) - \sqrt{\left(\frac{U_P}{U_S} + 1 \right)^2 - \frac{4Q}{\pi r_c^2(z) U_S}} \right) \exp \left(-2 \left(\frac{(x-x_{ni})^2 + (y-y_{ni})^2}{r_c(z)^2} \right)^2 \right), & \text{if } z \geq z_C, \end{cases} \quad (3.15)$$

where (x_{ni}, y_{ni}) is the center of nozzle $i = 1, 2$. For simplicity, we also write it as

$$\alpha_{ni}(x, y, z) = \alpha_2(z) \exp \left(-2 \left(\frac{(x - x_{ni})^2 + (y - y_{ni})^2}{r_c(z)^2} \right)^2 \right), \quad (3.16)$$

where α_2 depends now on z , instead of (r, z) as in the 2d axisymmetrical case. The critical height z_C is the same as for α_2 in 2d. The factor 2 in the exponential increases the smoothness of the transition between the gas plume and the liquid. Finally, the volume force was also smoothed in time during the first time steps (Eq. (3.11) with $t_0 = 0.05$ s) to facilitate convergence in the first time steps.

Altogether, the 3d model is summarized in Problem 3.3:

Problem 3.3 (Strong form of the NSE for the 3d ladle stirring):

$$\begin{aligned} \mathbf{u}_t + (\mathbf{u} \cdot \nabla) \mathbf{u} - 2\nu \nabla \cdot (\mathbb{D}(\mathbf{u})) + \nabla p &= (1 - (\alpha_{n1} + \alpha_{n2})\ell(t))\mathbf{g} && \text{in } (0, T] \times \Omega \\ \nabla \cdot \mathbf{u} &= 0 && \text{in } (0, T] \times \Omega \\ \mathbf{u} &= \mathbf{0} && \text{in } (0, T] \times \partial\Omega \setminus \Gamma_{\text{top}} \\ \mathbf{u} \cdot \mathbf{n} &= 0 && \text{in } (0, T] \times \Gamma_{\text{top}} \\ \mathbf{n}^\top \mathbb{S} \mathbf{t}_i &= 0, \quad 1 \leq i \leq d-1 && \text{in } (0, T] \times \Gamma_{\text{top}} \\ \mathbf{u}(0, \mathbf{x}) &= \mathbf{0} && \text{in } \Omega \\ \int_{\Omega} p \, d\mathbf{x} &= 0 && \text{in } (0, T] \\ \alpha_{ni} &\text{ given by (3.15), for } i = 1, 2. \end{aligned}$$

In 3d and in a Cartesian frame, the Navier–Stokes equations can be written as shown in Appendix A (Eqs. (A.1)).

3.3 Numerical results in 2d

As introduced in this chapter, the main advantages of the single-phase models over two-phase flows are their simplicity of implementation and their cheaper computational cost, which are two important criteria for the coming stirring optimization problem. Furthermore, their physical relevance has been demonstrated, when it comes to predict the order of magnitude and flow pattern of the bulk liquid, (Alia et al., 2019a, Mazumdar and Guthrie, 1995a). However, as shown in Section 3.1, the models of the literature present many variants and lack of a unified formulation. It is thus difficult to know which one is the most appropriate for an optimal control problem on a real ladle. After having fixed the modeling assumptions in the precedent section, the corresponding numerical results are now compared in this section with the idea behind to apply these models in the context of numerical optimization of ladle stirring.

In this regard, several aspects are taken into account. First, the influence of the mesh refinement on the solution needs to be checked. In general, it is indeed desirable to have a mesh-independent solution. For this, solutions on different grid refinements are compared qualitatively, with a starting grid which is fine enough

to resolve the high Reynolds number. If the simulation does not converge, then a stabilization or turbulence model should be applied.

This is the second aspect. Although many stabilization and turbulence models exist, they have in common the addition of viscosity in the equations. In this work, the turbulence models have been chosen among the most popular ones: the Smagorinsky model, which is implemented in the code PARMOON, and the $k - \epsilon$ model, which is the privileged model used in the literature for quasi-single phase models. For more convenience, the commercial software COMSOL MULTIPHYSICS has been used for the $k - \epsilon$ turbulence model because it is already implemented there. The influence of the turbulence model and its parameters, e. g., the turbulent viscosity constant, on the solution is also investigated.

Third, the evolution of the flow in time should be studied with a focus on its long-term behavior: does the solution reach a (nearly) periodic regime? It is known that turbulent flows are time-dependent. However, the flow can show some periodic structures in time, especially in the case where the Reynolds number is not too high. Indeed, different numerical studies showed that, for $\text{Re} \leq 8000$, the 2d lid-driven cavity problem has a stationary solution, and that, around 10000, it has a stable periodic solution (De Frutos et al., 2016). It is interesting to see if this is the case in the 2d and axisymmetric applications with $\text{Re} = 96000$. The main benefit of having a solution with regular pattern in time is that it makes it easier to define a suitable initial condition for the optimal control problem. In the industrial practice, the operator adjusts the stirring (i. e., the injected gas flow rate) until the surface of the liquid shows a vigorous flow mixing. When the surface is “satisfactory” (often in a subjective sense), the operator leaves the parameters unchanged and only monitors the stirring at the surface. If, for example, a change in the regularity and the intensity of the flow pattern occurs, he intervenes and corrects the flow rate. Otherwise, most of the time, the stirring is considered to be stable and the gas flow rate Q is generally constant and not changed in time. From an optimization perspective, it is thus relevant to start the optimal control after the initial transitional phase, or, in other words, once the flow is established and becomes relatively “stable”, e. g., “periodic”. The present numerical study checks whether such a regime is reached. This is also why a high end time ($T = 600$ s) has been chosen, with the hope that the initial development of the flow will be finished long before the end time, and that a regular flow pattern can be observed over a long time range. Another important reason to study the long-term behavior of the flow is to compute the average velocity on this long time range, and to be able to compare it with the models from the literature, which are based on the stationary NSE ¹.

Coming to the comparison with existing results, the fourth aspect of this study concerns the comparison of the boundary-driven and axisymmetric models with experimental measurements available in the literature. It is important to find which model coincides best with the physical reality. Finally, the last aspect concerns the applicability of the models in industrially-relevant cases, for example, in real ladles with two gas nozzles. This is discussed in the last part of this section.

¹Because the $k - \epsilon$ model is quite diffusive, the flow computed in the usual single-phase models from literature becomes constant; hence their use of the stationary Navier–Stokes equations.

3.3.1 Implementation

Two softwares are used to solve the 2d boundary-driven and axisymmetric models: the in-house and open-source code from the Weierstrass Institute PARMOON (Wilbrandt et al., 2017) and the commercial software COMSOL MULTIPHYSICS.

Using an open-source software has several advantages over commercial softwares: it gives more control over the implementation of the models, enables the use of state-of-the-art numerical models which are not available in commercial solvers, and the absence of charge is an attractive argument for industrial companies willing to use the code. A detailed discussion on the reasons of developing and using an in-house code can be found in (Wilbrandt et al., 2017). In the context of this project, where an optimal control problem should be implemented and may be applied in the industry, the use of PARMOON is thus a relevant choice.

On the other hand, the implementation of new models requires a non-negligible time investment in such codes. This is especially the case with non-trivial models, involving a set of coupled PDEs or requiring special care in the implementation. For example, the $k-\epsilon$ turbulence model involves two coupled PDEs with convection domination. This turbulence model is very popular in the literature for ladle stirring, and is not available in PARMOON. Using the same turbulence model as in literature is important because it allows to check the reproducibility of the results, before applying other turbulence models. As it will be seen in below, they can lead to very different results. Another example is the two-phase flow models, which involves the Navier–Stokes equations coupled with a transport equation. Here, the interface between the two phases needs to be treated correctly (e.g., adaptive mesh refinement or interface reconstruction). The optimization problem is a last example of complex problems which cannot be implemented in a straightforward fashion in in-house codes.

For these reasons, the commercial software COMSOL has also been used in this work. It can handle, among others, the $k-\epsilon$ turbulence model. Furthermore, the implementation of the 2d boundary-driven, axisymmetric, and 3d ladle models can be done quite easily. Indeed, commercial softwares are known to provide an integrated interface which offers the possibility to draw the geometry, mesh it, and set-up different types of equations and parameters at once and relatively fast.

Implementation in PARMOON. The boundary-driven and axisymmetric problems are discretized in space with structured and isotropic quadrilaterals. Initially, the geometry, a simple rectangle of size $H \times R$ with $H = 2R$, is split in two quadrilaterals of same size R (squares). One level of refinement then consists of splitting each quadrilateral in four quadrilaterals of equal size. More information on the mesh refinement can be found in (John and Matthies, 2004). Two levels of mesh refinement were applied for both models: levels 5 and 6. The corresponding grid size and number of cells are given in Table 3.6. The discretization of the PDEs in space is based on the standard Galerkin method. The implementation of the axisymmetric case can be practically derived from the Cartesian case: one only has to multiply each term of the variational equation by the distance to the axis r , and add one extra-term in both momentum and continuity equations (Section 2.3.3 for more details). As it will be seen, the axisymmetric case required the use of

Table 3.6: Mesh parameters. The abbreviation “Dof” refers to the number of degrees of freedom.

Mesh refinement level	5	6
Grid	32×64	64×128
Number of cells	2 048	8 192
Cell size	0.0133	0.00663
Dof \mathbf{u}	16 770	66 306
Dof p	6 144	24 576
Dof total	22 914	90 882

additional turbulent viscosity in order to converge. The Smagorinsky model was applied (Section 2.5.2), with the turbulent viscosity defined by Equation (2.61). Different values for the turbulent viscosity constant are applied to study its influence on the solution: $C_S = 0.001, 0.005, 0.01$, and 0.05 . Values which are smaller than 0.001 are insufficient, i. e., the solution blows up. The maximum value 0.05 ended up with a sufficiently dampened solution, so that it was not necessary to test higher values. In the boundary-driven configuration, no stabilization or turbulence model were needed. Concerning the choice of the finite elements, the main constraint is the inf-sup stability (Definition 2.5). A classical pair of inf-sup stable finite elements is the Taylor–Hood pair $\mathbf{Q}_i/\mathbf{Q}_{i-1}$, $i \geq 2$ (Section 2.3.2). Alternatively, one can use elements with discontinuous pressure such as $\mathbf{Q}_i/\mathbf{P}_{i-1}^{\text{disc}}$, $i \geq 2$. As pointed out in (John, 2016), due to the jump of the boundary condition at the corners, the solution is not sufficiently regular for the use of conforming finite elements. However, since a regularization is applied here, this problem does not occur. Finally, because the $\mathbf{Q}_2/\mathbf{P}_1^{\text{disc}}$ proved to perform well in (John and Matthies, 2001), it was used in both boundary-driven and axisymmetric models. The number of degrees of freedom are given in Table 3.6. The details of the discretization and linearization can be found in Section 2.3.2. A coarse time step is applied ($\Delta t = 0.01$) in order to avoid excessive computational time due to the long time range. The residual tolerance was set to 10^{-10} and was always reached after a few iterations, before the maximum number of iterations per time step (10).

Finally, a direct solver is used to solve the linear saddle point problem. This type of solver is indeed sufficient for 2d cases of the size of the present models. The more sophisticated methods, based on iterative solvers with preconditioning, become interesting mainly for the three-dimensional Navier–Stokes equations. Note that the performance of direct and iterative solvers can be significantly increased using parallelization. However, for the present model size, the computational time is not a problem and parallelization is clearly not needed. Altogether, the sequential (i. e., non-parallelized) direct solver UMFPACK was used.

The implementation of the models in the commercial software COMSOL MULTIPHYSICS will be discussed in Section 3.3.4.

3.3.2 Numerical solution

The 2d boundary-driven configuration. In this case, the model proved to be quite stable: the iterations converge easily without the need of additional stabilization, and the solution obtained with the two levels of mesh refinement are similar qualitatively (Figure 3.4), and quantitatively (see Figure 3.10 which will be discussed further below). Using different time steps, the solutions were similar as well, but the results are not shown here. This result was expected because of the choice of the Crank–Nicolson scheme. Furthermore, one can clearly see three regimes in the evolution of the flow in time. First, there is a transitional step where the velocity at the boundary propagates to the top boundary (Figure 3.4, left snapshots), reaches the right part, goes down into the bulk liquid, and starts to split the ladle into a large vortex at its upper zone and a smaller vortex at the bottom zone (Figure 3.4, central snapshots), rotating in opposite directions. This transitional phase lasts at least 60 s. In the second phase, one sees constantly growing vortices until some “balance” is reached between the top and the bottom parts (Figure 3.4, right snapshots). After that, the flow stabilizes with a small perturbation at the contact between them, which comes periodically in the flow. In order to quantify when the solution reaches a periodic or quasi-stationary state, the velocity amplitude at several points is computed with respect to time (Figure 3.5). The points are chosen to cover the main structures of the flow in the domain, i.e., the top and bottom vortices (Figure 3.6 and Table 3.7). One observes clearly the transitional phase between 0 and approximately 150 s. While some areas stabilize around 150 s (lower right and lower center), the velocity grows slowly in other areas of the domain. The final regime is established between 200 and 300 s. The mean velocity becomes rather constant with small fluctuations, except in the middle area of the domain (and in the lower left part to a certain extent). There, at the junction between both vortices around the point (M), the velocity fluctuations are the highest. This numerical example shows how a high Reynolds number like $Re = 96000$ does not necessarily lead to a turbulent flow in 2d “lid-driven-like” configurations.

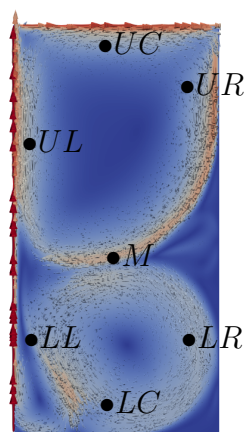


Figure 3.6: Location of the seven points of interest (background flow: mesh 6 at 237 s).

Table 3.7: Coordinates of seven points covering the main flow structures.

	Location	Coordinates (x, y)
LL	lower left	(0.038, 0.14)
UL	upper left	(0.038, 0.43)
LR	lower right	(0.26, 0.14)
UR	upper right	(0.26, 0.50)
LC	lower center	(0.15, 0.028)
UC	upper center	(0.15, 0.57)
M	middle	(0.15, 0.27)

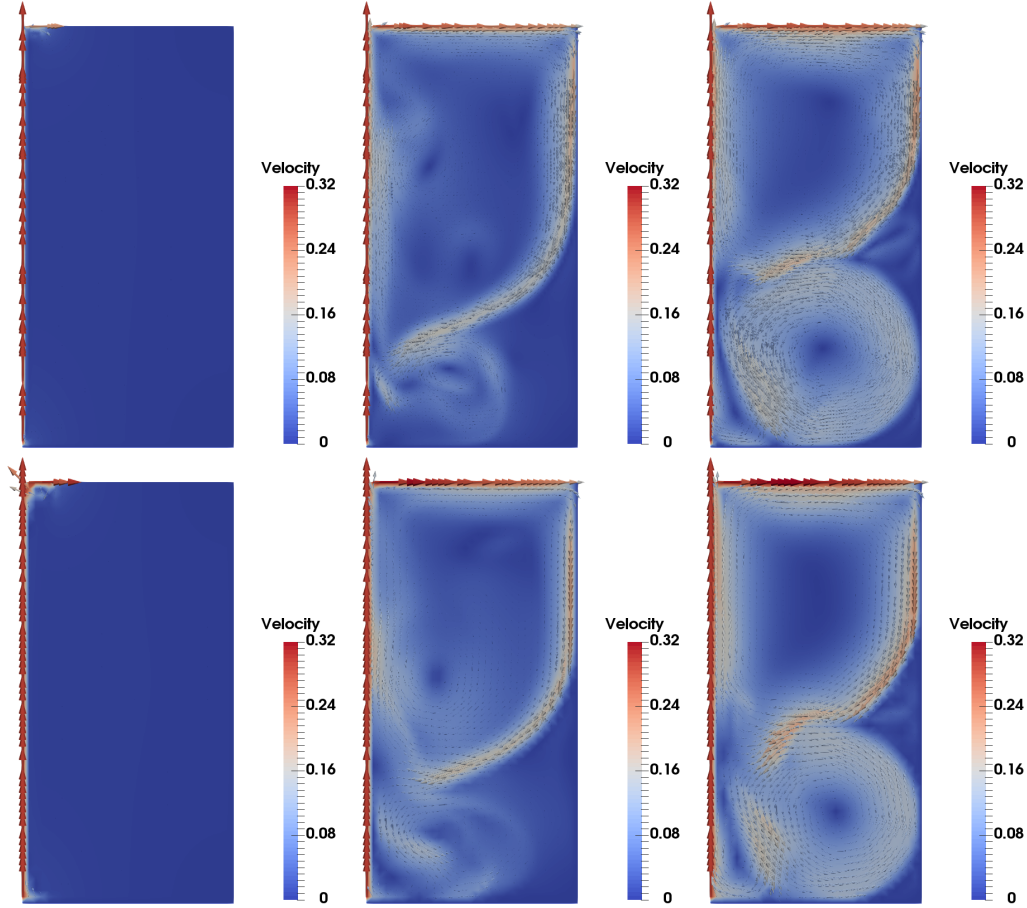


Figure 3.4: Snapshots of the velocity field with the 2d boundary-driven ladle model at $t = 1, 57$, and 237 s. Top: mesh 6. Bottom: mesh 5.

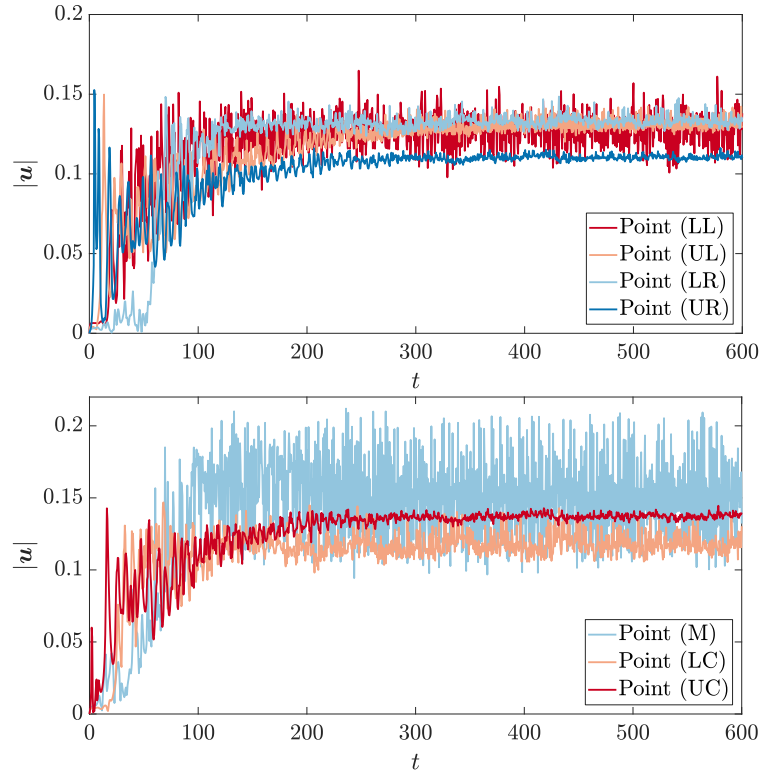


Figure 3.5: Time evolution of the Euclidean norm of the velocity at seven points of the domain (the curves are displayed in two different plots for more clarity).

A mesh fine enough to resolve the smallest flow structures can lead to a periodic solution without the need of a turbulence model. Furthermore, the fact that the flow seems to be independent of the mesh refinement and that it is periodic in time makes it practical for an optimal control problem. Indeed, one does not require a fine mesh such as the one with 6 refinement levels. The coarser mesh can be used, sparing a significant amount of time. In addition, the initial condition of the velocity can be taken from the periodic regime of this model, i. e., after 300 s.

The 2d axisymmetric configuration. The axisymmetric case resulted in very different numerical behavior and results. First, the computations could not converge without stabilization: the solution blew up. Therefore, the Smagorinsky turbulent viscosity was added and, as mentioned before, different values of the Smagorinsky constant C_S were tested: $C_S = 0.001, 0.005, 0.01$, and 0.05 . As a consequence, the solution is not expected to be independent of the mesh anymore. The results depend now on both the mesh and C_S . For high turbulent viscosity, namely $C_S = 0.005, 0.01$, and 0.05 , the flow results almost in a steady-state (Figure 3.7) after a few dozens of seconds, whereas for $C_S = 0.001$, the solution is time-dependent. More precisely, with mesh 5, the flow becomes periodic (Figure 3.8), and with mesh 6, there are no clear flow structures. In this last case, Figure 3.9 shows three snapshots of the velocity field for $C_S = 0.001$: when two or three vortices seem to appear clearly in the flow, they are distorted quickly and reappear only occasionally.

To illustrate the periodicity in the case of mesh 5, the evolution of the velocity in time is computed at the same seven points as in the boundary-driven case (Figure 3.8). Here, the periodicity of the flow can be clearly seen in the case $C_S = 0.001$. One can notice that the periodic flow structures are different from the boundary-driven case: instead of having two big vortices covering the domain, there is a small vortex on the top right corner, far from the nozzle, and a low-velocity vortex in the bottom part of the fluid. The periodic regime starts shortly before 100 s, faster than in the boundary-driven configuration. When the turbulent viscosity constant is higher (e. g., $C_S = 0.01$), the flow is dampened and a steady-state regime is reached even quicker: approximately at 50 s (dashed lines). Altogether, the different Smagorinsky constants lead either to a steady-state or a periodic regime. For a better qualitative comparison of the flows, the average velocity fields of the periodic flows are computed, and compared with the ones from the steady-states.

This further comparison is displayed in Figure 3.7. The three columns refer to α_1 , α_2 , and α_3 , from left to right, respectively, while the rows correspond to different meshes and C_S . The (average) velocity fields reveal the effect of the gas through the volume force. A strong upward flow is generated close to the left boundary. Its intensity close to the nozzle is higher with α_2 and α_3 than with α_1 , which can clearly be assigned to the higher gas fraction in this zone, see also Figure 3.2. On the contrary, on the top side of the domain, the velocity is slightly higher with α_1 than with α_2 and α_3 . In a similar way, this is due to the higher gas fraction for α_1 ($\sim 4.8\%$) in comparison to the others ($< 2\%$, Figure 3.2). Far from the left boundary, the velocity fields obtained with the three

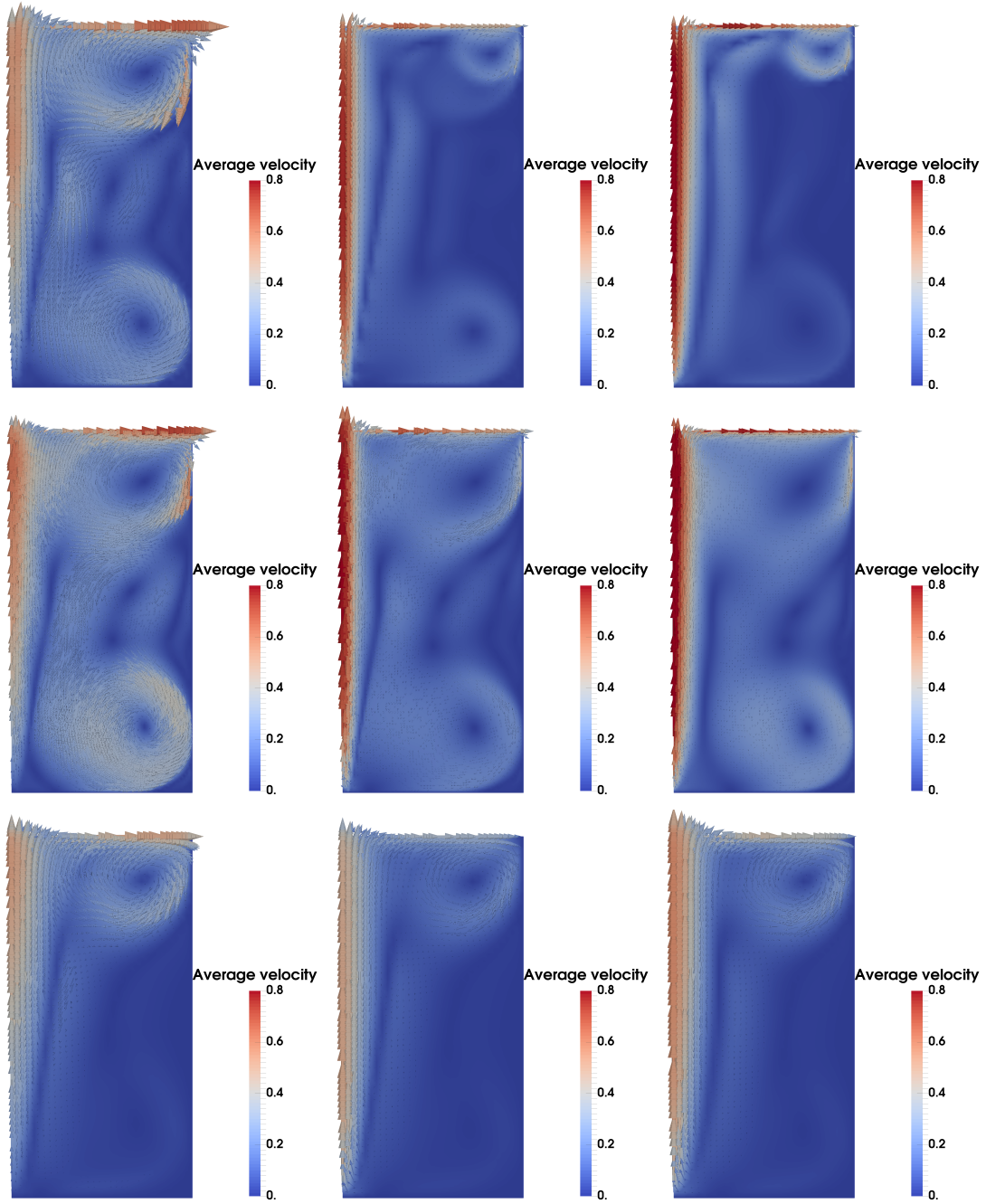


Figure 3.7: Comparison of the time-averaged velocity field between the gas fractions $\alpha_i, i = 1, 2, 3$ of the 2d axisymmetric ladle model. From left to right: α_1 , α_2 , and α_3 . Top: $C_S = 0.001$ with mesh refinement level 5. Middle: $C_S = 0.001$ with mesh 6. Bottom: $C_S = 0.05$ with mesh 5.

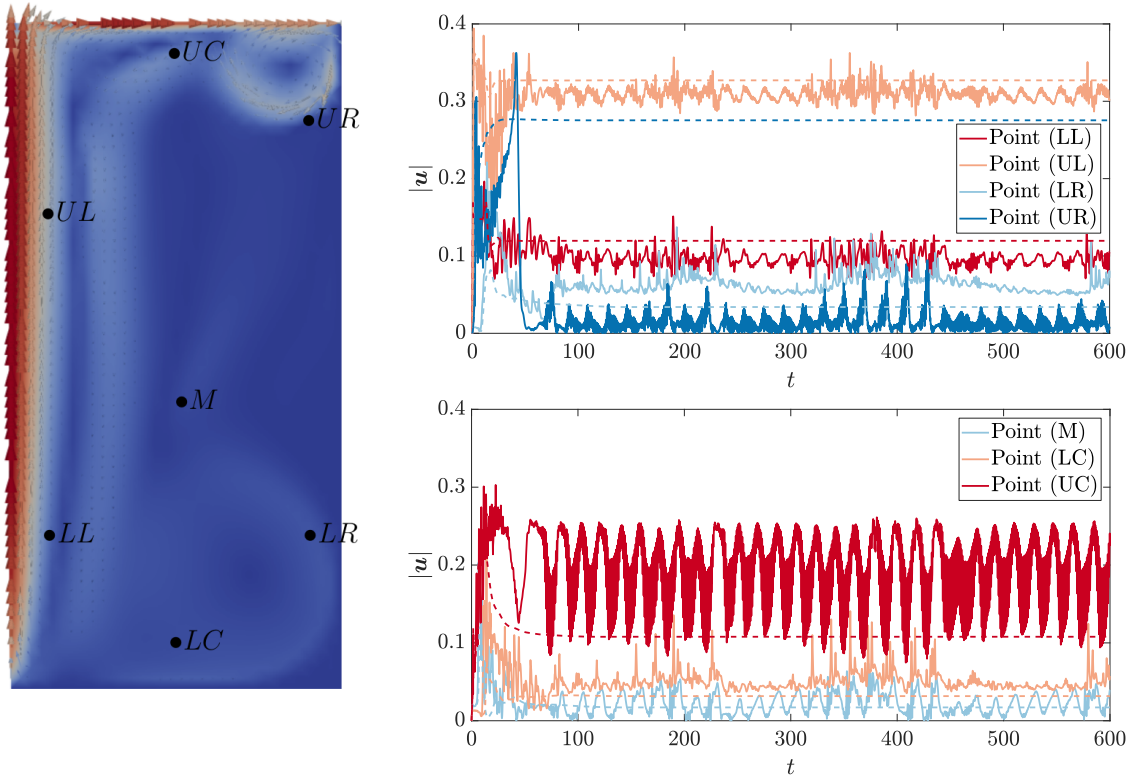


Figure 3.8: Left: location of the seven points of interest (background flow: mesh 5 with α_3 and $C_S = 0.001$). Right: time evolution of the Euclidean norm of the velocity at seven points of the domain (the curves are displayed in two different plots for more clarity). The results correspond to mesh 5 with α_3 . Solid lines: $C_S = 0.001$. Dashed lines: $C_S = 0.01$.

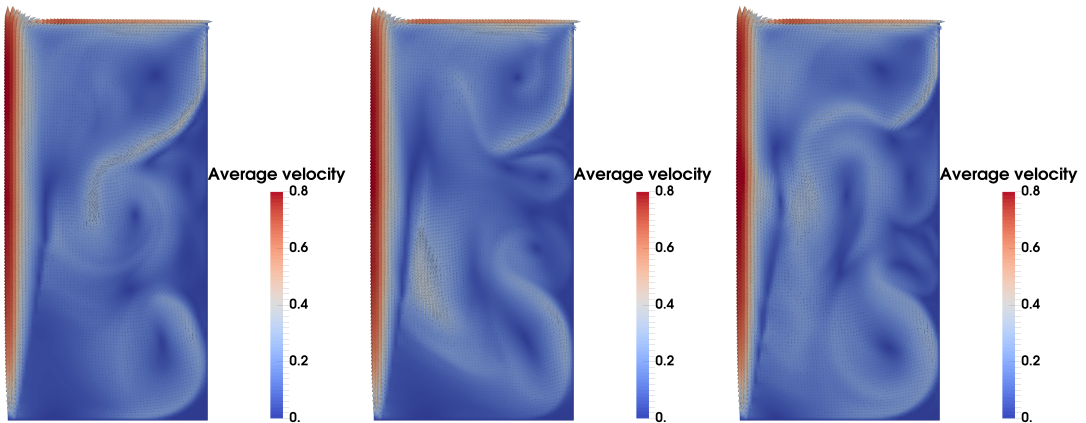


Figure 3.9: Snapshots of the velocity field with the 2d axisymmetric ladle model at $t = 500, 550$, and 600 s (using mesh refinement 6, $C_S = 0.001$, and gas fraction α_2).

gas fractions are relatively similar, in the sense that they all produce one vortex located in the upper right region. Comparing the snapshots from left to right in Figure 3.7, it can be noted that the velocity fields are qualitatively similar from one α to another, independently of the mesh and C_S . The resulting flow is basically composed of two vortices at the top right and bottom right corners. Only the velocity magnitude and the size of the vortices are slightly different. This similar pattern can be attributed to the form of the gas fraction α . They are defined in a plume cone whose effect is mainly concentrated on the axis and which becomes larger at the top of the ladle. Concerning the influence of the mesh, one can clearly see that the velocity amplitude increases between mesh 5 and 6 (top and middle rows in Figure 3.7). Furthermore, the higher the Smagorinsky constant the more dampened the flow (bottom snapshots in Figure 3.7 with $C_S = 0.05$).

Altogether, the axisymmetric model is numerically less stable at high Re than the boundary-driven model and its solution depends on the mesh and on the Smagorinsky constant. For low C_S , e.g., 0.001, it is difficult to recognize any periodicity in the flow (Figure 3.9). The higher values of C_S tested in this work ended up to a “quasi” steady-state earlier than in the boundary-driven model: too much viscosity was added. With some fine tuning, it may be possible to reach a periodic flow, as in the boundary-driven case. However, the flow is likely to have a different pattern.

As it will be seen in the next section, some of the observations made so far are reflected in the comparison with experimental measurements.

3.3.3 Comparison with experimental measurements

The results are compared with experimental measurements available in (Woo et al., 1990). These have been performed at three horizontal lines going from the center of the ladle to its wall, at $z/H = 0.3, 0.68$, and 0.98 , for two quantities: the mean velocity and the turbulent kinetic energy. However, a higher discrepancy is observed between the present simulations and the reported measurements at the level $z/H = 0.98$ and with the turbulent kinetic energy. The reasons for these discrepancies are still unclear. Since the authors also provide their equations (in particular with the $k - \epsilon$ turbulence model), we have tried to solve them on the commercial software COMSOL MULTIPHYSICS in order to check the reproducibility of their numerical results and see if their model matches the experimental measurements better than our model. It turned out that we did not obtain their results using their model on COMSOL MULTIPHYSICS. As in our model, high discrepancies were observed on the level $z/H = 0.98$ and with the turbulent kinetic energy. Therefore, in the following results, we consider only the experimental measurements of the mean velocities at the heights $z/H = 0.3$ and 0.68 .

The 2d boundary-driven configuration. Two post-processing steps have been performed on the solution \mathbf{u} for the comparison with experimental measurements: the average in time from the 500th to the 600th second (Figure 3.5) and the interpolation of the averaged velocity magnitude on the lines. The results are given in Figure 3.10. One can clearly see that both mesh refinement levels give very close

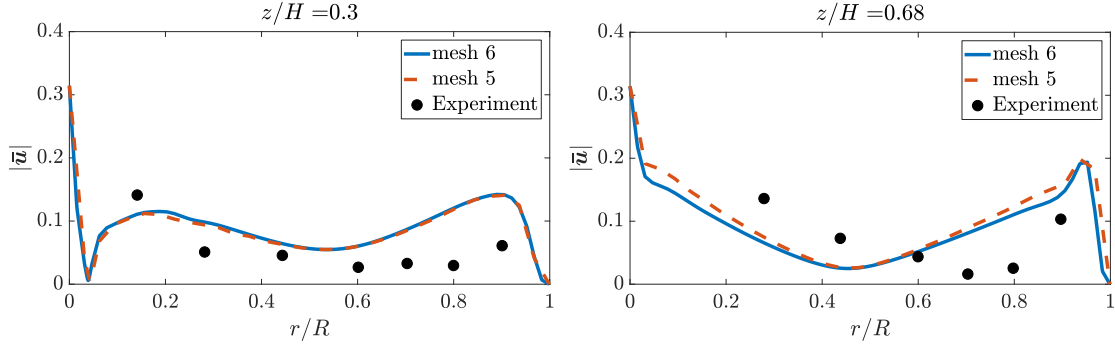


Figure 3.10: Euclidean norm of the time-averaged velocity vs. experimental measurements in the 2d boundary-driven configuration.

results. The shape of the curves at $z/H = 0.3$ agrees better with the measurements than at the height $z/H = 0.68$. At this higher level, one recognizes the wide vortex on the top part of the ladle, visible in Figure 3.4. The profile described by the experimental points do not cover the whole width of the ladle, suggesting that the vortex is rather narrower than the computed one. This difference can clearly be attributed to the modeling of the gas in the boundary-driven model: the boundary velocity acts only on the very axis and does not rise the liquid in a wider zone on the top area of the ladle. Therefore, the velocity is equal at the boundary velocity close to 0, but decreases then rather fast. On the contrary, the real gas plume induces a higher velocity at radius $0.2 \leq r/R \leq 0.5$ and induces a smaller vortex on the top right corner, than in the boundary-driven model. Despite this qualitative difference, the order of magnitude between the boundary-driven model and the experimental measurements agree quite well. At $z/H = 0.3$, one notices the sharp decrease close to $r = 0$, which indicates the presence of a “dead-zone”, i.e., a zone of the ladle with no circulation of the liquid. This is the kind of zone that one would like to avoid during stirring. This aspect will be discussed in Chapter 4.

The 2d axisymmetric configuration. For $C_S = 0.005, 0.01$, and 0.05 , the time average was performed in the period $[100, 135]$, when the steady-state is assumed to be reached. In this time range, the standard deviation is less than 5% (not represented). For $C_S = 0.001$, the time average is performed, like the boundary-driven case, in the period $[500, 600]$, see Figure 3.8. In this case, the standard deviation of the velocity was found to be high (in the order of 100%). Unfortunately, there are no measurements of the standard deviation available for the experiment. On Figure 3.11, the velocities along the lines at $z/H = 0.3$ and 0.68 reflect the dependency of the solution on the mesh refinement and the Smagorinsky constant C_S . One can clearly see the increase of the velocity magnitude on the finer mesh (plots on the right side). Furthermore, the lower the Smagorinsky constant C_S , the higher the velocity. Comparing the volume forces, α_1 (in red) clearly overestimates the velocities in comparison to the measurements and to α_2 and α_3 . On the fine mesh, the combination of α_2 with $C_S \leq 0.005$ also gives too high velocities. Altogether, only some specific choice of numerical parameters gives a satisfying result. They are given separately in Figure 3.12 for more clarity. For example, the gas fraction α_2 with $C_S = 0.01$ seems to be in good agreement with the measurements on both meshes.

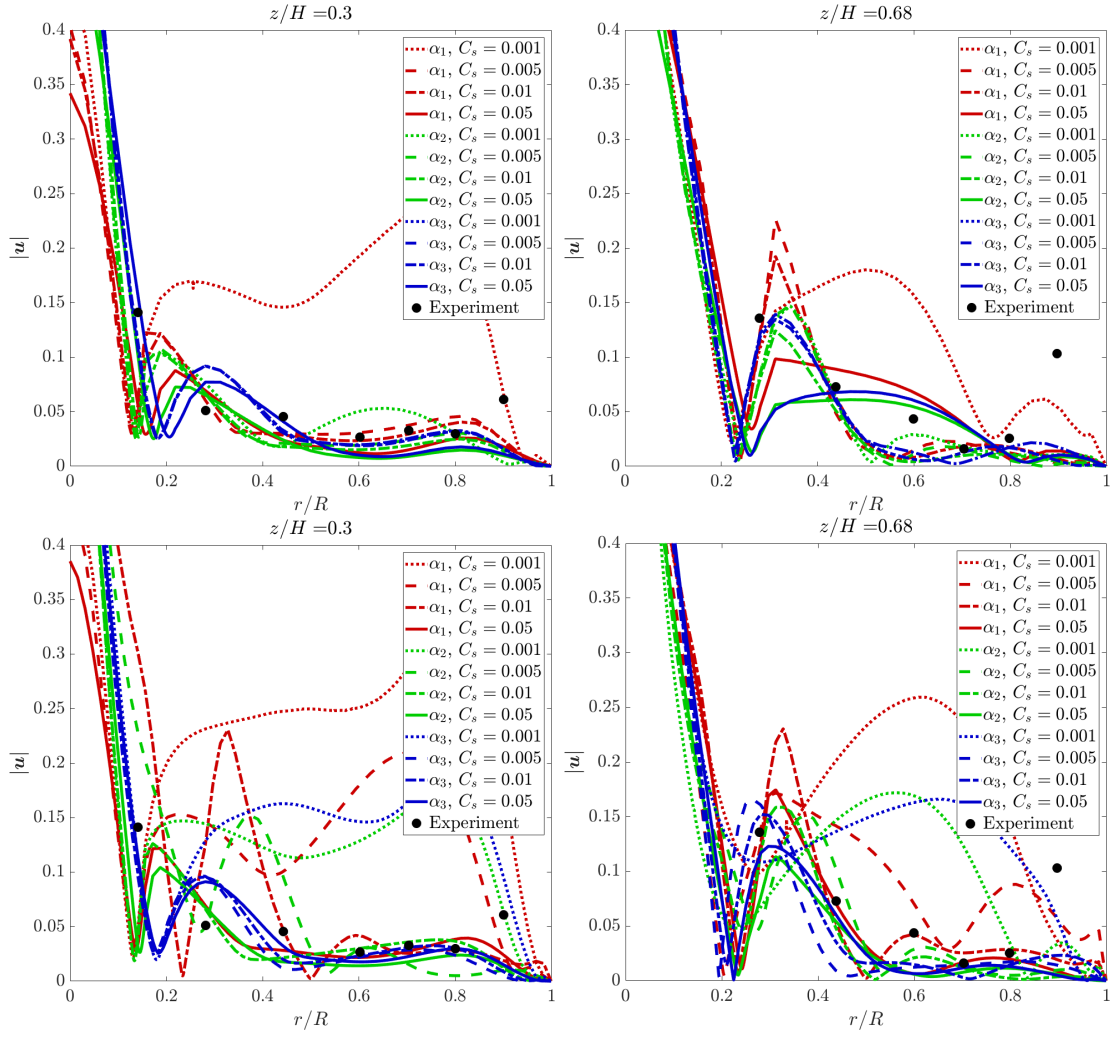


Figure 3.11: Comparison of the numerical velocity with experimental measurements. Top: mesh refinement 5. Bottom: mesh refinement 6.

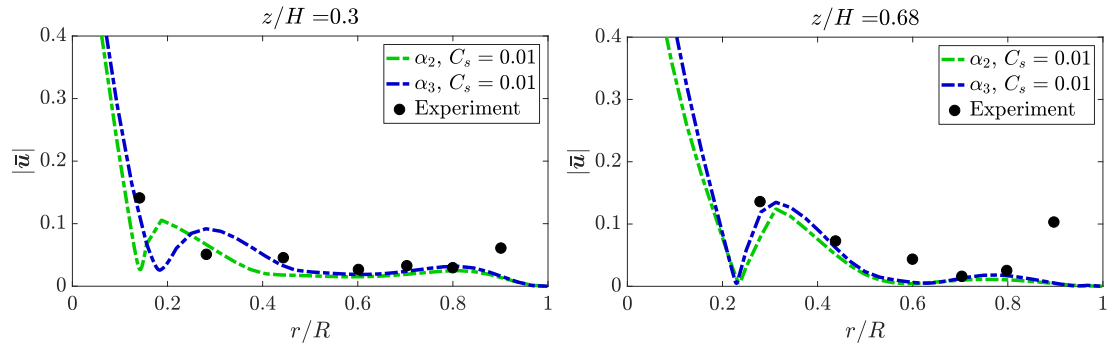


Figure 3.12: Two satisfying solutions in the axisymmetric case: gas fractions α_2 or α_3 , with $C_s = 0.01$, and mesh refinement level 5.

3.3.4 Comparison with the commercial software COMSOL

The main reason which can explain the discrepancies between the results of the present axisymmetric model and the numerical and experimental results in (Woo et al., 1990) is the turbulence model. In (Alia et al., 2019a), the same axisymmetric model as in Section 3.2.2 is computed using the $k - \epsilon$ turbulence model (with COMSOL). Thus, we can compare their results with the present model, which uses the Smagorinsky model (with PARMOON). Comparing the flow pattern in Figures 3.13 and 3.7, one notices a clear difference: the flow seems to be considerably dampened in the $k - \epsilon$ model, so that no vortices are formed. The solution is stationary, as in the literature. Unlike the Smagorinsky model, the solution computed in COMSOL seems to be independent of the mesh. An overall good agreement with experimental measurements is obtained, as shown in Figure 3.14. All three gas fractions $\alpha_i, i = 1, 2, 3$ give very similar results, except that α_1 slightly overestimates the velocity at height $z/H = 0.68$. All in all, it can be seen how the choice of the turbulent model can considerably change the nature of the computed flow.

3.3.5 Summary and outlook to 3d

The results between the boundary-driven and axisymmetric ladle models are qualitatively and quantitatively quite different. This can be explained by the difference of mechanism which induces the flow: boundary velocity and volume force.

The boundary-driven model proved to be satisfying in terms of numerical stability and its velocity has the same order of magnitude as experimental measurements. However, it does not take into account the width of the gas plume on the top part of the ladle, resulting in a large vortex instead of a small one at the right corner. The axisymmetric model requires stabilization. Only a good choice of numerical parameters can lead to a solution close to measurements.

It should be stressed that the comparison with the experimental measurements at two heights is clearly insufficient to validate the models. The best way to know the actual physical solution properly would have been to conduct one's own experiment and to measure the velocity at a higher number of points in the ladle.

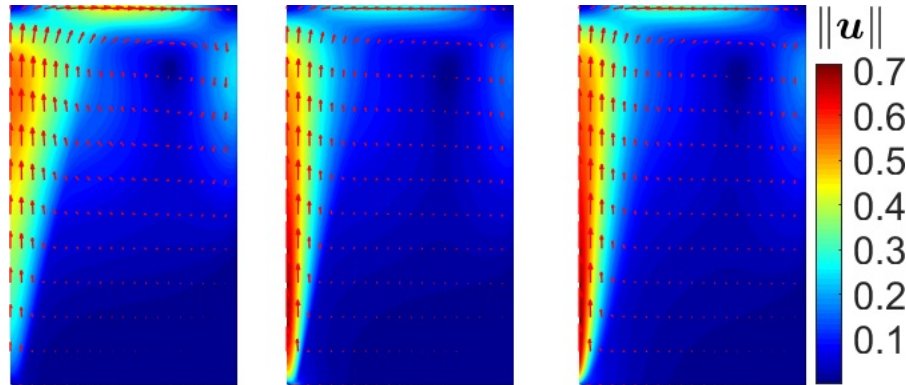


Figure 3.13: Velocity fields obtained using the $k - \epsilon$ turbulence model in COMSOL (Alia et al., 2019a). Left to right: α_1 , α_2 , and α_3 .

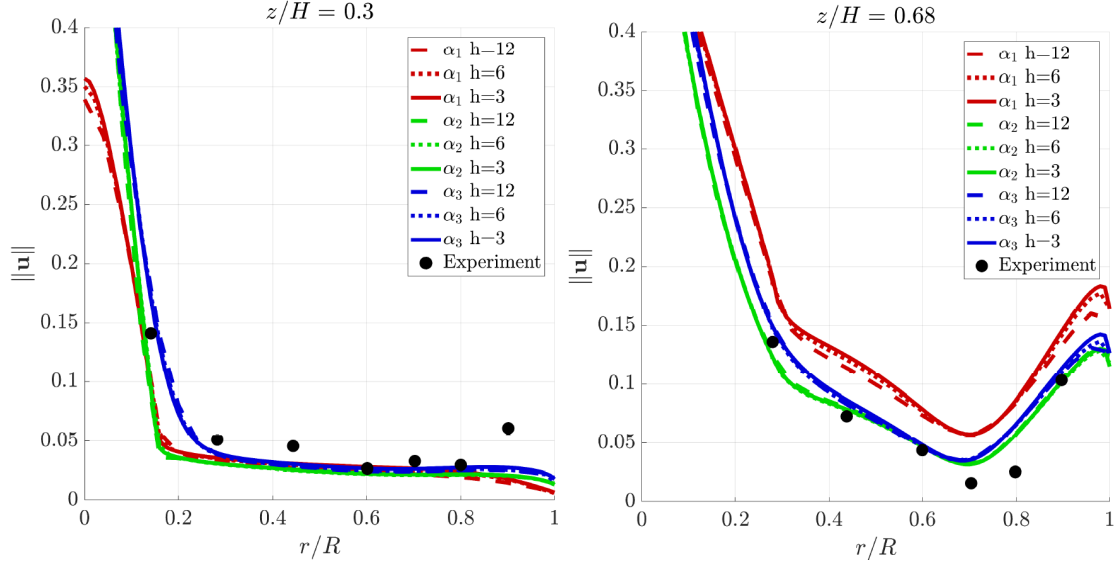


Figure 3.14: Results obtained using the $k - \epsilon$ turbulence model in COMSOL (Alia et al., 2019a): comparison of the Euclidean norm of the velocity at two different heights of the bath.

This can be done with, for example, Particle-Image-Velocimetry, see (Wuppermann et al., 2012, Owusu et al., 2019). Such an experiment, not foreseen in this work and whose equipment is available only in specialized laboratories, would have led to a more exhaustive comparison of the numerical models with the physical reality, and would have made the correction of the models according to experimental measurements easier.

The results presented in the previous section (axisymmetrical model with $k - \epsilon$ made by (Alia et al., 2019a)) seem to be the closest to the experimental measurements. The models using the Smagorinsky turbulent viscosity do not agree so well with the measurements, at least at the top line $z/H = 0.68$.

Coming to the applicability to real three-dimensional ladles, the boundary-driven ladle can not be reasonably extended to 3d: a boundary-driven surface is for sure not a correct modeling of ladle stirring. Therefore, the 3d ladle has to be modeled using the volume force. This modeling approach is more realistic and can also simulate different number and position of gas plumes in the liquid. As shown in the results of the axisymmetric case and the work from (Alia et al., 2019a), the gas fraction α_2 is physically more relevant than α_1 . Furthermore, it slightly improves the convergence of the nonlinear iterations in comparison to α_3 . This confirms that this gas fraction, as defined in Eq. (3.15), is a relevant choice for the 3d model.

3.4 Numerical results in 3d

3.4.1 Implementation

The space and time discretizations are similar to the ones in 2d. The geometry is meshed with tetrahedra and the conforming pair of FE P_2/P_1 has been used. The mesh size and number of degrees of freedom are given in Table 3.8.

Concerning the computational cost, it is well-known that the 3d time-dependent Navier–Stokes equations are quite expensive. This is due, on the one hand, to the high number of degrees of freedom, and, on the other hand, to the structure of the problem to be solved (saddle point problem). The computational time is often a bottleneck in the simulations of real-life flow problems. The solver and its parameters have to be chosen with special care in order to optimize its performance and minimize the computational time. The most interesting solvers for the current application are the direct solver MUMPS for coarse meshes, and the iterative solver FGMRES with a LSC preconditioner for finer meshes (Section 2.4). All the solvers used in the 3d application are run in parallel mode on distributed memory multiprocessors using MPI (Message Passing Interface). A preliminary study with several meshes of different sizes (very coarse to very fine) was made to check starting from which mesh, the iterative solver FGMRES with LSC preconditioning becomes more efficient than the direct solver MUMPS. It was found that, for the meshes in Table 3.8, FGMRES+LSC performs better.

In order to further reduce the computational cost while keeping a reasonable numerical precision, the following solver’s parameters have been chosen:

- the nonlinear iterations are stopped when the Euclidean norm of the residual vector is below 10^{-5} ,
- another stopping criteria is also used: 20 nonlinear loops maximum (in fact, the first criterion was always fulfilled before),
- a damping factor (0.5) is used in the nonlinear iterations to improve convergence,
- the residual tolerance for the iterations of the FGMRES solver is set to $8 \cdot 10^{-6}$, and the maximum number of iterations is 10,
- the velocity subproblem is solved using a Bi-CGStab iterative solver with SSOR preconditioner (residual tolerance 10^{-8} and maximum iterations number 100),
- the matrix blocks corresponding to the divergence constraint were scaled with the time step to improve the matrix conditioning,
- the pressure subproblem is solved with the direct solver MUMPS.

Table 3.8: Mesh parameters. The abbreviation “Dof” refers to the number of degrees of freedom.

Mesh abbreviation	71k	138k	274k
Number of cells	71 042	137 805	273 593
Min/max cell size	0.0147/0.068	0.014/0.053	0.012/0.046
Dof \mathbf{u}	314 742	594 216	1 147 554
Dof p	14 182	20 169	49 346
Dof total	328 929	620 385	1 196 900

In this real-life application, an exact (analytical) solution is not known. Furthermore, the measurements' errors of the experiment, which we compare our results with, are not given in (Palovaara et al., 2018). For these reasons, a tolerance of 10^{-5} was considered to be sufficient. This leads to substantial savings in the computational time in comparison to more precise solutions. Finally, the solvers are run in parallel on several Intel® Xeon® 2.7 GHz processors: 8 cores for mesh 71k, 20 for 138k, and 40 for 274k. The average time for one nonlinear iteration was around 8 s for each case (~ 2 days for a whole computation).

Concerning the time range, a high final time was chosen to let the initial development of the flow finish, similarly to the 2d applications. However, since the computations take much more time, T is fixed to 200 instead of 600 s. As the results will show later, this is long enough. The time step is $\Delta t = 0.01$ s.

3.4.2 Preliminary study with $Re = 1$

The question of the turbulence model arises again. Indeed, unlike the 2d case, where the boundary-driven configuration could be resolved at high Reynolds number without any stabilization, a 3d flow problem shows turbulent features already at Reynolds number of the order of a few hundreds (John, 2016). One can choose between the $k - \epsilon$ turbulence model (in COMSOL, (Alia et al., 2019a)) or the Smagorinsky turbulent viscosity (in PARMOON). Before presenting the results of these models, a test case is performed at low Reynolds number ($Re = 1$) and without any turbulence model. This laminar flow can be used to verify that the results of both softwares are the same without turbulence models.

One obtains a stationary solution after a few time steps (0.39s). The vertical component of the velocity at the middle line of the gas plumes is shown in Figure 3.15. The perfect agreement between both softwares confirms that the single-phase models solved in both softwares are the same. Therefore, the difference which will be observed in the case $Re = 96000$ can be attributed to the choice of the turbulence model.

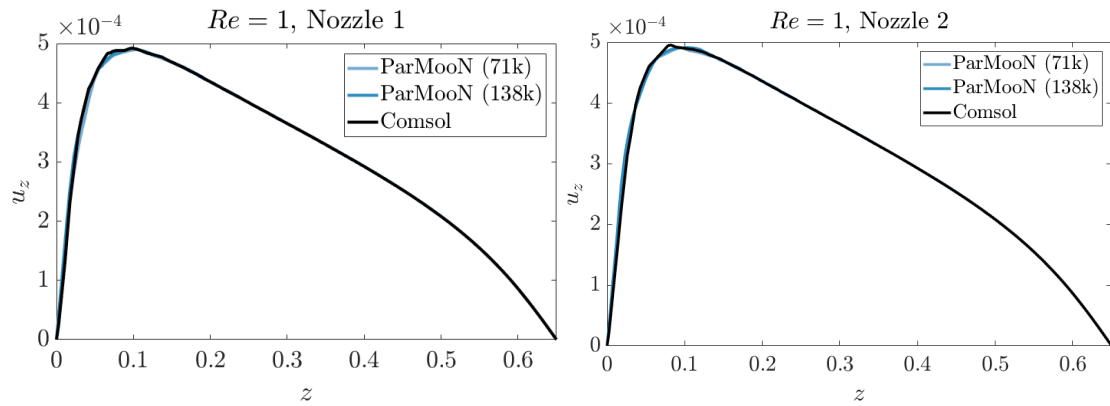


Figure 3.15: Vertical component of the velocity u_z along the vertical line at the middle of the (fictive) gas plumes, obtained with PARMOON and COMSOL. Case $Re = 1$. Left: $u_z(x_{n1}, y_{n1}, z)$ at nozzle 1. Right: $u_z(x_{n2}, y_{n2}, z)$ at nozzle 2.

3.4.3 Numerical results

The real turbulent flow is solved with six different values of the Smagorinsky constant $C_S = 0.00025, 0.0005, 0.001, 0.002, 0.005$, and 0.01 . With smaller C_S , the solution blew up. The velocity field at different time steps is illustrated in Figure 3.16. As expected, the volume force produces the desired gas plume effect: an upward flow is generated from the position of the nozzles at the bottom to the top surface, and its radius expands with z . After a transitional regime, the flow is fully developed with velocity fluctuations rising from the bottom to the top around the gas plumes, and spreading down in the domain once they reach the top boundary. The flow can be compared with the results obtained by (Alia et al., 2019a) with the $k - \epsilon$ turbulence model, reproduced in Figure 3.17. Here, the flow evolves slowly without fluctuations until a stationary solution is reached at around 150 s. In both cases, the order of magnitude of the velocity in the final regime is between 0.3 and 0.5 m s^{-1} . In the first seconds of the transitional phase, the velocity can exceed 0.6 m s^{-1} . A more quantitative comparison is performed in the next paragraphs.

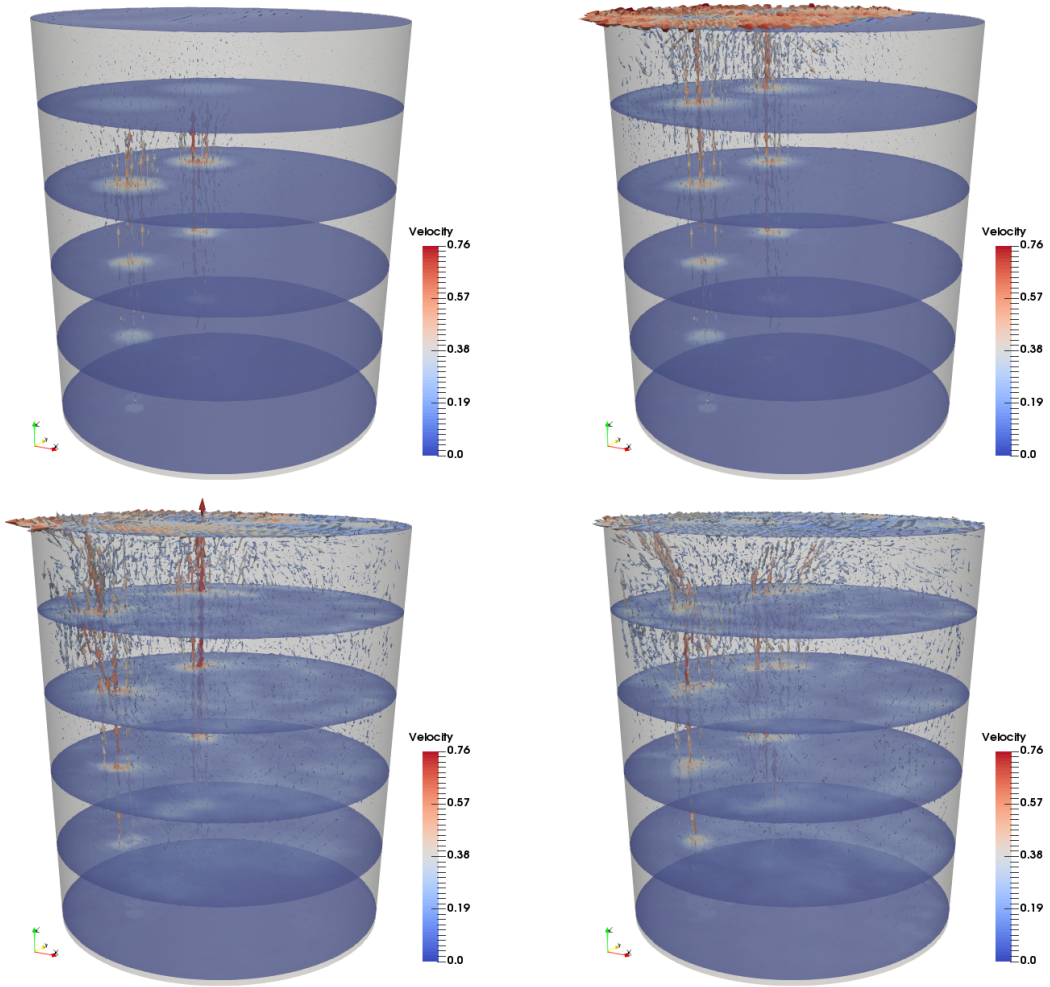


Figure 3.16: Snapshots of the velocity field obtained with PARMOON at $t = 1.2, 2.4, 16$, and 24 s, with mesh 138k and $C_S = 0.0005$.

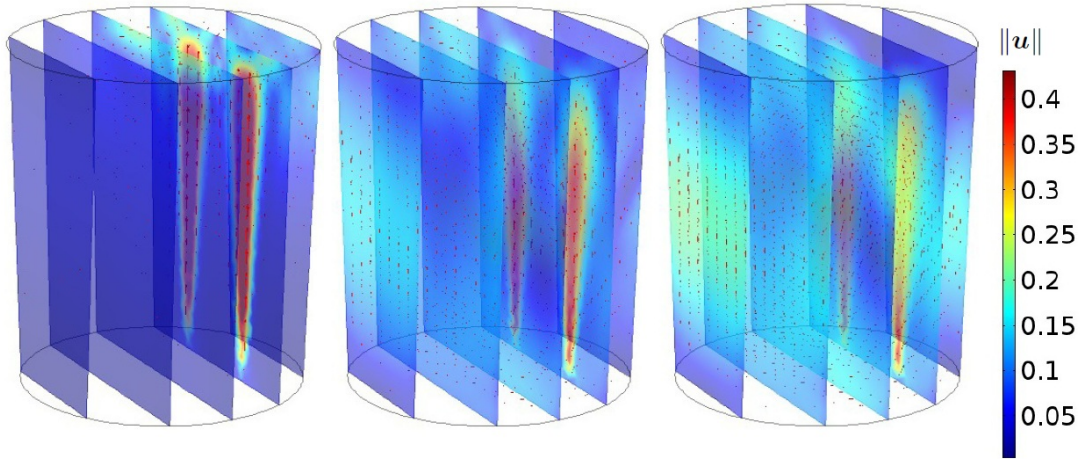


Figure 3.17: Snapshots of the velocity field obtained with COMSOL at $t = 2\text{s}$, 25s , and 200s , with the $k - \epsilon$ turbulence model (from (Alia et al., 2019a)).

Similarly to the axisymmetric case, the velocity computed with the Smagorinsky model in PARMOON needs to be averaged in time for the comparison. First, the distinction between transitional and stable regime has to be determined in order to choose a suitable time range for the computation of the mean velocity. The evolution of the velocity in time at two points of the gas plume is given in Figure 3.18. The results have been restricted to these two points, the mesh 138k and two values for C_S because the other configurations follow the same tendency and do not bring any additional information regarding the transitional and final regime of the flow. One can identify three phases or regimes:

- a first stable phase where the velocity reaches a nominal value very quickly in the gas plume ($\sim 1\text{s}$), and then remains constant until $\sim 20\text{s}$,
- a turbulent phase with a decreasing tendency between ~ 20 and $\sim 80\text{s}$, and
- a final turbulent regime where it is difficult to observe a clear periodicity.

The first two phases can be considered as the transitional regime, while the last phase seems to correspond to a final regime. Therefore, the time range $[100, 200]$ has been chosen to compute the average of the velocity.

Figure 3.19 compares the resulting vertical velocity at the central line of the gas plumes with the experimental measurements found in (Palovaara et al., 2018) and with the results of Alia et al. (2019a) ($k - \epsilon$ model on COMSOL). The velocity profile obtained with both models are relatively close to the experimental measurements and to the observations from (Mazumdar and Guthrie, 1995a): starting at a high value close to the nozzle (jet zone dominated by the kinetic energy of the gas), it slowly decreases a few decimeters above the nozzle and remains constant in most of the bath height (plume zone dominated by the buoyancy energy). The decrease close to the surface is due to the boundary condition and is observed with all models. In most cases, the Smagorinsky model seems to slightly overestimate the actual plume velocity measured experimentally, while the $k - \epsilon$ model underestimates it. A small difference can also be observed between the two nozzles, although the volume force is symmetric and the same gas fractions is applied. This difference may be attributed to the mesh and/or the velocity fluctuations.

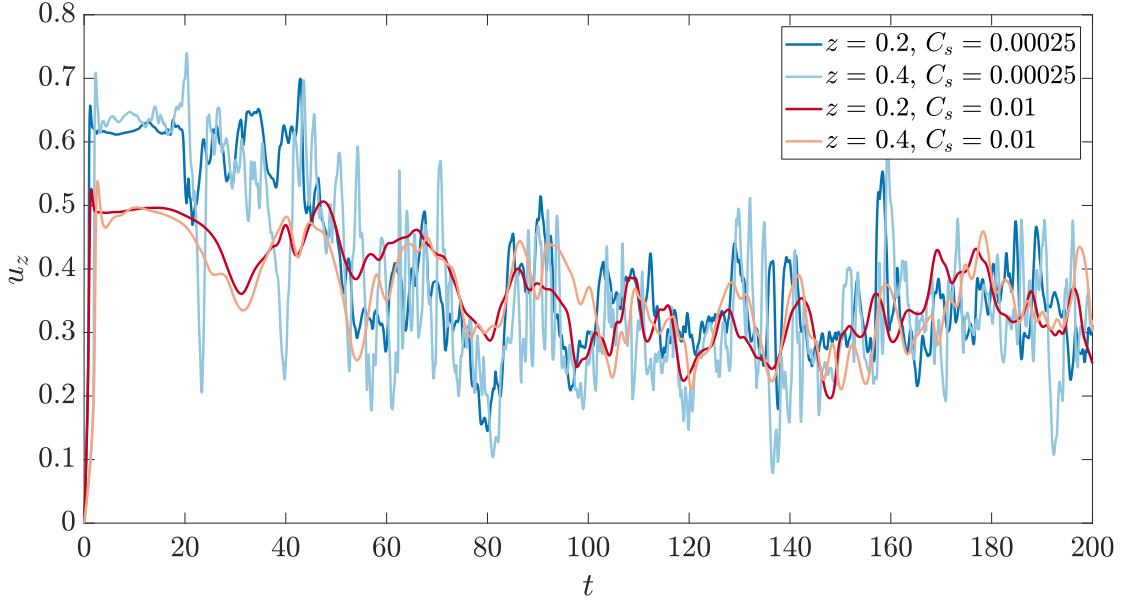


Figure 3.18: Time evolution of the vertical velocity at different heights above nozzle 2 (x_{n2}, y_{n2}) with mesh 138k.

Coming to the dependency of the solution on the mesh and on C_S , it can be seen that the difference between the results are not as significant as in the 2d axisymmetric case (Figure 3.11). If finer meshes sometimes lead to an increase in the velocity magnitude ($C_S = 0.00025$), in most cases, the solution does not change very much with respect to the mesh size. A similar observation can be done regarding the Smagorinsky constant. Increasing C_S from 0.00025 to 0.002 or 0.005 (not represented in Figure 3.19) does not change the plume velocity in a perceptible way. Only with a higher turbulent coefficient ($C_S = 0.01$), a change in the velocity profile in the height can be noticed. In this case, and using the coarser meshes, the velocity tends to stay constant all along the bath height, i.e., without the small decrease observed experimentally at $z \approx 0.1$, or the one which starts at $z \approx 0.5$.

Contrary to the axisymmetric case, the turbulent model does not lead to large and periodic structures. Increasing C_S does not “damp” the flow, as in the axisymmetric case. The Smagorinsky turbulence model induces indeed a different behavior between the 2d (or more precisely “2.5d”) and 3d ladles. While in 2d, large eddies (vortices) are built and formed by successive and progressive merging of smaller eddies, in 3d, there are no large vortices: the big flow structures are destroyed by turbulence, because the energy goes from large to small scales (Schroeder et al., 2019). This is the behavior described in Section 2.5.1.

In Figure 3.19, one can identify a few configurations where the numerical results match the experimental measurements the best, like in the axisymmetric model. For example, with $C_S = 0.001$ or $C_S = 0.0005$ and mesh 138k. The small turbulent constant $C_S = 0.00025$ is also a reasonable choice, but seems to be slightly more sensitive to the mesh size.

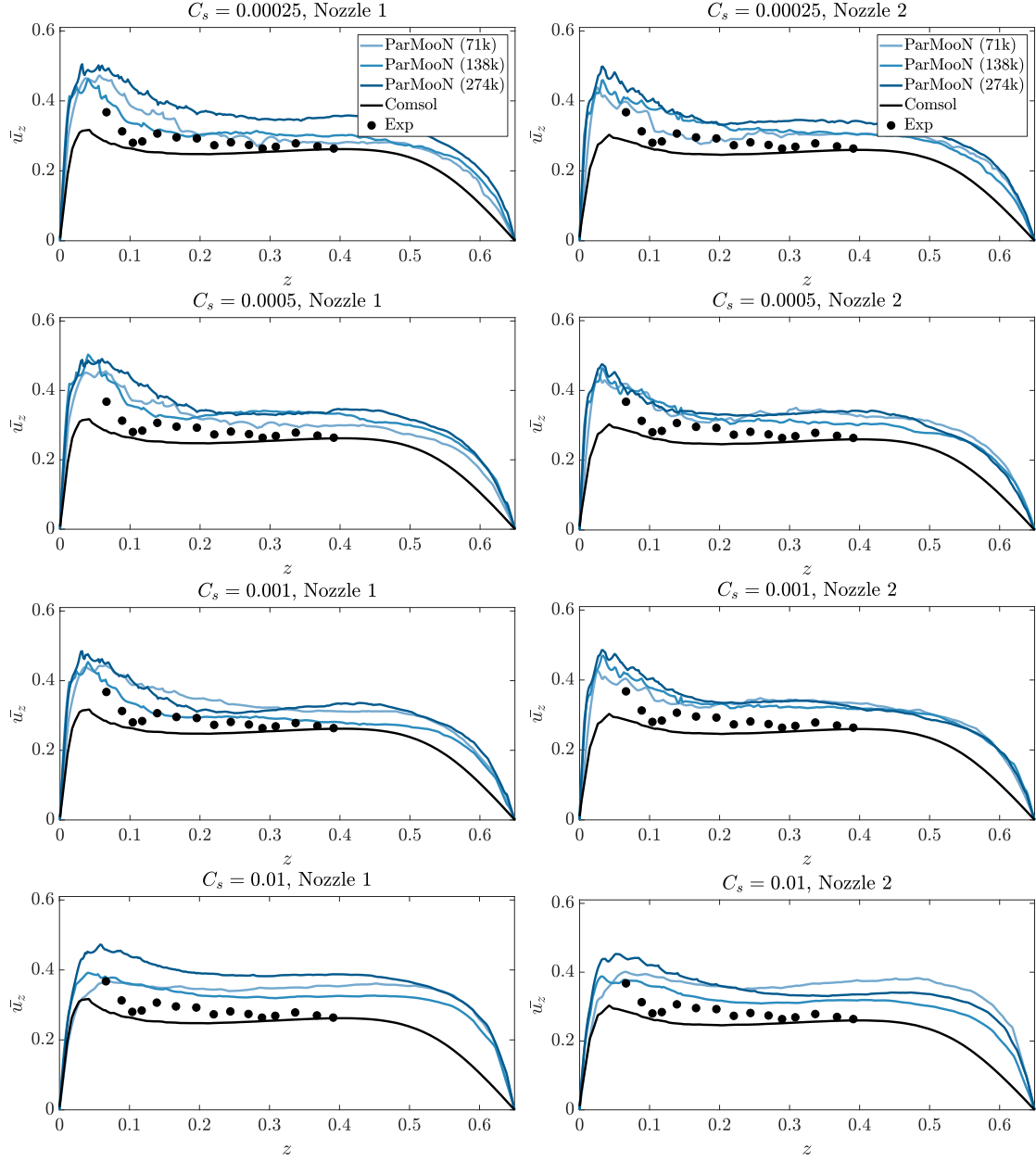


Figure 3.19: Comparison of the time-averaged vertical velocity \bar{u}_z between PAR-MOON, COMSOL (with the $k - \epsilon$ turbulence model), and the experimental measurements, for different meshes and values of C_s . Case $Re = 96000$. Left: nozzle 1, $u_z(x_{n1}, y_{n1}, z)$. Right: nozzle 2, $u_z(x_{n2}, y_{n2}, z)$.

Altogether, the solution computed with the Smagorinsky and the $k - \epsilon$ turbulence models agree quite well with experimental observations. If the stationary solution obtained with the $k - \epsilon$ model in COMSOL agrees well with the mean velocity measurements, it still slightly underestimates them and it lacks of physical realism, because the actual flow is clearly not stationary. From this perspective, the Smagorinsky model captures better the velocity fluctuations induced by the turbulence. On the other hand, the choice of an appropriate Smagorinsky constant C_S is not straightforward and is based on trial and error. However, the $k - \epsilon$ model also has several constants which need to be chosen. Note that, since the default values gave reasonable results, a fine-tuning of these parameters was not necessary. Concerning the sensitivity of the solution to the mesh, it was observed that both turbulence models yield similar results from one mesh to another. In COMSOL, the results obtained with two meshes match almost perfectly (Alia et al., 2019a), although the $k - \epsilon$ turbulence equations are convection-dominated and require stabilization. Like most stabilization methods, the solution is likely to depend on the stabilization parameters and on the mesh. It is unclear how the choice of the stabilization parameters is done internally in the software, and whether it plays a role on the fact that the solution seems to be independent of the mesh with the $k - \epsilon$ turbulence model.

3.5 Conclusion

Summary. Three single-phase models for ladle stirring have been studied:

1. a 2d boundary-driven model in Cartesian frame,
2. a “2.5d” axisymmetric model with three different gas fractions, and
3. a 3d model based on one of the gas fraction α .

The boundary-driven cavity model converges numerically without the need of any stabilization or turbulence models and leads to a periodic solution. Moreover, the computed velocity at two horizontal lines across the domain has the same order of magnitude as experimental measurements. These properties are relevant for an application in optimal control problems. However, the physical relevance of the model is questionable, and numerical optimization of the boundary-driven model may not reflect the actual optimal solution of a real ladle stirring. Furthermore, it is not possible to use this approach in 3d. It should thus be used in the context of numerical optimization with restricted perspectives about industrial application. The present study also delivers useful information for the optimal control problem, e. g., the initial solution, the time range, and the mesh to employ.

Concerning the axisymmetric models, the gain of physical realism using the axial-symmetry is lost by the choice of numerical parameters which have a significant impact on the solution, for instance, the Smagorinsky constant and the gas fraction α . This leads to various solutions, which can be, furthermore, mesh-dependent. If the flow is dampened enough, the results between the meshes and the volume forces are quite similar, but remain different from the solution of the boundary-driven ladle. The apparition of dead zones in the axisymmetric model is dependent on the numerical parameters. Optimizing such a flow can therefore lead to different conclusions, depending on C_S or the mesh. This is not suitable for the industrial practice. Thus, the main usage of axisymmetric models is to study

the gas fractions α in order to choose the most suitable one for 3d applications. Since α_2 gives a better order of magnitude than α_1 and converges easier than α_3 , it was considered as the best choice for the 3d application.

The 3d ladle with the Smagorinsky turbulence model shows that the velocity over the nozzles can be in good agreement with experimental measurements, almost independently of C_S and the mesh. The present study highlights and validates the physical realism of the 3d model, although it is a simplified single-phase flow where the gas bubbles are not taken into account explicitly. It can therefore be a reasonable model to be used in optimization. Its computational cost is much higher than the 2d models, but remains cheaper than a multiphase flow model. As in the boundary-driven case, the present computations also deliver valuable information for optimization purposes. For example, the mesh 138k is a reasonable choice because it has led to the best results. If the initial solution can be taken in the range $[100, 200]$, there is still some discrepancy from one time step to another (Figure 3.18). Therefore, it is necessary to check the sensitivity of the optimal solution with respect to the initial state of the flow. Concerning the time range, one may need a minimum range of 20 s, so that it corresponds to at least one of the “periods” in Figure 3.18 (most clearly visible for $C_S = 0.01$). Again, it is recommended to study the sensitivity of the optimal solution with respect to T .

Another important conclusion which comes out of this study is the importance of having one’s own experimental set-up and exhaustive measurements, e. g., several quantities at different points of the ladle. Furthermore, the evolution of the velocity in time is of particular importance to facilitate the choice of the turbulent model and parameters.

Outlook to two-phase flows for ladle stirring. Performing a multiphase simulation of ladle stirring rises anew the question of modeling: there are indeed a lot of possible multiphase models for gas-liquid bubbly flows. One family of models is based on fixed, rather than moving, grids. Typical examples are the *Volume Of Fluid (VOF)* and the *Level-Set (LS)* models. In such methods, the phases are identified by a *phase function*, which has values between 0 and 1. Ladle stirring can then be described by the following equations:

$$\begin{aligned}
\rho \mathbf{u}_t + \rho(\mathbf{u} \cdot \nabla) \mathbf{u} - 2\nabla \cdot (\mu \mathbb{D}(\mathbf{u})) + \nabla p &= \mathbf{f} && \text{in } (0, T] \times \Omega \\
\nabla \cdot \mathbf{u} &= 0 && \text{in } (0, T] \times \Omega \\
\mathbf{u} &= \mathbf{0} && \text{in } (0, T] \times \Gamma_{\text{wall}} \\
\mathbf{u} &= \mathbf{b} && \text{in } (0, T] \times \Gamma_{\text{in}} \\
\mathbb{S} \cdot \mathbf{n} &= \mathbf{0} && \text{in } (0, T] \times \Gamma_{\text{out}} \\
\rho &= \rho_g \varphi + \rho_l (1 - \varphi) \\
\mu &= \mu_g \varphi + \mu_l (1 - \varphi), \\
\varphi_t + (\mathbf{u} \cdot \nabla) \varphi &= 0 && \text{in } (0, T] \times \Omega \\
\varphi &= 1 && \text{in } (0, T] \times \Gamma_{\text{in}} \\
\nabla \varphi \cdot \mathbf{n} &= 0 && \text{in } (0, T] \times \Gamma_{\text{out}} \cup \Gamma_{\text{wall}} \\
\varphi(0, \mathbf{x}) &= \varphi^0(\mathbf{x}) && \text{in } \Omega \\
\varphi &\in [0, 1] && \text{in } (0, T] \times \Omega.
\end{aligned}$$

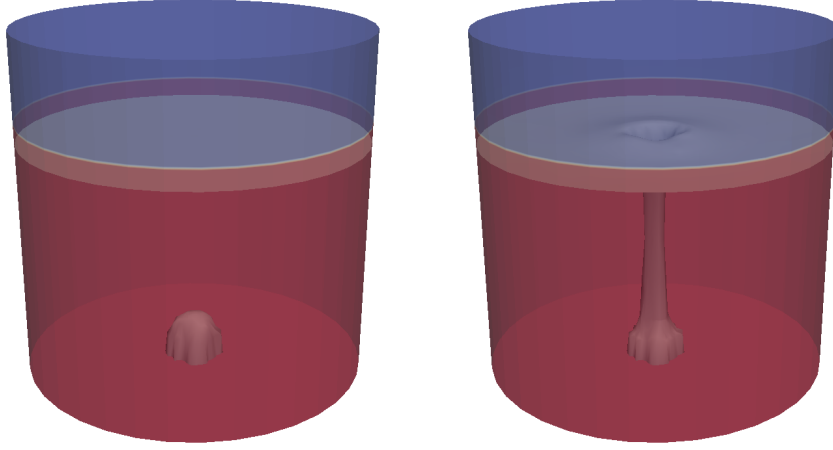


Figure 3.20: Illustration of a 3d two-phase flow for ladle stirring with one central nozzle on a coarse grid, based on the VOF method. The fluid properties do not correspond to the physical ones.

The first part corresponds to the incompressible Navier–Stokes equations with modified density, modified viscosity, and with inflow and outflow conditions for the gas phase. The second part is a convection equation which describes the evolution of the phase fraction φ and with a boundary condition for the gas injection. The initial condition is also important because it gives the distribution of the phases at the beginning of the process. The flow is induced by a normal boundary velocity \mathbf{b} at the porous plug Γ_{in} . It represents the velocity of the injected gas and is related to the physical gas flow rate $Q(t)$. The force \mathbf{f} corresponds to the gravity and the surface tension between gas and liquid. The gas outflow is described by a Neumann boundary condition at the top surface Γ_{out} . The model has been implemented and briefly explored during the thesis. The convection equation was stabilized with the state-of-the-art Algebraic Flux Correction scheme, and the Smagorinsky turbulence model was applied. One important problem which is still unsolved concerns the blow-up of the solution when real fluid properties are applied. In this case, the ratio between gas and liquid properties is of the order 1000. Further work is required, in particular regarding what happens on the gas-liquid interface. Figure 3.20 represents a 3d two-phase flow computed with the code PARMOON with a ratio 100 for the densities of the phases, and viscosity 1.

Modeling ladle stirring with two-phase flows is a natural extension of the work done with the single-phase approach. In particular, it enables to verify two important assumptions:

- if the two-phase models are significantly more expensive than single-phase ones in terms of computational time and memory,
- if they are more accurate in describing the bulk flow.

As it will be discussed in Section 4.6 and 5.4, a multiphase approach may be a more appropriate choice for optimal control problems and fluid-structure interactions.

The next chapter focuses on the application of the 2d boundary-driven and 3d models in the context of optimal flow control.

4. Optimal flow control in the ladle

Motivation. The improvement of ladle stirring control is a well-known need in the industry. The term “control” can be understood in terms of steel process. It refers to the physics of stirring, e. g., how to mix the bath to obtain the required steel quality. It can also be understood in terms of technical solution, i. e., how the operators can adjust the stirring. While the latter is discussed in the last chapter (Chapter 5), the optimal process control is the main focus of this chapter.

In the metallurgy literature, optimization studies consist in varying a small number of parameters (ladle geometry, gas nozzle position, gas flow rate, etc.) over a small, discrete set of values, computing or measuring the stirring performance (e. g., mixing time), and extrapolating the results. However, optimal control problems in the mathematical sense have not been explored very much yet in this area. Thus, the modeling approach and numerical results presented in this chapter can be considered as a new contribution to scientific research.

The following questions are addressed in detail in this chapter: how to formulate, physically speaking, the goals of stirring, along with the process control and constraints ? how to translate them into mathematics? Besides the modeling aspect, the numerical results of the optimal control model and their applicability in the industrial practice are discussed.

Outline. First, the objectives and constraints in the industrial practice have to be clearly defined. We use the terms *industrial*, *practical*, *physical*, or *process* equivalently. It is important to emphasize on the close cooperation with the industry, which allowed to define the practical objectives and constraints. In the introductory section (4.1), we discuss the information gathered from the industrial practice. Second, the mathematical modeling of the control variables and the cost functionals is presented (Section 4.2). Mathematically, the objective is to minimize the costs. Thus, we employ the notions *cost* and *objective* functionals equivalently. The formulation of the optimal control problem and the derivation of its adjoint system is given in Section 4.3. The adjoint equations derived formally can be used as a basis for future work using gradient-based optimization solvers. In this work, the numerical results were obtained with a gradient-free method. For more clarity, the 2d and 3d results are separated in Sections 4.4 and 4.5. The main findings of this work are summarized in the conclusion (Section 4.6). In addition, the main limits of the present optimal control model are discussed and an alternative formulation is proposed for future research.

4.1 Industrial problem

Objectives. The cooperation with the steel industry reveals that several optimization goals can be defined for the stirring process. They are closely related to, if not directly repeating, each other:

- maximize temperature and chemical composition homogeneity,
- minimize the quantity and size of inclusions,
- maximize interface areas between phases,
- minimize the treatment time, and
- minimize gas consumption.

Control. Concerning the process control, it is generally agreed that the main variable parameter which controls the stirring is the gas flow rate Q . One could think of the nozzles' position as a further control of stirring. However, this idea is applicable only to the long-term perspective, since the whole ladle design has to be changed if the nozzles' positions are modified. The ladle geometry, e.g., radius/height ratio, could also be considered as a control variable for the design of new ladles. In the context of the present work, the gas flow rate is considered as the main process control, and the nozzles' position will be considered in the last numerical application in 3d.

Constraints. Furthermore, several constraints related to the steel quality and process safety are well-known:

- reach the prescribed *cleanliness*, i.e., the amount of inclusions (H, N, C, O) should be below the limit required by the steel grade,
- form a *slag eye* to allow alloying in the case of vacuum stirring,
- control the slag *emulsification* to avoid droplets' entrapment in the liquid steel,
- limit the erosion of the refractory lining in the ladle, and
- limit steel splashes and prevent overflow.

These are examples of constraints which should be taken into consideration.

In practice, the objectives can be reached using a strong stirring, also called *strong bubbling*. However, a too high value of Q can lead to some undesirable phenomena, such as steel loss due to splashes and accelerated erosion of refractory material. On the other hand, a too low value of Q , or *soft bubbling*, can be insufficient to reach the prescribed steel cleanliness, to homogenize correctly the composition and the temperature, or to keep an area open in the slag (or *open eye*) in the vacuum case. Besides these practical constraints, gas consumption should be minimized to achieve cost savings in the process. Indeed, it might be unnecessary to use constantly high flow rates to fulfill the objectives of the treatment. In sum, the optimal gas flow rate should create a balance between strong and soft bubbling to avoid the problems raised by these two situations.

Table 4.1 summarizes the main objectives and constraints of ladle stirring from the point of view of the industry. Next, we discuss them in more details. In particular, we define the (mathematical) *box constraints*, i.e., the space of admissible controls. Then, we formulate the (physical) constraints in form of inequalities which should be satisfied by the control variable. The space of admissible controls can then be reduced to physically-relevant values.

Table 4.1: Main objectives and constraints of stirring.

Process	Stirring objectives	Stirring constraints
Steel	<ul style="list-style-type: none"> - Maximize homogenization - Minimize quantity of inclusions - Minimize treatment time - Maximize steel-gas interfacial area 	<ul style="list-style-type: none"> - Reach the required steel cleanliness - Limit steel splashes - Avoid bath overflow
Slag	<ul style="list-style-type: none"> - Maximize steel-slag interfacial area 	<ul style="list-style-type: none"> - Keep an area open in the slag (open eye) for alloying - Control slag emulsification
Gas	<ul style="list-style-type: none"> - Minimize gas consumption 	<ul style="list-style-type: none"> - Min. and max. values - Smoothness
Lining		<ul style="list-style-type: none"> - Minimize wear of refractory material

4.1.1 Physical control and constraints

The process control Q is a function of time which can have different profiles, e. g., constant or oscillating. In all cases, it is bounded. We define the box constraints

$$Q_{\min} \leq Q(t) \leq Q_{\max} \quad \forall t \in [0, T].$$

These box constraints can conveniently reflect the technical or economical restrictions imposed by the process in practice.

Modeling of the constraints. Indeed, one can now take into account the stirring constraints listed in the last column of Table 4.1. If one of them is directly related to Q , the others concern general aspects of the stirring process and are of importance in the industry. For example, they guarantee the steel quality (cleanliness, open slag eye for alloying, no emulsification), the safety of the operators (steel splashes, bath overflow), and the maintenance costs (refractory erosion).

It should be noted that some of these aspects have been dealt with in the literature, leading to empirical formulas to estimate the “critical” gas flow rate corresponding to these constraints. In particular, we can define:

- the minimal and maximal amounts, Q_{\min}^t and Q_{\max}^t , which can be technically injected in the ladle, see Annex B,
- the minimal amount which enables the opening of the slag, $Q_{\text{open eye}}$,
- the minimal amount which can cause an overflow outside the ladle, Q_{overflow} ,
- and the minimal amount which can provoke slag emulsification, Q_{emuls} .

Consequently, instead of describing the constraints as additional equations in the optimal control model, it is possible to use the existing empirical formulas from the literature and include them directly in the box constraints, such that

$$Q_{\min} = \max\{Q_{\min}^t, Q_{\text{open eye}}\}, \quad (4.1)$$

$$Q_{\max} = \min\{Q_{\max}^t, Q_{\text{overflow}}, Q_{\text{emuls}}\}. \quad (4.2)$$

Discussion of the four remaining constraints. Before detailing the empirical formulas for these constraints, we consider the remaining ones. At first glance, it can be argued that the cleanliness requirement is an objective rather than a constraint. We should distinguish between the objective of the stirring process and the one of the optimization problem. In terms of process, reaching the required cleanliness is the objective of *any successful stirring*. In terms of optimization, the required cleanliness has to be reached, and it has to be with *the most efficient stirring*, e. g., with the minimum time, energy, or the maximum homogeneity, etc. This explains why this criterion is considered as a constraint here¹. Unlike the criteria cited in the previous paragraph, it was not possible to find in the literature a relation between the gas flow rate and the final cleanliness. One can choose either to model the chemical reactions to include this constraint in the optimal control problem or ignore the concentration of inclusions and this constraint. As it will be discussed later, we will consider the flow homogeneity rather than the inclusions' concentration (Sections 4.2.3 and 4.2.4). In the conclusion, we will sketch an optimal control problem based on the inclusions' content (Section 4.6.2).

Steel splashes are a cause of material loss (liquid steel deposits and solidifies on top of slag) and safety concerns, but are hard to predict. The refractory wear is also a problem. It is mainly caused by the slag and the velocities at the level of the steel-slag interface. This is where the refractory material gets the most eroded and becomes thinner. It cannot continue to withstand high temperature. Therefore, the lining has to be replaced every few weeks usually. The maintenance department is responsible for following-up the lifetime of ladle linings and replacing them according to a schedule or urgent needs. The replacement operation is costly in time and material. By applying a smoother stirring, it is possible to extend the lifetime of refractory material and generate cost savings. In practice, those two criteria are left for the operator's own experience and decision. Thanks to the camera, the operator estimates the intensity of the stirring and decides if the gas flow rate can be reduced to a more gentle stirring in order to reduce steel splashes and erode the refractory material less aggressively. In the present work, we simplify the modeling work and neglect these two constraints.

Finally, the smoothness of the gas flow rate is imposed by the gas control system. If the operators can set a value on their control screens, the system is responsible for opening and closing the valves according to prescribed rates, e. g., progressively with a linear slope (ramp). Mathematically, one would assume that $Q(t)$ is continuous, and that, for example, its time-derivative is bounded. Additionally, one can prescribe given profiles to $Q(t)$, e. g., a periodic function of time. Using the Fourier transform, it can then be expressed through its coefficients (amplitudes and frequencies), which can be chosen as control variables. If such controls may be more realistic from the physical point of view, it cannot model easily any functions of time. One could "miss" some optimal control with a more "original" profile. In this thesis, we have not considered this constraint and allowed for any type of controls Q within Q_{\min} and Q_{\max} .

¹ Furthermore, the goal of optimization models is to minimize a *cost* functional. This term describes well the fact that we want to reach the required steel grade with the minimum cost, e. g., gas consumption or treatment time.

The following paragraphs present the empirical formulas used in (4.1) and (4.2).

Definition of $Q_{\text{open eye}}$. Although several publications reported analytical and experimental results on the size of the open eye, (Yonezawa and Schwerdtfeger, 1996, Mazumdar and Evans, 2003, Subyago and Irons, 2003), the critical gas flow rate which starts opening the slag was found mainly in (Irons et al., 2015, Krishnapisharody and Irons, 2015). The following empirical result computes the gas flow rate below which no open eye forms, in soft bubbling processes:

$$Q_{\text{open eye}} = 0.135 \left[\left(\frac{\rho - \rho_{\text{slag}}}{\rho} \right) h_{\text{slag}} \right]^{1.57} H^{0.91}. \quad (4.3)$$

In vacuum conditions, this formula does not hold, since it has been developed for standard ladles. In that case, it is expected that the critical gas flow rate for slag opening is much lower than the one given by (4.3).

Definition of Q_{overflow} . The following results are based on physical considerations. In order to estimate analytically the gas flow rate Q_{overflow} above which the bath can overflow, simplifying assumptions are made:

- the free surface of the bath is flat,
- the vertical distance between the free surface and the border of the ladle is h_{fr} ,
- a constant gas flow rate Q is injected,
- the pressures at the free surface and at the bottom are p_{fr} and $p = p_{\text{fr}} + \rho g H$,
- the rising gas velocity U is constant, so that the injected gas needs H/U seconds to reach the free surface. This assumption holds usually after the initial penetration region close to the nozzle.

The gas is compressible and follows the perfect gas law: $\dot{V}_{\text{gas}} = Q \frac{p}{p - \rho g U t}$ (Wichterle, 2010, Eq. (28)). Using the dimensionless parameter $p^* = 1 + \frac{p_{\text{fr}}}{\rho g H}$, which represents the ratio of the atmospheric to the hydrostatic (or ferrostatic) pressure, the total volume of gas in the bath is

$$V_{\text{gas}} = \int_0^{H/U} \dot{V}_{\text{gas}} dt = Q \int_0^{H/U} \frac{p^*}{p^* - \frac{U t}{H}} dt = -\frac{H}{U} Q p^* \ln \left(1 - \frac{1}{p^*} \right). \quad (4.4)$$

The logarithmic term reflects the volume expansion of the compressible gas during its buoyancy. For example, in a laboratory-scale water model with $H = 0.65$, the gas volume in the bath becomes 3% higher than the volume injected. In an industrial ladle with the height of $H = 2.25$, in STP conditions (see Appendix B), the expansion of the injected volume reaches 53%. In case of vacuum ($p_{\text{fr}} = 100$ Pa), the gas volume expands with a factor of 7.3. These small examples illustrate how critical the gas expansion can be in practice, especially in vacuum ladles. The reader is referred to (Wichterle, 2010) for a simplified, yet relevant, analytical modeling of the gas bubbles behavior in a ladle.

The condition to avoid overflow can now be written as

$$\begin{aligned} \pi R^2 H + V_{\text{gas}} &\leq \pi R^2 (H + h_{\text{fr}}), \\ \iff Q &\leq Q_{\text{overflow}} = -\pi R^2 \frac{h_{\text{fr}}}{H} U \left[p^* \ln \left(1 - \frac{1}{p^*} \right) \right]^{-1}. \end{aligned} \quad (4.5)$$

Note that this is only a rough estimate. In practice, the gas velocity is unsteady, the free surface is not flat and several parameters, such as bubbles merging and breakup, high temperature, and actual geometry, have to be taken into account for a more realistic overflow constraint. Although overflowing phenomena happen more frequently in vacuum conditions than in standard ladles, they are generally rare in practice.

Definition of Q_{emuls} . Slag emulsification is studied in (Sulasalmi et al., 2009, 2015, Wei and Oeters, 1992, Xiao et al., 1987), among others. (Xiao et al., 1987) proposes a criteria based on the Weber number for the emulsification threshold,

$$\text{We} = \frac{U_e^2 \rho_{\text{slag}}}{\sqrt{\tau g(\rho - \rho_{\text{slag}})}} \geq 12.3,$$

where τ is the interface tension between steel and slag and U_e the critical liquid velocity above which slag emulsification occurs. Its formula reads

$$U_e = \left(12.3 \frac{\sqrt{\tau g(\rho - \rho_{\text{slag}})}}{\rho_{\text{slag}}} \right)^{1/2}.$$

The corresponding gas flow rate Q_{emuls} can be computed from U_e using Eq. (3.9):

$$Q_{\text{emuls}} = \left[\frac{U_e}{4.5} \left(\frac{R}{H} \right)^{1/4} \right]^3. \quad (4.6)$$

Note that these formulas have been derived only for standard treatments. The slag emulsification and entrapment in vacuum conditions needs further investigation.

Summary. The order of magnitude of Q_{min} and Q_{max} can now be estimated in both laboratory and industrial cases. Table 4.2 lists the parameters' values of the laboratory and industrial conditions and Table 4.3 summarizes the values of the possible box constraints. One can observe different orders of magnitude, especially between Q_{overflow} and Q_{emuls} . It should be noted that the criteria are theoretical and their validity is restricted to the specific cases studied in the corresponding publications. Therefore, these values have to be considered as very rough estimates, whose only purpose is to exclude unrealistic values from the optimization study.

Table 4.2: Parameters' values in laboratory and industrial conditions assumed for the computations of the box constraints Q_{min} and Q_{max} (Table 4.3) (note: oil is used to imitate the slag in laboratories).

	H (m)	R (m)	U (m s ⁻¹)	h_{slag} (mm)	h_{fr} (m)	ρ (kg m ⁻³)	ρ_{slag} (kg m ⁻³)	τ (N m ⁻¹)
Laboratory	0.6	0.3	1	40	0.1	1000	880	0.07
Industry	2.25	1.4	1	80	0.5	7000	3000	1.15

Table 4.3: Values for the box constraints in laboratory and industrial conditions, given for one nozzle, expressed in l min^{-1} in STP conditions. Note: the more severe vacuum case was used for the overflow criterion.

	Q_{\min}^t	Q_{\max}^t	$Q_{\text{open eye}} (4.3)$	$Q_{\text{overflow}} (4.5)$	$Q_{\text{emuls}} (4.6)$
Laboratory	0	35	1	2700	17
Industry	0	750	49	2500	140

The overflow criteria Q_{overflow} falls out of the technical range of the gas flow rate. If the analytical formula (4.5) might be too simplistic, the overflow phenomena occurs nevertheless only extraordinarily, as mentioned earlier. Hence, it is reasonable to find such a high value and to exclude it from the box constraints. Only two constraints fall inside the technical range of gas flow rate: the opening of the slag eye and slag emulsification. The gas flow rate for the eye opening $Q_{\text{open eye}}$ is relatively close to the technical minimum Q_{\min}^t , whereas the one which induces slag emulsification, Q_{emuls} , is lower than the maximum limit Q_{\max}^t in both cases. However, in industrial ladles, the gas flow rate is most of the time operated at values higher than $Q_{\text{emuls}} = 140 \text{ l min}^{-1}$, which makes this estimate unrealistic for an upper bound, at least in the industrial case.

Therefore, based on this discussion and on the definition of Q_{\min} and Q_{\max} (Eqs (4.1) and (4.2)), the following box constraints are suggested:

- a box constraint for laboratory ladles, which takes into account the open eye criteria as a minimum bound ($Q_{\min} = Q_{\text{open eye}} = 1 \text{ l min}^{-1}$), and slag emulsification as an upper bound ($Q_{\max} = Q_{\text{emuls}} = 17 \text{ l min}^{-1}$):

$$\begin{aligned} Q_{\text{open eye}} &\leq Q(t) \leq Q_{\text{emuls}} & \forall t \in [0, T], \\ 1 &\leq Q(t) \leq 17 & \forall t \in [0, T], \end{aligned} \quad (4.7)$$

- and a box constraint for industrial ladles, which takes into account the open eye criteria as a minimum bound ($Q_{\min} = Q_{\text{open eye}} = 49 \text{ l min}^{-1}$), and the technical limit as an upper bound ($Q_{\max} = Q_{\max}^t = 750 \text{ l min}^{-1}$):

$$\begin{aligned} Q_{\text{open eye}} &\leq Q(t) \leq Q_{\max}^t & \forall t \in [0, T], \\ 49 &\leq Q(t) \leq 750 & \forall t \in [0, T]. \end{aligned}$$

These inequalities are an example of values for the industrial case, but they are not used in this dissertation.

Thanks to this preliminary work, the control variable is now formulated such that it should already satisfy some of the process constraints discussed in Section 4.1, without needing a detailed multiphase model of the slag and the gas phases. The control range excludes now undesirable physical phenomena and has become smaller. This was possible thanks to the existing empirical formulas and criteria derived in the literature specially for the industrial purpose. The next section focuses on the objectives of the optimal control problem.

4.1.2 Physical objectives

The variety of the stirring objectives in Table 4.1 can be explained by the different situations encountered in practice, depending, e. g., on the initial and final inclusions' content (sulfur, carbon, oxygen, hydrogen, and/or nitrogen), and the treatment time. Indeed, these parameters vary sometimes because of different production schedules or small variations in the previous steps. Thus, the performance of stirring has to adapt to these situations, (Nadif et al., 2011, p. 2). For example:

- if the treatment time is fixed, one aims at minimizing the inclusions' content.
- if there is no constraint on the production schedule, and if the initial and final contents are in usual ranges, the target would be to reduce the treatment time. In other words, the stirring should allow to gain some time.

The interfacial areas between steel, slag, and gas also play a role in the chemical reactions and removal of inclusions. In addition, temperature homogeneity and gas consumption are underlying objectives of the stirring, which should be optimized.

In the metallurgy community, one often uses an “all-in-one” term to designate these objectives: the *stirring, or mixing, efficiency*.

Review of the stirring efficiency. It is defined in (Cloete et al., 2009) as:

“both the quantity and the effective distribution of kinetic energy within the ladle. [...] Sufficient mixing in all regions of the steel melt ensures thermal and concentration homogenization, as well as effective inclusion removal.”

This definition reflects the process objectives discussed previously. Indeed, maximizing the stirring efficiency should maximize the thermal and chemical homogenization, and minimize the inclusions, the treatment time, the gas consumption, and so on. In practice, the stirring efficiency should also be measurable, if not in industrial, then at least in experimental conditions. Thus, instead of using directly the kinetic energy as a measure of stirring efficiency, several publications have proposed alternative quantities, which are more or less equivalent, e. g.:

- the mixing power,
- the bulk liquid recirculation rate, and
- the mixing time.

(Turkoglu and Farouk, 1991) define the mixing power as the sum of the gas kinetic and buoyancy energy $\frac{1}{2}\rho_g QU^2 + \rho_g QR_g\Theta \ln(1 + \frac{H\rho_g}{p_{fr}})$. The first term is the rate at which the gas jet transfers kinetic energy to the bath, where ρ_g is the gas density, Q the inflow rate, and U the gas velocity at the nozzle exit, respectively. The second term is the energy input to the system in unit time due to the work done by the buoyancy force, where R_g , Θ , ρ and p_{fr} are the universal gas constant, the temperature, the liquid density, and the atmospheric pressure, respectively. The logarithmic term describes the change in gas density due to the elevation, similarly to Eq. (4.4). Based on experimental and numerical results, a lot of papers proposed to express the stirring power in relation to process parameters, see the review (Mazumdar and Guthrie, 1995b).

The bulk liquid recirculation rate has been defined by (Turkoglu and Farouk, 1991) as “the total amount of liquid flowing upward (or downward) through the horizontal mid-plane”. For example, (Balaji and Mazumdar, 1991) apply the following formula: $\frac{\int_0^H \int_0^R \sqrt{u_r^2 + u_z^2} 2\pi r dr dz}{\int_0^H \int_0^R 2\pi r dr dz}$, which corresponds to the normalized L^1 -norm of the velocity in cylindrical coordinates.

The mixing time is a practical and measurable way to describe when chemical homogeneity has been reached in the ladle. (Turkoglu and Farouk, 1991) define it as “the time taken for the tracer concentration to attain, at every nodal location in the system, a value within $\pm 5\%$ of the tracer concentration of the well mixed steady state bath”. In other words, the bath is considered to be homogeneous when, everywhere in the bath, the tracer concentration is within 5% of its steady-state concentration. Sometimes, a criteria of 2.5% is applied. In laboratory experiments, the tracer can be some acid or colorant and its concentration is measured for example with a pH-meter. The stirring is considered to be good when the mixing time is low. It is interesting to note that, in their study, (Turkoglu and Farouk, 1991) obtained a similar behavior between mixing time and liquid recirculation rate. They conclude that both of them can be equivalently used to describe stirring efficiency. Similarly to the stirring power, a lot of studies proposed empirical formulas to express the mixing time in terms of process parameters, e. g., (Patil et al., 2010). The reader is also referred to (Geng et al., 2010, Irons et al., 2015, Mazumdar et al., 2017) for some other examples and details. As pointed out in (Mazumdar and Guthrie, 1995b), the main drawback of the mixing time is that it strongly depends on the positions of the initial injection and the pH-meter. Furthermore, mixing time measurements have a high deviation, are not easily reproducible, do not represent the homogeneity of the whole bath, and cannot be made easily in industrial conditions. They describe rather a local and experimental mixing time. In sum, if it is wide-spread to use the mixing time as an indicator of the stirring efficiency, one has to keep in mind its limits when it is applied to real industrial conditions.

As a final remark, it is difficult to quantify the stirring efficiency in industrial practice. Even if it is sometimes possible to do it, for example by estimating the mixing time using initial and final inclusions’ content, an *a priori* or live measurement of the stirring efficiency is not available so far: one has to wait until the end of the process to take a probe, measure the final content of inclusions in a small sample of the steel bath, and conclude *a posteriori* if the stirring was efficient or not. The problem of the stirring measurement is treated in Chapter 5.

Summary of the industrial problem. This section is a preliminary step towards mathematical modeling and formulation of the optimization problem. The most straightforward part is the control: the physical variable of interest for industrial practice is the gas flow rate Q . Thanks to empirical results, some stirring constraints have led to a reduction of the admissible control values. The less obvious part consists of defining a relevant objective functional. The stirring efficiency suffers from a lack of consensus in metallurgy. In the next section, we discuss the optimal control problem from a modeling point of view.

4.2 Mathematical modeling of the control and objective functionals

4.2.1 Control variables

The physical control parameter Q cannot be applied directly as a boundary condition for the gas inflow in the simplified ladle stirring models studied in Chapter 3, because there is no gas phase. Instead, Q appears as a factor representing the intensity of the gas. Because of the different modeling approaches in 2d (Section 3.2.1) and 3d (Section 3.2.3), we distinguish two cases for the control variable.

Control variable in 2d: $U_P(t)$ on the boundary. In 2d, we use the “equivalent” to $Q(t)$, i. e., the plume velocity $U_P(t)$. The two variables are related through the empirical formula (3.9). The plume velocity is applied as a tangent boundary velocity on Γ_{axis} (boundary-driven configuration). It is dependent on time only,

$$\mathbf{u} = \mathbf{b} = (0, U_P(t))^T \quad \text{in } (0, T] \times \Gamma_{\text{axis}}. \quad (4.8)$$

Note that this is not a boundary control in the common sense of optimal control theory because it is constant in space. Taking into account the lower and upper bounds of $Q(t)$ in the laboratory case (4.7), we define the control variable

$$U_P(t) \in [U_{P_{\min}}, U_{P_{\max}}] \quad \text{in } [0, T], \quad (4.9)$$

where $U_{P_{\min}} = 0.14$, and $U_{P_{\max}} = 0.36$ are the lower and upper bounds of the plume velocity, obtained by applying (3.9) to Q_{\min} and Q_{\max} . It should also be mentioned that, in the 2d case, there is no volume force ($\mathbf{f} = \mathbf{0}$).

Control variables in 3d: $Q(t)$ and nozzles’ positions in the volume force. In 3d, ladle stirring occurs through a volume force dependent on Q and on the nozzles’ positions $(x_{ni}, y_{ni})_{i=1,2}$, see Problem 3.3. In terms of control variables, one could optionally consider the nozzles’ position in addition to Q , as mentioned in Section 4.1. Unlike the 2d case, the control variables appear in the volume force

$$\mathbf{f} = (1 - (\alpha_{n1} + \alpha_{n2}))\mathbf{g} \quad \text{in } (0, T] \times \Omega,$$

through the gas fractions $(\alpha_{ni})_{i=1,2}$ (3.15) which we re-write now with the time-dependency:

$$\alpha_{ni}(x, y, z, t) = \begin{cases} \frac{1}{2} \left(\frac{U_P(t)}{U_S} + 1 \right) \exp \left(-2 \left(\frac{(x-x_{ni})^2 + (y-y_{ni})^2}{r_c(z)^2} \right)^2 \right), & \text{if } z \leq z_C, \\ \frac{1}{2} \left(\left(\frac{U_P(t)}{U_S} + 1 \right) - \sqrt{\left(\frac{U_P(t)}{U_S} + 1 \right)^2 - \frac{4Q(t)}{\pi r_c^2(z) U_S}} \right) \exp \left(-2 \left(\frac{(x-x_{ni})^2 + (y-y_{ni})^2}{r_c(z)^2} \right)^2 \right), & \text{if } z \geq z_C. \end{cases} \quad (4.10)$$

Note that $Q(t)$ implicitly appears in $U_P(t)$ through, again, the relation (3.9). Unlike classical volume controls, the control variables appear as parameters in \mathbf{f} .

While $Q(t)$ is a function of time constrained by (4.7), the positions $(x_{ni}, y_{ni})_{i=1,2}$ of the nozzles are four real numbers, on which we impose:

$$\sqrt{x_{ni}^2 + y_{ni}^2} < R_{\text{bot}}. \quad (4.11)$$

This simply states that the (fictive) nozzle has to be within the bottom radius of the ladle. One may apply other restrictions on x_{ni}, y_{ni} , e. g., to avoid overlapping. In this work, we do not consider other constraints and we allow for overlapping of the nozzles. Physically speaking, this would correspond to have only one nozzle in the ladle with a double gas flow rate. Finally, in the 3d case, there is no boundary velocity ($\mathbf{b} = \mathbf{0}$).

Remarks in the 3d case. As mentioned in Section 4.1.1, the gas flow rate cannot be changed erratically in practice. Mathematically, one can prevent sudden jumps and facilitate smooth changes of the control variable $Q(t)$ by using additional constraints in the form of bounds on the time derivative of $Q(t)$. Although more constraints have to be considered, it is physically more realistic. In our work, we consider a more general case without such constraints on the control.

Another important remark concerns the presence of two nozzles. We assume that it is possible to have different gas flow rates for each nozzle in Eq. (4.10). In other words, we define $Q_i(t)$ applied in the corresponding $\alpha_{ni}, i = 1, 2$. This leads to a maximum of six control variables: two flow rates and four nozzles' coordinates. Although the current industrial techniques do not allow different values for each nozzle, it may be nevertheless interesting to investigate numerically if different flow rates $Q_i(t)$ lead to better mixing than using the same one for both nozzles.

Regarding the number of control variables, one can either apply all of them at once or optimize separate problems. Altogether, five relevant combinations of control variables can be derived in the 3d case:

- optimization of $Q(t)$ only (same for both nozzles, fixed nozzles' position),
- optimization of $Q_i(t)$, $i = 1, 2$ (different for each nozzle, fixed nozzles' position),
- optimization of $(x_{ni}, y_{ni})_{i=1,2}$ only (Q given),
- optimization of $Q(t)$ (same for both nozzles) and $(x_{ni}, y_{ni})_{i=1,2}$ simultaneously,
- optimization of $Q_i(t)$ (different for each nozzle) and $(x_{ni}, y_{ni})_{i=1,2}$ simultaneously.

The first case is the closest to the industrial short-term interest but is the one with the least potential in terms of innovative solutions. Except for the last case, the configurations are likely to be suboptimal, because not all the possibilities for the control variables are explored simultaneously. On the contrary, an optimal solution computed in the last case seems to have the most potential but is also the most expensive in terms of computational time because of the higher number of control variables (6). In this work, we consider the second and third intermediate cases which offer a good balance between computational cost and innovation potential of the results for the industrial practice. Finally, let us mention the work from (Nadif et al., 2011), where a pulsed stirring was found to be more efficient in terms of mixing time, and the one from (Haiyan et al., 2016), where different flow rates on each nozzle also led to a reduction of the mixing time. Those cases are well-described in the present optimization problem. It is thus interesting to study whether similar conclusions can be obtained.

4.2.2 Objective functionals: review and discussion

As discussed in Section 4.1.2, the industrial objectives are dependent on each other and can be unified into one global concept called *stirring efficiency*. However, there is more than one physical variable describing the stirring efficiency. Furthermore, they have some drawbacks and represent only partially the stirring efficiency:

- the mixing power takes only into account the energy of the gas and does not describe the liquid velocity and mixing pattern,
- the bulk liquid recirculation rate, or, more generally, quantities based on some norm of the velocity (e.g., turbulent kinetic energy), describe a global mixing, and can miss the “effective distribution” of stirring in the liquid, in reference to the definition from (Cloete et al., 2009),
- the mixing time, although physically relevant, depends on the properties of the transported species and its initial concentration in the liquid, and is not an intrinsic property of the stirring, but rather a consequence, or an observation of it.

To gain more insight on objective functionals, we shall shortly review optimal flow control problems *from the literature of fluid physics and applied mathematics*.

Brief review of optimal flow controls. To the best of the author’s knowledge, mixing enhancement is a rather rare application of optimal flow control models. Typically, they are used to reduce turbulence, delaying its awake, or even laminarize a flow as much as possible. An example is to minimize the drag in aerodynamics applications. The reader is referred to (Gad-el Hak, 1996) for a detailed (and rather physical than mathematical) review of flow control. Examples of cost functionals minimizing the drag coefficient in turbulent flows are given in (Bewley et al., 1993, 2001, El Sherif, 2008). It is interesting to note the following observations made by (Bewley et al., 2001) (see also (El Sherif, 2008, p. 132)):

“[...] minimization of a cost functional representing exactly the quantity of interest (drag) is not necessarily the most effective means of reducing the quantity of interest over the long time [...] It is thus reasonable for the cost functional to target the turbulence (“the cause”) over each finite optimization horizon rather than the drag increase due to the turbulence (“the effect”).”

By considering the minimization of the kinetic energy $\frac{1}{2} \int_0^T \int_{\Omega} |\mathbf{u}|^2 \, d\mathbf{x} \, dt$, the optimal control problem could be solved more efficiently than with a cost functional based only on the drag quantity.

Another approach, more interesting for the present work, consists to describe turbulence by the *vorticity*. This is done in (Casas, 1995), where the goal is to minimize turbulence with volume or boundary control in stationary and time-dependent cases. Cost functionals such as

$$\int_{\Omega} |\nabla \times \mathbf{u}|^2 \, d\mathbf{x} \quad \text{and} \quad \frac{1}{6} \int_0^T \left(\int_{\Omega} |\nabla \times \mathbf{u}|^2 \, d\mathbf{x} \right)^3 \, dt,$$

provide an estimate of the level of turbulence within the flow (Casas, 1995).

Using the vorticity or the *enstrophy* has some mathematical advantages over the turbulent kinetic energy (TKE) but might be physically less relevant (Bewley et al., 2001, p. 198-199). The enstrophy is defined as the square of vorticity and the corresponding cost functional reads

$$\frac{1}{2} \int_0^T \int_{\Omega} |\nabla \times \mathbf{u}|^2 \, d\mathbf{x} \, dt.$$

For more details about these and other cost functionals, the reader is referred to (Bewley et al., 2001) and, for a general introduction to the optimal control of time-dependent Navier–Stokes equations, to (Hinze, 2002).

Based on the previous discussion and review, we propose two quantities for the objective functional of the optimal stirring control model:

- one based on the *maximization of the vorticity*, and
- one based on the *regulation of vorticity*, which, more precisely, takes into account its “distribution” in the domain, trying to avoid areas with low vorticity (*dead zones*).

In this work, the maximization and regulation of the vorticity have to be understood in the sense of (Bewley et al., 2001):

“a minimization problem [...]: solutions in which [the main term of the cost functional (i. e., excluding the control term)] are negative, if they exist, are preferred over those in which this term is zero.”

In the case of maximization, the main quantity of the cost functional is not bounded, while, in the regulation case, it is bounded from below by 0. It is also a regulation in the physical sense, as it will be seen in the next section.

4.2.3 First objective: Maximization of vorticity

In this context, we consider that the stirring efficiency is described by the turbulence of the flow. In other words, the higher the turbulence, the better the stirring. Consequently, the optimal stirring is reached with the maximal turbulence in the liquid bath. This should ensure thermal and concentration homogeneity, as well as effective inclusion removal, and thus, fulfill all the objectives at once.

The previous section has shown that the turbulence can be quantified by the vorticity, i. e., the curl of the velocity,

$$\mathbf{curl} \, \mathbf{u} := \nabla \times \mathbf{u}.$$

Thus, to maximize turbulence (or homogenization) during stirring, we should maximize the vorticity in the fluid domain Ω over a fixed period of time $[0, T]$, or, equivalently, minimize the cost functional

$$\min \quad \frac{1}{2} \int_0^T -\|\mathbf{curl}(\mathbf{u})\|_{L^2(\Omega)}^2 \, dt. \quad (4.12)$$

The cost functional (4.12) is global and does not take into account the repartition of the vorticity in the domain. This could lead to solutions where the vorticity

has high values only in a local area of the domain, giving a much higher contribution to the cost functional compared with other areas. *Dead zones*, i. e., areas with too low mixing or no fluid circulation, can appear. This is not desired in practice. In fact, preliminary numerical computations have shown that, in the 2d case at least, the vorticity magnitude is mainly located at the boundaries of the domain (remember that the flow is induced by a vertical boundary velocity). Thus, it is desirable to exclude these misleading areas from the cost functional, such that the vorticity is maximized somewhere inside the domain, more locally. Denoting a subdomain by $\Omega_0 \subset \Omega$, we define the following “local variant” of Eq. (4.12)

$$\min \quad \frac{1}{2} \int_0^T -\|\mathbf{curl}(\mathbf{u})\|_{L^2(\Omega_0)}^2 dt. \quad (4.13)$$

4.2.4 Second objective: Regulation of vorticity

The previous objective functionals have an important drawback: they do not inherently describe the distribution of the vorticity in the domain, only the global quantity. Using a local domain Ω_0 is not a practical solution, since it requires a priori knowledge to choose it. In order to better describe the repartition of vorticity, and, at the same time, obtain a vorticity field as homogeneous as possible, we define

$$\min \quad \frac{1}{2} \int_0^T \int_{\Omega} \max(m - |\mathbf{curl}(\mathbf{u})|^2, 0) d\mathbf{x} dt. \quad (4.14)$$

The integrand acts like a penalization: it has a positive contribution only where the vorticity is not high enough (namely, $< m$), and the higher the gap between the vorticity and the required “threshold” m , the higher the penalty. Physically, these areas correspond to dead zones. Where the vorticity is high enough ($\geq m$), it is 0, and the only contribution comes from the control cost, forcing a reduction of the vorticity. In other words, this functional takes into account both the “quantity and effective distribution” of turbulence in the domain (Cloete et al., 2009). It can model a balance between the maximization of the vorticity and its spatial repartition (homogeneity).

However, this additional flexibility was not made without any cost. The new formulation introduces a variable m which has now to be defined. It is indeed not straightforward to fix physically-relevant values for m , because there is no practical measurement or knowledge of how much the vorticity should be. In the context of numerical simulations, one could test several values of m and study its influence on the optimal solution. This means additional computational cost and difficulty.

Another problem is that the functional (4.14) is not differentiable, which is required to derive the optimality conditions. There are several ways to correct this. In our study, we regularize it by taking the L_2 -norm of the max term, instead of the L_1 -norm. Thus, we will consider the following cost functional in the rest of this study:

$$\min \quad \frac{1}{4} \int_0^T \|\max(m - |\mathbf{curl}(\mathbf{u})|^2, 0)\|_{L^2(\Omega)}^2 dt. \quad (4.15)$$

As in the previous section, it is possible to define a local variant of the objective functional, to avoid the artificial vorticity along the boundaries induced by the boundary velocity (in 2d):

$$\min \quad \frac{1}{4} \int_0^T \|\max(m - |\mathbf{curl}(\mathbf{u})|^2, 0)\|_{L^2(\Omega_0)}^2 dt.$$

However, the integrand in Eq. (4.15) is zero where the vorticity is high. Therefore, it is unnecessary to exclude these areas from the integration. Thus, this local variant is not studied in the rest of this chapter.

Summary of the objective functionals. For more convenience, we combine all previous functionals possible and define a general one:

$$\begin{aligned} \min \quad J_0(\mathbf{u}) = & -\frac{\beta_1}{2} \int_0^T \|\mathbf{curl}(\mathbf{u})\|_{L^2(\Omega_0)}^2 dt \\ & + \frac{\beta_2}{4} \int_0^T \|\max(m - |\mathbf{curl}(\mathbf{u})|^2, 0)\|_{L^2(\Omega_0)}^2 dt, \end{aligned} \quad (4.16)$$

where β_1 and β_2 are the weight of each term. With Ω_0 , they can be adjusted depending on the application. The following cases are of particular interest:

- global maximization of vorticity: $\beta_1 = 1$, $\beta_2 = 0$, and $\Omega_0 = \Omega$,
- local maximization of vorticity: $\beta_1 = 1$, $\beta_2 = 0$, and $\Omega_0 \subsetneq \Omega$,
- global regulation of vorticity: $\beta_1 = 0$, $\beta_2 = 1$, and $\Omega_0 = \Omega$.

4.2.5 Control cost

Besides the objectives related to the process itself, it is also required in practice to minimize the process cost, e. g., the energy required to reach the objectives. In the present case, the cost or the energy of the process control is the gas consumption (see Table 4.1). It is modeled here by the plume velocity U_P in 2d or the gas flow rate Q in 3d. As described in Section 4.2.1, these control variables appear either on the boundary or in the volume force, depending on the dimension of the problem. Thus, the cost term is defined by

$$J_c(\mathbf{f}, \mathbf{b}) = \frac{1}{2} \int_0^T \lambda_1 \|\mathbf{f}\|_{L^2(\Omega)}^2 + \lambda_2 \|\mathbf{b}\|_{L^2(\Gamma_{\text{axis}})}^2 dt, \quad (4.17)$$

where λ_1 and λ_2 are positive parameters corresponding to the weight of the cost term. Their values usually describe the energy cost and should be given by industrial practice. In absence of such information, one can test different values numerically and adjust them later depending on the application. The cost term J_c is then added to J_0 , see (4.16), to form the complete functional to be minimized.

Remarks about the cost term. First, the expression of the cost term depends on the dimension of the problem. In 3d, we have $\Gamma_{\text{axis}} = \emptyset$ and $\mathbf{b} = \mathbf{0}$ such that the cost term reads

$$J_c(\mathbf{f}, \mathbf{0}) = \frac{1}{2} \int_0^T \lambda_1 \|\mathbf{f}\|_{L^2(\Omega)}^2 dt.$$

In 2d, we have $\mathbf{f} = \mathbf{0}$ such that it is

$$J_c(\mathbf{0}, \mathbf{b}) = \frac{1}{2} \int_0^T \lambda_2 \|\mathbf{b}\|_{L^2(\Gamma_{\text{axis}})}^2 dt.$$

Second, in our application, the controls are not directly \mathbf{f} and \mathbf{b} but the functions U_P and Q (and the nozzles' coordinates) which appear implicitly in \mathbf{f} and \mathbf{b} . They depend on time only and not on space. Consequently, the main contribution of the cost term has the order of $\int_0^T |U_P(t)|^2 dt$ or $\int_0^T |Q(t)|^2 dt$. In the numerical implementation, the control cost is computed with these formulas which are more practical than (4.17). In the following, we keep the notation (4.17) for more clarity. Finally, in addition to its physical relevance, the cost term J_c acts mathematically as a regularization and avoids the so-called “bang-bang” effect, (Tröltzsch, 2010).

4.3 Optimal flow control problem

Let us summarize all modeling assumptions for the optimal control problem. First, there are two configurations for ladle stirring (Chapter 3): a 2d boundary-driven model and a 3d volume force-driven (or buoyancy-driven) turbulent model. They will also be referred to as the *direct*, *forward*, or *state* models. As explained in Section 3.5, the 2d axisymmetric case is not considered for optimization. Correspondingly, two types of optimal control problems are defined depending on the dimension:

- the 2d boundary-controlled ladle stirring optimal control problem, where the control is $U_P(t)$ and which has the following assumptions:

$$\mathbf{b} = (0, U_P(t))^\top, \quad \mathbf{f} = \mathbf{0}, \quad C_S = 0 \ (\nu_T = 0), \quad \lambda_1 = 0, \quad \lambda_2 = 1,$$

- the 3d volume-controlled buoyancy-driven ladle stirring optimal control problem, where the controls are Q_i and (x_{ni}, y_{ni}) for each nozzle $i = 1, 2$, and which has the following assumptions:

$$\mathbf{b} = \mathbf{0}, \quad \mathbf{f} = (1 - (\alpha_{n1} + \alpha_{n2}))\mathbf{g}, \quad C_S > 0 \ (\nu_T > 0) \quad \lambda_1 = 1, \quad \lambda_2 = 0.$$

Furthermore, depending on its coefficients, several variants for the cost functional (Eq. (4.16)) will be studied:

- global maximization of vorticity,
- local maximization of vorticity, and
- regulation around a threshold value m .

In the following sections, the model is formulated to express all the above-mentioned cases at once. Then, the optimality system is derived formally, leading to the adjoint equations and optimality conditions. The numerical implementation is briefly described. The results in 2d and 3d are presented in detail followed by a summary in the conclusion. New perspectives for the optimal control problem of ladle stirring are also provided at the end of the chapter.

4.3.1 Definition of the optimal control problem

The cost functional consists of minimizing the terms based on the vorticity (4.16) and the cost term (4.17). The optimal control problem reads:

Problem 4.1 (Optimal control of the ladle stirring):

$$\begin{aligned}
& \min J(\mathbf{u}, (\mathbf{f}, \mathbf{b})), \\
& \text{with } J(\mathbf{u}, (\mathbf{f}, \mathbf{b})) := J_0(\mathbf{u}) + J_c(\mathbf{f}, \mathbf{b}) \\
& \quad = -\frac{\beta_1}{2} \int_0^T \|\mathbf{curl}(\mathbf{u})\|_{L^2(\Omega_0)^d}^2 dt \\
& \quad + \frac{\beta_2}{4} \int_0^T \|\max\{m - |\mathbf{curl}(\mathbf{u})|^2, 0\}\|_{L^2(\Omega_0)}^2 dt \\
& \quad + \frac{1}{2} \int_0^T \lambda_1 \|\mathbf{f}\|_{L^2(\Omega)}^2 + \lambda_2 \|\mathbf{b}\|_{L^2(\Gamma_{\text{axis}})}^2 dt,
\end{aligned}$$

subject to:

$$\begin{aligned}
& \mathbf{u}_t + (\mathbf{u} \cdot \nabla) \mathbf{u} - 2\nabla \cdot ((\nu + \nu_T) \mathbb{D}(\mathbf{u})) + \nabla p = \mathbf{f} & \text{in } (0, T] \times \Omega, \\
& \nabla \cdot \mathbf{u} = 0 & \text{in } (0, T] \times \Omega, \\
& \text{in 3d: } \mathbf{f} = (1 - (\alpha_{n1} + \alpha_{n2})) \mathbf{g}, \\
& \text{in 2d: } \mathbf{f} = \mathbf{0}, \\
& \text{in 3d: } \mathbf{u} = \mathbf{0} \text{ (Dirichlet)} & \text{in } (0, T] \times \partial\Omega \setminus \{\Gamma_{\text{top}}\}, \\
& \text{in 2d: } \mathbf{u} = \mathbf{0} \text{ (Dirichlet)} & \text{in } (0, T] \times \partial\Omega \setminus \{\Gamma_{\text{top}} \cup \Gamma_{\text{axis}}\}, \\
& \text{in 2d: } \mathbf{u} = \mathbf{b} \text{ (control)} & \text{in } (0, T] \times \Gamma_{\text{axis}}, \\
& \mathbf{u} \cdot \mathbf{n} = 0 \text{ (no penetration)} & \text{in } (0, T] \times \Gamma_{\text{top}}, \\
& \mathbf{n}^\top \mathbb{S} \mathbf{t}_i = 0 \text{ (free slip), } 1 \leq i \leq d-1 & \text{in } (0, T] \times \Gamma_{\text{top}}, \\
& \mathbf{u}(0, \mathbf{x}) = \mathbf{u}^0(\mathbf{x}) & \text{in } \Omega, \\
& \int_{\Omega} p \, d\mathbf{x} = 0 & \text{in } [0, T], \\
& \nu = 1/96000, \\
& \text{in 3d: } \nu_T = C_S \delta^2 \|\mathbb{D}(\mathbf{u})\|_F, \\
& \text{in 2d: } \nu_T = 0,
\end{aligned}$$

$$\alpha_{ni}(x, y, z, t) = \begin{cases} \frac{1}{2} \left(\frac{U_{Pi}(t)}{U_S} + 1 \right) \exp \left(-2 \left(\frac{(x-x_{ni})^2 + (y-y_{ni})^2}{r_c(z)^2} \right)^2 \right), & \text{if } z \leq z_C, \\ \frac{1}{2} \left(\left(\frac{U_{Pi}(t)}{U_S} + 1 \right) - \sqrt{\left(\frac{U_{Pi}(t)}{U_S} + 1 \right)^2 - \frac{4Q_i(t)}{\pi r_c^2(z) U_S}} \right) \exp \left(-2 \left(\frac{(x-x_{ni})^2 + (y-y_{ni})^2}{r_c(z)^2} \right)^2 \right), & \text{if } z \geq z_C, \end{cases}$$

$$U_P(t) \in [U_{P_{\min}}, U_{P_{\max}}] \quad \text{in } (0, T],$$

$$Q_i(t) \in [Q_{\min}, Q_{\max}] \quad \text{in } (0, T],$$

$$\sqrt{x_{ni}^2 + y_{ni}^2} < R, \quad i = 1, 2.$$

Remarks. In practice, the stirring is always active. In the VTD for example, it should be vigorous enough to open a slag eye and allow the alloying in the first steps of the treatment. After that, the operators adjust the gas flow rate. This means that the fluid is not at rest at the beginning. Thus, the optimal control should be used with a fully developed flow as an initial condition. Numerically, one could start with zero initial conditions ($\mathbf{u}^0 = \mathbf{0}$), and replace the bounds of the time integrals in Eqs. (4.16) and (4.17) to compute the cost functional only after the flow fully develops. This is an expensive approach because it computes the solution until T from a fluid at rest, at each optimization iteration. Instead, we pre-compute a solution corresponding to a fully developed flow $\mathbf{u}^0 \neq \mathbf{0}$ and use it as initial condition in the optimal control problem. Note that the solution of the latter may depend on \mathbf{u}^0 .

For more clarity, we list the assumptions and parameters which may significantly influence the solution of the optimal control problem:

- the initial condition \mathbf{u}^0 ,
- the time horizon T ,
- the weights of the control cost λ_i ,
- the observation subdomain Ω_0 ,
- the threshold for vorticity regulation m (when $\beta_2 \neq 0$),
- in 3d, the mesh and Smagorinsky constant C_S ,
- in 3d, the choice of the control variables (among the combinations available).

One way to solve a minimization problem is to use *gradient-based* solvers. They can determine which direction to take, i. e., which controls to choose in order to minimize the objective functional, based on its derivative. The following pages detail the formal calculations to obtain it, but their results are not used afterwards in the thesis. Thus, the reader interested in the numerical investigations may skip sections 4.3.2 and 4.3.3 and move to Section 4.3.4. There, he will find more details on optimization solvers.

4.3.2 Formal derivation of the optimality system

Notations. For more generality, we introduce the following notations independently of the ladle application. Let Γ_c be the boundary where the control is applied (corresponds to Γ_D in Chapter 2), Γ_0 the boundary with homogeneous Dirichlet condition, and Γ_{slip} the boundary with no-penetration condition. In the 2d application, we have $\Gamma_c = \Gamma_{\text{axis}}$ and $\Gamma_0 = \partial\Omega \setminus \{\Gamma_{\text{top}} \cup \Gamma_{\text{axis}}\}$, while in 3d $\Gamma_c = \emptyset$ and $\Gamma_0 = \partial\Omega \setminus \{\Gamma_{\text{top}}\}$. The slip boundary is the same in 2d and 3d: $\Gamma_{\text{slip}} = \Gamma_{\text{top}}$. Denoting dual spaces with \cdot^* and a subset $M \subset \partial\Omega$, we define

$$\begin{aligned} \mathbf{V}_M &= \left\{ \mathbf{v} \in (H^1(\Omega))^d, \mathbf{v} = \mathbf{0} \text{ on } M, \mathbf{v} \cdot \mathbf{n} = 0 \text{ on } \Gamma_{\text{slip}} \right\}, \\ W_M &= \left\{ \mathbf{v} \in L^2(0, T; \mathbf{V}_M) : \mathbf{v}_t \in L^2(0, T; \mathbf{V}_M^*) \right\}, \\ \mathcal{Q} &= L_0^2(\Omega) = \left\{ q \in L^2(\Omega), \int_{\Omega} q \, d\mathbf{x} = 0 \right\}. \end{aligned}$$

Note that the space \mathbf{V}_M encodes the no-penetration condition, in addition to the usual homogeneous Dirichlet on the boundary. The space W_M is a Hilbert space continuously embedded into $C([0, T], (L^2(\Omega))^d)$ (Tröltzsch, 2010, p.144, Theorem 3.10 p.148). We recall the definition of the space (Tröltzsch, 2010, p.143):

$$L^2(0, T; X) = \left\{ \mathbf{v}(t, \cdot) \in X \quad \forall t \in [0, T], \int_0^T \|\mathbf{v}(t, \cdot)\|_X^2 dt < \infty \right\}.$$

Contrary to Problem 2.2 in Chapter 2, we do not write the weak formulation for a fixed t , but integrate over time. The spaces have to be chosen accordingly. The state space is given by

$$X = W_{\Gamma_0 \cup \Gamma_c} \times L^2(0, T; \mathcal{Q}).$$

The control space for the volume force \mathbf{f} and boundary velocity \mathbf{b} is

$$Y = L^2\left(0, T; (L^2(\Omega))^d\right) \times H^1\left(0, T; \left(H_{00}^{1/2}(\Gamma_c)\right)^d\right),$$

where $H_{00}^{1/2}(\Gamma_c)$ is a Lions–Magenes space (Wilbrandt, 2019b). Note that the volume term is likely to be smoother in time because the nozzle injections are smooth (see discussion in Section 4.1.1). The second part of Y needs to be such that there exists a continuous extension to W_{Γ_0} . This extension will be denoted with the same notation. The solution \mathbf{u} is decomposed into $\mathbf{u}_0 \in W_{\Gamma_0 \cup \Gamma_c}$ and $\mathbf{b} \in W_{\Gamma_0}$: $\mathbf{u} = \mathbf{u}_0 + \mathbf{b}$. The cost functional J is defined from $X \times Y$ to \mathbb{R} by

$$\begin{aligned} J((\mathbf{u}_0, p), (\mathbf{f}, \mathbf{b})) = & -\frac{\beta_1}{2} \int_0^T \|\mathbf{curl}(\mathbf{u})\|_{L^2(\Omega_0)^d}^2 dt \\ & + \frac{\beta_2}{4} \int_0^T \|\max\{m - |\mathbf{curl}(\mathbf{u})|^2, 0\}\|_{L^2(\Omega_0)}^2 dt \\ & + \frac{1}{2} \int_0^T \lambda_1 \|\mathbf{f}\|_{L^2(\Omega)}^2 + \lambda_2 \|\mathbf{b}\|_{L^2(\Gamma_c)}^2 dt. \end{aligned}$$

The equations to be solved for a given control $(\mathbf{f}, \mathbf{b}) \in Y$ are

$$\begin{aligned} \mathbf{u}_t + (\mathbf{u} \cdot \nabla) \mathbf{u} - 2\nabla \cdot ((\nu + \nu_T) \mathbb{D}(\mathbf{u})) + \nabla p &= \mathbf{f} && \text{in } (0, T] \times \Omega \\ \nabla \cdot \mathbf{u} &= 0 && \text{in } (0, T] \times \Omega \\ \text{in 3d: } \mathbf{u} &= \mathbf{0} \text{ (Dirichlet)} && \text{in } (0, T] \times \partial\Omega \setminus \{\Gamma_{\text{top}}\} \\ \text{in 2d: } \mathbf{u} &= \mathbf{0} \text{ (Dirichlet)} && \text{in } (0, T] \times \partial\Omega \setminus \{\Gamma_{\text{top}} \cup \Gamma_{\text{axis}}\} \\ \text{in 2d: } \mathbf{u} &= \mathbf{b} \text{ (control)} && \text{in } (0, T] \times \Gamma_{\text{axis}} \\ \mathbf{u} \cdot \mathbf{n} &= 0 \text{ (no penetration)} && \text{in } (0, T] \times \Gamma_{\text{top}} \\ \mathbf{n}^\top \mathbb{S} \mathbf{t}_i &= 0 \text{ (free slip), } 1 \leq i \leq d-1 && \text{in } (0, T] \times \Gamma_{\text{top}} \\ \mathbf{u}(0, \mathbf{x}) &= \mathbf{u}^0(\mathbf{x}) && \text{in } \Omega \\ \int_{\Omega} p \, d\mathbf{x} &= 0 && \text{in } [0, T]. \end{aligned}$$

Approach based on the gradient of the reduced functional. The results of the following paragraph mostly come from (Wilbrandt, 2019a, unpublished). We assume that the operators are well-defined and sufficiently smooth to be differentiable, in particular the solution operator S (see also Section 2.2.2). Let us define the residual operator $e : X \times Y \rightarrow X^*$ describing the momentum and mass conservation equations satisfied by the state variables (\mathbf{u}, p) , in weak form,

$$\begin{aligned} \langle e((\mathbf{u}_0, p), (\mathbf{f}, \mathbf{b})), (\mathbf{v}, q) \rangle_{X^* \times X} &:= \int_0^T \left(\langle \mathbf{u}_t, \mathbf{v} \rangle_{* \times} + (2(\nu + \nu_T) \mathbb{D}(\mathbf{u}), \mathbb{D}(\mathbf{v})) \right) dt \\ &+ \int_0^T \left(((\mathbf{u} \cdot \nabla) \mathbf{u}, \mathbf{v}) - (\nabla \cdot \mathbf{v}, p) - (\nabla \cdot \mathbf{u}, q) - (\mathbf{f}, \mathbf{v}) \right) dt \\ &+ (\mathbf{u}(0) - \mathbf{u}^0, \mathbf{v}(0)), \end{aligned} \quad (4.18)$$

for $(\mathbf{v}, q) \in X$. While the control \mathbf{f} enters explicitly in the above definition through an L_2 product, the boundary control \mathbf{b} appears implicitly in $\mathbf{u} = \mathbf{u}_0 + \mathbf{b}$. The solution operator $S : Y \rightarrow X$ is implicitly (and assumingly well) defined as

$$e(S(\mathbf{f}, \mathbf{b}), (\mathbf{f}, \mathbf{b})) = e((\mathbf{u}_0, p), (\mathbf{f}, \mathbf{b})) = 0. \quad (4.19)$$

More details about the well-posedness of the Navier–Stokes equations and the solution operator S have been given in Section 2.2.2. The reduced objective functional $\hat{J} : Y \rightarrow \mathbb{R}$ can now be defined as

$$\hat{J}(\mathbf{f}, \mathbf{b}) := J(S(\mathbf{f}, \mathbf{b}), (\mathbf{f}, \mathbf{b})).$$

Since the argument $(S(\mathbf{f}, \mathbf{b}), (\mathbf{f}, \mathbf{b}))$ will appear repeatedly and may reduce the readability of the equations, it will be written in a smaller size and in gray in the following. Its derivative $\hat{J}' : Y \rightarrow Y^*$ is given by the chain rule

$$\hat{J}'(\mathbf{f}, \mathbf{b}) = J_{\mathbf{u}_0, p}(S(\mathbf{f}, \mathbf{b}), (\mathbf{f}, \mathbf{b})) S'(\mathbf{f}, \mathbf{b}) + J_{\mathbf{f}, \mathbf{b}}(S(\mathbf{f}, \mathbf{b}), (\mathbf{f}, \mathbf{b})), \quad (4.20)$$

using the partial derivatives $J_{\mathbf{u}_0, p} : X \times Y \rightarrow X^*$ and $J_{\mathbf{f}, \mathbf{b}} : X \times Y \rightarrow Y^*$ of J . The derivative $S' : Y \rightarrow \mathcal{L}(Y, X)$ of the solution operator S , where $\mathcal{L}(Y, X)$ is the space of linear continuous operators from Y to X , is not known. To find an expression for $S'(\mathbf{f}, \mathbf{b})$, we define the “reduced” residual $\hat{e} : Y \rightarrow X^*$ which depends only on the control variables through the solution operator S

$$\hat{e}(\mathbf{f}, \mathbf{b}) := e(S(\mathbf{f}, \mathbf{b}), (\mathbf{f}, \mathbf{b})),$$

which satisfies $\hat{e} = 0$ according to equation (4.19). Consequently, its derivative \hat{e}' also vanishes, leading to an equation for S' :

$$\hat{e}'(\mathbf{f}, \mathbf{b}) = e_{\mathbf{u}_0, p}(S(\mathbf{f}, \mathbf{b}), (\mathbf{f}, \mathbf{b})) S'(\mathbf{f}, \mathbf{b}) + e_{\mathbf{f}, \mathbf{b}}(S(\mathbf{f}, \mathbf{b}), (\mathbf{f}, \mathbf{b})) = 0, \quad (4.21)$$

where the partial derivatives are defined in the following spaces: $e_{\mathbf{u}_0, p} : X \times Y \rightarrow \mathcal{L}(X, X^*)$ and $e_{\mathbf{f}, \mathbf{b}} : X \times Y \rightarrow \mathcal{L}(Y, X^*)$.

At this point assume that $e_{\mathbf{u}_0, p}(S(\mathbf{f}, \mathbf{b}), (\mathbf{f}, \mathbf{b}))$ is invertible, i. e., $(e_{\mathbf{u}_0, p}(S(\mathbf{f}, \mathbf{b}), (\mathbf{f}, \mathbf{b})))^{-1}$ in $\mathcal{L}(X^*, X)$ exists. We will also write $(e_{\mathbf{u}_0, p}(S(\mathbf{f}, \mathbf{b}), (\mathbf{f}, \mathbf{b})))^{-1} = e_{\mathbf{u}_0, p}^{-1}(S(\mathbf{f}, \mathbf{b}), (\mathbf{f}, \mathbf{b}))$. Then, the derivative of S at (\mathbf{f}, \mathbf{b}) can be expressed via equation (4.21) as

$$S'(\mathbf{f}, \mathbf{b}) = -e_{\mathbf{u}_0, p}^{-1}(S(\mathbf{f}, \mathbf{b}), (\mathbf{f}, \mathbf{b})) e_{\mathbf{f}, \mathbf{b}}(S(\mathbf{f}, \mathbf{b}), (\mathbf{f}, \mathbf{b})).$$

This in turn can be inserted into (4.20) to yield the following equation (in Y^*):

$$\hat{J}'(\mathbf{f}, \mathbf{b}) = -J_{\mathbf{u}_0, p}(S(\mathbf{f}, \mathbf{b}), (\mathbf{f}, \mathbf{b})) e_{\mathbf{u}_0, p}^{-1}(S(\mathbf{f}, \mathbf{b}), (\mathbf{f}, \mathbf{b})) e_{\mathbf{f}, \mathbf{b}}(S(\mathbf{f}, \mathbf{b}), (\mathbf{f}, \mathbf{b})) + J_{\mathbf{f}, \mathbf{b}}(S(\mathbf{f}, \mathbf{b}), (\mathbf{f}, \mathbf{b})). \quad (4.22)$$

The first term in $\hat{J}'(\mathbf{f}, \mathbf{b})$ can be reformulated: for all $(\mathbf{k}, \mathbf{h}) \in Y$ it holds

$$\begin{aligned} & - \langle J_{\mathbf{u}_0, p}(S(\mathbf{f}, \mathbf{b}), (\mathbf{f}, \mathbf{b})) e_{\mathbf{u}_0, p}^{-1}(S(\mathbf{f}, \mathbf{b}), (\mathbf{f}, \mathbf{b})) e_{\mathbf{f}}(S(\mathbf{f}, \mathbf{b}), (\mathbf{f}, \mathbf{b})), (\mathbf{k}, \mathbf{h}) \rangle_{Y^* \times Y} \\ & = - \langle J_{\mathbf{u}_0, p}(S(\mathbf{f}, \mathbf{b}), (\mathbf{f}, \mathbf{b})), e_{\mathbf{u}_0, p}^{-1}(S(\mathbf{f}, \mathbf{b}), (\mathbf{f}, \mathbf{b})) e_{\mathbf{f}}(S(\mathbf{f}, \mathbf{b}), (\mathbf{f}, \mathbf{b}))(\mathbf{k}, \mathbf{h}) \rangle_{X^* \times X} \\ & = - \langle e_{\mathbf{f}}(S(\mathbf{f}, \mathbf{b}), (\mathbf{f}, \mathbf{b}))(\mathbf{k}, \mathbf{h}), e_{\mathbf{u}_0, p}^{-*}(S(\mathbf{f}, \mathbf{b}), (\mathbf{f}, \mathbf{b})) J_{\mathbf{u}_0, p}(S(\mathbf{f}, \mathbf{b}), (\mathbf{f}, \mathbf{b})) \rangle_{X^* \times X} \\ & = - \langle e_{\mathbf{f}}^*(S(\mathbf{f}, \mathbf{b}), (\mathbf{f}, \mathbf{b})) e_{\mathbf{u}_0, p}^{-*}(S(\mathbf{f}, \mathbf{b}), (\mathbf{f}, \mathbf{b})) J_{\mathbf{u}_0, p}(S(\mathbf{f}, \mathbf{b}), (\mathbf{f}, \mathbf{b})), (\mathbf{k}, \mathbf{h}) \rangle_{Y^* \times Y}. \end{aligned} \quad (4.23)$$

One can define the adjoint state $(\mathbf{U}, P) \in X^{**} = X$ such that

$$(\mathbf{U}, P) := -e_{\mathbf{u}_0, p}^{-*}(S(\mathbf{f}, \mathbf{b}), (\mathbf{f}, \mathbf{b})) J_{\mathbf{u}_0, p}(S(\mathbf{f}, \mathbf{b}), (\mathbf{f}, \mathbf{b})), \quad (4.24)$$

i. e., (\mathbf{U}, P) solves the adjoint equation

$$\begin{aligned} e_{\mathbf{u}_0, p}^*(S(\mathbf{f}, \mathbf{b}), (\mathbf{f}, \mathbf{b}))(\mathbf{U}, P) &= -J_{\mathbf{u}_0, p}(S(\mathbf{f}, \mathbf{b}), (\mathbf{f}, \mathbf{b})) \\ \iff J_{\mathbf{u}_0, p}(S(\mathbf{f}, \mathbf{b}), (\mathbf{f}, \mathbf{b})) + e_{\mathbf{u}_0, p}^*(S(\mathbf{f}, \mathbf{b}), (\mathbf{f}, \mathbf{b}))(\mathbf{U}, P) &= 0. \end{aligned} \quad (4.25)$$

Consequently, the adjoint equations are formed using the partial derivative, with respect to the state variables, of the state equations (left-hand side) and the cost functional (right-hand side).

Using Equations (4.22), (4.23), and (4.24) leads to the following formulation for the derivative of \hat{J} :

$$\hat{J}'(\mathbf{f}, \mathbf{b}) = e_{\mathbf{f}, \mathbf{b}}^*(S(\mathbf{f}, \mathbf{b}), (\mathbf{f}, \mathbf{b}))(\mathbf{U}, P) + J_{\mathbf{f}, \mathbf{b}}(S(\mathbf{f}, \mathbf{b}), (\mathbf{f}, \mathbf{b})) \in Y^*.$$

At this point, all the terms are known and \hat{J}' can be computed. This equation can be used to obtain the *optimality conditions*. Indeed, when the optimal solution $(\mathbf{f}^{\text{opt}}, \mathbf{b}^{\text{opt}})$ is reached, the cost functional \hat{J} reaches a (local) minimum, which gives the following condition on its gradient:

$$\begin{aligned} & \hat{J}'(\mathbf{f} - \mathbf{f}^{\text{opt}}, \mathbf{b} - \mathbf{b}^{\text{opt}}) \geq 0 \\ \iff & J_{\mathbf{f}, \mathbf{b}}(S(\mathbf{f} - \mathbf{f}^{\text{opt}}, \mathbf{b} - \mathbf{b}^{\text{opt}}), (\mathbf{f} - \mathbf{f}^{\text{opt}}, \mathbf{b} - \mathbf{b}^{\text{opt}})) \\ & + e_{\mathbf{f}, \mathbf{b}}^*(S(\mathbf{f} - \mathbf{f}^{\text{opt}}, \mathbf{b} - \mathbf{b}^{\text{opt}}), (\mathbf{f} - \mathbf{f}^{\text{opt}}, \mathbf{b} - \mathbf{b}^{\text{opt}}))(\mathbf{U}, P) \geq 0, \end{aligned} \quad (4.26)$$

for all (admissible) $(\mathbf{f} - \mathbf{f}^{\text{opt}}, \mathbf{b} - \mathbf{b}^{\text{opt}})$ in Y .

Approach based on the Lagrangian formalism. A detailed application of the Lagrangian formalism to an optimal control problem of the instationary Navier–Stokes equations can be found in (Hinze, 2002) and (Tröltzsch, 2010, Section 5.10.2.). As pointed out in (Tröltzsch, 2010, p. 318), the formal Lagrange method allows to determine what kind of first-order necessary conditions can be expected.

These conditions coincide with those provided by a rigorous analysis. Let us define the following Lagrangian function $\mathcal{L} : X \times Y \times X \rightarrow \mathbb{R}$,

$$\begin{aligned} \mathcal{L}((\mathbf{u}_0, p), (\mathbf{f}, \mathbf{b}), (\mathbf{U}, P)) &:= J((\mathbf{u}_0, p), (\mathbf{f}, \mathbf{b})) - \\ &\int_T \int_{\Omega} (\mathbf{u}_t + (\mathbf{u} \cdot \nabla) \mathbf{u} - 2\nabla \cdot ((\nu + \nu_T) \mathbb{D}(\mathbf{u})) + \nabla p - \mathbf{f}) \cdot \mathbf{U} \, d\mathbf{x} \, dt + \\ &\int_T \int_{\Omega} (\nabla \cdot \mathbf{u}) P \, d\mathbf{x} \, dt + \int_{\Omega} (\mathbf{u}(0) - \mathbf{u}^0, \mathbf{U}(0)) \, d\mathbf{x}. \end{aligned} \quad (4.27)$$

Using our notation with the residual operator $e : X \times Y \rightarrow X^*$, it also reads

$$\mathcal{L}((\mathbf{u}_0, p), (\mathbf{f}, \mathbf{b}), (\mathbf{U}, P)) = J((\mathbf{u}_0, p), (\mathbf{f}, \mathbf{b})) - \langle e((\mathbf{u}_0, p), (\mathbf{f}, \mathbf{b})), (\mathbf{U}, P) \rangle_{X^* \times X}. \quad (4.28)$$

Unlike the approach proposed by (Hinze, 2002), where an additional integral on the boundary is introduced as a constraint, the homogeneous Dirichlet, the no-penetration and the control boundary conditions are encoded in implicit form, i.e., they are taken into account in the definition of the state space X . Similarly, the author suggests the addition of a constraint for the pressure when the flow is enclosed, which we do not need here because of the choice of the space \mathcal{Q} . It would have been possible to do the same for the continuity equation, i.e., consider divergence-free spaces and avoid the second integral in the definition of the Lagrangian (4.27). We choose the usual procedure, i.e., we include it explicitly.

By virtue of the formal Lagrange method, a locally optimal solution, which we denote by $((\mathbf{u}^{\text{opt}}, p^{\text{opt}}), (\mathbf{f}^{\text{opt}}, \mathbf{b}^{\text{opt}}), (\mathbf{U}, P))$, satisfies the relations

$$\mathcal{L}_{\mathbf{u}_0, p}((\mathbf{u}^{\text{opt}}, p^{\text{opt}}), (\mathbf{f}^{\text{opt}}, \mathbf{b}^{\text{opt}}), (\mathbf{U}, P)) = 0, \quad (4.29)$$

$$\mathcal{L}_{\mathbf{f}, \mathbf{b}}((\mathbf{u}^{\text{opt}}, p^{\text{opt}}), (\mathbf{f} - \mathbf{f}^{\text{opt}}, \mathbf{b} - \mathbf{b}^{\text{opt}}), (\mathbf{U}, P)) \geq 0, \quad \forall (\mathbf{f}, \mathbf{b}) \in Y. \quad (4.30)$$

Using Eq. (4.28), one can compute the derivative of the Lagrangian with respect to the state variables $\mathcal{L}_{\mathbf{u}_0, p} : X \times Y \times X \rightarrow X^*$, such that Eq. (4.29) becomes (see also (Hinze, 2002, Eq.(128), p.115))

$$\begin{aligned} &\mathcal{L}_{\mathbf{u}_0, p}((\mathbf{u}^{\text{opt}}, p^{\text{opt}}), (\mathbf{f}^{\text{opt}}, \mathbf{b}^{\text{opt}}), (\mathbf{U}, P)) = 0 \\ \iff &J_{\mathbf{u}_0, p}((\mathbf{u}^{\text{opt}}, p^{\text{opt}}), (\mathbf{f}^{\text{opt}}, \mathbf{b}^{\text{opt}})) - e_{\mathbf{u}_0, p}^*((\mathbf{u}^{\text{opt}}, p^{\text{opt}}), (\mathbf{f}^{\text{opt}}, \mathbf{b}^{\text{opt}}))(\mathbf{U}, P) = 0, \end{aligned} \quad (4.31)$$

which corresponds to the adjoint equations. Here, it should be noted that the minus sign introduced in the definition of the adjoint state (4.24) is a notational convention. It is also possible to ignore it, in which case Eq. (4.31) becomes similar to (4.25). The optimality conditions can be obtained with the condition (4.30), which uses the derivative of the Lagrangian with respect to the control $\mathcal{L}_{\mathbf{f}, \mathbf{b}} : X \times Y \times X \rightarrow Y^*$ (see also (Hinze, 2002, p.117,119)):

$$\begin{aligned} &\mathcal{L}_{\mathbf{f}, \mathbf{b}}((\mathbf{u}^{\text{opt}}, p^{\text{opt}}), (\mathbf{f} - \mathbf{f}^{\text{opt}}, \mathbf{b} - \mathbf{b}^{\text{opt}}), (\mathbf{U}, P)) \geq 0, \\ \iff &J_{\mathbf{f}, \mathbf{b}}((\mathbf{u}^{\text{opt}}, p^{\text{opt}}), (\mathbf{f} - \mathbf{f}^{\text{opt}}, \mathbf{b} - \mathbf{b}^{\text{opt}})) - \\ &\quad e_{\mathbf{f}, \mathbf{b}}^*((\mathbf{u}^{\text{opt}}, p^{\text{opt}}), (\mathbf{f} - \mathbf{f}^{\text{opt}}, \mathbf{b} - \mathbf{b}^{\text{opt}}))(\mathbf{U}, P) \geq 0, \end{aligned} \quad (4.32)$$

for all (admissible) $(\mathbf{f} - \mathbf{f}^{\text{opt}}, \mathbf{b} - \mathbf{b}^{\text{opt}}) \in Y$, which is similar to Eq. (4.26), up to the minus sign due to the notational convention, as explained earlier.

4.3.3 Adjoint equations and optimality conditions

Partial derivatives. In total, four partial derivatives have to be computed: the ones from the cost functional J and the ones from the residual e , once with respect to the state variables $(\mathbf{u}_0, p) \in X$ and once with respect to the control $(\mathbf{f}, \mathbf{b}) \in Y$. The different terms of the functional J are quadratic ((4.16) and (4.17)). While the first, third and fourth terms are straightforward to differentiate, the second term

$$\begin{aligned} F : X &\rightarrow \mathbb{R} \\ F(\mathbf{u}_0) &= \frac{\beta_2}{4} \int_0^T \left\| \max\{m - |\mathbf{curl}(\mathbf{u}_0)|^2, 0\} \right\|^2 dt, \\ &= \frac{\beta_2}{4} \int_0^T \int_{\Omega_0} \left| \max\{m - |\mathbf{curl}(\mathbf{u}_0)|^2, 0\} \right|^2 d\mathbf{x} dt, \end{aligned}$$

involves the max-function and requires more attention. We detail its derivative here. Let us define

$$f(\mathbf{u}_0) = |m - |\mathbf{curl}(\mathbf{u}_0)|^2|^2.$$

For $(\mathbf{v}, \cdot) \in X$ and $\eta > 0$,

$$\begin{aligned} f(\mathbf{u}_0 + \eta \mathbf{v}) - f(\mathbf{u}_0) &= (m - |\mathbf{curl}(\mathbf{u}_0 + \eta \mathbf{v})|^2)^2 - (m - |\mathbf{curl}(\mathbf{u}_0)|^2)^2 \\ &= (m^2 - 2m|\mathbf{curl}(\mathbf{u}_0 + \eta \mathbf{v})|^2 + |\mathbf{curl}(\mathbf{u}_0 + \eta \mathbf{v})|^4) \\ &\quad - (m^2 - 2m|\mathbf{curl}(\mathbf{u}_0)|^2 + |\mathbf{curl}(\mathbf{u}_0)|^4). \end{aligned}$$

Next, we expand the terms and keep only the elements of order η :

$$\begin{aligned} f(\mathbf{u}_0 + \eta \mathbf{v}) - f(\mathbf{u}_0) &= \left(m^2 - 2m|\mathbf{curl}(\mathbf{u}_0)|^2 - 4m\eta(\mathbf{curl}(\mathbf{u}_0), \mathbf{curl}(\mathbf{v})) + \mathcal{O}(\eta^2) \right. \\ &\quad \left. + |\mathbf{curl}(\mathbf{u}_0)|^4 + 4\eta|\mathbf{curl}(\mathbf{u}_0)|^2(\mathbf{curl}(\mathbf{u}_0), \mathbf{curl}(\mathbf{v})) + \mathcal{O}(\eta^2) \right) \\ &\quad - (m^2 - 2m|\mathbf{curl}(\mathbf{u}_0)|^2 + |\mathbf{curl}(\mathbf{u}_0)|^4) \\ &= \left(-4m\eta(\mathbf{curl}(\mathbf{u}_0), \mathbf{curl}(\mathbf{v})) + 4\eta|\mathbf{curl}(\mathbf{u}_0)|^2(\mathbf{curl}(\mathbf{u}_0), \mathbf{curl}(\mathbf{v})) + \mathcal{O}(\eta^2) \right) \\ &= -4\eta(\mathbf{curl}(\mathbf{u}_0), \mathbf{curl}(\mathbf{v}))(m - |\mathbf{curl}(\mathbf{u}_0)|^2) + \mathcal{O}(\eta^2). \end{aligned}$$

The derivative of F can then be obtained by the chain rule

$$\begin{aligned} \lim_{\eta \rightarrow 0} \frac{1}{\eta} (F(\mathbf{u}_0 + \eta \mathbf{v}) - F(\mathbf{u}_0)) &= -\beta_2 \int_0^T \int_{\Omega_0} (\mathbf{curl}(\mathbf{u}_0), \mathbf{curl}(\mathbf{v})) (\max\{m - |\mathbf{curl}(\mathbf{u}_0)|^2, 0\}) d\mathbf{x} dt \\ &= -\beta_2 \int_0^T (\mathbf{curl}(\mathbf{u}_0) (\max\{m - |\mathbf{curl}(\mathbf{u}_0)|^2, 0\}), \mathbf{curl}(\mathbf{v}))_{L^2(\Omega_0)} dt. \end{aligned}$$

Note that the derivative is 0 when $m - |\mathbf{curl}(\mathbf{u}_0)|^2 = 0$.

Altogether, the partial derivatives $J_{\mathbf{u}_0,p} : X \times Y \rightarrow X^*$ and $J_{\mathbf{f},\mathbf{b}} : X \times Y \rightarrow Y^*$ are given by

$$\langle J_{\mathbf{u}_0,p}((\mathbf{u}_0, p), (\mathbf{f}, \mathbf{b})), (\mathbf{v}, q) \rangle_{X^* \times X} \quad (4.33)$$

$$= -\beta_1 \int_0^T (\mathbf{curl}(\mathbf{u}), \mathbf{curl}(\mathbf{v}))_{L^2(\Omega_0)} dt \quad (4.34)$$

$$\begin{aligned} & + \beta_2 \int_0^T (\mathbf{curl}(\mathbf{u})(|\mathbf{curl}(\mathbf{u})|^2 - m), \mathbf{curl}(\mathbf{v}))_{L^2(\Omega_0)} dt \\ & = \int_0^T (\mathbf{curl}(\mathbf{u})(-\beta_1 + \beta_2(|\mathbf{curl}(\mathbf{u})|^2 - m)), \mathbf{curl}(\mathbf{v}))_{L^2(\Omega_0)} dt, \end{aligned} \quad (4.35)$$

for $(\mathbf{v}, q) \in X$, and

$$\langle J_{\mathbf{f},\mathbf{b}}((\mathbf{u}_0, p), (\mathbf{f}, \mathbf{b})), (\mathbf{k}, \mathbf{h}) \rangle_{Y^* \times Y} \quad (4.36)$$

$$\begin{aligned} & = \int_0^T (\mathbf{curl}(\mathbf{u})(-\beta_1 + \beta_2(|\mathbf{curl}(\mathbf{u})|^2 - m)), \mathbf{curl}(\mathbf{h}))_{L^2(\Omega_0)} dt \\ & \quad + \int_0^T \lambda_1(\mathbf{f}, \mathbf{k})_{L^2(\Omega)} + \lambda_2(\mathbf{b}, \mathbf{h})_{L^2(\Gamma_{\text{axis}})} dt, \end{aligned} \quad (4.37)$$

for $(\mathbf{k}, \mathbf{h}) \in Y$.

There remain, on the other hand, the partial derivatives $e_{\mathbf{u}_0,p}$ and $e_{\mathbf{f},\mathbf{b}}$. Instead of starting from the weak form of e (Eq. (4.18)), we follow the lines of (Tröltzsch, 2010) and start from the form appearing in (4.27). Let us detail the derivative of the two nonlinear terms (in \mathbf{u}_0), $F_1 : X \times X \rightarrow \mathbb{R}$ and $F_2 : X \times X \rightarrow \mathbb{R}$, defined as

$$\begin{aligned} F_1(\mathbf{u}_0, \mathbf{U}) &= \int_0^T \int_{\Omega} ((\mathbf{u}_0 \cdot \nabla) \mathbf{u}_0) \cdot \mathbf{U} \, d\mathbf{x} \, dt, \\ F_2(\mathbf{u}_0, \mathbf{U}) &= \int_0^T \int_{\Omega} (-2\nabla \cdot (\nu_T(\mathbf{u}_0) \mathbb{D}(\mathbf{u}_0))) \cdot \mathbf{U} \, d\mathbf{x} \, dt, \end{aligned}$$

where we recall the definition of the turbulent viscosity $\nu_T(\mathbf{u}_0) = C_S \delta^2 \sqrt{\mathbb{D}(\mathbf{u}_0) : \mathbb{D}(\mathbf{u}_0)}$ (Equation (2.65)). The derivative of the convective term reads, for $\mathbf{v} \in X$,

$$F_{1,\mathbf{u}_0} \mathbf{v} = \int_0^T \int_{\Omega} ((\mathbf{u}_0 \cdot \nabla) \mathbf{v} + (\mathbf{v} \cdot \nabla) \mathbf{u}_0) \cdot \mathbf{U} \, d\mathbf{x} \, dt,$$

Using the properties of the trilinear form $b(\mathbf{u}_0, \mathbf{v}, \mathbf{U}) = ((\mathbf{u}_0 \cdot \nabla) \mathbf{v}) \cdot \mathbf{U}$ (John, 2016, Section 6.1.2), for the first term,

$$b(\mathbf{u}_0, \mathbf{v}, \mathbf{U}) = -b(\mathbf{u}_0, \mathbf{U}, \mathbf{v}),$$

and the second term,

$$\begin{aligned} b(\mathbf{v}, \mathbf{u}_0, \mathbf{U}) &= \sum_{i,j=1}^d \left(v_i \frac{\partial u_j}{\partial x_i} U_j \right) = \sum_{i,j=1}^d \left(\frac{\partial u_j}{\partial x_i} U_j v_i \right) = \sum_{i=1}^d ((\nabla \mathbf{u}_0)^{\top} \mathbf{U})_i v_i \\ &= ((\nabla \mathbf{u}_0)^{\top} \mathbf{U}) \cdot \mathbf{v}, \end{aligned}$$

the derivative of the convective term can be rearranged in order to collect the test function \mathbf{v} , such that

$$F_{1,\mathbf{u}_0}\mathbf{v} = \int_0^T \int_{\Omega} (-(\mathbf{u}_0 \cdot \nabla)\mathbf{U} + (\nabla\mathbf{u}_0)^\top \mathbf{U}) \cdot \mathbf{v} \, d\mathbf{x} \, dt, \quad (4.38)$$

where $\nabla\mathbf{u}_0 = (\nabla u_1 \, \nabla u_2 \, \nabla u_3)^\top$ is the same as the term appearing in the deformation tensor (2.2).

Next, we compute the derivative of the turbulent viscosity term F_2 . A similar derivation can also be found in (El Sherif, 2008, Annex J.1.5 and J.1.6) in the more general case of a dynamic C_S . First, let us re-write F_2 in weak form (see Section 2.2.1 and Problem 2.7):

$$F_2(\mathbf{u}_0, \mathbf{U}) = \int_0^T \int_{\Omega} 2\nu_T(\mathbf{u}_0) \mathbb{D}(\mathbf{u}_0) : \mathbb{D}(\mathbf{U}) \, d\mathbf{x} \, dt = \int_0^T (2\nu_T(\mathbf{u}_0) \mathbb{D}(\mathbf{u}_0), \mathbb{D}(\mathbf{U})) \, dt.$$

For $\mathbf{v} \in X$ and $\eta > 0$ small enough,

$$\begin{aligned} & F_2(\mathbf{u}_0 + \eta\mathbf{v}, \mathbf{U}) - F_2(\mathbf{u}_0, \mathbf{U}) \\ &= \int_0^T (2\nu_T(\mathbf{u}_0 + \eta\mathbf{v}) \mathbb{D}(\mathbf{u}_0 + \eta\mathbf{v}), \mathbb{D}(\mathbf{U})) \, dt - \int_0^T (2\nu_T(\mathbf{u}_0) \mathbb{D}(\mathbf{u}_0), \mathbb{D}(\mathbf{U})) \, dt \\ &= \int_0^T \left(2 \underbrace{(\nu_T(\mathbf{u}_0 + \eta\mathbf{v}) - \nu_T(\mathbf{u}_0)) \mathbb{D}(\mathbf{u}_0)}_D, \mathbb{D}(\mathbf{U}) \right) \, dt + \eta \int_0^T (2\nu_T(\mathbf{u}_0 + \eta\mathbf{v}) \mathbb{D}(\mathbf{v}), \mathbb{D}(\mathbf{U})) \, dt. \end{aligned}$$

By dividing by η and in the limit $\eta \rightarrow 0$, the second term converges to

$$\int_0^T (2\nu_T(\mathbf{u}_0) \mathbb{D}(\mathbf{v}), \mathbb{D}(\mathbf{U})) \, dt = \int_0^T (2\nu_T(\mathbf{u}_0) \mathbb{D}(\mathbf{U}), \mathbb{D}(\mathbf{v})) \, dt.$$

As it will be seen later, this term, which uses the turbulent viscosity of the state variable \mathbf{u}_0 , is in some sense the adjoint equivalent of the Smagorinsky term of the state equations.

In the first term, the derivative D of the turbulent viscosity ν_T at \mathbf{u}_0 in direction \mathbf{v} appears. It can be computed using the explicit definition of $\nu_T(\mathbf{u}_0)$, and assuming that $\mathbb{D}(\mathbf{u}_0) \neq \mathbf{0}$ almost everywhere,

$$\begin{aligned} D &= \nu_T(\mathbf{u}_0 + \eta\mathbf{v}) - \nu_T(\mathbf{u}_0) \\ &= C_S \delta^2 \left(\sqrt{\mathbb{D}(\mathbf{u}_0 + \eta\mathbf{v}) : \mathbb{D}(\mathbf{u}_0 + \eta\mathbf{v})} - \sqrt{\mathbb{D}(\mathbf{u}_0) : \mathbb{D}(\mathbf{u}_0)} \right) \\ &= C_S \delta^2 \left(\frac{\mathbb{D}(\mathbf{u}_0 + \eta\mathbf{v}) : \mathbb{D}(\mathbf{u}_0 + \eta\mathbf{v}) - \mathbb{D}(\mathbf{u}_0) : \mathbb{D}(\mathbf{u}_0)}{\sqrt{\mathbb{D}(\mathbf{u}_0 + \eta\mathbf{v}) : \mathbb{D}(\mathbf{u}_0 + \eta\mathbf{v})} + \sqrt{\mathbb{D}(\mathbf{u}_0) : \mathbb{D}(\mathbf{u}_0)}} \right) \\ &= \eta C_S \delta^2 \left(\frac{2\mathbb{D}(\mathbf{u}_0) : \mathbb{D}(\mathbf{v})}{\sqrt{\mathbb{D}(\mathbf{u}_0 + \eta\mathbf{v}) : \mathbb{D}(\mathbf{u}_0 + \eta\mathbf{v})} + \sqrt{\mathbb{D}(\mathbf{u}_0) : \mathbb{D}(\mathbf{u}_0)}} \right) + \mathcal{O}(\eta^2), \end{aligned}$$

such that

$$\lim_{\eta \rightarrow 0} \frac{D}{\eta} = \frac{C_S \delta^2 \mathbb{D}(\mathbf{u}_0) : \mathbb{D}(\mathbf{v})}{\|\mathbb{D}(\mathbf{u}_0)\|_F},$$

where we have used the Frobenius norm (2.64).

It is important to take into account the case $\mathbb{D}(\mathbf{u}_0) = \mathbf{0}$ in the numerical implementation. Since $\mathbb{D}(\mathbf{u}_0)$ appears also as an ansatz function in the previous limit, fixing D to 0, and, consequently, the derivative F_{2,\mathbf{u}_0} also, when $\mathbb{D}(\mathbf{u}_0) = \mathbf{0}$ seems to be a reasonable assumption.

Using the following equality to write the test function on the right-hand side:

$$((\mathbb{D}(\mathbf{u}_0) : \mathbb{D}(\mathbf{v}))\mathbb{D}(\mathbf{u}_0), \mathbb{D}(\mathbf{U})) = ((\mathbb{D}(\mathbf{u}_0) : \mathbb{D}(\mathbf{U}))\mathbb{D}(\mathbf{u}_0), \mathbb{D}(\mathbf{v})),$$

the derivative of F_2 can finally be summarized as

$$F_{2,\mathbf{u}_0}\mathbf{v} = \int_0^T \left(\frac{2C_S\delta^2\mathbb{D}(\mathbf{u}_0) : \mathbb{D}(\mathbf{U})}{\|\mathbb{D}(\mathbf{u}_0)\|_F} \mathbb{D}(\mathbf{u}_0), \mathbb{D}(\mathbf{v}) \right) + (2\nu_T(\mathbf{u}_0)\mathbb{D}(\mathbf{U}), \mathbb{D}(\mathbf{v})) \, dt. \quad (4.39)$$

Integrating by parts, one retrieves the strong form of the nonlinear terms:

$$F_{2,\mathbf{u}_0}\mathbf{v} = \int_0^T \int_{\Omega} -2\nabla \cdot \left(\frac{C_S\delta^2\mathbb{D}(\mathbf{u}_0) : \mathbb{D}(\mathbf{U})}{\|\mathbb{D}(\mathbf{u}_0)\|_F} \mathbb{D}(\mathbf{u}_0) + \nu_T(\mathbf{u}_0)\mathbb{D}(\mathbf{U}) \right) \cdot \mathbf{v} \, d\mathbf{x} \, dt. \quad (4.40)$$

Before putting all the terms together, let us integrate by parts the first term of $e_{\mathbf{u}_0,p}$ with respect to t to avoid a time derivative on the test function:

$$\int_0^T (\mathbf{v}_t, \mathbf{U}) \, dt = - \int_0^T (\mathbf{U}_t, \mathbf{v}) \, dt + (\mathbf{U}(T), \mathbf{v}(T)) - (\mathbf{U}(0), \mathbf{v}(0)). \quad (4.41)$$

Differentiating the initial term $(\mathbf{u}(0) - \mathbf{u}^0, \mathbf{v}(0))$ from Eq. (4.18) and adding it to 4.41 yields:

$$\int_0^T (\mathbf{v}_t, \mathbf{U}) \, dt + (\mathbf{U}(0), \mathbf{v}(0)) = - \int_0^T (\mathbf{U}_t, \mathbf{v}) \, dt + (\mathbf{U}(T), \mathbf{v}(T)). \quad (4.42)$$

Gathering (4.38), (4.40), and (4.42), the partial derivative $e_{\mathbf{u}_0,p} : X \times Y \rightarrow \mathcal{L}(X, X^*)$ with respect to the state variables can be written as

$$\begin{aligned} \langle e_{\mathbf{u}_0,p}((\mathbf{u}, p), (\mathbf{f}, \mathbf{b}))(\mathbf{U}, P), (\mathbf{v}, q) \rangle_{X^* \times X} = \\ \int_0^T \int_{\Omega} \left(-\mathbf{U}_t - 2\nabla \cdot \left((\nu + \nu_T(\mathbf{u}))\mathbb{D}(\mathbf{U}) + \frac{C_S\delta^2\mathbb{D}(\mathbf{u}) : \mathbb{D}(\mathbf{U})}{\|\mathbb{D}(\mathbf{u})\|_F} \mathbb{D}(\mathbf{u}) \right) - (\mathbf{u} \cdot \nabla)\mathbf{U} \right. \\ \left. + (\nabla\mathbf{u})^\top \mathbf{U} + \nabla P \right) \cdot \mathbf{v} \, d\mathbf{x} \, dt + \int_{\Omega} \mathbf{U}(T)\mathbf{v}(T) \cdot + \int_0^T \int_{\Omega} -(\nabla \cdot \mathbf{U})q \, d\mathbf{x} \, dt. \end{aligned} \quad (4.43)$$

This form, which is not exactly the weak form, allows to see more easily how the strong adjoint equations look like. Before getting to this point, let us write the weak form for completeness. The main differences are the use of (4.39) instead of (4.40), and the integration by parts of the pressure term:

$$\begin{aligned} \langle e_{\mathbf{u}_0,p}((\mathbf{u}_0, p), (\mathbf{f}, \mathbf{b}))(\mathbf{U}, P), (\mathbf{v}, q) \rangle_{X^* \times X} = \\ \int_0^T \left((-\mathbf{U}_t, \mathbf{v}) + (2(\nu + \nu_T(\mathbf{u}))\mathbb{D}(\mathbf{U}), \mathbb{D}(\mathbf{v})) + \left(\frac{2C_S\delta^2\mathbb{D}(\mathbf{u}) : \mathbb{D}(\mathbf{U})}{\|\mathbb{D}(\mathbf{u})\|_F} \mathbb{D}(\mathbf{u}), \mathbb{D}(\mathbf{v}) \right) \right. \\ \left. - ((\mathbf{u} \cdot \nabla)\mathbf{U}, \mathbf{v}) + ((\nabla\mathbf{u})^\top \mathbf{U}, \mathbf{v}) - (P, \nabla \cdot \mathbf{v}) - (\nabla \cdot \mathbf{U}, q) \right) dt + (\mathbf{U}(T), \mathbf{v}(T)). \end{aligned}$$

The fourth and last partial derivative $e_{\mathbf{f}, \mathbf{b}} : X \times Y \rightarrow \mathcal{L}(Y, X^*)$ is then given by

$$\begin{aligned} \langle e_{\mathbf{f}, \mathbf{b}}((\mathbf{u}_0, p), (\mathbf{f}, \mathbf{b}))(U, P), (\mathbf{h}, \mathbf{k}) \rangle_{Y^* \times Y} = \\ \int_0^T \left((-U_t, \mathbf{h}) + (2(\nu + \nu_T(\mathbf{u}))\mathbb{D}(U), \mathbb{D}(\mathbf{h})) + \left(\frac{2C_S \delta^2 \mathbb{D}(\mathbf{u}) : \mathbb{D}(U)}{\|\mathbb{D}(\mathbf{u})\|_F} \mathbb{D}(\mathbf{u}), \mathbb{D}(\mathbf{h}) \right) \right. \\ \left. - ((\mathbf{u} \cdot \nabla)U, \mathbf{h}) + ((\nabla \mathbf{u})^\top U, \mathbf{h}) - (P, \nabla \cdot \mathbf{h}) - (U, \mathbf{k}) \right) dt + (U(T), \mathbf{h}(T)). \end{aligned} \quad (4.44)$$

Adjoint equations. We can now write the adjoint equations. According to Equation (4.31) (or, equivalently, (4.25)) derived in the previous section, one has to set $e_{(\mathbf{u}_0, p)}$ (4.43) equal to $J_{(\mathbf{u}_0, p)}$ (4.35), for all test functions $(\mathbf{v}, q) \in X$. By applying specific test functions (Hinze, 2002), one retrieves the strong form of the adjoint equations:

- using $q = 0$ and \mathbf{v} with compact support on Ω leads to the momentum equation for the adjoint variables,
- applying $\mathbf{v} = \mathbf{0}$ and q with compact support on Ω leads to the mass conservation of the adjoint variable,
- the “initial condition” for U is obtained by applying $\nabla \mathbf{v} \cdot \mathbf{n} = 0$ on $\partial\Omega$ and $\mathbf{v}(T, \cdot)$ with compact support Ω .

Furthermore, given the definition of the space X , the adjoint variable U satisfies similar boundary conditions as the state variable \mathbf{u}_0 (in particular, homogeneous Dirichlet and free slip), and the constraint on the pressure to fix the additive constant is satisfied by P , just as p does. All in all, the strong form of the adjoint problem reads:

Problem 4.2 (Adjoint problem of the 2d boundary-controlled and 3d volume-controlled turbulent Navier–Stokes equations for ladle stirring):

$$\begin{aligned} -U_t - 2\nabla \cdot \left((\nu + \nu_T(\mathbf{u}))\mathbb{D}(U) + \left(\frac{C_S \delta^2 \mathbb{D}(\mathbf{u}) : \mathbb{D}(U)}{\|\mathbb{D}(\mathbf{u})\|_F} \mathbb{D}(\mathbf{u}) \right) \right) - (\mathbf{u} \cdot \nabla)U \\ + (\nabla \mathbf{u})^\top U + \nabla P = -(\mathbf{curl}(\mathbf{u})(-\beta_1 + \beta_2(m - |\mathbf{curl}(\mathbf{u})|^2)), \mathbf{curl} \cdot) \quad \text{in } (0, T] \times \Omega \\ \nabla \cdot U = 0 \quad \text{in } (0, T] \times \Omega \\ \text{in 3d: } U = \mathbf{0} \text{ (Dirichlet)} \quad \text{in } (0, T] \times \partial\Omega \setminus \Gamma_{\text{top}} \\ \text{in 2d: } U = \mathbf{0} \text{ (Dirichlet)} \quad \text{in } (0, T] \times \partial\Omega \setminus \{\Gamma_{\text{axis}} \cup \Gamma_{\text{top}}\} \\ \text{in 2d: } U = \mathbf{0} \quad \text{in } (0, T] \times \Gamma_{\text{axis}} \\ U \cdot \mathbf{n} = 0 \text{ (no penetration)} \quad \text{in } (0, T] \times \Gamma_{\text{top}} \\ \mathbf{n}^\top \mathbb{S}(U) \mathbf{t}_i = 0 \text{ (free slip), } 1 \leq i \leq d-1 \quad \text{in } (0, T] \times \Gamma_{\text{top}} \\ U(T, \cdot) = \mathbf{0} \quad \text{in } \Omega \\ \int_{\Omega} P \, d\mathbf{x} = 0 \quad \text{in } [0, T]. \end{aligned}$$

In other words, the adjoint variables (U, P) solve a linear equation, backward in time with “initial” value $U(\cdot, T) = \mathbf{0}$.

Optimality conditions. Similarly, the optimality conditions (4.32) can now be written based on $e_{\mathbf{f},\mathbf{b}}$ (4.44) and $J_{\mathbf{f},\mathbf{b}}$ (4.37). For simplicity, we consider only the 3d case with volume control. The case with boundary control can be found in (Hinze, 2002, Tröltzsch, 2010), and the references therein. One tests with $\mathbf{h} = \mathbf{0}$ and \mathbf{k} arbitrary on Ω (see also (Hinze, 2002, p.118,119)), such that there remains only the term $\int_0^T \lambda_1(\mathbf{f}, \mathbf{k})_{L^2(\Omega)}$ in $J_{\mathbf{f},\mathbf{b}}$ and the term $\int_0^T -(\mathbf{U}, \mathbf{k})_{L^2(\Omega)} dt$ in $e_{\mathbf{f},\mathbf{b}}$. Thus, the optimality condition for the volume-controlled 3d problem gives the following *variational inequality* (Tröltzsch, 2010, p. 320):

$$\int_0^T \int_{\Omega} (\lambda_1 \mathbf{f}^{\text{opt}} + \mathbf{U}) \cdot (\mathbf{f} - \mathbf{f}^{\text{opt}}) d\mathbf{x} dt \geq 0, \quad \forall \text{ (admissible) } \mathbf{f}.$$

Arrived to this point, the formal derivation of the optimality system and optimality conditions is finished. These equations can serve as a basis for future numerical simulations of optimal control problems using gradient-based solvers.

4.3.4 Numerical aspects: gradient-based vs. gradient-free solvers

It is usual to distinguish two classes of solvers to compute solutions of optimal control problems: gradient-based and gradient-free solvers. The key difference between those is the way they search for the solution of the minimization problem. While gradient-based solvers use the property that the derivative of a function should be zero when a (local) minimum is reached, gradient-free solvers use approximation or interpolation approaches to move in the correct direction, i. e., to minimize the cost functional, iteration after iteration. This procedure often requires a high, sometimes prohibitive, number of iterations in comparison to gradient-based solvers. This is especially true when the number of control variables, e. g., the number of degrees of freedom of \mathbf{f} or \mathbf{b} , is big. Its main advantage lies on its capability to solve optimal problems with smooth, as well as, non-smooth objective functionals. Furthermore, their simple implementation offers a practical start for optimization studies: one basically just needs to solve the direct (state) problem and compute the cost functional several times iteratively. To deduce the control variable in the next iteration, gradient-free solver packages can be used. They often consist of a “black box”, where operations are done internally, and can be coupled to existing flow solvers and enrich them. On the other hand, when the objective functional is differentiable, gradient-based solvers apply a Newton-like algorithm to find a zero of the gradient. These algorithms converge often faster to the optimal solution than gradient-free methods, but require the additional computation of the gradient of the cost functional and of the adjoint equations, as described in the previous sections. In the following, results obtained with a gradient-free solver are presented. The computations were performed with the software PARMOON (Wilbrandt et al., 2017) combined with the optimization library NLOPT (Johnson, 2019).

4.4 Numerical results for the 2d boundary-driven ladle

4.4.1 Description of the numerical studies

This section describes the numerical parameters of the 2d boundary-controlled ladle stirring optimal control problem. The control variable $U_P(t)$ can freely vary in time within the box constraints (4.9). In a discrete setting, the number of degrees of freedom N_c of the control variable, i.e., the dimension of the control space, is equal to the number of time steps, $N_c = T/\Delta t$. We consider two cases:

1. a case where U_P is constant in time ($N_c = 1$), and
2. the case where U_P is time-dependent.

In order to avoid too expensive computations in the second case, a large time step is chosen, e.g., $\Delta t = 0.1$. There are several reasons for studying the case of a constant control separately:

- the results can be implemented directly in the industrial practice. Fixing the value of the gas flow rate to a constant value is indeed the most simple control for the process.
- the optimal solution can be computed relatively fast because of the reduced number of control variables ($N_c = 1$). This allows to study the effect of different numerical parameters on the optimal solution.
- the optimal constant control can be used as a relevant initial guess for the more complex case with time-dependent control. This may facilitate the convergence of the optimization in the second case.
- the solution can be compared with the optimal time-dependent control. Depending on the improvement or deterioration of the cost functional, one can decide if it is worth making an investment for a time-dependent gas injection.

The end time T is fixed to 10 s (such that $N_c = 100$ in the second case). The initial condition \mathbf{u}^0 is taken from a previously computed flow (Figure 3.6).

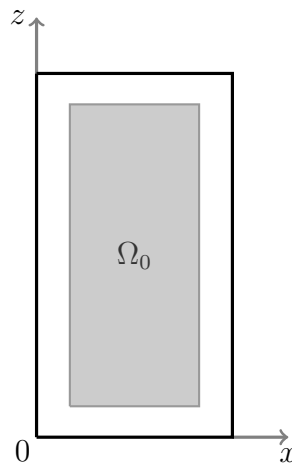


Figure 4.1: Definition of the subdomain Ω_0 : $\{(x, y) \in [0.05, 0.025] \times [0.05, 0.55]\}$.

Regarding the cost functional J , the parameters β_1 , β_2 , Ω_0 , and m are fixed according to the relevant cases mentioned earlier in the chapter:

1. global maximization of the vorticity: $\beta_1 = 1$, $\beta_2 = 0$, $\Omega_0 = \Omega$

$$J_1 := -\frac{1}{2} \int_0^T \|\mathbf{curl}(\mathbf{u})\|_{L^2(\Omega)}^2 dt + \frac{\lambda_2}{2} \int_0^T \|\mathbf{b}\|_{L^2(\Gamma_{\text{axis}})}^2 dt.$$

2. local maximization: $\beta_1 = 1$, $\beta_2 = 0$, $\Omega_0 \subsetneq \Omega$

$$J_2 := -\frac{1}{2} \int_0^T \|\mathbf{curl}(\mathbf{u})\|_{L^2(\Omega_0)}^2 dt + \frac{\lambda_2}{2} \int_0^T \|\mathbf{b}\|_{L^2(\Gamma_{\text{axis}})}^2 dt.$$

More precisely, the subdomain Ω_0 is chosen as a rectangle which excludes a small area close to the boundaries: $\{(x, y) \in [0.05, 0.025] \times [0.05, 0.55]\}$ (Figure 4.1). This choice is motivated by preliminary computations showing that, in the boundary-driven configuration, the vorticity is much higher close to the boundaries than inside the domain, because of the imposed (non-physical) boundary velocity on Γ_{axis} .

3. regulation with a low threshold: $\beta_1 = 0$, $\beta_2 = 1$, $\Omega_0 = \Omega$, $m = 10$

$$J_3(10) := \frac{1}{4} \int_0^T \|\max\{10 - |\mathbf{curl}(\mathbf{u})|^2, 0\}\|_{L^2(\Omega)}^2 dt + \frac{\lambda_2}{2} \int_0^T \|\mathbf{b}\|_{L^2(\Gamma_{\text{axis}})}^2 dt.$$

4. regulation with a higher threshold: $\beta_1 = 0$, $\beta_2 = 1$, $\Omega_0 = \Omega$, $m = 100$

$$J_3(100) := \frac{1}{4} \int_0^T \|\max\{100 - |\mathbf{curl}(\mathbf{u})|^2, 0\}\|_{L^2(\Omega)}^2 dt + \frac{\lambda_2}{2} \int_0^T \|\mathbf{b}\|_{L^2(\Gamma_{\text{axis}})}^2 dt.$$

In the last two cases, a small and a high threshold value m are chosen in order to favor more or less the distribution of vorticity, to the detriment of local peaks. Three values for the cost's weight are chosen: $\lambda_2 = 1$, 10, and 100 ($\lambda_1 = 0$ in 2d).

Concerning the parameters of the optimization solvers, the so-called COBYLA (Constraint Optimization BY Linear Approximation) algorithm is applied (Powell, 1994). The maximum number of iterations is set to 500. Other stopping criteria based on the convergence of the cost functional and of the control variable are also used: the value of J (criteria fixed to -10^{10} for J_1 and J_2 , to 10^{-8} for $J_3(10)$ and $J_3(100)$), the absolute value of the difference $|J^k - J^{k-1}|$ between two iterations (fixed to 10^{-5}), and the absolute value of the difference $|\|\mathbf{b}^k\| - \|\mathbf{b}^{k-1}\||$ of the control variable between two iterations (fixed to 10^{-4}). In each case, the computations were started with three different initial “guesses” of the control variable for the first optimization iteration: $U_{P_{\min}} = 0.14$, an intermediate value 0.25, and the upper bound $U_{P_{\max}} = 0.36$. This means that the first iteration is computed either with $U_P(t) = U_{P_{\min}}$, or $U_P(t) = 0.25$, or $U_P(t) = U_{P_{\max}}$, for all $t \in [0, T]$.

Altogether, there are two types of control, four cost functionals, three control costs, and three initial guesses, leading to a total of 72 cases (Table 4.4). Next, we present the results with constant and time-dependent controls in two separate sections.

Table 4.4: Numerical campaign for the optimal control problem in 2d.

Type of control	First guess	λ_2	Number of cases (per J)
Constant	$U_P^0 = 0.14, 0.25, 0.36$	1, 10, 100	9
Time-dependent	$U_P^0 = 0.14, 0.25, 0.36$	1, 10, 100	9

4.4.2 Results with constant control

Convergence and cost functional. The optimization solver converges in all 36 cases with constant control (Table 4.5) and required only a few number of iterations (7 to 19). The evolution of the cost functionals during the optimization procedure is given in Figure 4.2. It can be seen that J decreases in all cases, and, in each case, the minimum is the same for all the initial guesses. For more clarity, the optimum values are summarized in Table 4.6.

The optimal values, obtained with a constant control, will be used as a reference in the case with time-dependent control: one can then conclude if some time variation of the control U_P can improve the optimum reached with a constant U_P .

One can also observe in Figure 4.2 that, in some cases, J increases in the first optimization iteration before decreasing. This trial-and-error behavior is typical of a gradient-free solver: several points are needed to construct an approximation of the cost functional, such that it is impossible for this type of solver to know a relevant control already after the first iteration.

Optimal control. As expected, when the cost λ_2 is low enough, the optimal control is $U_{P_{\max}}$. When it becomes dominant, this is $U_{P_{\min}}$. However, the results depend on the cost functional and, in the case $J_3(10)$ with $\lambda_2 = 1$, on the initial guess (Table 4.6). As described earlier, the case with a constant U_P is quite practical, because one can rapidly verify if there are “obvious” minima, identify what is a good starting guess, and obtain an order of magnitude of the cost functional for comparison with the case using a time-dependent control.

Table 4.5: Convergence of the optimization solver in the different configurations, where $|\Delta U_P| = |U_{P_i}^k - U_{P_i}^{k-1}|$ and $|\Delta J| = |J^k - J^{k-1}|$ (case with constant control).

Configurations		Stopping criteria reached	
		$ \Delta U_P \leq 10^{-4}$	$ \Delta J \leq 10^{-5}$
J_1	all 9 cases	✓	-
J_2	all 9 cases	✓	-
$J_3(10)$	$\lambda_2 = 1, U_P^0 = 0.14, 0.25, 0.36$	-	✓
	all other cases	✓	-
$J_3(100)$	$\lambda_2 = 10, U_P^0 = 0.14, 0.25, 0.36$	-	✓
	all other cases	✓	-

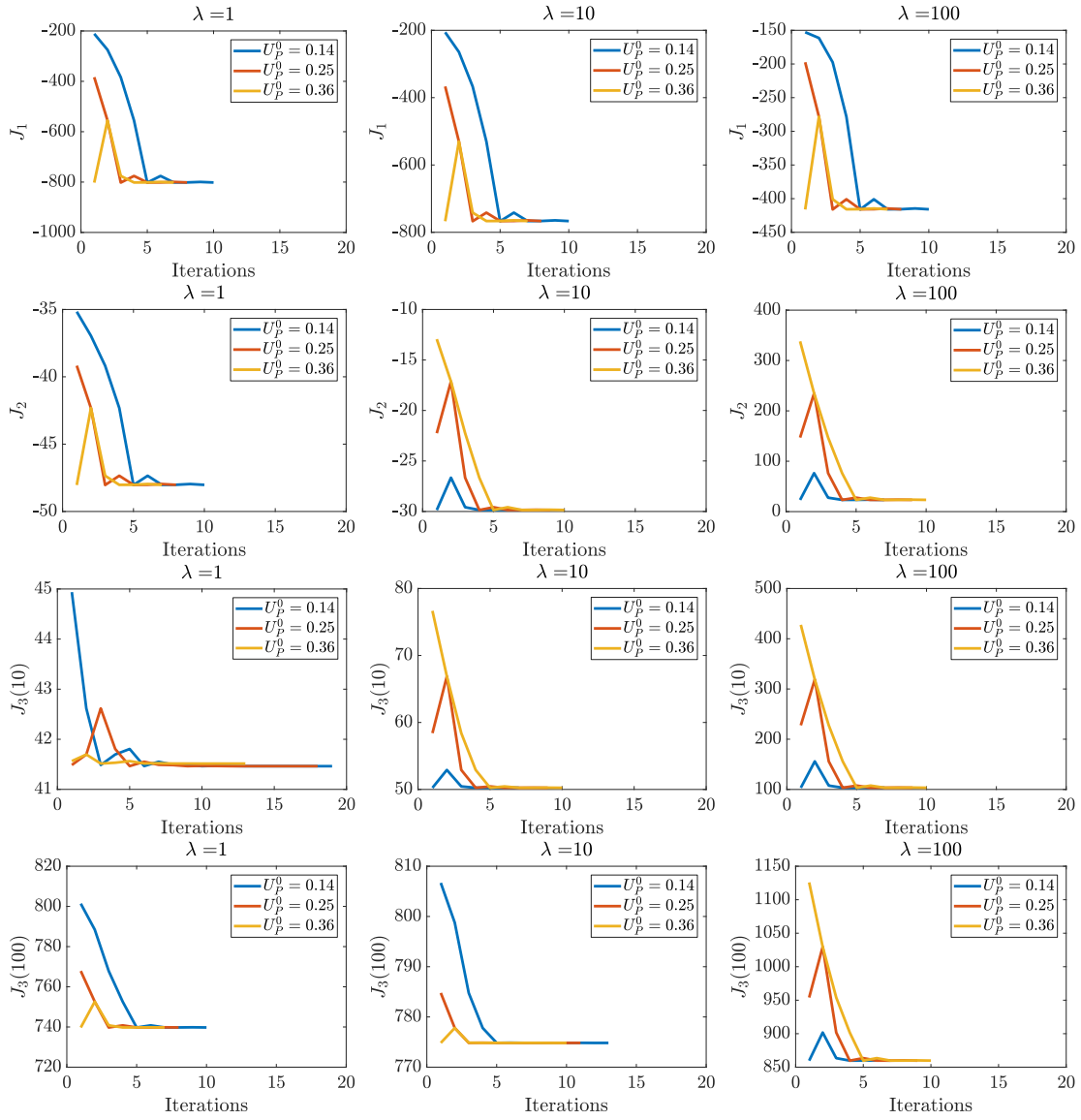


Figure 4.2: Evolution of the cost functionals during the optimization algorithm in 2d. From top to bottom: J_1 , J_2 , $J_3(10)$, and $J_3(100)$. From left to right: $\lambda_2 = 1$, 10, and 100 (case with constant control).

Table 4.6: Optimum value J^{opt} of the cost functionals and corresponding optimal control U_P^{opt} in 2d (case with constant control).

$J^{\text{opt}}/U_P^{\text{opt}}$	$\lambda_2 = 1$	$\lambda_2 = 10$	$\lambda_2 = 100$
J_1	-801.7 / 0.36	-766.6 / 0.36	-415.8 / 0.36
J_2	-48 / 0.36	-29.9 / 0.14	23.3 / 0.14
$J_3(10)$	41.5 / 0.26, 0.35	50.2 / 0.14	103.4 / 0.14
$J_3(100)$	739.8 / 0.36	774.8 / 0.36	859.8 / 0.14

4.4.3 Results with time-dependent control

Next, we look at the results of the time-dependent case. We are in particular interested in knowing if some time variations of U_P can further reduce the minimum obtained with the constant control.

Convergence and cost functional. The convergence of J is illustrated in Figure 4.3. The corresponding values coming from the case with constant control (Table 4.6) are also displayed in dashed lines for comparison. The algorithm stops after having reached the maximum number of iterations, 500. This is due to the relatively high number of controls ($N_c = 100$) and the use of gradient-free solvers. A higher number of iterations may be needed here. However, in most cases, the cost functional stagnates, such that this might not necessarily improve the results. Sometimes, the solver returned an invalid value after approximately 100 loops but continued the optimization until 500. As described later, a similar behavior occurs in 3d and one reason to explain this failure is the bad initial guess. Here, this explanation does not hold because at low cost, e. g., $\lambda_1 = 1$, the high plume velocity $U_P^0 = 0.36$ fails for J_2 and $J_3(10)$, while it is expected to be a good initial guess. In sum, the reasons for such a behavior could not be found in 2d. One could test alternative optimization solvers to further investigate this point.

In any case, initial guesses which are far from the optimal constant control obtained in the previous section make the convergence of J slower, as expected. On the contrary, in the cases where $U_P^0(t) = U_P^{\text{opt. const}}$, $\forall t \in [0, T]$, the first iteration gives already a small value for J . In some cases, e. g., J_1 with $\lambda = 100$ and initial control 0.14, the computations “lock” quite far from the minimum value obtained so far. For such cases, a higher number of iterations is required to check if the cost functional is further reduced, or if there is a local minimum.

By focusing on the cases computed with the initial guess of interest, one observes that the objective functional is very close to its equivalent with constant-in-time control (dashed lines). It means that a time-dependent control does not improve significantly a constant control. Table 4.7 gives the reduction, in percent, of the cost functional. The only cases where the reduction becomes clear are $J_3(10)$ and $\lambda_2 = 1$ (1.25%), and, to some extent, J_2 and $\lambda_2 = 1$ (0.7%). In all other cases, the decrease of the cost functional with a time-dependent control is negligible.

Optimal control. The time profiles of $U_P(t)$ leading to the optimal J are given in Figure 4.4. If there is no clear pattern to be identified in the plots, one can notice that U_P remains close, if not equal, to the optimum constant control, in the whole time range. For example, in the cases J_2 , $J_3(10)$ and $J_3(100)$ with $\lambda_2 = 100$, the optimal solution is equal to the optimum constant-in-time control², $U_P(t) \simeq U_{P_{\min}}$, $\forall t \in [0, T]$. With J_1 , some peaks appear but they are less “effective” than a constant maximum value, in terms of minimization of the cost functional. The two cases which improve the most the cost functional are: $J_3(10)$ and J_2 with $\lambda_2 = 1$. They are characterized by irregular (non-periodic) oscillations or peaks of different amplitudes.

² There is actually an imperceptible difference, leading to the reduction of the cost functional found in Table 4.7: -0.29, -0.01, and -0.06% which are negligible.

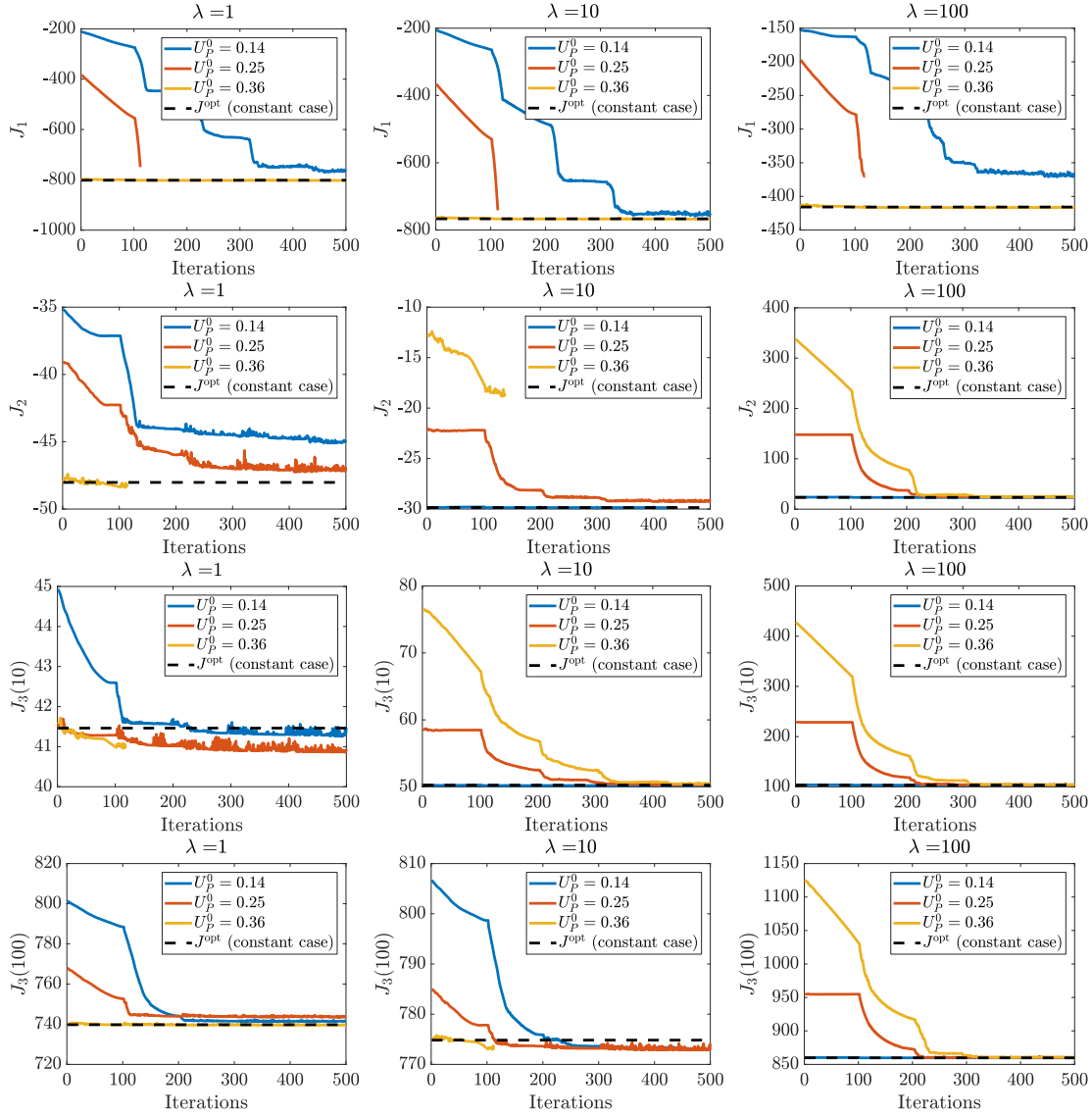


Figure 4.3: Evolution of the cost functionals during the optimization algorithm in the different configurations: From top to bottom: J_1 , J_2 , $J_3(10)$, and $J_3(100)$. From left to right: $\lambda_2 = 1, 10$, and 100 (case with time-dependent control).

Table 4.7: Reduction, in %, of the cost functional in comparison to $J^{\text{opt. cst}}$ from the constant control. The value of J^{opt} can be read in Figure 4.3 (last iteration of the smallest cost functional). The value of $J^{\text{opt. cst}}$ corresponds to the dashed lines (see also Table 4.6).

$\frac{J^{\text{opt}} - J^{\text{opt. cst}}}{J^{\text{opt. cst}}} \text{ (in \%)}$	$\lambda_2 = 1$	$\lambda_2 = 10$	$\lambda_2 = 100$
J_1^{opt}	-0.1	-0.12	-0.23
J_2^{opt}	-0.7	-0.02	-0.29
$J_3^{\text{opt}}(10)$	-1.25	-0.09	-0.06
$J_3^{\text{opt}}(100)$	-0.02	-0.24	-0.01

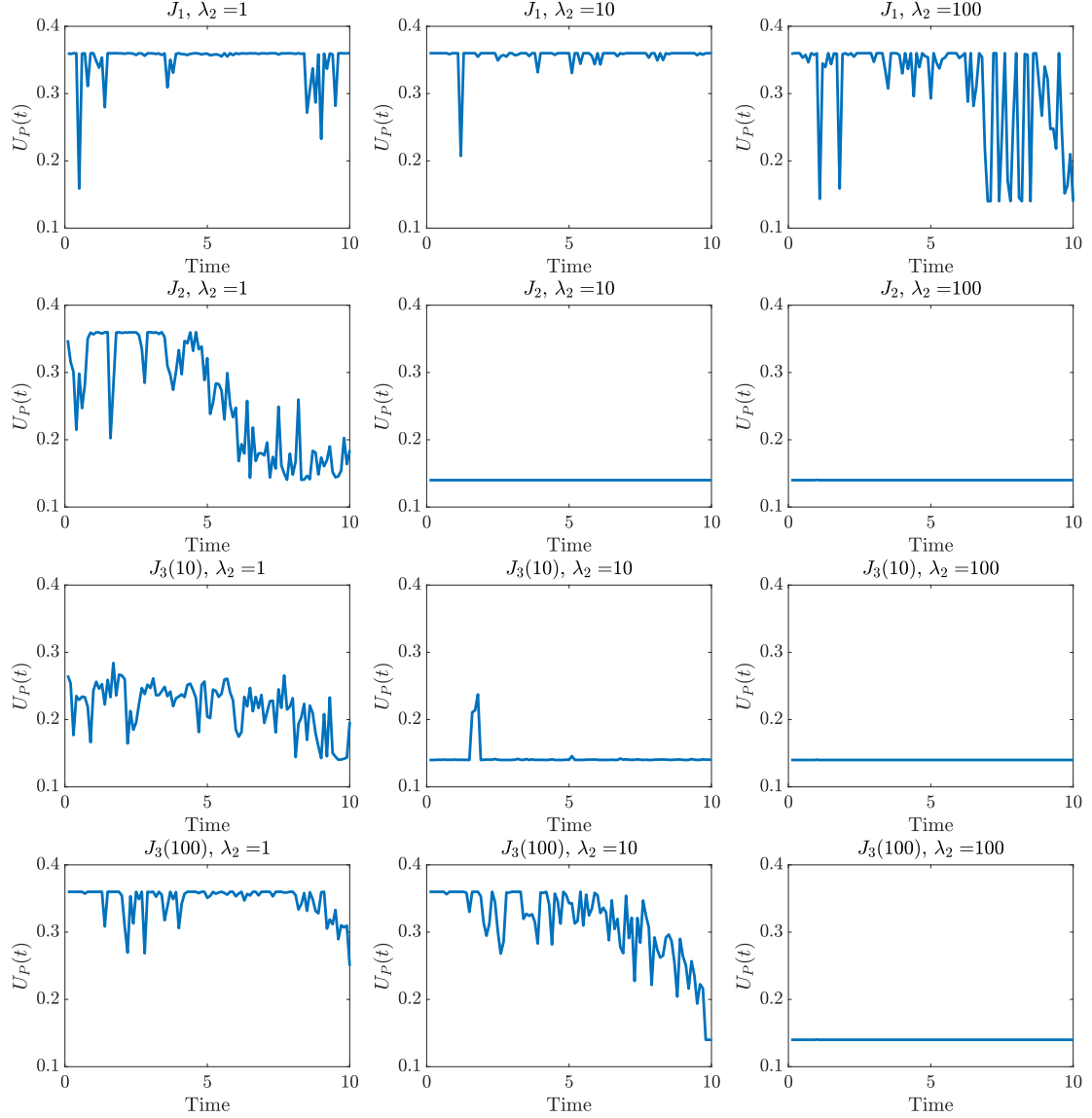


Figure 4.4: Time profile of U_P corresponding to the “optimized” stirring. From top to bottom: J_1 , J_2 , $J_3(10)$, and $J_3(100)$. From left to right: $\lambda_2 = 1, 10$, and 100 .

These oscillations are presumably dependent on the instantaneous flow structures and on the initial condition \mathbf{u}^0 . Furthermore, the mean value of the control tends to decrease in the last seconds of the time range. Since the objective functional is integrated over the whole time period, it can happen that the main contribution to the vorticity is generated only in a part of the time range, e.g., up to a few seconds before T . Then, in the last few seconds, only the cost of the control J_c contributes to the cost functional. Thus, the cost can be reduced by reducing U_P at the end of the simulation, without losing vorticity, thanks to the contribution from previously generated vorticity. This might explain the decrease of U_P at the last seconds in the two cases. It is not clear yet if the reduction of the cost functional can be obtained by one of these two features (the oscillations of U_P or its decrease at the end), or, if one has to do both in order to reduce the cost functional.

4.4.4 Summary and outlook to 3d

The results obtained in 2d show how the optimal solution depends on the choice of the cost functional and the cost coefficient. Other parameters which may influence it, but which have not been investigated in this work, are, e. g., the initial condition \mathbf{u}^0 , the time step Δt , and the end time T . The comparison between the constant and time-dependent cases suggests that the constant-in-time optimal solutions are generally better than time-dependent solutions. This is practical for the industry, since there is no need to make further investments on the process control. A constant control can be implemented immediately in the plant. In one case, an improvement of 1.25% of the cost functional was achieved using a non-periodic oscillating $U_P(t)$. In practice however, it may be difficult to impose such an irregular profile. First, it might be optimal for one but not all stirrings and, second, there are sometimes sharp peaks, which may be technically infeasible. The only feature which can be realistically implemented is the drop of U_P at the end of the stirring process to save some gas cost. It consists then only in turning-off the gas at the end of the operation. In all cases, the 2d optimization model needs to be investigated more extensively in order to propose robust solutions to the industry. These preliminary results illustrate the kind of optimal solutions (constants, or, to some extent, oscillating and decreasing at the end), and the order of magnitude of the improvement brought by these optimized solutions ($\sim 1\%$).

The proof-of-concept cannot be meaningful for the industrial practice with the 2d boundary-driven ladle stirring. Indeed, the flow does not take into account the real geometry with two excentric nozzles. The 3d model is more relevant to deliver realistic results. It can reproduce the same configurations as in 2d, namely, constant and time-dependent controls, with more physically-relevant flows. In addition, it allows to explore other optimization possibilities, for example, applying different gas flow rates for each nozzle or changing the nozzles' positions. These aspects have been investigated in the 3d optimization application and the results are presented in the next section.

4.5 Numerical results for the 3d ladle

4.5.1 Description of the numerical studies

In the 3d optimal control problem, the control variable is not the plume velocity $U_P(t)$, but directly the gas flow rate $Q(t)$, because it appears explicitly in the right-hand side \mathbf{f} , (Eq. (3.15)), and not only implicitly in U_P as in 2d (Eq. (3.9)). The 3d ladle is fundamentally different from the 2d case:

- the control is in the volume force,
- there are two nozzles which can have different flow rates, $Q_1(t)$ and $Q_2(t)$,
- the position of the nozzles can be changed, and
- the results depend on the mesh size and on the Smagorinsky constant C_S .

In the rest of this study, the computations are performed on a coarse mesh (~ 10000 cells) for faster computations. The constant C_S is fixed to 0.005, which is, according to the results of Section 3.4.3, a reasonable choice. The influence of the mesh and C_S on the optimal solutions can be investigated in future studies. Three optimization cases are studied:

1. a case where Q_1 and Q_2 are constant in time ($N_c = 2$), as in 2d,
2. the case where they are time-dependent ($N_c = 2T/\Delta t$), as in 2d, and
3. a case where the nozzles' positions $(x_{n1}, y_{n1}, x_{n2}, y_{n2})$ are optimized, at fixed Q_1 and Q_2 ($N_c = 4$).

The first two cases are particularly interesting to compare with the results from (Haiyan et al., 2016) and (Nadif et al., 2011), where a constant flow rate with different values per nozzle and a pulsed stirring are applied, respectively.

Four cost functionals are defined similarly to the 2d case. The only differences are the cost term, which is based on Q_1 and Q_2 , instead of \mathbf{b} , the subdomain Ω_0 , and the order of magnitudes of λ_1 :

1. global maximization of the vorticity: $\beta_1 = 1, \beta_2 = 0, \Omega_0 = \Omega$,

$$J_1 := -\frac{1}{2} \int_0^T \|\mathbf{curl}(\mathbf{u})\|_{L^2(\Omega)}^2 dt + \frac{\lambda_1}{2} \int_0^T \sum_{i=1}^2 |Q_i(t)|^2 dt.$$

2. local maximization: $\beta_1 = 1, \beta_2 = 0, \Omega_0 \subsetneq \Omega$,

$$J_2 := -\frac{1}{2} \int_0^T \|\mathbf{curl}(\mathbf{u})\|_{L^2(\Omega_0)}^2 dt + \frac{\lambda_1}{2} \int_0^T \sum_{i=1}^2 |Q_i(t)|^2 dt.$$

Here, Ω_0 corresponds to the lower half of the ladle: $\{(x, y, z) \in \Omega, z \leq H/2\}$ (Figure 4.5). This is the region where we expect the most dead zones, and therefore, where it is more desirable to increase the vorticity.

3. regulation with a low threshold: $\beta_1 = 0, \beta_2 = 1, \Omega_0 = \Omega, m = 10$,

$$J_3(10) := \frac{1}{4} \int_0^T \|\max\{10 - |\mathbf{curl}(\mathbf{u})|^2, 0\}\|_{L^2(\Omega)}^2 dt + \frac{\lambda_1}{2} \int_0^T \sum_{i=1}^2 |Q_i(t)|^2 dt.$$

4. regulation with a higher threshold: $\beta_1 = 0, \beta_2 = 1, \Omega_0 = \Omega, m = 100$,

$$J_3(100) := \frac{1}{4} \int_0^T \|\max\{100 - |\mathbf{curl}(\mathbf{u})|^2, 0\}\|_{L^2(\Omega)}^2 dt + \frac{\lambda_1}{2} \int_0^T \sum_{i=1}^2 |Q_i(t)|^2 dt.$$

Figure 4.5: Subdomain Ω_0 in 3d: $\{(x, y, z) \in \Omega, z \leq H/2\}$.

Table 4.8: Numerical campaign for the optimal control problem in 3d.

Study case/ Type of control	Max. iter.	T	Init. cond.	First guess	λ_1
1/ Constant gas	100	10	200s	$Q_1^0, Q_2^0 = 1, 6, 17$	0.001, 0.01, 1
2/ Time-dependent gas	500	10	200s	$Q_1^0, Q_2^0 = 1, 6, 17$	0.001, 0.01, 1
3/ Nozzles' position	200	20	0s	$(x_{n1}^0, y_{n1}^0, x_{n2}^0, y_{n2}^0)$	0

The weight of the cost are chosen as: $\lambda_1 = 0.001, 0.01$, and 1 ($\lambda_2 = 0$ in 3d). The time parameters are different between the study cases. In the first two cases, the end time T is equal to 10 s ($N_c = 200$ control variables when Q_1 and Q_2 are time-dependent), as in 2d. The initial condition \mathbf{u}^0 is also taken from a previously computed flow (200 s). In the last study case, since the position of the nozzles changes, we consider a fluid at rest at the beginning and compute over a longer time range: $\mathbf{u}^0 = \mathbf{0}$ and $T = 20$. Preliminary computations showed that the flow can be considered as developed after 20 s. The fact that this value is lower than the ones found in Section 3.4.3 is due to the choice of the mesh and C_S . In all cases, a large time step as in 2d is chosen to reduce computational time: $\Delta t = 0.1$. The derivative-free COBYLA solver is applied, with a maximum number of iterations equal to 100, 500, and 200, for the first, second, and third study respectively. The other stopping criteria are the same as in 2d. In the studies 1 and 2, two initial guesses of the control variables are taken as the bounds $Q_{\min} = 1$ and $Q_{\max} = 17$ of the box constraints (4.7). Note that these values correspond to the plume velocities used in the 2d model, $U_{P\min} = 0.14$ and $U_{P\max} = 0.36$, through the formula (3.9). The third initial guess is an intermediate value in the box constraints. One could use the mean value 9 l min^{-1} , but this would not end up in an average control because the volume force is not proportional to Q , but to $Q^{1/3}$. Indeed, it is of the order of the plume velocity U_P , see (4.10), which scales with $Q^{1/3}$. Thus, an intermediate value of U_P is more appropriate to have an average volume control, for example, 0.25 m s^{-1} as in 2d. Consequently, we choose the gas flow rate which is equivalent to $U_P = 0.25$, namely, 6 l min^{-1} , see Equation (3.9).

Table 4.9: Convergence of the optimization solver, where $|\Delta Q| = \sqrt{\sum_i |Q_i^k - Q_i^{k-1}|^2}$ and $|\Delta J| = |J^k - J^{k-1}|$ (case with constant control).

Configurations		Stopping criteria reached		
		$ \Delta Q \leq 10^{-4}$	$ \Delta J \leq 10^{-5}$	nb. iter. ≥ 100
J_1	$\lambda_1 = 0.001, Q^0 = 1$	-	-	✓
	all other cases	✓	-	-
J_2	$\lambda_1 = 0.001, Q^0 = 1$	-	-	✓
	$\lambda_1 = 0.01, Q^0 = 6$	-	✓	-
	all other cases	✓	-	-
$J_3(10)$	$\lambda_1 = 1, Q^0 = 17$	-	-	✓
	all other cases	✓	-	-
$J_3(100)$	$\lambda_1 = 0.001, Q^0 = 1$	-	-	✓
	all other cases	✓	-	-

Since we always use the same initial guess for both nozzles, the notation Q^0 will be sometimes used instead of $Q_i^0, i = 1, 2$. In sum, we have: $Q^0(t) = 1, 6$, or 17 l min^{-1} , for all $t \in [0, T]$. In the last study case, the initial position of the nozzles is the same as in the default case: $(x_{n1}^0, y_{n1}^0, x_{n2}^0, y_{n2}^0) = (-0.105, -0.105, -0.105, 0.105)$ (Table 3.4). Altogether, 73 configurations are computed (Table 4.8).

4.5.2 Results with constant control

In the study case 1 (Table 4.8), the effect of two parameters are varied for each cost functional: the control cost factor λ_1 and the initial guesses Q_1^0 and Q_2^0 .

Convergence and cost functional. The stopping criteria reached by the solver in each case is given in Table 4.9. The optimization has converged in almost all cases. In most configurations, the solver stops when the variation of the control is small enough, and in four cases, the maximum number of iterations is reached. As it will be described in the next paragraph, it appeared from the results that it is not necessary to increase the maximum number of iterations for these configurations.

Looking now at the cost functionals (Figure 4.6), one can make several observations. First, it can be seen that, in most cases, all three initial guesses lead to the same minimum J . Second, in the case $\lambda_1 = 1$ (high cost), the initial guess $Q^0 = 1$ converges the fastest to the minimum, while, in the case $\lambda_1 = 0.001$, it is $Q^0 = 17$ which converges the fastest to the minimum. The two values 1 and 0.001 seem to be extreme cases: the control cost is either too high or too low. An order of magnitude in between may lead to a better balance between the cost term and the main term of the cost functional, i.e., the vorticity term in J_1 and J_2 , and the “max-”term in $J_3(10)$ and $J_3(100)$. For example, values of λ_1 between 0.001 and 0.01 seem to result in the same order of magnitude between the two terms. Looking at the cases where the maximum number of iterations is reached, one observes that the cost functional stagnates quite close to the minimum.

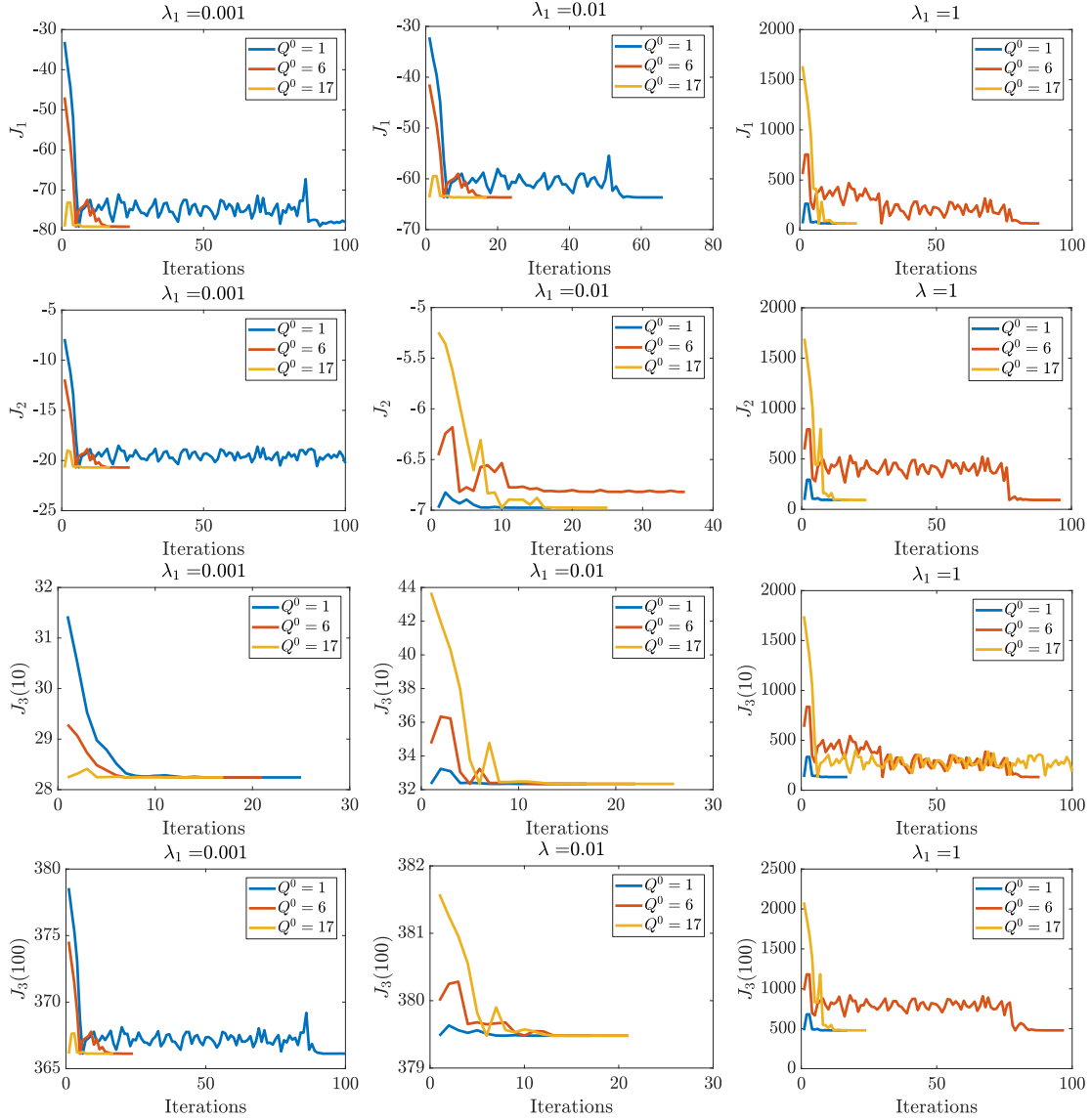


Figure 4.6: Evolution of the cost functionals during the optimization algorithm in the different configurations. From top to bottom: J_1 , J_2 , $J_3(10)$, and $J_3(100)$. From left to right: $\lambda_1 = 0.001$, 0.01 , and 1 (case with constant control).

Table 4.10: Optimum value J^{opt} of the cost functionals and corresponding optimal control Q^{opt} in 3d. There holds $Q^{\text{opt}} = Q_1^{\text{opt}} = Q_2^{\text{opt}}$ (case with constant control).

$J^{\text{opt}}/Q^{\text{opt}}$	$\lambda_1 = 0.001$	$\lambda_1 = 0.01$	$\lambda_1 = 1$
J_1	-79.1 / 17	-63.7 / 17	67.8 / 1
J_2	-20.7 / 17	-7 / 1	93 / 1
$J_3(10)$	28.24 / 17	32.4 / 1	132 / 1
$J_3(100)$	366 / 17	379 / 1	479 / 1

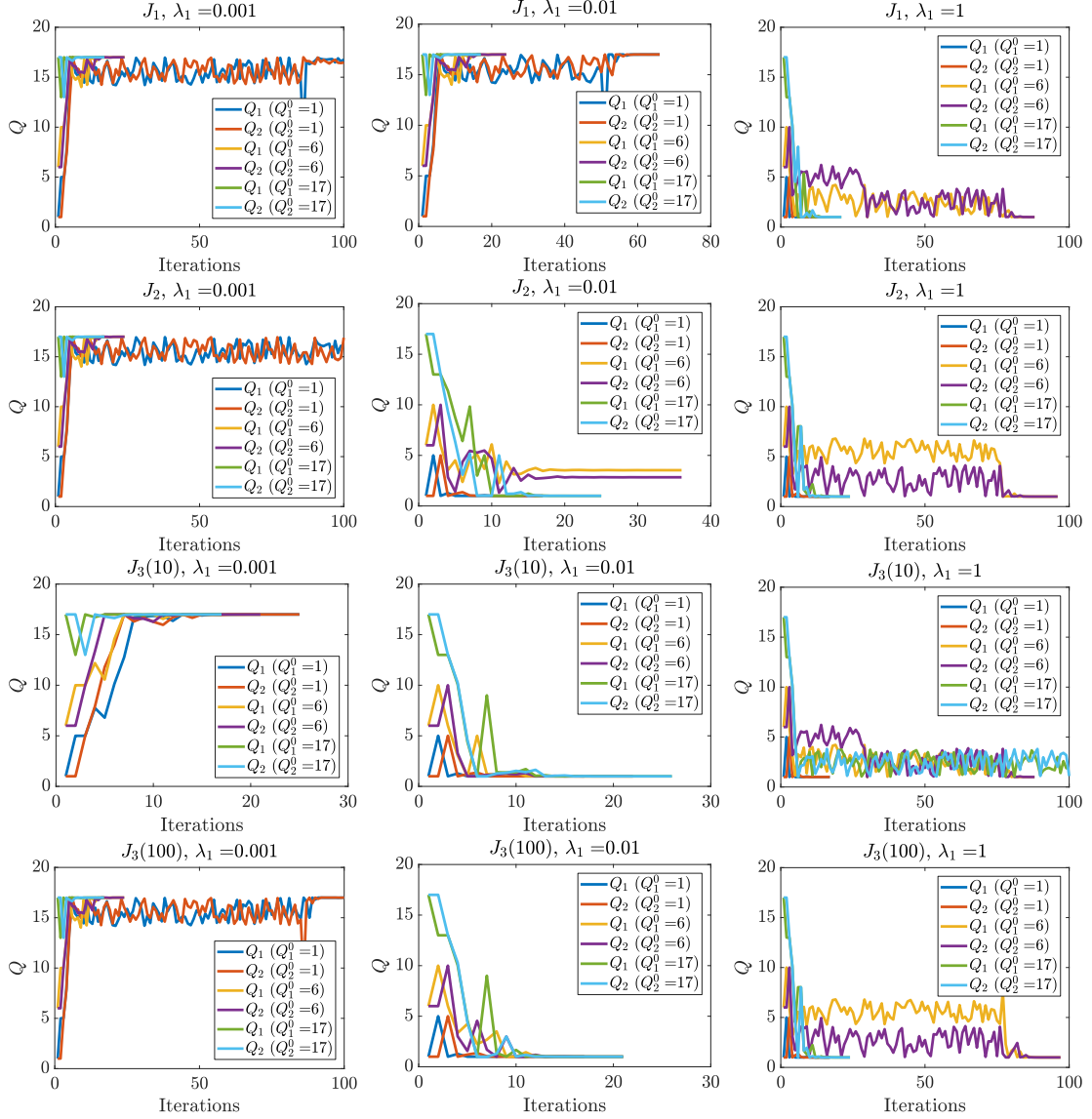


Figure 4.7: Evolution of the controls Q_1 and Q_2 during the optimization algorithm.

Thus, we do not expect other minima if more iterations are performed. In any case, a slightly higher number of iterations seems to be enough for the solver to reach one of the two other stopping criteria. For more clarity, the minimum values of the cost functionals are summarized in Table 4.10. As in 2d, these values will be compared to those of the case with time-dependent control. One can then conclude if some time variation of the controls Q_1 and Q_2 can improve the optimum reached with constant Q_1 and Q_2 .

Optimal control. Figure 4.7 shows the evolution of Q_1 and Q_2 . The optimal (constant) solution is either $Q_i^{\text{opt}} = Q_{\min}$ or Q_{\max} , $i = 1, 2$, depending on λ_1 and J . Furthermore, no solution with $Q_1 \neq Q_2$ was obtained, meaning that both nozzles with the same flow rate give a better result than with different flow rates. For a high coefficient λ_1 , the control is minimized: $Q^{\text{opt}} = Q_{\min}$, while for a low one, it is maximized: $Q^{\text{opt}} = Q_{\max}$. As in the 2d case, these results were expected. The optimal control values are summarized in Table 4.10.

4.5.3 Results with time-dependent control

In study case 2 (Table 4.8), λ_1 and the initial guess Q^0 are also varied.

Convergence and cost functional. Because the number of control variables is relatively high ($N_c = 200$) and we are using a gradient-free solver, a high number of iterations is expected. In fact, in most cases, the maximum number of iterations 500 was reached, while in the remaining cases, the solver failed after around 200 iterations and returned invalid values, see Table 4.11. This behavior can be attributed to a bad initial guess. Indeed, from the results established earlier, starting from, for instance, $Q^0 = 17$ with $\lambda_1 = 1$, is far from the optimum. Alternative gradient-free solvers, such as the Nelder-Mead method (Powell, 2007), could be tested, but this was not investigated in the present work. Nevertheless, by taking the cost functional J at the last computed iteration, a small reduction of the cost functional, in the order of 1% in comparison to the constant case, was found in some of the cases which reached 500 iterations. The most noticeable improvements are obtained with:

- J_2 and $\lambda_1 = 0.01$: $\sim -4.3\%$,
- J_1 and $\lambda_1 = 0.01$: $\sim -1\%$, and
- $J_3(10)$ and $\lambda_1 = 0.001$: $\sim -0.3\%$.

The values are detailed in Table 4.12 and can be compared with the previous study with constant controls (Table 4.10). Figure 4.8 shows the evolution of the three cost functionals listed above.

Table 4.11: Convergence of the optimization solver in the different configurations (case with time-dependent control).

		Stopping criteria	
Configurations		nb. iter. ≥ 500	Solver failure
J_1	$\lambda_1 = 1, 0.01, 0.001, Q^0 = 1$	✓	-
	$\lambda_1 = 1, 0.01, Q^0 = 6$	✓	-
	$\lambda_1 = 0.01, Q^0 = 17$	✓	-
	three other cases	-	X
J_2	$\lambda_1 = 1, 0.01, Q^0 = 1$	✓	-
	$\lambda_1 = 1, 0.01, Q^0 = 6$	✓	-
	five other cases	-	X
$J_3(10)$	$\lambda_1 = 1, 0.01, 0.001, Q^0 = 1$	✓	-
	$\lambda_1 = 1, 0.01, 0.001, Q^0 = 6$	✓	-
	$\lambda_1 = 0.01, 0.001, Q^0 = 17$	✓	-
	$\lambda_1 = 1, Q^0 = 17$	-	X
$J_3(100)$	$\lambda_1 = 1, 0.01, Q^0 = 1$	✓	-
	$\lambda_1 = 1, 0.01, Q^0 = 6$	✓	-
	five other cases	-	X

Table 4.12: Value of the cost functionals computed at the last iteration (case with time-dependent control). Between parenthesis, the reduction, in %, of the cost functional in comparison to the optimal constant case: $\frac{J^{\text{opt}} - J^{\text{opt. cst}}}{|J^{\text{opt. cst}}|}$.

	$\lambda_1 = 0.001$	$\lambda_1 = 0.01$	$\lambda_1 = 1$
J_1^{opt}	-79.1 (0%)	-64.3 (-1%)	67.8 (0%)
J_2^{opt}	-20.7 (0%)	-7.3 (-4.3%)	93 (0%)
$J_3^{\text{opt}}(10)$	28.14 (-0.3%)	32.3 (-0.08%)	132.3 (0%)
$J_3^{\text{opt}}(100)$	366 (0%)	379 (-0.09%)	479 (0%)

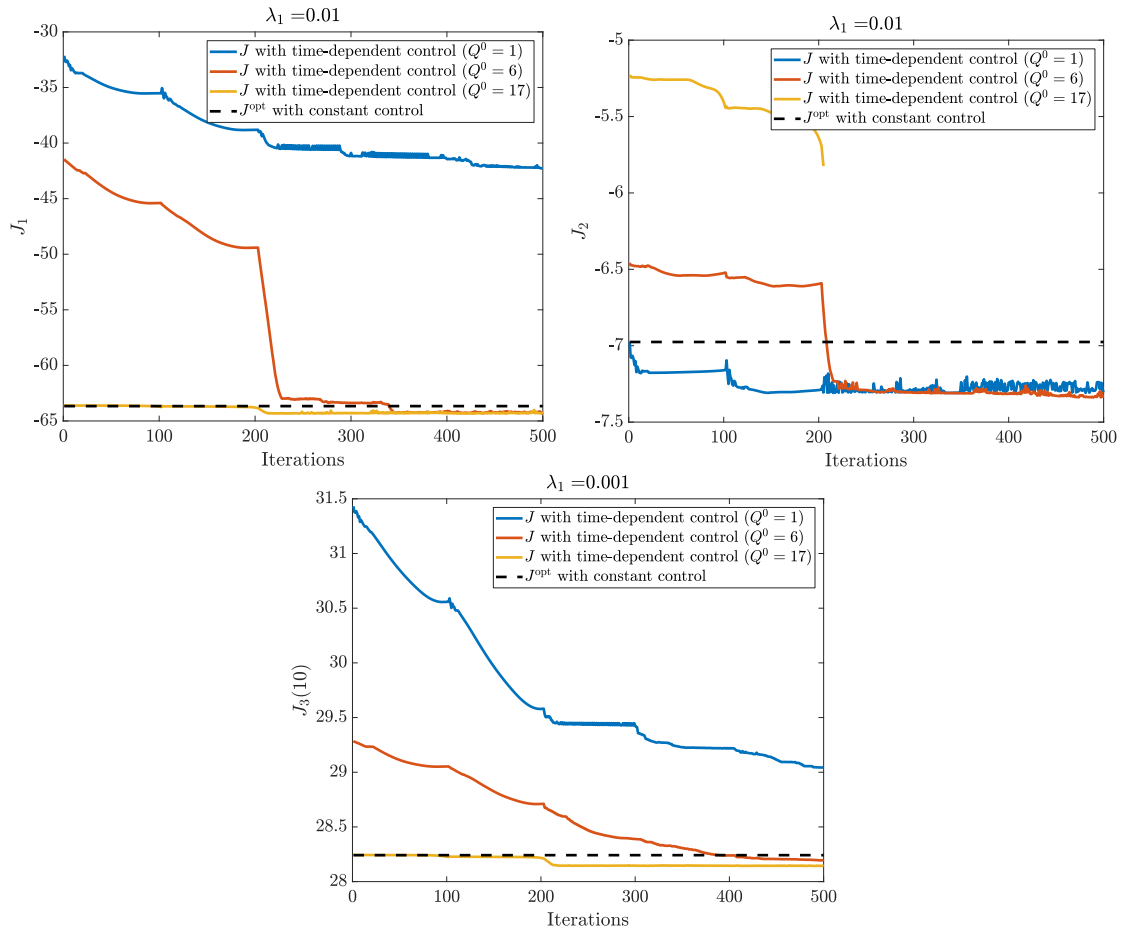


Figure 4.8: Evolution of the cost functionals during the optimization algorithm in the configurations J_1 and $\lambda_1 = 0.01$, J_2 and $\lambda_1 = 0.01$, and $J_3(10)$ and $\lambda_1 = 0.001$.

As in 2d, the closer the initial guess to the constant optimum, the lower the cost functional. After around 200 iterations, the lowest cost functionals stagnate and no further reduction is visible. It can be seen that the difference between the time-dependent and the constant optima is relatively small. In the next paragraph, the control corresponding to the “optimized” solution is illustrated and may give an explanation for the (small) decrease of the cost functional.

Optimal control. Figure 4.9 illustrates the time profile of Q_1 and Q_2 corresponding to the three configurations discussed in the previous paragraph. In the first and third cases, the slight decrease of the cost functional is obtained by turning off the control in the last seconds. This result is similar to the 2d boundary-driven optimization: the savings in the cost compensate the reduction of the stirring efficiency. Figure 4.10 illustrates the flow at the first and last time steps. The velocity magnitude (red vectors) is smaller at the last step, because of the decrease of the volume force (through Q_1 and Q_2).

The interpretation of the optimal control in the case J_2 with $\lambda_1 = 0.01$ is more delicate. In fact, two optimal controls are displayed: the one where the optimization solver started with an initial guess equal to 1, and the other with the initial guess 6. As it can be seen in the second plot of Figure 4.8, these initial guesses (blue and red lines) give very close values of J . However, the optimal controls leading to these values of J are quite different from each other: in the case $Q^0 = 1$, the controls remain close to 1 before being “turned-off” after 5 seconds, while in the case $Q^0 = 6$, the controls vary irregularly with a high amplitude, and decrease at the end of time range. This may indicate that there is not a unique optimal solution for the time-dependent case with J_2 and $\lambda_1 = 0.01$.

Originally, the idea behind using a time-dependent control consisted to check if a variation of the flow rate can induce a better stirring. In some cases, the optimization solver tested indeed some original profiles, more or less smooth (Figure 4.11). It is possible to recognize a “bang-bang-like” effect and different values for $Q_1(t)$ and $Q_2(t)$ on the left plot.

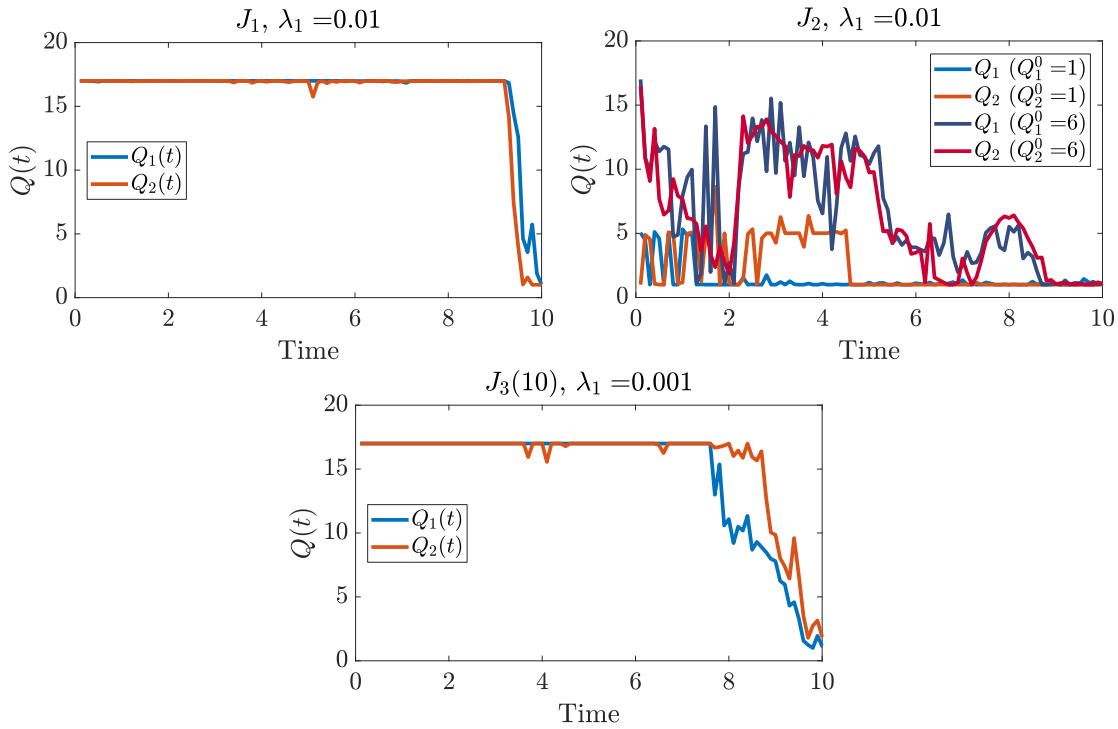


Figure 4.9: Time profile of Q_1 and Q_2 corresponding to the “optimized” solutions (see the corresponding configurations in Figure 4.8).

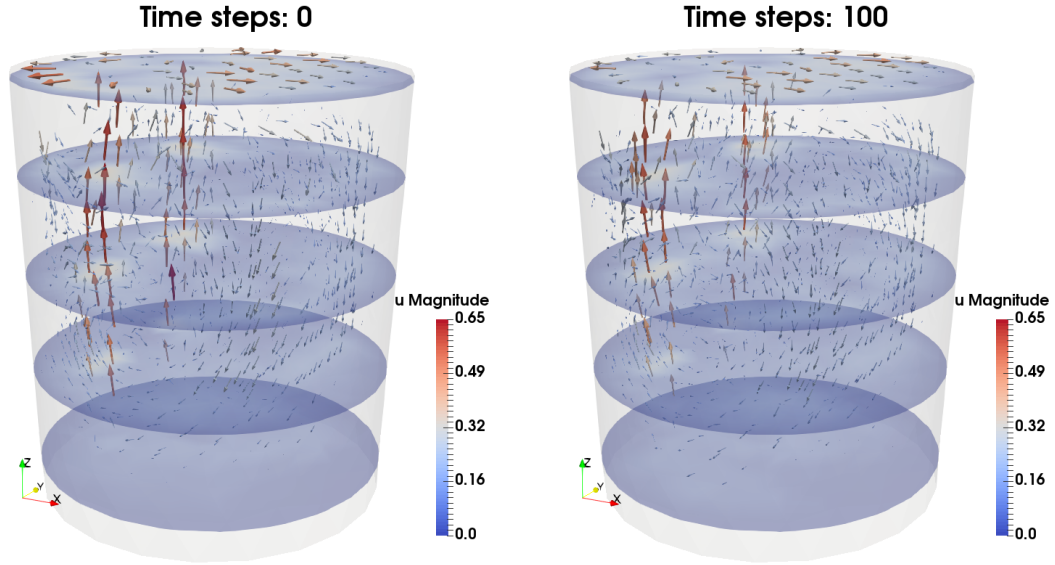


Figure 4.10: Flow at $t = 0$ and $t = 10$ with the “optimized” solution obtained with J_1 and $\lambda_1 = 0.01$. In the last steps, the velocities decrease because the flow rates Q_1 and Q_2 , which appear in the volume force, are reduced to Q_{\min} .

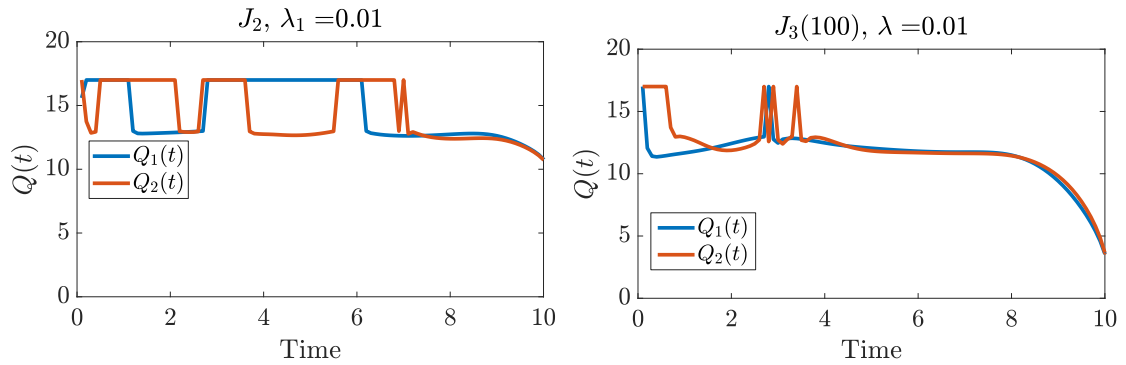


Figure 4.11: Examples of time profiles obtained during the optimization algorithm with time-dependent control. They correspond to suboptimal cost functionals.

However, in these cases, the cost functional is higher than constant-in-time results, i.e., these time profiles are less efficient than constant controls. Further investigations with some adjustment of the parameters (e.g., λ_1 and m) are needed to settle the question of whether a constant or pulsed flow rate is better for the mixing.

4.5.4 Optimization of the nozzles' positions

The objective of the third case study (Table 4.8) is to optimize the position of the nozzles at a fixed flow rate. In the industrial practice, the ladles are designed with given nozzles' positions. They cannot be moved. Usually, ladles with a unique nozzle are designed such that it is excentric. Ladles with two nozzles are similar to the experimental one studied in this work: the nozzles are approximately at the mid-radius and form a central angle of around 90° . The aim of this numerical study is to provide new ideas for the design of ladles for the long-term industrial practice, based on the optimal control theory and numerical investigations. The re-design of ladles being a very expensive investment, a solution obtained numerically has to be robust in terms of sensitiveness to numerical parameters (e. g., mesh size or modeling parameters such as C_S) and should be tested experimentally on a small laboratory-scale water ladle before having a chance to be adopted by the industry.

In the following, one configuration is considered. The gas flow rate is $Q = 17 \text{ l min}^{-1}$. We recall that the initial condition is zero and the flow is computed until $T = 20$. Furthermore, since the cost is independent of the nozzles' positions, any value of λ_1 leads to the same optimal configuration. We thus assume $\lambda_1 = 0$.

The nozzles can be located anywhere in the bottom without any penalty. In fact, since the only constraint on the nozzles' positions is Eq. (4.11), there is an infinite number of optimal solutions because of the central symmetry of the ladle. The solutions are obtained by rotations around the ladle center. To avoid this, one could fix the angular position of, e. g., nozzle 1. In this case, the number of solutions is reduced to two: one solution and its symmetry with the axis passing through nozzle 1 and the origin. The main benefit of using the constraint is that the optimization space is smaller. Since the optimization solver did not have convergence difficulties with the current controls, it was not necessary to add a constraint on the nozzles' position.

Convergence and cost functional. Convergence is reached with all four cost functionals (Table 4.13). Figure 4.12 shows the decrease of the Euclidean norm of the vector Δx . One can notice that the solver continues to iterate for J_1 (blue line) and $J_3(10)$ (yellow) although $|\Delta x|$ got smaller than 10^{-4} (at the 70th and 42th iteration, respectively). It is still unclear why the solver did not stop immediately when the stopping criteria was reached. The decrease of the cost functional is given in Figure 4.13. The value of the initial guess J^0 (first iteration in the plots) corresponds to the default nozzles' position. The optimal value J^{opt} (last iteration) corresponds to the optimized one. Comparing the reduction $\frac{J^{\text{opt}} - J^0}{J^0}$ of the cost functional, one observes that the most remarkable improvements, in comparison to the default position, are obtained with J_1 , J_2 , and $J_3(10)$:

- J_1 : $\sim -33\%$,
- J_2 : $\sim -16\%$,
- $J_3(10)$: $\sim -10\%$, and
- $J_3(100)$: $\sim -1\%$.

Table 4.13: Convergence of the solver, where $|\Delta x| = \sqrt{\sum_i |x_i^k - x_i^{k-1}|^2}$ and $|\Delta J| = |J^k - J^{k-1}|$ (optimization of the nozzles' positions).

Stopping criteria reached			
	$ \Delta x \leq 10^{-4}$	$ \Delta J \leq 10^{-5}$	nb. iter. ≥ 200
J_1	✓ (98 iter.)	-	-
J_2	✓ (48 iter.)	-	-
$J_3(10)$	✓ (49 iter.)	-	-
$J_3(100)$	-	✓ (58 iter.)	-

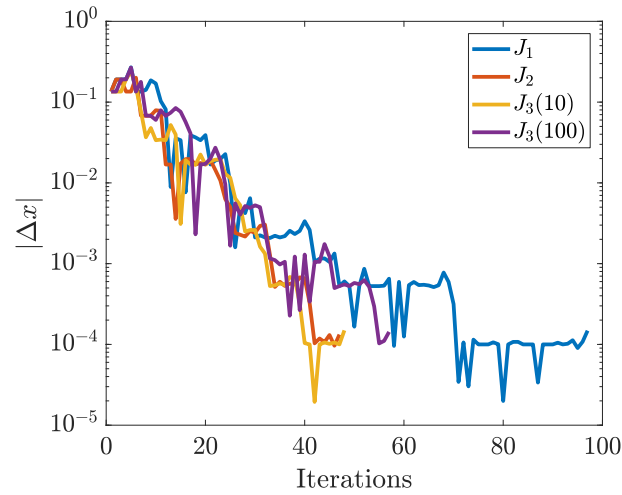


Figure 4.12: Convergence of $|\Delta x|$ (optimization of the nozzles' positions).

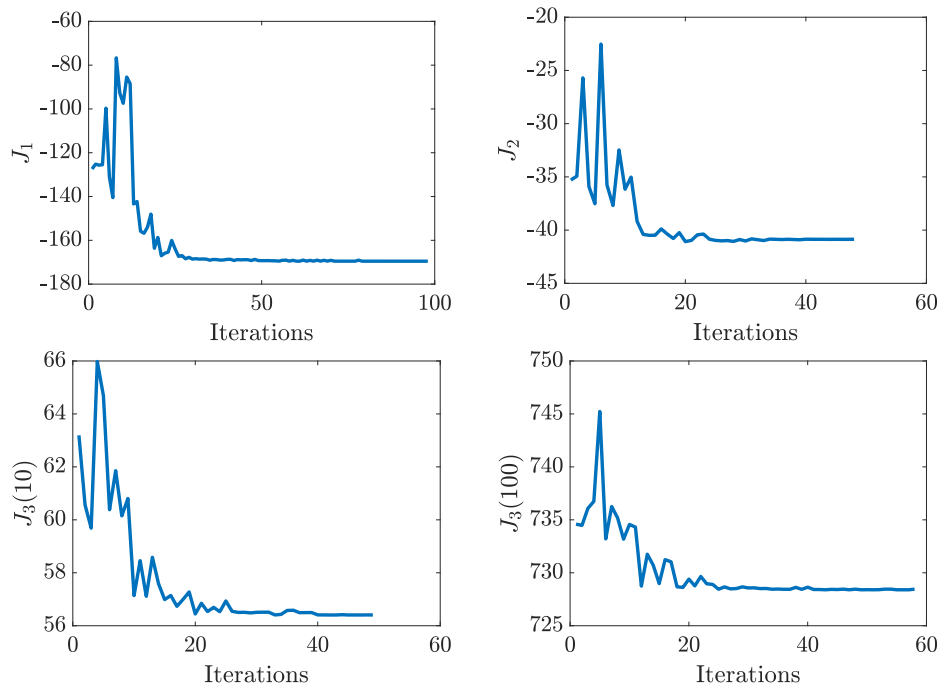


Figure 4.13: Cost functionals (optimization of the nozzles' position).

Optimal control. The computed optimal positions of the nozzles are given in Figure 4.14. The default one (top left) corresponds to the real positions of the water ladle of University of Oulu. As mentioned before, it is also chosen as the initial guess. With the cost functional J_1 (global maximization of vorticity), one obtains the following optimal solution: the two nozzles are superimposed at an excentric position, as if there were only one nozzle with the double amount of flow rate, leading to a reduction of 33% of the cost functional. The new position is closer to the wall than the default initial position. This configuration seems to correspond to the usual design of ladles with one eccentered nozzle. It is interesting to see that this position can be retrieved in the optimization study. In other words, the design of ladles with one excentric nozzle (at a distance 0.14 from the center) can be justified as being the one which maximizes the vorticity globally, i. e., on average in the ladle. In practice, this type of solution may be implemented immediately without designing a new ladle: one could close the gas valve of one of the nozzles, such that the total flow rate goes only through the other one. The current position is however a bit closer to the center ($0.105 < 0.14$), but the difference is not very high. Note that there is also some similarity between this solution and the 2d boundary-driven ladle: positioning the nozzles close to the wall with a high flow rate produces a high velocity along the walls, as it is done in the 2d case. The high vorticity generated locally suffices to increase the average in the ladle.

With J_2 (local maximization in the lower half of the ladle), the nozzles are more distanced from each other, and slightly closer to the wall than in the default case. The cost functional is improved by around 16%. With $J_3(10)$ (vorticity regulation over the threshold value 10), one nozzle is almost at the center, while the other one remains unchanged. The central nozzle perturbs the downward movement of the flow coming from the excentric nozzle, causing higher values on the sides of the ladle than in other solutions. Finally, the solution obtained with $J_3(100)$ is close to the default case, up to a central rotation of around 45° counter-clockwise. Consequently, the reduction of the cost functional is negligible ($< 1\%$) in comparison to the default positions.

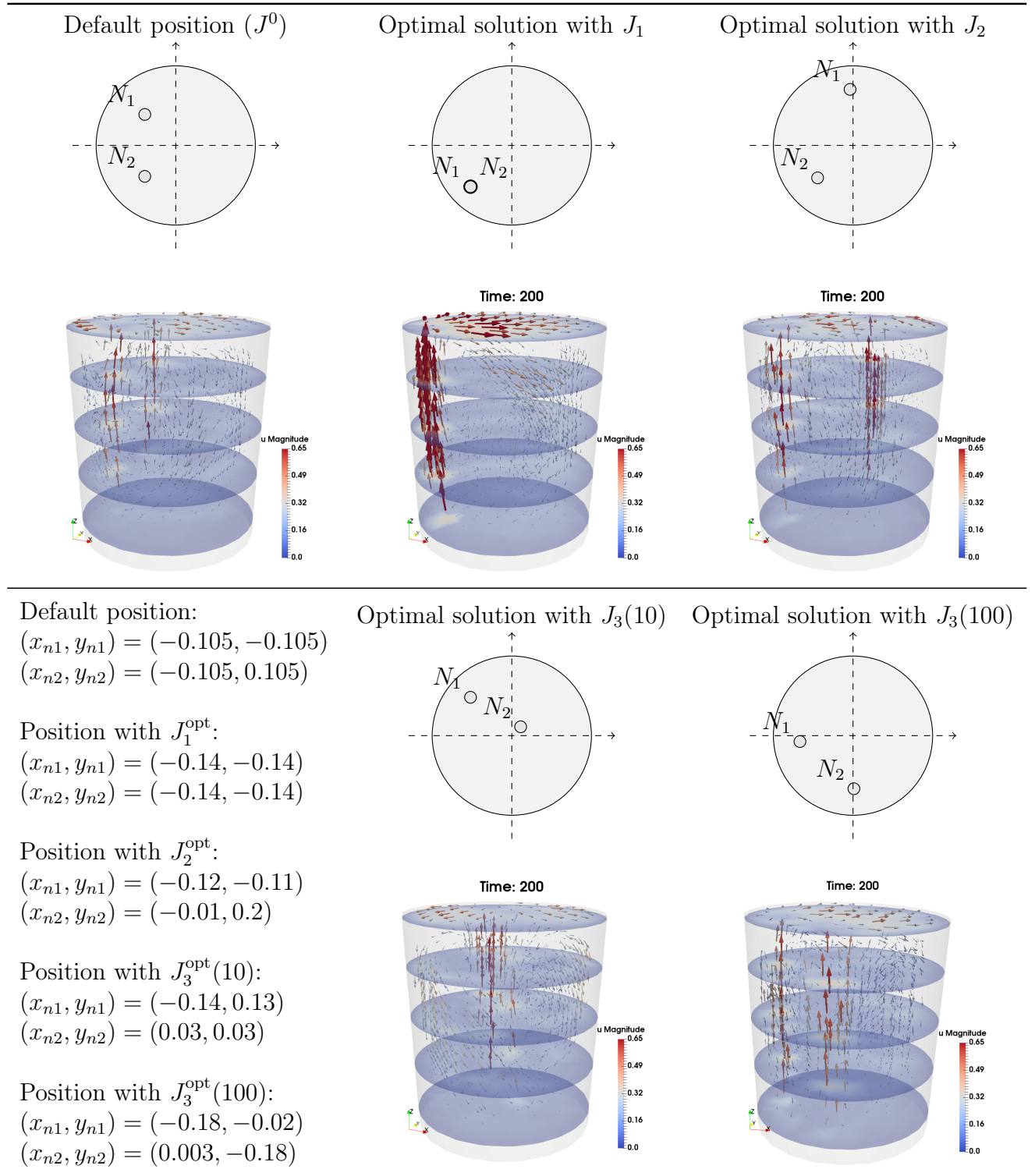


Figure 4.14: Optimal nozzles' positions for each of the four cost functionals and snapshot of the velocity field at the last time step.

4.5.5 Summary

The 3d model confirms somewhat the outcome of the 2d results. Indeed, several conclusions obtained in the boundary-driven model have been retrieved, for example:

- depending on the cost of the control λ_1 , a constant gas flow rate is generally a good solution, let it be $U_{P_{\max}}$ or $U_{P_{\min}}$,
- the optimal time-dependent control does not improve very much the constant control (order of magnitude $\sim 1\%$),
- the optimal control is also turned-off at the end of the time range,
- the profile of the control does not show periodic or regular oscillations but is rather irregular and may be technically difficult to implement.

Furthermore, the 3d model offers the possibility to optimize the nozzles' positions. The results show that there might be some room for improvement. In fact, the nozzles' position has more impact on the stirring pattern than the gas flow rate. Depending on the criteria, i.e., the cost functional, the optimal nozzle's position and the resulting stirring flow are quite different from one situation to the other. The case $J_3(100)$ seems to be the closest to the default case.

It may be interesting to test other values for the coefficients in the cost functional to check if one can obtain less obvious or intuitive solutions, in terms of gas flow rate, as well as nozzles' position. For example, by combining the two main terms using $\beta_1 \neq 0$ and $\beta_2 \neq 0$, applying other subdomains Ω_0 , and testing more values for λ_1 and m . It should also be kept in mind that the mesh, the time step Δt , the time range $[0, T]$, the Smagorinsky constant C_S , and the initial condition \mathbf{u}^0 can influence the resulting flow. Because all these aspects have not been investigated yet, the present work should be considered as a preliminary study or a proof-of-concept. It gives an idea of what one can obtain with the optimization of the Navier–Stokes equations applied to an industrial application. It also gives new orientations for future work, from the mathematical and numerical point of view, as well as the industrial perspective.

From the mathematical perspective, besides the aforementioned needed investigations, one should consider a more realistic description of the control Q rather than a freely evolving control. One can assume that the derivative of $Q(t)$ is bounded for example, in order to smooth the gas flow rate, or that $Q(t)$ has a given periodic profile, which is physically feasible. Only its shape, amplitude and frequency would be then optimized (see Section 4.1.1).

Regarding the industrial practice, it is important to compare the gas cost and the objectives of stirring process, in order to estimate λ_1 realistically. Based on this estimation, the presented results can provide some recommendation about the optimal control.

4.6 Conclusion

In an attempt to formulate the industrial ladle stirring problem within the framework of optimal flow control, several optimization models and numerical investigations were presented in this chapter. The variety of the models finds its origin, on the one hand, in the variety of state models described in Chapter 3, and on the other hand, in the different possibilities for the cost functional. Several configurations were set up for the numerical investigation. For example, one objective was to study if constant but different gas flow rates for each nozzle could improve the stirring. In (Haiyan et al., 2016), it was found, indeed, that this can reduce the mixing time. Similarly, by allowing a time-dependency for the control, the objective was to study whether a constant or a varying one is better for stirring, as in (Nadif et al., 2011). Even though the type of stirring is different, the authors found experimentally and industrially that a pulsed stirring reduces the mixing time and/or gas consumption. The last study case focused on the optimization of the nozzles' position.

The results obtained so far, using a gradient-free optimization solver, show a tendency of the control variables towards their minimum or maximum bounds, depending on the weight of the control cost. As summarized earlier, a constant gas flow rate for both nozzles is already equal or close to the optimum. An oscillating or pulsed control was not found to be better than a constant control. In comparison to literature, our preliminary results could not reproduce numerically the findings from (Nadif et al., 2011, Haiyan et al., 2016). The study also evidenced that, by turning-off the control at the end of stirring, one could spare some gas cost without deteriorating the stirring efficiency. Altogether, the gain of cost is around or smaller than 1%.

If the numerical results obtained here were to be translated to the industrial practice, one would suggest, first, to determine the order of magnitude of the ratio β_i/λ_i . Indeed, it is still not clear how important the control cost is in relation to the cost of a loss in stirring efficiency. If the cost of the control is negligible, then one can apply a constant gas flow rate as high as possible and just turn it off in the last seconds or dozens of seconds of the stirring process. Although simple and not innovative, this result has the merit of not contradicting intuition.

Second, the study showed that there is room for optimization concerning the nozzles' position. Significant improvements seem to be feasible. This could be taken into account in the long-term industrial perspective, when designing new ladles for example. In order to provide robust recommendations, a more detailed numerical study is currently under investigation.

4.6.1 Limits and outlook

It is important to stress the limits of the model before drawing any definitive conclusion for the industrial practice. First of all, it is not straightforward to define an appropriate cost functional. One ends up either in the ambiguities of the stirring efficiency concept or in the intangibility of the vorticity. The current cost functionals, based on the vorticity, suffer indeed from the lack of measurability,

i.e., there is currently no way to relate the vorticity to a measurable quantity, and to know what a “good vorticity” is. To overcome this difficulty, it is possible to use an alternative definition of stirring efficiency: the *mixing time*. This offers a balance between the modeling aspect and the reality: the cost functional can be easily expressed in mathematical terms and its physical interpretation is clear and measurable. However, if the problem becomes more realistic, it ends up in a difficult *time optimal control*, which is addressed only rarely in literature. In the next section, we sketch this innovative approach and present some aspects of it. The idea can be investigated in future works.

The second serious limit of the present models concerns the description of gas stirring. The modeling of gas in the single-phase model has intrinsically a local effect in space. In 2d, it is incorporated as a boundary velocity (4.8) while in 3d, it is a volume force localized in a form of two truncated cones (4.10). The control variable U_P and Q acts like a factor in these models. Therefore, its effects apply rather on the *flow magnitude* than on the *flow structure*. Thus, it is difficult to improve, or even influence, the flow globally in space using optimization on the too simplistic single-phase models. One could think of using multiphase models to overcome this difficulty. The optimization problem may be more complex, but it describes more realistically the flow structures because it can take into account bubbles’ wandering, merging, breakups, and expansion, which are all absent from the single-phase model. The mixing pattern might be better described with multiphase models than with single-phase models. However, there is some doubt about a significant change of the results with multiphase models: the control is still focused on the gas quantity Q and does not impact directly the flow structures.

In order to induce a significant change in the flow pattern, modifying the nozzles’ position is an interesting control variable. If it is rather difficult to change on real ladles, it is not the case in BOF converters. In these converters, up to eight gas injection devices can be positioned almost freely in the bottom because they are mounted into the refractory bricks. Thus, the question of the optimal location of the nozzles becomes more interesting for this application. They can be treated with an optimization model similar to the present work.

In all cases, the particular control mechanism of gas stirring, i.e., bottom injection, might be the fundamental limit for the results obtained so far. In order to control the stirring precisely in space, a volume control is the most suitable. Here, we can stress on the existence of *electromagnetic ladle stirring*, where inductors are placed around the ladle and generate a magnetic field. Because the steel is ferromagnetic, it can flow according to the amplitude and frequency of the magnetic field. Such *magnetohydrodynamic (MHD) processes* are studied, e.g., in (Marioni et al., 2017), where the authors compute a magnetically-driven two-phase turbulent flow. In terms of optimal control problem, the control is a volume force appearing in the Navier–Stokes equations, see (Tröltzsch, 2010, Section 5.10.2).

The electromagnetic stirring is, with the multiphase models, the mixing time optimal control problem, and the optimization of BOF converters, one of four research directions which can be explored to overcome some of the limits of this work, or to extend its scope, with potentially interesting results for both applied mathematics and metallurgy research communities.

4.6.2 Towards new approaches for the optimal stirring control

In Section 4.2.2, one of the definitions of stirring efficiency pointed out was the mixing time. Using this definition in the context of optimal control of ladle stirring leads to an interesting alternative to the models considered so far. Therefore, we propose to discuss it in the next paragraphs and develop some ideas.

The mixing time can be considered as a good indicator of the stirring efficiency: a short mixing time means that the stirring was efficient. Consequently, the stirring is optimal when the mixing time is minimized. This is physically easier to interpret than the ones based on the vorticity, because mixing times can be measured in laboratory conditions, for example by using a tracer in water models.

Mathematically, the model has to compute the evolution of the species' concentration c being mixed in the fluid. This is typically a convection-diffusion equation of the form (Zhu et al., 1996, Geng et al., 2010, Li et al., 2015):

$$\frac{\partial}{\partial t}(\rho c) + \mathbf{u} \cdot \nabla(\rho c) = \nabla \cdot (\mu \nabla c). \quad (4.45)$$

Equation (4.45) is coupled to the flow equations through \mathbf{u} and depends therefore on the control variables. The mixing time T_{mix} is defined as the minimum time needed for the concentration to reach its steady-state value c_∞ up to, e.g., $\pm 5\%$,

$$\begin{aligned} T_{\text{mix}} &:= \inf\{t \in [0, T], \|c(\mathbf{x}, t) - c_\infty\|_{L_2}^2 \leq 0.05\} \\ \iff \forall t \geq T_{\text{mix}} \quad &\|c(\mathbf{x}, t) - c_\infty\|_{L_2}^2 \leq 0.05. \end{aligned} \quad (4.46)$$

It depends implicitly on the controls. Using these notations, the objective is to minimize the mixing time, regularized by the cost of the controls:

$$\min \quad \frac{1}{2} T_{\text{mix}}^2 + \frac{1}{2} \int_0^T \lambda_1 \|\mathbf{f}\|_{L^2(\Omega)}^2 + \lambda_2 \|\mathbf{b}\|_{L^2(\Gamma_{\text{axis}})}^2 dt,$$

subject to the flow equations, to (4.45), to the mixing time constraint (4.46), and to the initial and boundary conditions, namely,

$$\begin{aligned} T_{\text{mix}} &= \inf\{t \in [0, T], \|c(\mathbf{x}, t) - c_\infty\|_{L_2}^2 \leq 0.05\}, \\ \frac{\partial}{\partial t}(\rho c) + \mathbf{u} \cdot \nabla(\rho c) &= \nabla \cdot (\mu \nabla c), \\ \nabla c \cdot \mathbf{n} &= 0 \quad \text{in } (0, T] \times \partial\Omega, \\ c(\mathbf{x}, 0) &= c^0. \end{aligned}$$

Such an optimization problem which *minimizes the time needed to reach some desired state* is called a *time optimal control problem*. The formulation above is inspired by (Nguyet et al., 2019), where Navier–Stokes–Voigt equations are studied. The main difference in our model is that the “desired state” is not based on \mathbf{u} , like in their paper, but on c , which intervenes in an additional equation coupled to the Navier–Stokes equations. The initial condition c^0 models the initial concentration of the tracer in the bath: it is often zero everywhere except in a small area, where

the tracer is injected at the beginning of the measurement of the mixing time. The end concentration c_∞ is given by $\frac{\int_\Omega c^0(\mathbf{x}) \, d\mathbf{x}}{|\int_\Omega d\mathbf{x}|}$. We restrict ourselves here with the formulation of the optimization problem. The reader is referred to (Nguyet et al., 2019), and (Fernández-Cara, E., 2012) for more details on time optimal control problems based on the Navier–Stokes equations.

In the problem above, one minimizes the treatment time given initial and end concentrations of a species. One can move a step backward and consider a closely related but more classical *tracking-type optimal control problem*, by modeling the removal of inclusion using the species' concentration c . In this case, the efficiency of the stirring is described by the end value of inclusions after a given time of treatment. The lower the level of inclusions, the better the stirring. The optimal stirring delivers the minimum value of inclusions at the end of the treatment.

The computation of the species' concentration is widely spread in the metallurgy literature. For example, (Yu, 2014) models the removal of hydrogen (dehydrogenation) and nitrogen (denitrogenation) using species transport equations of the form (4.45) with an additional source term S . The author considers a two-phase flow (gas-liquid) where the phase fraction of phase q is given by φ_q . Defining the concentration $c_{X,q}$ of species $X = \text{Hydrogen}$ or $X = \text{Nitrogen}$, in the phase $q = \text{steel}$ or $q = \text{gas}$, one has

$$\frac{\partial}{\partial t}(\varphi_q \rho_q c_{X,q}) + \mathbf{u}_q \cdot \nabla(\varphi_q \rho_q c_{X,q}) = \nabla \cdot (\mu_q \nabla \varphi_q c_{X,q}) + S_{X,q}. \quad (4.47)$$

Equation (4.47) is coupled to the flow equations through \mathbf{u}_q , and depends therefore on the control variables. Using these notations, the objective is to minimize the final content of the dissolved species $c_{[X],\text{steel}}(t = T)$ in the liquid steel, for both $X = \text{Hydrogen}$ and $X = \text{Nitrogen}$, at the end time of the treatment T :

$$\min \quad \frac{1}{2} \|c_{[X],\text{steel}}(\mathbf{x}, T)\|_{L^2(\Omega)}^2,$$

subject to the flow equations and to (4.47). Such an optimization problem is studied in, e.g., (Abergel and Temam, 1990, Section 3.). There, the authors minimize the turbulence induced by the temperature gradient by controlling the boundary velocity in a lid-driven square unit. The reader is referred to this article for more details on the optimization of coupled systems of PDEs.

One can see how these approaches, which have an easier physical interpretation than the vorticity, are more complex and more difficult to solve in terms of optimization problems. A set of coupled PDEs has to be taken into account, and the time optimal control introduces new theoretical and algorithmic difficulties. From the perspective of computational numerics, these approaches require more resources than the models computed in this work. This is, finally, one major reason for choosing, in this thesis, a simplified model based on the single-phase model and the vorticity in the cost functional.

5. Ladle vibrations induced by gas stirring: a first step towards an operational stirring control

Motivation. One important aspect of the thesis is the application of the results in the industrial practice. If one can compute the optimal stirring parameters mathematically, implementing it in practice introduces new challenges related to the process control (Section 1.3). Currently, the most common way to control the stirring process consists to monitor the image of the bath surface captured by a video camera placed above the tank. Operators can observe how the steel and the slag behave under gas stirring. Furthermore, a gas flow-meter displays the quantity of gas injected in the ladle. Depending on the desired steel grade, on the initial quantity of inclusions measured before stirring, and on other practical constraints (temperature, alloying, etc...), the operators adjust the flow rate manually. The main problem of this kind of control is that it depends on the operators' experience and "feelings", which are quite subjective. Although the flow-meter might provide a more objective, quantitative, and reproducible way of controlling the process, it is known, from experience, to be sometimes unreliable. For example, the operators can observe a calm bath surface whereas the flow-meter displays a strong stirring. This overestimation of the actual flow rate can happen when there is a gas leakage or when a nozzle is clogged. Thus, the question of finding a reliable measurement of the real stirring is still of interest for the industry. Only with such a measurement, it is possible to control precisely and automatically the stirring process in an optimal way.

Outline. There are mainly two techniques to measure the actual stirring: the open eye area measurement and the ladle vibrations. They are presented and compared in Section 5.1. It turns out that, in general, the open eye area measurement is appropriate in standard ladles, while vibration measurements are considered to be more suitable for vacuum treatments. Then, the vacuum degassing process of the industrial partner is described in Section 5.2, as well as the existing results concerning vibration measurements. Since this work focuses on the vacuum tank degassing process, the vibrations measurements are studied. Due to the complexity of the industrial reality, an experimental campaign on a physical model of a steelmaking ladle has been performed, with the objective of quantifying the link between ladle vibrations and stirring intensity. The laboratory experiment is described in Section 5.3.

5.1 Literature review of stirring control techniques

The two research subjects focused on the problem of stirring control gained attention quite recently:

- open eye area: (Burty et al., 2006, 2007, Valentin et al., 2008, Alexis et al., 2011, Dannert et al., 2012, Nadif et al., 2012, Rödl et al., 2016, Ramasetti et al., 2019a,b),
- vibration: (Burty et al., 2007, Nadif et al., 2012, Behera et al., 2014, Yenus et al., 2016, Fischer et al., 2017, Alia et al., 2019b).

Most of the papers focus on standard ladles. Vacuum stirring is treated in (Koehle et al., 2001, Burty et al., 2006, Nadif et al., 2012).

Process control based on the open eye. The first technique is based on the measurement of the *open eye* by a camera. The open eye, also called *slag eye*, is the name of the area of liquid steel which is in contact with the atmosphere at the bath surface. When the stirring is strong enough, the rising gas breaks through the slag and pushes it away, letting an area of liquid steel be not covered by slag (Figure 5.1). It was found that this area is a good indicator of the internal stirring in the bath. It can be used as an on-line measurement of the actual stirring in the following way:

- 1) a video-camera captures the open eye continuously and in real time,
- 2) an image-treatment software estimates its area \mathcal{A} (Figure 5.1),
- 3) using preliminary numerical simulations, the relation between stirring intensity and slag eye area is computed, e.g., $\mathcal{A} = f(Q)$,
- 4) using the measured area, one can estimate the actual stirring: $Q = f^{-1}(\mathcal{A})$.

The gas flow rate can then be increased or decreased to obtain the desired stirring intensity. This technique was successfully used in, e.g., (Burty et al., 2007, Nadif et al., 2012, Rödl et al., 2016). However, it has several drawbacks. At high gas flow rate (*strong stirring*), the area of the open eye is often big and irregular, and therefore, difficult to measure. This is in particular true in vacuum tank degassers, where the gas stirring is so intense, and the slag eye so big, that its border is beyond the perspective of the camera. At low flow rates (*soft stirring*), the open eye is usually too small to be clearly detected by the camera. It was also mentioned that the image treatment is difficult to implement in the industrial practice and that it can sometimes give unreliable measurements of \mathcal{A} . Finally, the area depends on the slag properties, e.g., thickness, density, and viscosity (Ramasetti et al., 2019b). These are not always known accurately and can vary from a batch to another (Burty et al., 2007). If the same numerical model is used for all heats, it can give incorrect estimations of the gas flow. One possibility is to use stochastic models to take into account the variability of the slag properties. To the best of the author's knowledge, no model of this kind has been proposed so far in the literature. In sum, the measurements of the open eye area require favorable stirring conditions, which are difficult to find in vacuum tank degassers. If this technique proved to work in standard ladles, its application for vacuum stirring is more challenging.

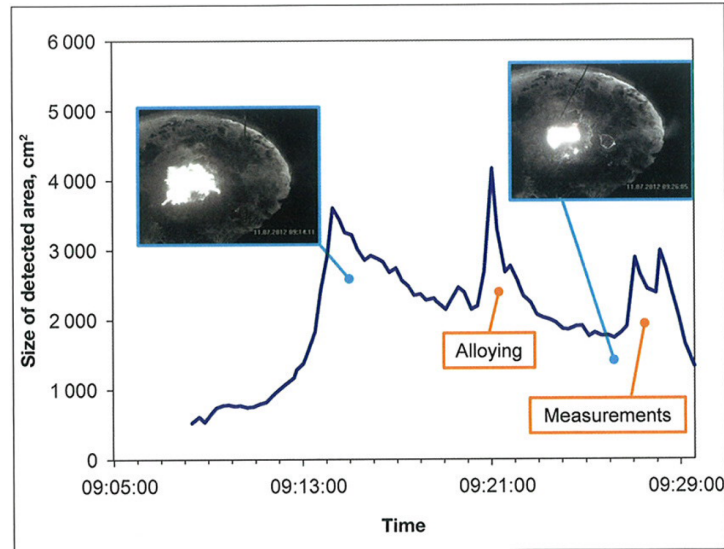


Figure 5.1: Evolution of the open eye area during the stirring (Rödl et al., 2016).

Process control based on the ladle vibrations. The second possibility is based on the measurements of the ladle wall vibrations. Preliminary studies have shown that the vibration increase with the stirring intensity. Unlike the slag eye technique, which uses numerical simulations, the vibration models are empirical: the relation between the vibration and the stirring intensity is based on statistical regression of a large amount of process and quality data, (Nadif et al., 2012). Then, following the same principle as the open eye, it is possible to retrieve the actual stirring efficiency from the vibration measurements. This solution has been successfully implemented in industrial conditions, (Nadif et al., 2012, Behera et al., 2014). Its main advantage in comparison to the slag eye measurement is its relatively cheap cost: the vibration sensors and the signal treatment can usually be found on-the-shelf, which is less expensive than designing a specific image treatment software. Another advantage is that it is applicable on vacuum tank degassers (Nadif et al., 2012), e.g., the vibrations intensity increases with the gas flow rate also in vacuum conditions. In addition, it works when the sensors are not directly placed on the ladle, but on the outside tank. However, its main drawback is the sensitivity of the vibrations to noise disturbances (Rödl et al., 2016): the signal needs to be filtered and treated correctly to eliminate perturbation noise coming from, e.g., surrounding equipments. Also the age and shape of the refractory lining inside the ladle might influence the vibration level. All in all, interpreting the measurements is a delicate task and requires proper signal analysis techniques.

In the context of the present joint work with the industry, we focus on the need of the partner company, SSAB: vacuum tank degassing. It was observed that the open eye could not be measured reliably in vacuum conditions either because it covers the whole image or because of the dust and splashes during the process. Furthermore, internal studies with one vibration sensor on the outside tank were undertaken with promising results. For these reasons, the rest of this chapter considers the vibration measurements technique.

5.2 Description of the industrial process

5.2.1 Vacuum tank degasser (VTD)

A schematic vacuum tank degasser (VTD) is illustrated in Figure 5.2. The whole structure comprises different solid components, but the main ones are: the ladle, the housing, and the cover. The different steps of the process and the role of each part are briefly explained here:

1. The ladle (⑤) is the vessel containing the liquid steel. Once filled, it is moved from one process station to another in the plant, via a crane. The interior of the ladle is built with layers of different refractory materials (called lining) which can resist to very high temperatures and chemical wear. For more clarity, they are not represented in Figure 5.2.
2. When it arrives to the VTD, it is put in the housing (⑥) with the crane (the VTD station is first uncovered). Two supporting arms on the left and the right in the interior of the housing hold the ladle, i. e., the ladle is hanging.
3. When the ladle is installed inside the VTD, the plugs for gas injection (②) are connected to gas pipes in the housing through a spring mechanism, without any direct intervention of the operators. Thanks to the crane, the positioning of the ladle is very precise, thus allowing the connection to be done correctly. The gas pipes are not represented in Figure 5.2.
4. Once the ladle is put and connected, the whole housing, which is actually on a moving platform, moves to the vacuum station, below the cover (⑦). Two rails guide the wheels of the platform.
5. The cover goes down and is sealed into the housing. The interior of the cover is composed of refractory material to withstand the very high temperatures. It also has several openings to allow alloying, temperature measurements and steel sampling. A camera is placed in the cover and enables to see the steel surface in live conditions through a hole in the refractory materials. These details are not represented in Figure 5.2. The previous steps take approximately 10 minutes.

- ① Fluid domain
- ② Porous plugs for gas input
- ③ Ladle wall, interface between fluid and structure
- ④ Gas outflow/exhaust induced by vacuum pump
- ⑤ Ladle
- ⑥ Housing
- ⑦ Cover to confine ladle for vacuum
- ⑧ Vibration sensor on the external wall of the housing

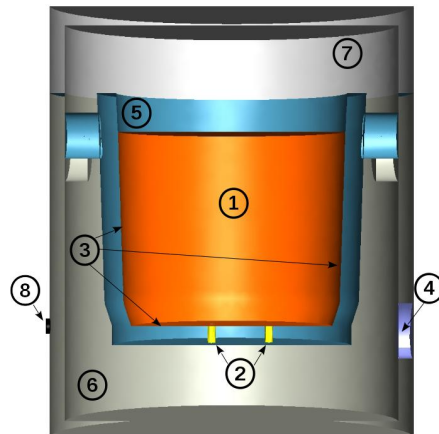


Figure 5.2: Cut plane view of a schematic vacuum tank degasser.

6. Vacuum pumping (4) starts (~ 5 minutes). The stirring process in vacuum conditions begins (15 to 25 minutes).
7. Once the process is finished, temperature measurements and steel sampling are performed (~ 10 minutes). Then, the opposite steps are done: return to atmospheric pressure, opening of the cover, movement of the station to its initial position, and uplift of the ladle with the crane, towards the casting station. In total, the treatment takes 40 to 50 minutes.

5.2.2 Vibrations of the VTD

The objective of this subsection is to give a brief overview on the existing work done on the vibrations of the VTD at SSAB Europe Oy in Raahé, Finland.

Position of the accelerometers. As in other industrial cases (Nadif et al., 2012, Fischer et al., 2017), a sensor has been placed on the exterior wall of the housing. Since the ladle itself is at very high temperature and because it moves in the plant, it is not practical to place the sensor on the ladle wall. The housing is more suitable for a process control: vibrations of all the batches can be measured, the temperature is not too high for the sensor, and maintenance of the sensor can be done easily. Furthermore, preliminary internal studies have shown that a correlation between stirring and vibration intensity exists, even when the vibration is not measured directly on the ladle wall, but on the outside tank. The exact position of the sensor then depends mainly on ease of access and mounting. To give a rough idea of the position of the sensor on the VTD, it is represented in Figure 5.2 (number (8)).

Preliminary vibrations study. The main existing results regarding vibrations measurements in SSAB are reported in (Pylvänäinen et al., 2016). The study consisted in gathering and analyzing a large amount of data to quantify the correlation between vibrations and stirring intensity. The vibrations in horizontal and vertical directions of roughly 220 heats were collected. It was shown that the relationship between the gas flow rate and the vibration velocity is linear, but the slope of the regression line can vary by a factor of up to 2 from one heat to another. This slope coefficient can be understood as an indicator for the efficiency of gas-stirring. For example, a significant change in the slope may indicate clogging of a gas nozzle. Another study focuses on the use of vibrations data to model desulfurization, i.e., to predict the final content of sulfur given the initial content and the vibrations during stirring (Pylvänäinen et al., 2018, unpublished). It was shown that the uncertainty of some kinetic parameter is unsatisfactorily high, which makes the model not suitable for prediction. The necessity of vibrations filtering and treatment are also stressed. Altogether, although the vibrations measurements are relatively easy to perform, the data treatment and its application for stirring control are not straightforward.

5.2.3 From industrial to laboratory measurements

A better understanding of the vibrations is necessary for a successful industrial application. Ideally, a proof-of-concept should be performed to demonstrate how

the vibrations technique can work. In this regard, the laboratory-scale water ladles are again of interest. Some justifications in favor of a laboratory campaign are: the absence of noise perturbations and simplified assumptions for numerical modeling.

The industrial environment is full of vibrating machines around the VTD. They can perturb the measured ladle vibration. In laboratory, the noise perturbations are more likely to be negligible, so that the vibrations measured are only due to gas stirring. This leads to clearer measurements and a better correlation between vibrations and gas flow rate. From the point of view of numerical modeling, one could be interested in computing the “optimal vibration level”, e. g., the one induced by some optimal stirring, as the ones obtained in Chapter 4. This, in turn, can be used as target values, to be reached by on-line vibration measurements, and to control the stirring treatment automatically. Such a modeling process requires not only a fluid-structure model, but also a proper (sub-)model for the structure alone. Modeling the real ladle geometry is a difficult task:

- Because it contains several materials (refractory material inside the ladle and steel frame of the ladle and housing), the structure is heterogeneous. In other words, the material properties, e. g., the density and the Lamé coefficients, are not constant in the structure domain. They might even be discontinuous.
- Since the vibration sensor is located at the exterior of the housing, the propagation of the vibrations from the ladle to the housing has to be taken into account. In other words, the contact between the ladle and the housing has to be carefully modeled (one solid or two solids with contact friction).
- Finally, another difficulty comes from the refractory materials. Because of intense erosion, their thickness varies a lot between ladles, and even inside the same ladle. After several treatments, the ladle goes to maintenance and the vessel is relined. Some information can be found about the nominal thickness but there is a lack of information on the on-line lining thickness.

Given the complexity of the structure and its interfaces, a simplified geometry might be interesting to overcome these obstacles. Since the geometry is much simplified in the laboratory case, it is worthwhile to start modeling the laboratory-scale ladle instead of treating directly the industrial problem. This strategy offers several other advantages. First, a fluid model has already been computed and validated by comparing the numerical results with experimental measurements (Chapter 3). Second, the fluid-structure model can be validated more easily when it is compared with the vibration of the laboratory-scale ladle, than with industrial measurements. Finally, the cost for performing vibration measurements in laboratory is relatively reduced: one just needs to mount accelerometers at the wall of an existing water tank and acquire the vibration with different air flow rates. Since the water ladle was available in the laboratory of the Process Metallurgy Research Unit in the University of Oulu, an experimental campaign could be conducted quickly and at reduced costs. For all these reasons, a laboratory-scale ladle was considered. The objectives of the experimental campaign were to investigate the vibrations, collect data, and give new insights for the industrial applications with respect to the number and position of sensors.

5.3 Laboratory-scale ladle experiment with multiple sensors

A detailed literature review concerning vibrations measurements in ladle metallurgy is given in (Alia et al., 2019b). It has been shown that most of the studies use only one sensor, whose position is chosen after preliminary trials or with maintenance-related criteria (ease of access and mounting). An alternative approach consists in using multiple sensors. They allow simultaneous measurements at different radial and axial positions, and may improve the interpretation of vibrations signals, especially in the case of excentric gas injection nozzles. Indeed, such nozzles generate plumes which are not axial-symmetrical and whose effect on the ladle walls is therefore expected to be not symmetrical as well. In this regard, the use of multiple sensors at different locations of the ladle wall combined with excentric nozzles appears relevant.

The main objective of the experimental campaign is to provide new recommendations concerning the optimal number and position of vibrations sensors for industrial stirring monitoring. More specifically, the study focuses on a laboratory-scale ladle with two excentric nozzles and eight accelerometers covering the ladle wall. A side benefit of the experiment is to collect experimental data, at several points of the ladle surface, which can be later used for the validation of fluid-structure interaction models. For comparison, the industrial data with only one sensor might be insufficient for evaluating the relevance of a numerical model. Most of the results presented in this section can be found in (Alia et al., 2019b).

5.3.1 Experimental set-up

The water ladle, illustrated in Figure 5.3, is the same modeled numerically in the previous chapters. The influence of four process parameters on the vibration are studied, with a total of 108 configurations (Table 5.1). Concerning the vibrations measurements, eight mono-axial accelerometers of type MMF KS80D have been used. Existing results from literature have shown that the vibrations have the highest amplitude when the sensors are perpendicular to the ladle wall, i.e., on the horizontal axis (Nadif et al., 2012, Yenus et al., 2017). PVC blocks were specially manufactured with an appropriate shape to fit on the outside tank wall. The vibration sensors are then screwed on these blocks. The total mass of one accelerometer with its mounting PVC block is 99 g and is negligible in comparison to the ladle mass. Therefore, it is assumed that the eight mounted sensors do not impact the mechanical and vibrational behavior of the ladle to a significant extent.

Table 5.1: Configurations of the experimental campaign (Alia et al., 2019b).

Water height	Q for each nozzle	Oil level	Nozzles
$H_1 = 32.5$ cm	5, 10, 15,	0 cm (without oil)	Nozzle NW only
$H_2 = 54$ cm	20, 25, 30 l min ⁻¹	3 cm (with oil)	Nozzle SW only
$H_3 = 65$ cm			Both nozzles

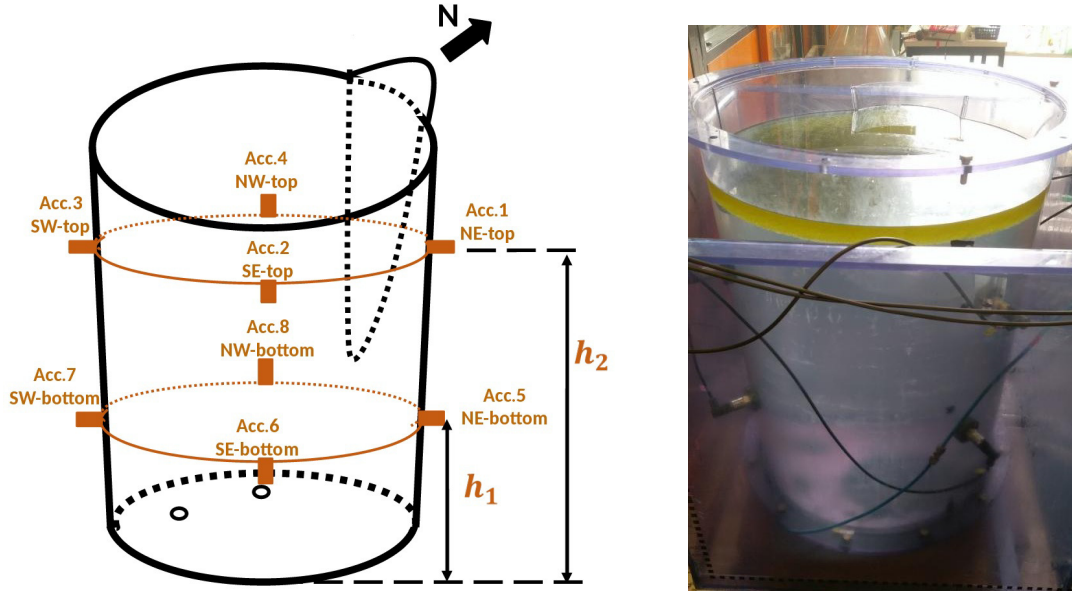


Figure 5.3: Water tank vibration experiment. Left: Position and designation of accelerometers ($h_1 = 25$ cm and $h_2 = 54$ cm). Right: Real water tank model with oil layer. Two sensors at h_1 can be seen clearly and two sensors at h_2 are behind the cables (Alia et al., 2019b).

In each of the 108 tested cases, five minutes of stirring are recorded simultaneously for the eight sensors using a data acquisition module (sampling frequency 25.6 kHz).

The recording process is as follows:

- (1) initially, the ladle is at rest during 30 s.,
- (2) at the 30th second, the gas valves are opened to the target flow rate value,
- (3) the stirring runs at a constant gas flow rate during 180 s.,
- (4) at the 210th second, the gas valves are closed, and the bath returns to rest until the end of the recording (300th second).

A suitable quantity to represent the vibration amplitude or intensity is the root mean square (RMS) value of the acceleration signals, in m s^{-2} , (Norton, 2003). The root mean square values are computed between the 40th and 200th s in order to avoid transitional phases and to capture a stirring as constant as possible.

5.3.2 Experimental results

Figure 5.4 shows the vibration signal and the corresponding frequency spectrum with increasing gas flow rates, in one of the configurations. If there is no clear pattern in the vibration signals, one can nevertheless observe the increasing amplitudes when the gas flow rate increases. Among all configurations, we focus here on the nominal case, i. e., the one which is physically similar to the industrial ladle: water height H_3 , presence of oil, two nozzles operating.

The evolution of the vibration RMS of the eight sensors with respect to the gas flow rate is illustrated in Figure 5.5. As reported in, e. g., (Nadif et al., 2012, Yenus et al., 2017), the vibration amplitude increases with the gas flow rate.

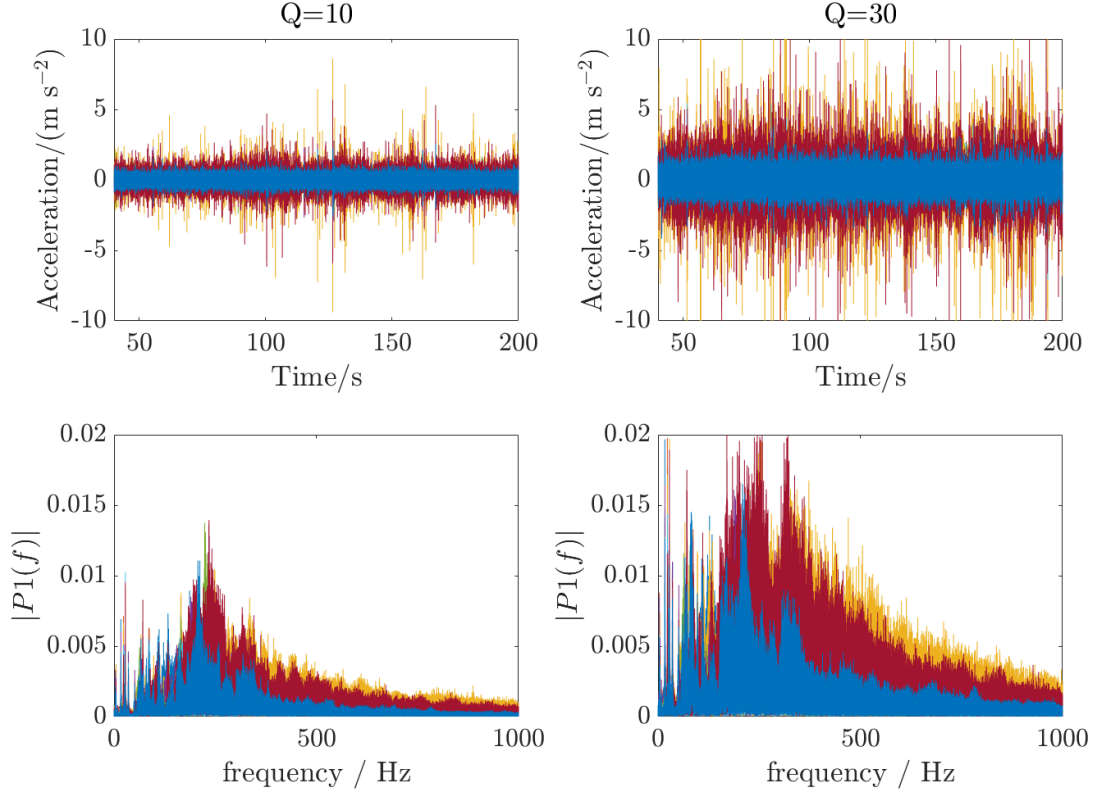


Figure 5.4: Vibration and frequency spectrum at two gas flow rates. The line colors correspond to the different accelerometers.

The relationship between the vibration level and the gas flow rate seems to be nonlinear. This shape is similar to the ones obtained in (Yenus et al., 2017), although different geometries and materials are used in the physical model. Furthermore, it can be clearly seen in Figure 5.5 that the vibration RMS of the four accelerometers close to the nozzles (sensors 3, 4, 7, and 8) are significantly higher than the sensors which are diametrically opposed to them (1, 2, 5, and 6). They also increase faster with the gas flow rate than the other sensors. This indicates that the radial position of the sensors plays a major role in the measured vibration intensity. Staying close to the nozzles, the comparison between the top sensors (i.e., at height h_2) and bottom sensors (at h_1) shows that the vibration amplitude in the top tends to be slightly stronger than the ones in the bottom (compare accelerometers 3 and 4 with 7 and 8).

The level of water height also plays a role on the vibrations (Alia et al., 2019b, Fig. 5). The vibration tend to increase with higher baths. By choosing a correct vertical position for the sensors, one can capture the stirring-induced vibration reliably. The authors thus recommend to place the sensors between the ladle bottom and the open eyes, or, in other words, along the gas plumes.

Another aspect of the experiment concerns the detection of nozzle clogging. Figure 5.6 shows the difference between three operating conditions: both nozzles SW and NW, nozzle SW only, and nozzle NW only. One can notice that the vibration of the sensors SW (respectively NW) in the case where only nozzle SW (respectively NW) operates are very similar to their level when both nozzles operate simultaneously.

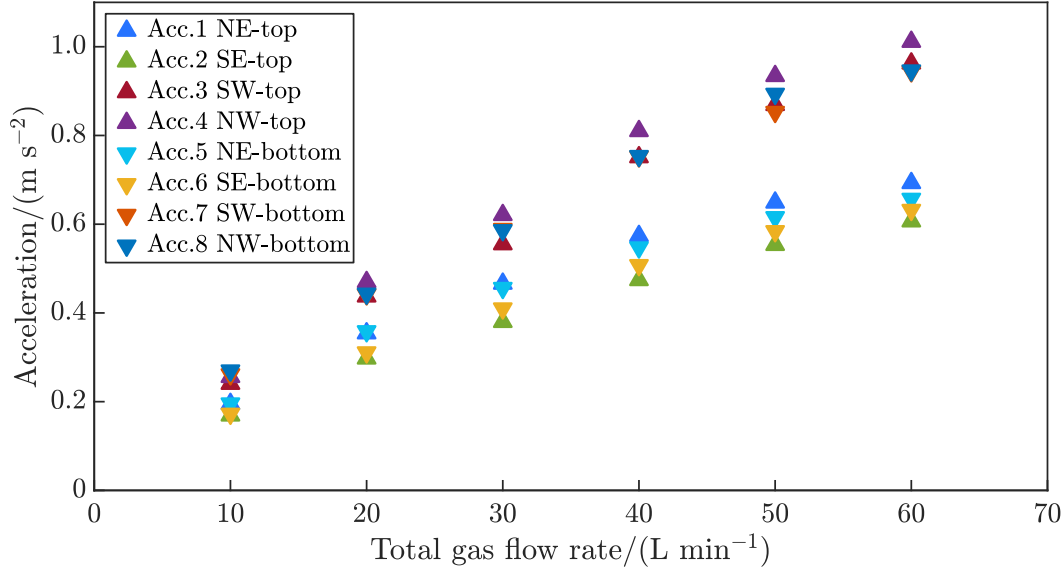


Figure 5.5: RMS of the acceleration signals versus total gas flow rate in the configuration: H_3 , oil layer and two nozzles operating (Alia et al., 2019b).

In other words, the vibrations close to one nozzle (e.g., SW) seem to be relatively independent of the operating condition of the other nozzle (e.g., NW). This is an important result, since it makes it easier to distinguish the operating conditions of the two nozzles. One can indeed use (at least) one sensor close to each nozzle. By computing the differences of RMS amplitudes between the three operating configurations, it can be shown that the nozzle clogging results in a significant drop of the RMS value (-36 to -59%) of the sensors located close to the clogged nozzle, in comparison to its value where both nozzles work normally (Alia et al., 2019b, Table 4). If only one sensor was used to detect the clogging of one of the two nozzles, it would have been difficult to identify the reason for a vibration drop, e.g., gas leakage of the one nozzle or the clogging of the other. Using several sensors can be, in this regard, more advantageous.

These are the main outcome of the experimental campaign. The reader is referred to (Alia et al., 2019b) for more details.

5.4 Conclusion

Summary. After a brief description of state-of-the-art stirring control techniques in the industry, this chapter described the vacuum degassing process of the partner company. It was stressed how it is delicate to implement a vibrations-based control, and how several reasons led to conduct an experimental campaign. Although it might be far from numerical considerations at first glance, the experimental results obtained can be on the contrary beneficial for future mathematical modeling. First, the measurements of the frequency range during stirring helps to identify which phenomenon is dominant: hydroelasticity at low frequencies, or vibroacoustics at high frequencies, see (Morand and Ohayon, 1995). In the case of hydroelasticity for example, the fluid can be considered as incompressible. The main parameter inducing the sloshing is gravity.

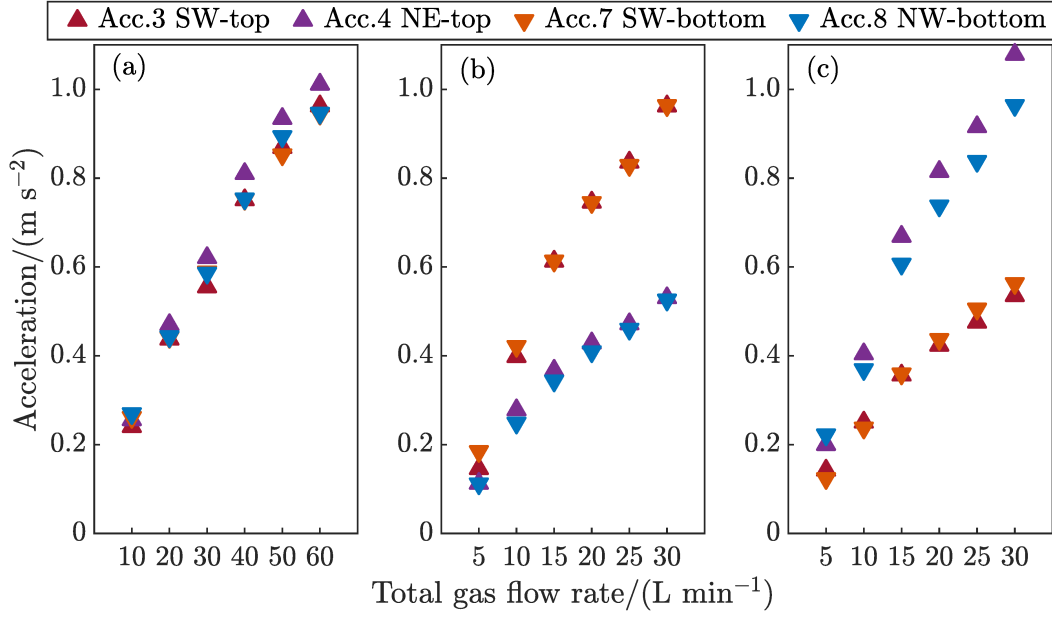


Figure 5.6: RMS values of sensors close to nozzles versus total gas flow rate. a) Two nozzles operating. b) Nozzle SW only. c) Nozzle NW only (Alia et al., 2019b).

On the other hand, if vibroacoustics phenomena are dominant, one has to take into account the compressibility of the fluid in the model and the gravity is likely to be negligible (Morand and Ohayon, 1995). Using the frequency spectrum in Figure 5.4, it is actually not clear if one phenomenon dominates. In fact, both play an important role: the liquid water sloshes strongly and the rising gas generates pressure (acoustic) waves in the liquid. For a realistic modeling, both phases should be modeled in a two-phase model with compressible gas. In a second step, the fluid-structure interaction model should be compared with experimental measurements for a numerical validation. For this purpose, the data collected at the eight points of the ladle are useful. These aspects were partially studied during the doctoral work and are mentioned in the last paragraph.

Besides the importance of experimental data for numerical modeling, the campaign may be useful from the industrial perspective as well. Indeed, it can provide guidelines for optimizing the position and the number of accelerometers in order to better identify the operating conditions of gas stirring. The results show that the vibration RMS values are strongly dependent on the radial and axial location of the accelerometers. The results suggest that the sensors located close to the gas nozzles are able to capture higher intensity levels, than the ones which are diametrically opposed. The recommended positions for each sensor seem to be along the gas plume, between the ladle bottom and the open eye of the corresponding operating nozzle. This leads to the strongest vibration levels and helps to estimate more precisely the stirring conditions. Concerning the number of accelerometers, using at least one close to each nozzle can facilitate the measurement of the stirring intensity of the corresponding gas plume, the quantification of a drop in the stirring efficiency (due to gas leakage for example), and the detection of nozzle clogging. Moreover, the stirring intensity and condition of each nozzle can be estimated separately and independently. This knowledge could be used to design a reliable control, detect nozzle clogging, and improve maintenance planning.

Outlook to fluid-structure interaction for process control There are several approaches for computing the ladle vibrations induced by the stirring. In an exploratory work, we have considered the time-dependent approach and computed the surface force of the liquid on the areas corresponding to the actual sensors (Figure 5.7).

The surface force intervenes as a coupling condition between the liquid and the structure in fluid-structure interaction models. If the structure is assumed to be a linear material, the acceleration at the wall is proportional to the surface force. This is quite practical because it allows to compare the computed surface force and the measured acceleration without needing a full fluid-structure interaction model. However, the preliminary results have pointed out that the surface force is quite sensitive to the mesh size and the Smagorinsky constant, and that a one-way coupling is likely to be insufficient to obtain correct results.

Furthermore, its time evolution is difficult to compare to real measurements because of the absence of clear pattern. One should rather consider the frequency spectrum, as in (Wuppermann et al., 2013). In sum, the correct modeling of the ladle vibrations remains a challenging problem.

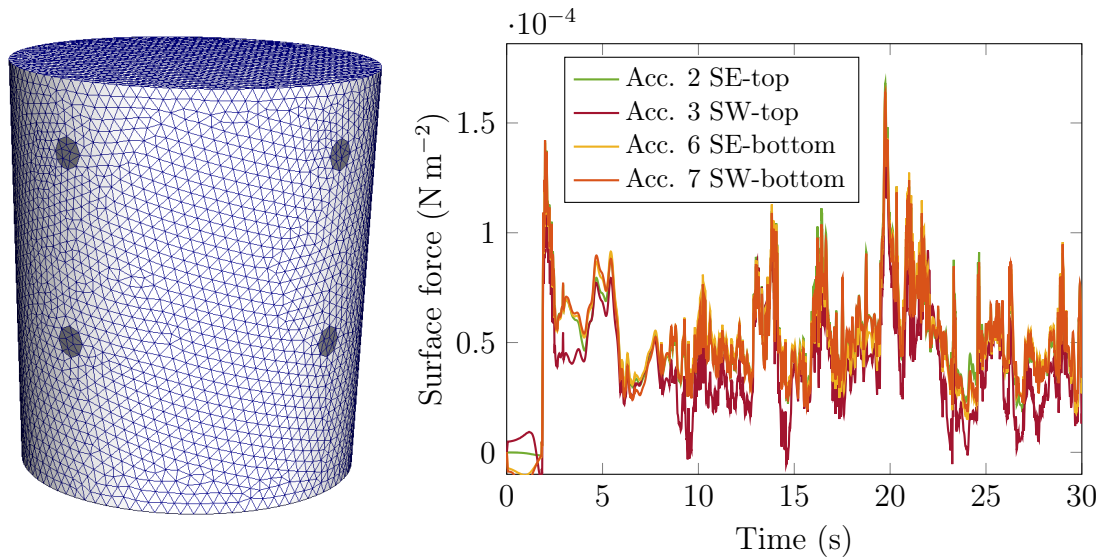


Figure 5.7: Preliminary investigation of the ladle vibration. Left: Mesh of the ladle and the accelerometers' surfaces (grey areas). Right: Time evolution of the surface force applied by the liquid on four sensors.

6. Conclusion

With the objective of improving a complex industrial process using mathematical tools, the present thesis focused on the mathematical modeling, numerical simulation, and optimization of steel ladle stirring. As the reader may have noticed, a large part of the work deals with the question of modeling, let it be about the single-phase models, or the definition of stirring efficiency and the cost functional. Because of the variety of aspects to take into account (gas and slag phases, inclusions' content, wear of the refractory, open eye, alloying, etc.), modeling assumptions are necessary to be able to focus on one specific question, like the optimization of the stirring pattern.

If the single-phase model may appear oversimplifying at first glance, the present work showed that they are quite satisfactory when it comes to describing the stirring pattern (see Chapter 3 and (Alia et al., 2019a)). This point is the first main contribution of the thesis. Furthermore, the single-phase model has the advantage of being relatively cheap in comparison to models with several phases, a free surface, or moving interfaces. Thus, it is quite convenient for iterative computations, as in optimal control problems. Coming to this subject, it has to be stressed here that, to the best of the author's knowledge, the application of optimal flow control for steel ladle stirring could not be found in the literature. Usual optimization studies consist rather to test different values of control parameters and conclude which one is the best. Our approach, based on the optimal control theory, seems to be innovative. This is the second main contribution of the thesis (Chapter 4). Although the 2d boundary-driven stirring model is far from being realistic, it has been studied for completeness. For the industrial practice, the 3d model should be used as a reference. It appears that the 2d and 3d optimization solutions have some similarities, as far as the gas plume intensity is concerned (U_P in 2d and Q in 3d). Furthermore, some findings of the numerical investigation correspond to intuition. For example, at low gas cost, it is optimal to maximize the gas inflow to improve the stirring, or, turning-off the gas inflow shortly before the end of the process spares some gas cost without deteriorating the overall stirring performance. An additional novelty concerns the optimization of the nozzles' position. For more robust recommendations to the industry, the numerical investigation should be extended to finer meshes and different sets of parameters. For example, several values of the time step Δt , the end time T , the Smagorinsky constant C_S , and the threshold m should be tested. This is the subject of coming work. Concerning the limits of our optimal control problem, the reader is referred to Section 4.6.1.

We recall the research directions concerning optimization of ladle stirring: optimal nozzles' positions in a BOF converter, application of multiphase flows, use of "mixing time optimal control", and electromagnetic stirring for a volume control. Since we have encountered the multiphase models in our work, we have briefly presented preliminary results in Section 3.5. The mixing time optimization has been described in Section 4.6.2. Finally, in the third and last contribution of this thesis, we explored the possibility of using ladle vibrations for the industrial process control (see Chapter 5 and (Alia et al., 2019b)). There, we also proposed a new approach in comparison to the literature and to usual practice. Using several sensors located close to the gas nozzles, one can better describe how intense the stirring is, and identify more easily if the nozzles need maintenance. From the point of view of modeling, one could be interesting in computing the vibration of the ladle. This approach and preliminary results obtained during the thesis have been briefly discussed in Sections 5.2.3 and 5.4. Although there are already some research papers on this subject (e. g., (Wuppermann et al., 2013)), there is still a long path ahead.

In conclusion, the optimization of steel ladle stirring is a subject rich from the complexity and variety of physical phenomena involved. It therefore leaves a lot of room for improvement. The use of mathematical modeling and numerical simulation has proved to be an appropriate way to exploit this potential and to solve industrial problems.

A. Detailed form of the Navier–Stokes equations

The Navier–Stokes equations (2.9) and (2.10) are written in vector notations, independently of the system of coordinates. Coming to computations, let it be analytical or numerical, one has to explicit the scalar equations, and requires therefore to fix a coordinate system, e. g., Cartesian, cylindrical, or spherical.

In this appendix, the explicit form of the NSE are given in the Cartesian and cylindrical space frame. In particular, the assumptions needed to derive the 2d Cartesian and axisymmetrical formulations out of the 3d expressions are given.

A.1 In Cartesian coordinates (x, y, z)

In 3d, the Navier–Stokes equations in Cartesian coordinates are as follows:

$$\begin{aligned} \frac{\partial u_x}{\partial t} + u_x \frac{\partial u_x}{\partial x} + u_y \frac{\partial u_x}{\partial y} + u_z \frac{\partial u_x}{\partial z} + \frac{\partial p}{\partial x} - \nu \left[\frac{\partial^2 u_x}{\partial x^2} + \frac{\partial^2 u_x}{\partial y^2} + \frac{\partial^2 u_x}{\partial z^2} \right] &= f_x, \\ \frac{\partial u_y}{\partial t} + u_x \frac{\partial u_y}{\partial x} + u_y \frac{\partial u_y}{\partial y} + u_z \frac{\partial u_y}{\partial z} + \frac{\partial p}{\partial y} - \nu \left[\frac{\partial^2 u_y}{\partial x^2} + \frac{\partial^2 u_y}{\partial y^2} + \frac{\partial^2 u_y}{\partial z^2} \right] &= f_y, \\ \frac{\partial u_z}{\partial t} + u_x \frac{\partial u_z}{\partial x} + u_y \frac{\partial u_z}{\partial y} + u_z \frac{\partial u_z}{\partial z} + \frac{\partial p}{\partial z} - \nu \left[\frac{\partial^2 u_z}{\partial x^2} + \frac{\partial^2 u_z}{\partial y^2} + \frac{\partial^2 u_z}{\partial z^2} \right] &= f_z, \\ \frac{\partial u_x}{\partial x} + \frac{\partial u_y}{\partial y} + \frac{\partial u_z}{\partial z} &= 0. \end{aligned} \quad (\text{A.1})$$

If we assume that \mathbf{u} depends only on two directions, e. g., x and y (y can also be equivalently replaced by z):

$$\frac{\partial u_x}{\partial z} = 0, \quad \frac{\partial u_y}{\partial z} = 0, \quad u_z = 0,$$

then the flow can be reduced to 2d:

$$\begin{aligned} \frac{\partial u_x}{\partial t} + u_x \frac{\partial u_x}{\partial x} + u_y \frac{\partial u_x}{\partial y} + \frac{\partial p}{\partial x} - \nu \left[\frac{\partial^2 u_x}{\partial x^2} + \frac{\partial^2 u_x}{\partial y^2} \right] &= f_x, \\ \frac{\partial u_y}{\partial t} + u_x \frac{\partial u_y}{\partial x} + u_y \frac{\partial u_y}{\partial y} + \frac{\partial p}{\partial y} - \nu \left[\frac{\partial^2 u_y}{\partial x^2} + \frac{\partial^2 u_y}{\partial y^2} \right] &= f_y, \\ \frac{\partial u_x}{\partial x} + \frac{\partial u_y}{\partial y} &= 0. \end{aligned} \quad (\text{A.2})$$

This model represents the flow in an infinitely long rectangular box, see the picture on the left of Figure A.1.

A.2 In cylindrical coordinates (r, θ, z)

The 3d Navier–Stokes equations can also be written in cylindrical coordinates:

$$\begin{aligned}
& \frac{\partial u_r}{\partial t} + u_r \frac{\partial u_r}{\partial r} + \frac{u_\theta}{r} \frac{\partial u_r}{\partial \theta} - \frac{u_\theta^2}{r} + u_z \frac{\partial u_r}{\partial z} + \frac{\partial p}{\partial r} \\
& \quad - \nu \left[\frac{1}{r} \frac{\partial}{\partial r} \left(r \frac{\partial u_r}{\partial r} \right) - \frac{u_r}{r^2} + \frac{1}{r^2} \frac{\partial^2 u_r}{\partial \theta^2} - \frac{2}{r^2} \frac{\partial u_\theta}{\partial \theta} + \frac{\partial^2 u_r}{\partial z^2} \right] = f_r, \\
& \frac{\partial u_\theta}{\partial t} + u_r \frac{\partial u_\theta}{\partial r} + \frac{u_\theta}{r} \frac{\partial u_\theta}{\partial \theta} + \frac{u_\theta u_r}{r} + u_z \frac{\partial u_\theta}{\partial z} + \frac{1}{r} \frac{\partial p}{\partial \theta} \\
& \quad - \nu \left[\frac{1}{r} \frac{\partial}{\partial r} \left(r \frac{\partial u_\theta}{\partial r} \right) - \frac{u_\theta}{r^2} + \frac{1}{r^2} \frac{\partial^2 u_\theta}{\partial \theta^2} + \frac{2}{r^2} \frac{\partial u_r}{\partial \theta} + \frac{\partial^2 u_\theta}{\partial z^2} \right] = f_\theta, \\
& \frac{\partial u_z}{\partial t} + u_r \frac{\partial u_z}{\partial r} + \frac{u_\theta}{r} \frac{\partial u_z}{\partial \theta} + u_z \frac{\partial u_z}{\partial z} + \frac{\partial p}{\partial z} \\
& \quad - \nu \left[\frac{1}{r} \frac{\partial}{\partial r} \left(r \frac{\partial u_z}{\partial r} \right) + \frac{1}{r^2} \frac{\partial^2 u_z}{\partial \theta^2} + \frac{\partial^2 u_z}{\partial z^2} \right] = f_z, \\
& \quad \frac{\partial u_r}{\partial r} + \frac{u_r}{r} + \frac{1}{r} \frac{\partial u_\theta}{\partial \theta} + \frac{\partial u_z}{\partial z} = 0.
\end{aligned}$$

In axisymmetrical flows, the three velocity components and the pressure are assumed to be independent of the angular coordinate θ :

$$\frac{\partial u_r}{\partial \theta} = 0, \quad \frac{\partial u_\theta}{\partial \theta} = 0, \quad \frac{\partial u_z}{\partial \theta} = 0, \quad \frac{\partial p}{\partial \theta} = 0.$$

The 3d axisymmetric equations are given by:

$$\begin{aligned}
& \frac{\partial u_r}{\partial t} + u_r \frac{\partial u_r}{\partial r} - \frac{u_\theta^2}{r} + u_z \frac{\partial u_r}{\partial z} + \frac{\partial p}{\partial r} - \nu \left[\frac{1}{r} \frac{\partial}{\partial r} \left(r \frac{\partial u_r}{\partial r} \right) - \frac{u_r}{r^2} + \frac{\partial^2 u_r}{\partial z^2} \right] = f_r, \\
& \frac{\partial u_\theta}{\partial t} + u_r \frac{\partial u_\theta}{\partial r} + \frac{u_\theta u_r}{r} + u_z \frac{\partial u_\theta}{\partial z} - \nu \left[\frac{1}{r} \frac{\partial}{\partial r} \left(r \frac{\partial u_\theta}{\partial r} \right) - \frac{u_\theta}{r^2} + \frac{\partial^2 u_\theta}{\partial z^2} \right] = f_\theta, \\
& \frac{\partial u_z}{\partial t} + u_r \frac{\partial u_z}{\partial r} + u_z \frac{\partial u_z}{\partial z} + \frac{\partial p}{\partial z} - \nu \left[\frac{1}{r} \frac{\partial}{\partial r} \left(r \frac{\partial u_z}{\partial r} \right) + \frac{\partial^2 u_z}{\partial z^2} \right] = f_z, \\
& \quad \frac{\partial u_r}{\partial r} + \frac{u_r}{r} + \frac{\partial u_z}{\partial z} = 0.
\end{aligned} \tag{A.3}$$

If, furthermore, the ortho-radial component of \mathbf{u} is assumed to be zero, these equations can reduce to a two-dimensional problem:

$$\begin{aligned}
& \frac{\partial u_r}{\partial t} + u_r \frac{\partial u_r}{\partial r} + u_z \frac{\partial u_r}{\partial z} + \frac{\partial p}{\partial r} - \nu \left[\frac{1}{r} \frac{\partial}{\partial r} \left(r \frac{\partial u_r}{\partial r} \right) - \frac{u_r}{r^2} + \frac{\partial^2 u_r}{\partial z^2} \right] = f_r, \\
& \frac{\partial u_z}{\partial t} + u_r \frac{\partial u_z}{\partial r} + u_z \frac{\partial u_z}{\partial z} + \frac{\partial p}{\partial z} - \nu \left[\frac{1}{r} \frac{\partial}{\partial r} \left(r \frac{\partial u_z}{\partial r} \right) + \frac{\partial^2 u_z}{\partial z^2} \right] = f_z, \\
& \quad \frac{\partial u_r}{\partial r} + \frac{u_r}{r} + \frac{\partial u_z}{\partial z} = 0.
\end{aligned} \tag{A.4}$$

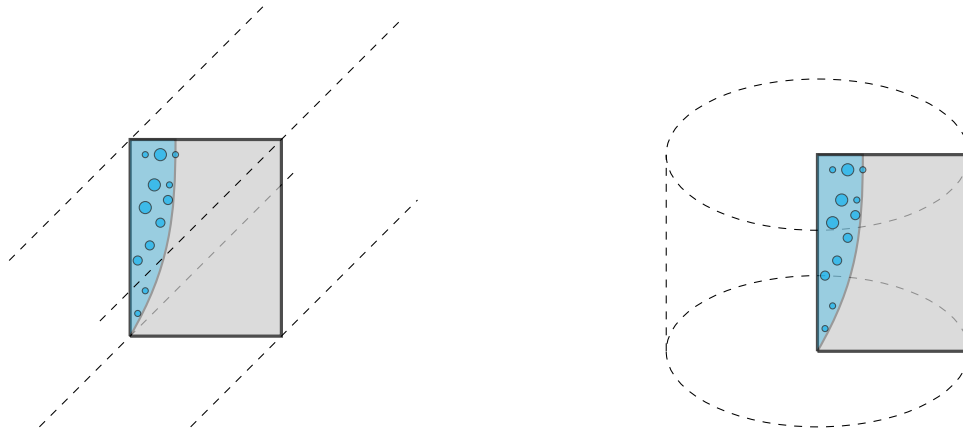


Figure A.1: View of simplified 2d flows for different space frames. Left: Cartesian space frame. Right: cylindrical space frame.

This last assumption corresponds to applications such as the picture on the right of Figure A.1.

B. Unit convention for gas flow rates

This small note describes the unit convention $\text{Nm}^3(\text{STP}) \text{min}^{-1}$ for gas flow rates and the difference between industrial and laboratory conditions.

The flow rate of any gas depends on its operating temperature and pressure. Therefore, it is necessary to have a reference unit to be able to compare flow rates. The unit Nm^3 stands for “normal m^3 ”, which refers to a cubic meter in “normal conditions”, defined by the Standard Temperature and Pressure (STP) conditions. In Europe, they are $\Theta_{\text{STP}} = 273.15 \text{ K}$ (0°C) and $p_{\text{STP}} = 1.10^5 \text{ Pa}$, respectively, (McNaught and Wilkinson, 1997).

In the steelmaking practice, the typical range of the gas flow rate is between 0 and $0.015 \text{ Nm}^3(\text{STP}) \text{min}^{-1} \text{tons}^{-1}$, where tons refers to the steel mass in the ladle. Using the standard unit of the industry, the inflow of gas ranges between 0 and 1575 lmin^{-1} for a steel heat of 105 tons. Note that they correspond to the total amount of injected gas. In cases where multiple nozzles are used, the total flow rate has to be divided by the number of nozzles (often 2). In Section 4.1.1, we have assumed $Q_{\text{min}}^t = 0$ and $Q_{\text{max}}^t = 750$ for the industrial case.

In operating conditions, the real flow rate entering a ladle is computed with the perfect gas law (see also (Mukhopadhyay et al., 2001)),

$$\frac{Qp}{\Theta} = \frac{Q_{\text{STP}}p_{\text{STP}}}{\Theta_{\text{STP}}} \iff Q = Q_{\text{STP}} \left(\frac{p_{\text{STP}}}{p} \frac{\Theta}{\Theta_{\text{STP}}} \right). \quad (\text{B.1})$$

This relation is used in numerical two-phase models to calculate a suitable boundary condition for the gas. Replacing p by the hydrostatic pressure $p_{\text{fr}} + \rho g(H - z)$, where p_{fr} is the pressure at the free surface (atmospheric or vacuum) and ρ is the steel density, one can rewrite (B.1) as (see also (Goldschmit and Owen, 2001))

$$Q = Q_{\text{STP}} \cdot \left(\frac{\frac{p_{\text{STP}}}{\rho g H}}{\frac{p_{\text{fr}}}{\rho g H} + 1 - \frac{z}{H}} \frac{\Theta}{\Theta_{\text{STP}}} \right).$$

In real conditions, for example $\Theta = 1273.15 \text{ K}$, $p_{\text{fr}} = p_{\text{STP}}$, $H = 2.25 \text{ m}$, and $\rho = 7000 \text{ kg m}^{-3}$, the effective gas flow rate injected at the nozzle ($z = 0$) is almost twice its value in STP conditions: $Q \approx 1.8 Q_{\text{STP}}$. In vacuum conditions ($p_{\text{fr}} = 100 \text{ Pa}$), it is three times higher.

In laboratory conditions, one has $\Theta = 298.15 \text{ K}$, $p_{\text{fr}} = p_{\text{STP}}$, $H = 0.65 \text{ m}$, and $\rho = 1000 \text{ kg m}^{-3}$, such that $Q \approx 1.03 Q_{\text{STP}}$. Thus, it can be assumed that the flow rate is constant in the bath and is equal to the injected gas flow rate:

$$Q \approx Q_{\text{STP}}.$$

List of notations

Symbol	Meaning	Section
\mathcal{A}	generic system matrix	2.4
\mathcal{A}	open eye area	5.1
A	stiffness matrix (with blocks or elements A_{ij})	2.3.1
a	“artificial” origin of the conical gas plume shape r_c	2.3.3
α	gas phase fraction	3.1
$\alpha_1, \alpha_2, \alpha_3, \alpha_4$	gas phase fraction formulas	3.1
α_{n1}, α_{n2}	gas phase fraction for nozzles 1 and 2 in 3d	3.1
α -ferrite	name of a ferrite phase	1.1
B	pressure-velocity rectangular matrix	2.3.1
$b(\mathbf{u}, \mathbf{v}, \mathbf{U})$	trilinear form $b(\mathbf{u}, \mathbf{v}, \mathbf{U}) = ((\mathbf{u} \cdot \nabla) \mathbf{v}) \cdot \mathbf{U}$	4.3.2
\mathbf{b}	boundary velocity on Γ_D or Γ_{axis}	2.1, 4.2.3
β_1, β_2	parameters in the cost functional	4.2.3
C	convection matrix (with blocks or elements C_{ij})	2.3.1
C_S	Smagorinsky (turbulence) constant	2.5.1
C_ν, C_1, C_2	constants of the $k - \epsilon$ turbulence model	2.5.1
c_i	constants in α_3 and α_4 ($i = 0, \dots, 5$)	3.2.2
$\mathbb{D}(\cdot)$	fluid deformation tensor of vector field \cdot	2.1
D	diagonal matrix	2.4
d	dimension (2d or 3d)	2.1
d_{nozzle}	nozzle or porous plug diameter	3.1
δ	small length scale, filter width in the LES model	2.5.1
$\delta_K, \delta_{K,2d}$	Kolmogorov length in 3d and 2d	2.5.1
e	residual operator	4.3.2
\hat{e}	reduced residual operator	4.3.2
$(\mathbf{e}_x, \mathbf{e}_y, \mathbf{e}_z)$	unit vector basis of the Cartesian space frame	2.1
ϵ	rate of dissipation of turbulent energy	2.5.1, 3
F, F_1, F_2	terms of J and e whose differentiation is detailed	4.3.2
Fr	Froude number	1.2
\mathbf{f}	volume force	2.1 4.2.3
φ	phase fraction scalar field	3.5
$\phi_{h,i}$	component of i –th basis function of \mathbf{V}_h	2.3.1
$\Phi_{h,i}$	i –th basis function of \mathbf{V}_h	2.3.1
G	turbulent kinetic energy production rate	2.5.1
g	gravity constant	1.2

\mathbf{g}	gravity vector field	2.1
Γ_{axis}	central (symmetry) axis boundary	3.1.2
Γ_c	boundary where the control applies	4.3.2
Γ_D	Dirichlet boundary	2.1
Γ_{in}	inflow boundary	3.5
Γ_{out}	outflow boundary	3.5
Γ_{slip}	free slip boundary	2.1
Γ_{top}	top surface boundary	3.1.2
Γ_{wall}	wall boundary	3.5
Γ_0	no-slip boundary	2.1
γ	inf-sup constant	2.3.1
γ_1, γ_2	penetration resistance and frictions coefficients	2.1
H	cylinder height	1.2
H_1, H_2, H_3	water heights in the ladle vibration experiment	5.3
$H^1(\Omega)$	Sobolev space $W^{1,2}(\Omega)$ (also a Hilbert space)	2.2.1
$H_{00}^{1/2}(\Gamma_c)$	Lions-Maganes space (Wilbrandt, 2019b)	4.3.2
h_{fr}	distance between bath free surface and border of the ladle	4.1.1
h_{slag}	slag thickness	4.1
h_1, h_2	sensors' heights in the ladle vibration experiment	5.3
\mathbf{h}	test function from the space Y (boundary control)	4.3.2
η	arbitrarily small constant	4.3.2
I	identity matrix	2.1
J	cost functional	4.3.2
\hat{J}	reduced cost functional	4.3.2
J_c	part of the cost functional describing the cost of the control	4.2.3
J_0	part of the cost functional describing the maximization and/or regulation of vorticity	4.2.3
$J_1, J_2, J_3(m)$	cost functionals in the numerical application	4.4, 4.5
k	turbulent kinetic energy	2.5.1, 3
\mathbf{k}	test function from the space Y (volume control)	4.3.2
\mathcal{L}	Lagrangian function	4.3.2
L	characteristic length	1.2
$L^2(\Omega)$	Lebesgue space	2.2.1
$\ell(t)$	“ramp-like” function to smooth initial time steps	3.2.1
λ_1, λ_2	weights of the control cost in J_c	4.2.3
M	mass matrix (with blocks or elements M_{ij})	2.3.1
m	threshold parameter used for the vorticity in the cost functional (stands for “mixing”)	4.2.3
μ	fluid dynamic viscosity	2.1
μ_g	gas dynamic viscosity	3.5
μ_l	liquid dynamic viscosity	3.5

N_c	dimension of the control space (or number of degrees of freedom of the control variables)	4.4
N_p	dimension of pressure space \mathcal{Q}_h	2.3.1
N_v	number of Dofs for one velocity component (dN_v is the dimension of space \mathbf{V}_h)	2.3.1
\mathbf{n}	unit normal vector	2.1
ν	fluid kinematic viscosity or dimensionless viscosity	2.1, 3, 4
ν_T	turbulent (or eddy) viscosity	2.5.1, 3, 4
Ω	fluid domain	2.1
Ω_0	subdomain used in the optimal control problems	4.2.3
\mathcal{P}	preconditioner	2.4
P	adjoint pressure	4.3.2
P_k/P_{k-1}	pair of finite elements , $k \geq 2$	2.3.1
p	pressure field	2.1
p_{fr}	pressure at the free surface (e.g., atmospheric or vacuum)	4.1.1
p_h	discrete pressure field	2.3.1
\underline{p}_h	discrete pressure vector	2.3.1
p_{STP}	pressure of the STP conditions	Annex B
$\psi_{h,i}$	i -th basis function of \mathcal{Q}_h	2.3.1
\mathcal{Q}	pressure function space	2.2.1, 2.5.1, 4.3
\mathcal{Q}_h	finite element space	2.3.1
Q	gas volumetric flow rate	3.1
Q_{emuls}	gas flow rate from which slag starts to emulsify in steel	4.1
Q_k/Q_{k-1}	pair of finite elements , $k \geq 2$	2.3.1
Q_{max}	maximum gas flow rate	4.1
Q_{min}	minimum gas flow rate	4.1
$Q_{\text{open eye}}$	gas flow rate from which open eye starts	4.1
Q_{overflow}	gas flow rate from which bath may overflow	4.1
Q_{max}^t	maximum gas flow rate technically allowed	4.1
Q_{min}^t	minimum gas flow rate technically allowed	4.1
Q_{STP}	gas flow rate in STP conditions	Annex B
Q_1, Q_2	gas volumetric flow rate for nozzles 1 and 2	4.2.1, 4.5
q	test function from \mathcal{Q}	2.2.1
q_h	test function from \mathcal{Q}_h	2.3.1
R	radius of cylinder	1.2
Re	Reynolds number	2.1
R_g	universal gas constant (used only once)	4.1.2
$R_{\text{top}}, R_{\text{bot}}$	top and bottom radius of the 3d ladle model	3.2.3
(r, θ, z)	radial, angular, and axial coordinates in cylindrical frame	2.3.1
r_{av}	average radius of plume	3.1

r_c	radius of plume cylinder or cone	3.1
$\text{reg}(z)$	regularization function used in lid-driven models	3.2.1
$\mathbf{r}, \mathbf{r}_u, \mathbf{r}_p$	right-hand sides	2.3.1, 2.4
ρ	fluid density	2.1
ρ_g	gas density	3.1, 3.5
ρ_l	liquid density (e. g., water or steel)	3.1, 3.5
ρ_{slag}	slag density	4.1
$\mathbb{S}(\cdot)$	fluid stress tensor of vector field \cdot	2.1
S	solution operator	2.2.1
$S_C, S_{C,\text{LSC}}$	Schur complements	2.4
$\sigma_k, \sigma_\epsilon$	constants of the $k - \epsilon$ turbulence model	2.5.1
\mathbb{T}	Reynolds (or subgrid-scale) stress tensor	2.5.1
T	end time	2.1
t	time variable	2.1
t_0	time parameter used in a smoothing function	3.2.1
\mathbf{t}_i	unit tangential vector, $i = 1, \dots, d - 1$	2.1
Θ	temperature	Annex B
Θ_{STP}	temperature of the STP conditions	Annex B
θ	coefficient in the time discretization θ -scheme in 2.3.1, angular coordinate elsewhere	2.3.1, 2.3.3
τ	surface tension	4.1.1
U	characteristic velocity	1.2
U_e	critical liquid velocity where emulsification of slag in steel starts	4.1.1
U_P	plume velocity	3.1
$U_{P\max}$	upper bound for U_P in the optimal control problem	4.2.1
$U_{P\min}$	lower bound for U_P in the optimal control problem	4.2.1
U_S	slip velocity between gas and liquid	3.1
U_δ	characteristic velocity at scale δ	2.5.1
\mathbf{U}	adjoint velocity	4.3.2
(u_r, u_θ, u_z)	components of the velocity in cylindrical frame	Annex A
(u_x, u_y, u_z)	components of the velocity in Cartesian frame	Annex A
\mathbf{u}	velocity vector field	2.1
\mathbf{u}_b	extension of \mathbf{b} into Ω	2.2.1
\mathbf{u}_h	discrete velocity vector field	2.3.1
$\underline{\mathbf{u}}_h$	discrete velocity vector	2.3.1
\mathbf{u}_0	velocity with zero value at prescribed boundaries	4.3.2
V_{gas}	gas volume in the bath (the volumetric flow rate is given by the time derivative \dot{V}_{gas})	4.1.1
\mathbf{V}	velocity function space	2.2.1
\mathbf{V}_h	finite element space	2.3.1
\mathbf{V}_M	velocity function space with homogeneous Dirich- let on M (and no penetration on Γ_{slip})	4.3.2
\mathbf{v}	test function from \mathbf{V}	2.2.1
\mathbf{v}_h	test function from \mathbf{V}_h	2.3.1

$W^{k,p}(\Omega)$	Sobolev space, $k \in \mathbb{N}, 1 \leq p \leq \infty$	2.3.1
W_M	velocity function space with homogeneous Dirichlet on M (and no penetration on Γ_{slip})	4.3.2
\mathbf{w}	wind vector	2.1
X	state space in the optimal control problem	4.3.2
(x, y, z)	coordinates in Cartesian frame	2, 3, 4
x_i	coordinates with numbered indices, $i = 1, \dots, d$	
$(x_{n1}, y_{n1}),$ (x_{n2}, y_{n2})	coordinates of the two nozzles in 3d	3.2.3, 4.5
\mathbf{x}	coordinates vector	2.1
χ	apex angle of the conical gas plume shape r_c	2.3.3
Y	control space in the optimal control problem	4.3.2
z_C	critical height for the gas fraction α	3.2.2
z_0	arbitrary fraction of the height H used in the regularization function $\text{reg}(z)$	3.2.1
$\partial\Omega$	boundary of the fluid domain	2.1
(\cdot, \cdot)	L_2 -inner product	2.2.1
$\langle \cdot, \cdot \rangle_{X^* \times X}$	dual product	4.3.2
\cdot^*	dimensionless change of variable if \cdot is a variable	2.1.1, 4.1.1
	dual space if \cdot is a space	4.3.2
$\bar{\cdot}$	average of (vector or scalar) field \cdot	2.5.1, 3.4
\cdot'	fluctuations of (vector or scalar) field \cdot	2.5.1
\cdot_h	subscript to designate finite-dimensional spaces and discrete variables	2.3.2
\cdot^k	superscript index in, e. g., time or optimization iterations	2.3.1
\cdot^{opt}	superscript to designate optimal variables	4.3.2, 4.4, 4.5
\cdot^0	superscript to designate initial conditions or initial guesses in optimization	2.1, 3, 4
$\ \mathbb{D}(\cdot)\ _F$	Frobenius norm of deformation tensor	2.5.1

List of abbreviations

Abbreviation	Meaning
AHSS	Advanced High-Strength Steels
BCC	Body-Centered Cubic
BF	Blast Furnace
Bi-CGStab	Bi-Conjugate Gradient Stabilized (iterative solver)
BOF	Basic Oxygen Furnace
C	Carbon
CFD	Computational Fluid Dynamics
CFL	Courant–Friedrich–Lewy (condition)
COBYLA	Constraint Optimization BY Linear Approximation
DNS	Direct Numerical Simulation
Dof	Degree of freedom
EAF	Electric Arc Furnace
FDM	Finite Difference Method
FE	Finite Element
FEM	Finite Element Method
FGMRES	Flexible Generalized Minimal RESidual (iterative solver)
FVM	Finite Volume Method
H	Hydrogen
IF	Interstitial-Free steels
LES	Large Eddy Simulation
LS	Level-Set method
LSC	Least Square Commutator (preconditioner)
MHD	Magnetohydrodynamics
MPI	Message Passing Interface
N	Nitrogen
NSE	Navier–Stokes Equations
NW	North-West (refers to the accelerometers’ position)
O	Oxygen
ODE	Ordinary Differential Equation
PDE	Partial Differential Equation
RH	Ruhrstahl Heraeus degasser
RMS	Root Mean Square
SI	Système International (d’unité) - International units system
SSAB	A specialized Nordic and US-based steel company

SSOR	Symmetric Successive Over-Relaxation (preconditioner)
STP	Standard Temperature and Pressure conditions
SUPG	Streamline Upwind Petrov–Galerkin (stabilization method)
SW	South-West (refers to the accelerometers' position)
TKE	Turbulent Kinetic Energy
ULC	Ultra-Low Carbon steels
VOF	Volume Of Fluid method
VTD	Vacuum Tank Degasser

List of units

Name	Meaning
$^{\circ}\text{C}$	degree Celsius (temperature)
cm	centimeter
K	Kelvin (temperature)
kg m^{-3}	mass per cubic meter (density)
kHz	kiloHertz (frequency)
km h^{-1}	kilometer per hour (velocity)
l min^{-1}	liter per minute (volumetric flow rate)
m	meter
m^3	cubic meter (volume)
mm	millimeter
m s^{-1}	meter per second (velocity)
m s^{-2}	meter per squared second (acceleration)
$\text{m}^2 \text{s}^{-1}$	squared meter per second (kinematic viscosity)
$\text{m}^3 \text{s}^{-1}$	cubic meter per second (volumetric flow rate)
Mt	millions of tons
N	Newton (body force)
N kg^{-1}	Newton per unit mass (body force per unit mass)
N m^{-1}	Newton per unit length (surface tension)
N m^{-3}	Newton per cubic meter (volumetric force)
Nm^3 , $\text{Nm}^3(\text{STP})$	normal cubic meter, cubic meter in STP conditions
$\text{Nm}^3 \text{min}^{-1}$	normal cubic meter per minute (volumetric flow rate)
$\text{Nm}^3 \text{min}^{-1} \text{tons}^{-1}$	normal cubic meter per minute per ton (volumetric flow rate)
Pa	Pascal (pressure)
Pa s	Pascal second (dynamic viscosity)
ppm	parts per million ($=0.001\%$)
s	second
wt%	percentage in weight

Bibliography

- Abergel, F. and Temam, R. (1990). On some control problems in fluid mechanics. Theoretical and Computational Fluid Dynamics, 1(6):303–325.
- Ahmed, N., Bartsch, C., John, V., and Wilbrandt, U. (2018). An assessment of some solvers for saddle point problems emerging from the incompressible Navier–Stokes equations. Computer Methods in Applied Mechanics and Engineering, 331:492–513.
- Ahmed, N. and Rubino, S. (2019). Numerical comparisons of finite element stabilized methods for a 2d vortex dynamics simulation at high reynolds number. Computer Methods in Applied Mechanics and Engineering, 349:191–212.
- Alexis, J., Andersson, M., Björkvall, J., Sichen, D., and Sandberg, A. (2011). Optimization of secondary metallurgy with respect to non-metallic inclusions. Jernkontorets Forskning, D(836):1–50.
- Alia, N., John, V., and Ollila, S. (2019a). Revisiting the single-phase flow model for liquid steel ladle stirred by gas. Applied Mathematical Modelling, 67:549–556.
- Alia, N., Pylvänäinen, M., Visuri, V.-V., John, V., and Ollila, S. (2019b). Vibrations of a laboratory-scale gas-stirred ladle with two eccentric nozzles and multiple sensors. Journal of Steel and Iron Research International, 1:1–10.
- Amestoy, P. R., Duff, I. S., L’Excellent, J.-Y., and Koster, J. (2001). A fully asynchronous multifrontal solver using distributed dynamic scheduling. SIAM Journal on Matrix Analysis and Applications, 23(1):15–41.
- Andrianov, N. (2003). Analytical and numerical investigation of two-phase flows. PhD thesis, Otto-von-Guericke Universität Magdeburg.
- Balaji, D. and Mazumdar, D. (1991). Numerical computation of flow phenomena in gas-stirred ladle svstems. Steel Research, 62(1):16–23.
- Bartsch, C. (2018). A coupled stochastic-deterministic method for the numerical solution of population balance systems. PhD thesis, FU Berlin.
- Behera, N., Wohaiishi, A., Subramanian, R., Tewari, N., and Bommaraju, R. (2014). Optimization of argon stirring at Hadeed ladle furnace by application of Trustir technology. AISTech Proceedings of the Iron & Steel Technology Conference, II:1423–1432.

- Bernard, R. S., Maier, R. S., and Falvey, H. T. (2000). A simple computational model for bubble plumes. Applied Mathematical Modelling, 24(3):215–233.
- Bewley, T. R., Choi, H., Temam, R., and Moin, P. (1993). Optimal feedback control of turbulent channel flow. Center for Turbulence Research - Annual Research Briefs, pages 3–14.
- Bewley, T. R., Moin, P., and Temam, R. (2001). DNS-based predictive control of turbulence: An optimal benchmark for feedback algorithms. Journal of Fluid Mechanics, 447:179–225.
- Bruneau, C.-H. and Saad, M. (2006). The 2d lid-driven cavity problem revisited. Computational Fluids, 35:326–348.
- Burty, M., Boher, M., De Santis, M., Matzkeit, M., and Gudenau, H. W. (2006). EUR 22388 – Steelmaking processes - Improvement of inclusion flotation during RH treatment. European Commission - Technical steel research series, pages 1–116.
- Burty, M., Pusse, C., Sheng, D., Dannert, C., Koechner, H., Sancho, L., Diaz, J., Valenti, P., Bruch, C., and Arteaga, A. (2007). EUR 22988 - Development of advanced methods for the control of ladle stirring process. European Commission - Technical steel research series, pages 1–139.
- Callister, W. D. J. (2007). Materials Science and Engineering: An Introduction, Seventh Edition. John Wiley.
- Casas, E. (1995). Optimality conditions for some control of turbulent flows. In Flow Control, pages 127–147. Springer, New York.
- Castillejos, A. and Brimacombe, J. (1987). Measurements of physical characteristics of bubbles in gas-liquid plumes: Part II. Local properties of turbulent air-water plumes in vertically injected jets. Metallurgical Transactions B, 18:595–601.
- Castillejos, A. and Brimacombe, J. (1989). Physical characteristics of gas jets injected vertically upward into liquid metal. Metallurgical Transactions B, 20(5):595–601.
- Chacón Rebollo, T. and Lewandowski, R. (2014). Mathematical and numerical foundations of turbulence models and applications. Birkhäuser, New York, NY.
- Cloete, S. W. P., Eksteen, J. J., and Bradshaw, S. M. (2009). A mathematical modelling study of fluid flow and mixing in full-scale gas-stirred ladles. Progress in Computational Fluid Dynamics, 9(6/7):345–356.
- Courant, R., Friedrichs, K., and Lewy, H. (1928). Über die partiellen Differenzengleichungen der mathematischen Physik. Mathematische Annalen, 100(1):32–74.

- Dannert, C., Koechner, H., Strack-Thor, U., Valentin, P., Bruch, C., Sichen, D., Holappa, L., Louhenkilpi, S., and Väyrynen, P. (2012). EUR 25068 – Improvement of ladle stirring to minimize slag emulsification and reoxidation during alloying and rinsing. European Commission - Research fund for coal and steel series, pages 1–194.
- Davis, T. A. (2004). UMFPACK - An unsymmetric-pattern multifrontal method with a column pre-ordering strategy. ACM Trans. Math. Software, 30(204):196–199.
- De Frutos, J., John, V., and Novo, J. (2016). Projection methods for incompressible flow problems with WENO finite difference schemes. Journal of Computational Physics, 309:368–386.
- Debroy, R., Majumdar, A., and Spalding, D. (1978). Numerical prediction of recirculation flows with free convection encountered in gas-agitated reactors. Applied Mathematical Modelling, 2(3):146–150.
- El Sherif, A. (2008). Contrôle optimal par simulation aux grandes échelles d’un écoulement turbulent. PhD thesis, Institut Polytechnique National de Lorraine.
- Elman, H. C. (2005). Preconditioning strategies for models of incompressible flow. Journal of Scientific Computing, 25(1):347–366.
- Fefferman, C. L. (2006). Existence and smoothness of the Navier–Stokes equations. The millennium prize problems, 57:67.
- Fernández-Cara, E. (2012). Motivation, analysis and control of the variable density Navier–Stokes equations. Discrete & Continuous Dynamical Systems - S, 5(6):1021–1090.
- Ferziger, J. H. and Peric, M. (2002). Computational Methods for Fluid Dynamics. Springer.
- Fischer, A., Krüger, K., and Weinberg, M. (2017). Bewertung der Behandlung von Stahlschmelzen mithilfe von Schallsensoren. Stahl und Eisen, 137(4):39–48.
- Gad-el Hak, M. (1996). Modern developments in flow control. Applied Mechanics Review, 49(7):365–379.
- Ganesan, S. and Tobiska, L. (2008). An accurate finite element scheme with moving meshes for computing 3d-axisymmetric interface flows. International Journal for Numerical Methods in Fluids, 57(2):119–138.
- Ganguly, S. and Chakraborty, S. (2004). Numerical investigation on role of bottom gas stirring in controlling thermal stratification in steel ladles. ISIJ International, 44(3):537–546.
- Geng, D. Q., Lei, H., and He, J. C. (2010). Optimization of mixing time in a ladle with dual plugs. International Journal of Minerals, Metallurgy and Materials, 17(6):709–714.

- Goldschmit, M. and Owen, A. (2001). Numerical modelling of gas stirred ladles. Ironmaking and Steelmaking, 28(4):337–340.
- Grevet, J. H., Szekely, J., and El-Kaddah, N. (1982). An experimental and theoretical study of gas bubble driven circulation systems. International Journal of Heat and Mass Transfer, 25(4):487–497.
- Haiyan, T., Xiaochen, G., Guanghui, W., and Yong, W. (2016). Effect of gas blown modes on mixing phenomena in a bottom stirring ladle with dual plugs. ISIJ International, 56(12):2161–2170.
- Hannasch, D. and Neda, M. (2012). On the accuracy of the viscous form in simulations of incompressible flow problems. Numerical Methods for Partial Differential Equations, 28(2):523–541.
- Hinze, M. (2002). Optimal and instantaneous control of the instationary Navier–Stokes equations. Habilitation thesis.
- Hoile, S. (2000). Processing and properties of mild interstitial free steels. Materials Science and Technology, 16:1079–1093.
- Irons, G., Senguttuvan, A., and Krishnapisharody, K. (2015). Recent advances in the fluid dynamics of ladle metallurgy. ISIJ International, 55(1):1–6.
- Ishii, M. (1975). Thermo-fluid dynamic theory for two-phase flows. Eyrolles.
- Ishii, M. and Hibiki, T. (2010). Thermo-fluid dynamics of two-phase flows. Springer Science & Business Media.
- John, V. (2002). Slip with friction and penetration with resistance boundary conditions for the Navier–Stokes equations - numerical tests and aspects of the implementation. Journal of Computational and Applied Mathematics, 147(2):287–300.
- John, V. (2016). Finite Element Methods for incompressible flow problems. Springer.
- John, V., Knobloch, P., and Wilbrandt, U. (2019). Finite element pressure stabilizations for incompressible flow. WIAS Preprint 2587.
- John, V. and Matthies, G. (2001). Higher-order finite element discretizations in a benchmark problem for incompressible flows. International Journal for Numerical Methods in Fluids, 37(8):885–903.
- John, V. and Matthies, G. (2004). MooNMD - a program package based on mapped finite element methods. Computing and Visualization in Science, 6:163–170.
- Johnson, S. G. (2019). The NLOpt nonlinear-optimization package. <http://ab-initio.mit.edu/nlopt>.

- Koehle, S., Kleimt, B., Lichterbeck, R., Johann, K.-P., Stender-Robertz, J., Larau-dogoitia, J., and Ors, F. (2001). EUR 19484 – Secondary steelmaking - Dynamic modelling and control of the vacuum degassing process. European Commission - Technical steel research series, pages 1–70.
- Kor, G. J. W. and Glaws, P. C. (1998). Chapter 11: Ladle refining and vacuum degassing. The making, shaping and treating of steel 11th Ed., pages 661–713.
- Krishnapisharody, K. and Irons, G. (2015). A model for slag eyes in steel refining ladles covered with thick slag. Metallurgical and Materials Transactions B, 46B(-):191–198.
- Ladyzhenskaya, O. A. (1967). New equations for the description of the motions of viscous incompressible fluids, and global solvability for their boundary value problems. Trudy Matematicheskogo Instituta Imeni VA Steklova, 102:85–104.
- Li, L., Liu, Z., Cao, M., and Li, B. (2015). Large eddy simulation of bubbly flow and slag layer behavior in ladle with discrete phase model (DPM)-volume of fluid (VOF) coupled model. JOM, 67(7):1459–1467.
- Marioni, L., Khalloufi, M., Bay, F., and Hachem, E. (2017). Two-fluid flow under the constraint of external magnetic field. International Journal of Numerical Methods for Heat & Fluid Flow, 27(11):2565–2581.
- Mazumdar, D., Dhandapani, P., and Sarvanakumar, R. (2017). Modeling and optimization of gas stirred ladle systems. ISIJ International, 57(2):286–295.
- Mazumdar, D. and Evans, J. (2003). Some considerations concerning empirical correlations for plume (spout) eye area in slag covered metallic melt. ISIJ International, 43(12):2076–2078.
- Mazumdar, D. and Evans, J. W. (2009). Modeling of steelmaking processes. CRC Press.
- Mazumdar, D. and Guthrie, R. I. L. (1985). Hydrodynamic modeling of some gas injection procedures in ladle metallurgy operations. Metallurgical Transactions B, 16(1):83–90.
- Mazumdar, D. and Guthrie, R. I. L. (1994). A Comparison of three mathematical modeling procedures for simulating fluid flow phenomena in bubble-stirred ladles. Metallurgical and Materials Transactions B, 25(2):308–312.
- Mazumdar, D. and Guthrie, R. I. L. (1995a). On the numerical computation of turbulent fluid flow in CAS steelmaking operations. Applied Mathematical Modelling, 19(9):519–524.
- Mazumdar, D. and Guthrie, R. I. L. (1995b). The physical and mathematical modelling of gas stirred ladle systems. ISIJ International, 35(1):1–20.

- Mazumdar, D., Guthrie, R. I. L., and Sahai, Y. (1993). On mathematical models and numerical solutions of gas stirred ladle systems. Applied Mathematical Modelling, 17(5):255–262.
- Mazumdar, D., Narayan, T., and Bansal, P. (1992). Mathematical modelling of mass transfer rates between solid and liquid in high-temperature gas-stirred melts. Applied Mathematical Modelling, 16(5):255–262.
- McNaught, A. and Wilkinson, A. (1997). Compendium of chemical terminology, compiled by blackwell scientific publications.
- Morand, H. J.-P. and Ohayon, R. (1995). Fluid structure interaction. John Wiley.
- Mukhopadhyay, A., Deb, P., Ghosh, A., Basu, B., Dutta, R., and Kumar, P. (2001). Prediction of temperature in secondary steelmaking : mathematical modelling of fluid flow and heat transfer in gas purged ladle. Steel Research, 72(5):192–199.
- Nadif, M., Orue, L., Lachmund, H., Abdullah, H., and Roessler, R. (2012). EUR 25091 – Online control of desulphurisation and degassing through ladle bubbling under vacuum. European Commission - Research fund for coal and steel series, pages 1–156.
- Nadif, M., Pusse, C., Domgin, J., Bertoletti, C., Perrin, E., Sevilla, D., and Cantarini, C. (2011). New stirring for an efficient steel desulfurization. In The 6th European Oxygen Steelmaking Conference, pages 1–13, Stockholm.
- Nguyet, T. M. et al. (2019). Time optimal control of the unsteady 3D Navier–Stokes–Voigt equations. Applied Mathematics & Optimization, 79(2):397–426.
- Norton, M. P. (2003). Fundamentals of noise and vibration analysis for engineers. Cambridge University Press, United Kingdom.
- Owusu, K. B., Haas, T., Gajjar, P., Eickhoff, M., Kowitwarangkul, P., and Pfeifer, H. (2019). Interaction of injector design, bubble size, flow structure, and turbulence in ladle metallurgy. Steel Research International, 90(2):1800346.
- Palovaara, T., Visuri, V.-V., and Fabritius, T. (2018). Physical modelling of gas injection in a ladle. In Proceedings of the 7th International Congress on Science and Technology of Steelmaking.
- Patil, S. P., Satish, D., Peranandhanathan, M., and Mazumdar, D. (2010). Mixing models for slag covered, argon stirred ladles. ISI International, 50(8):1117–1124.
- Powell, M. J. (1994). A direct search optimization method that models the objective and constraint functions by linear interpolation. In Advances in optimization and numerical analysis, pages 51–67. Springer.

- Powell, M. J. (2007). A view of algorithms for optimization without derivatives. Mathematics Today-Bulletin of the Institute of Mathematics and its Applications, 43(5):170–174.
- Pylvänäinen, M., Visuri, V.-V., Laurila, J., and Lienes, T. (2018). Vibrations-based prediction of desulfurization kinetics in a vacuum tank degasser. Unpublished.
- Pylvänäinen, M., Visuri, V.-V., Lienes, T., Laurila, J., Karioja, K., Pikkupeura, S., Ollila, S., and Fabritius, T. (2016). Vibration-based assessment of gas stirring intensity in ladle treatments. In Proceedings of the 5th International Conference on Process Development in Iron and Steelmaking. Swerea MEFOS, Luleå, Sweden.
- Ramasetti, E. K., Visuri, V.-V., Sulasalmi, P., Mattila, R., and Fabritius, T. (2019a). Modeling of the effect of the gas flow rate on the fluid flow and open-eye formation in a water model of a steelmaking ladle. Steel Research International, 90(2):1800365.
- Ramasetti, E. K., Visuri, V.-V., Sulasalmi, P., Palovaara, T., Gupta, A. K., and Fabritius, T. (2019b). Physical and cfd modeling of the effect of top layer properties on the formation of open-eye in gas-stirred ladles with single and dual-plugs. Steel Research International, pages 1–13.
- Rang, J. (2008). Pressure corrected implicit θ -schemes for the incompressible navier–stokes equations. Applied Mathematics and Computation, 201(1-2):747–761.
- Reynolds, O. (1895). IV. On the dynamical theory of incompressible viscous fluids and the determination of the criterion. Philosophical transactions of the Royal Society of London, 186:123–164.
- Richardson, L. F. (1922). Weather prediction by numerical process. Cambridge University Press.
- Rödl, S., Kleimt, B., Köchner, H., Jung, H.-P., and Klung, J.-S. (2016). Optimization of steel cleanliness during secondary steelmaking. Stahl und Eisen, 136(4):49–56.
- Saad, Y. (2003). Iterative methods for sparse linear systems, volume 82. SIAM.
- Sahai, Y. and Guthrie, R. I. (1982a). Hydrodynamics of gas stirred melts: Part I. Gas/liquid coupling. Metallurgical Transactions B, 13(2):193–202.
- Sahai, Y. and Guthrie, R. I. (1982b). Hydrodynamics of gas stirred melts: Part II. Axisymmetric flows. Metallurgical Transactions B, 13(2):203–211.
- Schroeder, P. W., John, V., Lederer, P. L., Lehrenfeld, C., Lube, G., and Schöberl, J. (2019). On reference solutions and the sensitivity of the 2D Kelvin–Helmholtz instability problem. Computers and Mathematics with Applications, 77(4):1010–1028.

- Sheng, Y. Y. and Irons, G. (1993). Measurement and modeling of turbulence in the gas/liquid two-phase zone during gas injection. Metallurgical Transactions B, 24:695–705.
- Subyago, G. B. and Irons, G. (2003). Spout eyes area correlation in ladle metallurgy. ISIJ International, 43(2):262–263.
- Sulasalmi, P., Karna, A., Fabritius, T., and Savolainen, J. (2009). CFD model for emulsification of slag into the steel. ISIJ International, 49(11):1661–1667.
- Sulasalmi, P., Visuri, V.-V., Kärnä, A., and Fabritius, T. (2015). Simulation of the effect of steel flow velocity on slag droplet distribution and interfacial area between steel and slag. Steel Research International, 86(3):212–222.
- Takechi, H. (1994). Metallurgical aspects on interstitial free sheet steel from industrial viewpoints. ISIJ Journal, 34(1):1–8.
- Tröltzsch, F. (2010). Optimal control of partial differential equations. Graduate studies in mathematics, 112.
- Tryggvason, G., Esmaeeli, A., Lu, J., and Biswas, S. (2006). Direct numerical simulations of gas/liquid multiphase flows. Fluid Dynamics Research, 38(9):660–681.
- Turkoglu, H. and Farouk, B. (1991). Mixing time and liquid circulation rate in steelmaking ladles with vertical gas injection. ISIJ International, 31(12):1371–1380.
- Valentin, P., Bruch, C., Kyrylenko, Y., Köchner, H., and Dannert, C. (2008). Influence of stirring gas in a 170-t ladle on mixing phenomena - formation and on-line control of open-eye at an industrial LD steel plant. Steel Research International, 80(8):2–8.
- Van der Vegt, J. J. and Van der Ven, H. (2002). Space-time discontinuous Galerkin finite element method with dynamic grid motion for inviscid compressible flows: I. General formulation. Journal of Computational Physics, 182(2):546–585.
- Wei, T. and Oeters, F. (1992). A model test for emulsion in gas-stirred ladles. Steel Research International, 63(2):60–68.
- Wichterle, K. (2010). Breakup of gas bubbles rising in molten metals. Steel Research International, 81(5):356–361.
- Wilbrandt, U. (2019a). Optimization with Navier–Stokes constraints. Unpublished notes, as of 13th March 2019.
- Wilbrandt, U. (2019b). Stokes-Darcy equations. Lecture Notes in Mathematical Fluid Mechanics. Birkhäuser/Springer, Cham. Analytic and numerical analysis.

- Wilbrandt, U., Bartsch, C., Ahmed, N., Alia, N., Anker, F., Blank, L., Caiazzo, A., Ganesan, S., Giere, S., Matthies, G., Meesala, R., Shamim, A., Venkatesan, J., and John, V. (2017). ParMooN – A modernized program package based on mapped finite elements. Computers and Mathematics with Applications, 74(1):74–88.
- Woo, J., Szekely, J., Castillejos, A., and Brimacombe, J. (1990). A study on the mathematical modeling of turbulent recirculating flows in gas-stirred ladles. Metallurgical Transactions B, 21(21B):269–277.
- Wuppermann, C., Giesselmann, N., Rückert, A., Pfeifer, H., Odenthal, H., and Hovestadt, E. (2012). A novel approach to determine the mixing time in a water model of an AOD converter. ISIJ International, 52(10):1817–1823.
- Wuppermann, C., Rückert, A., Pfeifer, H., and Odenthal, H. (2013). Physical and Mathematical Modeling of the Vessel Oscillation in the AOD Process. ISIJ International, 53(3):441–449.
- Xiao, Z., Peng, Y., and Liu, C. (1987). Modelling study of the entrapment phenomena at the slag-metal interface in the gas-stirred ladle. Chinese Journal of Metal Science and Technology, 3(4):187–193.
- Yenus, J., Brooks, G., and Dunn, M. (2016). Multivariate analysis of ladle vibration. Metallurgical and Materials Transactions B: Process Metallurgy and Materials Processing Science, 47(4):2681–2689.
- Yenus, J., Brooks, G., Dunn, M., Li, Z., and Goodwin, T. (2017). Study of low flow rate ladle bottom gas stirring using triaxial vibration signals. Metallurgical and Materials Transactions B: Process Metallurgy and Materials Processing Science, 49(1):1–11.
- Yonezawa, K. and Schwerdtfeger, K. (1996). Spout eyes formed by an emerging gas plume at the surface of a slag-covered metal melt. ISIJ International, 36(9):1127–1134.
- Yu, S. (2014). Numerical Modeling of Dehydrogenation and Denitrogenation in Industrial Vacuum Tank Degassers. PhD thesis, Aalto University.
- Yu, S., Zou, Z.-S., Shao, L., and Louhenkilpi, S. (2017). A theoretical scaling equation for designing physical modeling of gas-liquid flow in metallurgical L ladles. Steel Research International, 88(1):1600156.
- Zhu, M.-Y., Sawada, I., Yamasaki, N., and Hsiao, T.-C. (1996). Numerical simulation of three-dimensional fluid flow and mixing process in gas-stirred ladles. ISIJ International, 36(5):503–511.

Zusammenfassung der Dissertation

Diese Dissertation beschäftigt sich mit der mathematischen Modellierung, Simulation, und Optimierung eines wichtigen Prozesses der Stahlindustrie, nämlich dem Rühren der Stahlschmelze. In diesem Prozess wird Gas vom Boden des Rührkessels kontinuierlich eingespritzt. Durch den Auftrieb wird die Schmelze intensiv gerührt. Dieser Prozess wurde in der Literatur numerisch und experimentell eingehend studiert, sodass der Einfluss von Prozessparametern auf das Rühren besser verstanden ist und ein Fortschritt der industriellen Praxis erzielt werden konnte. Jedoch wurden optimale Steuerungsprobleme in diesem Bereich bisher nicht betrachtet. Der Beitrag der vorliegenden Dissertation besteht aus drei Teilen.

Erstens kann die Simulation mehrphasiger Strömungsmodelle numerisch aufwändig werden, sodass die optimale Steuerung solcher Strömungen numerisch nicht praktikabel ist. Deshalb beschränkt sich diese Dissertation auf vereinfachte einphasige Navier–Stokes Modelle. Drei Konfigurationen werden untersucht: eine 2d kartesische Konfiguration, wo der Effekt des Gasauftriebs durch eine inhomogene Dirichlet Randbedingung modelliert wird, eine 2d axialsymmetrische Konfiguration und eine 3d Konfiguration, bei der das Gas als Volumenkraft nachgebildet wird. Die numerischen Simulationen und der Vergleich mit experimentellen Daten der Literatur zeigen, dass alle drei Konfigurationen geeignete Ergebnisse liefern.

Zweitens werden optimale Steuerungsprobleme diskutiert. Hauptsächlich Schwierigkeiten sind zum einen die Formulierung des industriellen Problems und zum anderen die mathematische Formulierung der Kontroll- und Kostenfunktionale. Der Prozesskontrollparameter in der Praxis ist der Gasdurchfluss in der Schmelze. Dazu müssen noch einige Nebenbedingungen beachtet werden. Da der betrachtete Prozess physikalisch komplex ist, gibt es verschiedene, sich überlappende Ziele, etwa die Maximierung der Homogenität des Fluids, die Minimierung der Prozesszeit oder auch der Konzentration von Einschlüssen (Defekten). Die Kontrollvariablen, ihre Nebenbedingungen und die Ziele des Steuerungsproblems werden mathematisch übersetzt, was zu sogenannten “Box”-Nebenbedingungen führt, wobei verschiedene Kostenfunktionale für die Beschreibung der Mischungseffizienz vorgeschlagen werden. Numerische Simulationen werden durchgeführt, aus denen Schlussfolgerungen für die industrielle Praxis gezogen werden.

Der letzte Teil beschreibt eine im Rahmen der Zusammenarbeit mit dem industriellen Partner des Projektes durchgeführte Arbeit. Es wird ein Überblick über die hauptsächlichsten technologischen Lösungen für die Steuerung des Rührens gegeben, von welchen die Nutzung von Vibrationssensoren ausgewählt wird. Ein experimentelle Untersuchung von Vibrationen beim Mischen im Rührkessel wird durchgeführt. Die Ergebnisse erlauben es, einige praktische Empfehlungen für die industrielle Praxis zu geben und sie verbessern unser Verständnis von Vibrationsphänomenen für zukünftige Modellierungsarbeiten.

Selbstständigkeitserklärung

Ich versichere hiermit, alle Hilfsmittel und Hilfen angegeben zu haben, und die Arbeit selbstständig und ausschließlich auf Grundlage der angegebenen Hilfsmittel und Hilfen angefertigt zu haben. Des Weiteren versichere ich, die Arbeit oder Teile der Arbeit nicht schon einmal in einem früheren Promotionsverfahren eingereicht zu haben.

Berlin, 16. Juli 2019

Najib Alia